

Sheffield Hallam University

Study of electrostatically self-assembled thin films of CdS and ZnS nanoparticle semiconductors.

SURYAJAYA.,

Available from the Sheffield Hallam University Research Archive (SHURA) at:

<http://shura.shu.ac.uk/20410/>

A Sheffield Hallam University thesis

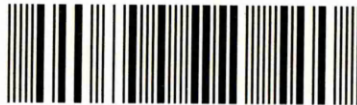
This thesis is protected by copyright which belongs to the author.

The content must not be changed in any way or sold commercially in any format or medium without the formal permission of the author.

When referring to this work, full bibliographic details including the author, title, awarding institution and date of the thesis must be given.

Please visit <http://shura.shu.ac.uk/20410/> and <http://shura.shu.ac.uk/information.html> for further details about copyright and re-use permissions.

Sheffield S1 1WB
101 876 069 5



Sheffield Hallam University
Learning and IT Services
Assets Centre City Campus
Sheffield S1 1WB

REFERENCE

Return to Learning Centre of issue
Fines are charged at 50p per hour

ProQuest Number: 10701056

All rights reserved

INFORMATION TO ALL USERS

The quality of this reproduction is dependent upon the quality of the copy submitted.

In the unlikely event that the author did not send a complete manuscript and there are missing pages, these will be noted. Also, if material had to be removed, a note will indicate the deletion.



ProQuest 10701056

Published by ProQuest LLC (2017). Copyright of the Dissertation is held by the Author.

All rights reserved.

This work is protected against unauthorized copying under Title 17, United States Code
Microform Edition © ProQuest LLC.

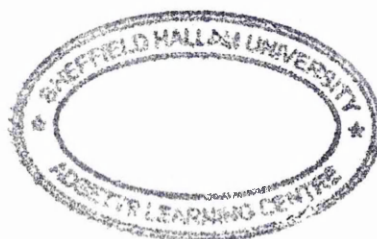
ProQuest LLC.
789 East Eisenhower Parkway
P.O. Box 1346
Ann Arbor, MI 48106 – 1346

**STUDY OF ELECTROSTATICALLY SELF-ASSEMBLED
THIN FILMS OF CdS AND ZnS NANOPARTICLE
SEMICONDUCTORS**

SURYAJAYA

A thesis submitted in partial fulfilment of the requirements of
Sheffield Hallam University
for the degree of Doctor of Philosophy

October 2007



**MATERIALS AND ENGINEERING RESEARCH INSTITUTE
FACULTY OF ACES**

DECLARATION

I hereby declare that this thesis submitted for the degree of Doctor of Philosophy is the result of my own research and that this thesis has been not submitted for a higher degree to any other university or institution.

Signed

Suryajaya

DEDICATION

To my parents:

Budi Hartono and Susanawati

To my brothers and sister:

Suryawati, Surya, Suryanata and their family

**STUDY OF ELECTROSTATICALLY SELF-ASSEMBLED THIN FILMS OF
CdS AND ZnS NANOPARTICLE SEMICONDUCTORS**

by

Suryajaya

ABSTRACT

In this work, CdS and ZnS semiconducting colloid nanoparticles coated with organic shell, containing either SO_3^- or NH_2^+ groups, were deposited as thin films using the technique of electrostatic self-assembly. The films produced were characterized with UV-vis spectroscopy and spectroscopic ellipsometry - for optical properties; atomic force microscopy (AFM) - for morphology study; mercury probe - for electrical characterisation; and photon counter - for electroluminescence study.

UV-vis spectra show a substantial blue shift of the main absorption band of both CdS and ZnS, either in the form of solutions or films, with respect to the bulk materials. The calculation of nanoparticles' radii yields the value of about 1.8 nm for both CdS and ZnS.

The fitting of standard ellipsometry data gave the thicknesses (d) of nanoparticle layers of around 5 nm for both CdS and ZnS which corresponds well to the size of particles evaluated from UV-vis spectral data if an additional thickness of the organic shell is taken into account. The values of refractive index (n) and extinction coefficient (k) obtained were about 2.28 and 0.7 at 633 nm wavelength, for both CdS and ZnS.

Using total internal reflection (TIRE), the process of alternative deposition of poly-allylamine hydrochloride (PAH) and CdS (or ZnS) layers could be monitored in-situ. The dynamic scan shows that the adsorption kinetic of the first layer of PAH or nanoparticles was slower than that of the next layer. The fitting of TIRE spectra gave

thicknesses of about 7 nm and 12 nm for CdS and ZnS, respectively. It supports the suggestion of the formation of three-dimensional aggregates of semiconductor nanoparticles intercalated with polyelectrolyte.

AFM images show the formation of large aggregates of nanoparticles, about 40-50 nm, for the films deposited from original colloid solutions, while smaller aggregates, about 12-20 nm, were obtained if the colloid solutions were diluted.

Current-voltage (I-V) and capacitance-frequency (C-f) measurements of polyelectrolyte/nanoparticles (CdS or ZnS) films suggest the tunnelling behaviour in the films while capacitance- voltage (C-V) and conductance-voltage (G-V) measurements suggest that these nanoparticles are conductive. The electroluminescence was detected in sandwich structures of (PAH/CdS/PAH)_N using a photon counting detector, but not in the case of ZnS films.

ACKNOWLEDGEMENTS

First and foremost, I would like to give my special appreciations and thanks to my director of studies, Dr. Alexei Nabok for his excellent supervision, guidance and support during my study, and for his excellent and fruitful discussion of various aspects of science, experimental procedures and the results obtained.

I would also like to thank, my supervisor, Dr. Aseel Hassan for his continuous encouragement, discussion, and advice. I would like to thank, Prof. Jan Evans-Freeman, as my second supervisor for her advice and help. I would like to express my thanks to Dr. Frank Davis, Cranfield University for his help, advice and suggestions in chemistry.

I would like to take this opportunity to thank all my PhD colleagues for their continuous support over the past three years: Syed Malik, Saharuddin Haron, Abbas Hashim, Alistair Vale and Alan Holloway. Many thanks are also to Anna Tsargorodskaya for her essential help and discussions regarding AFM and Ellipsometry measurements.

My special thanks also go to the TPSDP Project of Physics Study Program Lambung Mangkurat University, Indonesia for their financial support.

Finally, I would like to express my special thanks to my father, Budi Hartono and my mother, Susanawati for their continuing love, encouragement and support and also to my brothers and sister: Suryawati, Surya, Suryanata and their family.

LIST OF PUBLICATIONS

Journal Publications

1. *Suryajaya*, A. Nabok, F. Davis, A. Hassan, S.P.J. Higson, J. Evans-Freeman,
Optical Properties of Electrostatically Assembled Films of CdS and ZnS Colloid Nanoparticles, published online at: <http://arxiv.org/pdf/cond-mat/0604249>.
2. *Suryajaya*, A.V. Nabok, A. Tsargorodskaya, A.K. Hassan, F. Davis,
Electrostatically Self-assembled Films Containing II-VI Semiconductor Nanoparticles: Optical and Electrical Properties, **Thin Solid Films**, 2007 (in press).
3. *Suryajaya*, A. Nabok, F. Davis, A. Hassan, S.P.J. Higson, J. Evans-Freeman,
Optical and AFM Study of Electrostatically Assembled Films of CdS and ZnS Colloid Nanoparticles, **Journal of Materials Science** (submitted: 14th August 2007).

Conference Publications

1. *Multilayers of CdS and ZnS Nanoparticles Prepared by Reverse Micelle Method*, presented at “Britain's Younger Physicist at the House of Commons”, London, 15 November 2005
2. *Electrostatically Self-assembled Films Containing II-VI Semiconductor Nanoparticles: Optical and Electrical Properties*, Oral Presentation in The European Conference on Organised Films (ECOF 10), Riga Latvia, 21-24 August 2006.
3. *Electrostatically Self-Assembled Films Containing CdS and ZnS Colloid Nanoparticles: Optical and Electrical Properties*, presented at Nano-Molecular Analysis for Emerging Technologies II (NMAET II), National Physics Laboratory, Teddington, Middlesex United Kingdom, 17-18 October 2006.

CONTENTS

DEDICATION	i
ABSTRACT	ii
ACKNOWLEDGEMENTS	iv
LIST OF PUBLICATIONS	v
CONTENTS	vi
LIST OF FIGURES	x
LIST OF TABLES	xxiii

CHAPTER 1 INTRODUCTION

1.1. General introduction	1
1.2. The aims and objectives	3
1.3. Dissertation outline	4
REFERENCES	5

CHAPTER 2 PHYSICS OF SEMICONDUCTOR NANOSTRUCTURES

(LITERATURE REVIEW)

2.1. Introduction to semiconductors	10
2.1.1. Electrons in a crystal lattice	15
2.1.2. Direct and indirect semiconductors	17
2.1.3. Excitons in semiconductors and Bohr radius	18
2.2. Semiconductor nanostructures	22
2.2.1. High dispersity of nanocrystalline systems	22
2.2.2. Quantum confinement	24
2.2.2.1. Three-dimensional systems (bulk material)	25

2.2.2.2. Two-dimensional systems	30
2.2.2.3. One-dimensional systems (quantum wires)	32
2.2.2.4. Zero-dimensional systems (quantum dots)	34
2.3. Energy levels in a semiconductor quantum dot	35
2.4. Optical properties of quantum dots	37
2.5. Theoretical models of quantum confinement effects	40
2.5.1. The effective-mass approximation (EMA) model	40
2.5.2. Empirical pseudo-potential method (EPM)	44
2.5.3. Semi-empirical tight-binding calculations	50
2.5.4. Effective bond order model (EBOM)	51
2.6. Electron transport in quantum dots	53
2.6.1. Conductivity of thin films	53
2.6.2. Electron tunnelling in thin films	55
2.6.3. Resonance tunnelling	57
REFERENCES	60

**CHAPTER 3 ELECTROSTATIC SELF-ASSEMBLY DEPOSITION AND
OTHER METHODS FOR II-VI NANOSTRUCTURES'
FABRICATION (LITERATURE REVIEW)**

3.1. Introduction	64
3.2. Electrostatic self-assembly method	64
3.2.1. ESA deposition process	65
3.2.2. Kinetic of polyions adsorption	68
3.2.3. Nanoparticles/ polyelectrolites multilayers	75
3.3. Previous work on CdS and ZnS nanoparticles	76
REFERENCES	86

CHAPTER 4 EXPERIMENTAL METHODS

4.1. Introduction	94
4.2. Samples preparation	95
4.2.1. Preparation of CdS and ZnS colloid nanoparticles	95
4.2.2. Substrate modification procedures	97
4.2.3. Multilayer deposition procedures	97
4.3. Absorption spectra measurements	102
4.3.1. Basic principles of UV-Vis spectrophotometry	107
4.3.2. UV-Vis spectrophotometer–Varian Cary 50	108
4.3.3. Procedure of UV-Vis spectrophotometry measurements	110
4.4. Ellipsometry measurements	110
4.4.1. Reflectance and Brewster angle	111
4.4.2. Delta (Δ) and Psi (Ψ)	113
4.4.3. J. A. Woollam Variable Angle Spectroscopic Ellipsometry (VASE) - M2000V	114
4.4.4. Total internal reflection ellipsometry (TIRE)	118
4.4.5. Modelling and data analysis	122
4.4.6. The procedure of ellipsometry measurements	125
4.4.6.1. External reflection ellipsometry	125
4.4.6.2. Total internal reflection ellipsometry	126
4.5. Atomic force microscopy measurements	127
4.5.1. Basic principles	127
4.5.2. Imaging and measurements	132
4.5.3. Quantitative analysis on AFM Images	137
4.5.4. The procedure of AFM measurements	139
4.6. Electrical properties study using mercury probe	140

4.6.1. I-V characterisation	141
4.6.2. C-V characterisation	142
4.7. Electroluminescence measurements	142
REFERENCES	146

CHAPTER 5 RESULTS AND DISCUSSION

5.1. Introduction	150
5.2. Optical properties of CdS and ZnS nanoparticles	150
5.2.1. Absorption spectra measurements	150
5.2.1.1. Absorption spectra of the colloid and polyion solutions	150
5.2.1.2. Absorption spectra of CdS and ZnS nanoparticles embedded in organic films	156
5.2.2. Ellipsometry measurements	169
5.2.2.1. External Reflection Ellipsometry	169
5.2.2.2. Total Internal Reflection Ellipsometry	176
5.3. Morphology study using atomic force microscopy	186
5.4. Electrical study of CdS and ZnS nanoparticles	200
5.4.1. I-V characteristic of polyelectrolite films	200
5.4.2. I-V characteristic of films containing CdS (or ZnS) nanoparticles	204
5.4.3. C-V characteristic of films containing CdS (or ZnS) nanoparticles	208
5.5. Electroluminescence study	213
REFERENCES	222

CHAPTER 6 CONCLUSIONS AND SUGGESTIONS FOR FUTURE WORK

6.1. Conclusions	223
6.2. Suggestions for future work	225

LIST OF FIGURES

Figure 2.1.	Conductivities of conducting, semiconducting and insulating materials.	10
Figure 2.2.	Schematic band diagrams for a metal and semiconductor (or insulator).	11
Figure 2.3.	Elements found in elemental and compound semiconductors: group IV are elemental semiconductors; compound semiconductors can be formed by combining groups III and V or II and VI.	12
Figure 2.4.	Two possible structures of tetrahedral sites for a compound: bases of tetrahedral parallel and in line vertically (a); bases of tetrahedral parallel and 60° out of line vertically (b).	13
Figure 2.5.	Wurtzite structure formed from tetrahedral sites.	14
Figure 2.6.	Crystallographic lattice of zinc blende structure.	15
Figure 2.7.	The E versus k diagram for: free electrons (a) and electron inside a one-dimensional crystal (b).	15
Figure 2.8.	Direct electron transition in a direct band semiconductor with accompanied photon emission (a). Indirect electron transitions in an indirect semiconductor via defect level (b).	17
Figure 2.9.	Exciton movement in the semiconductor crystal.	20
Figure 2.10.	Schematic view of surface relaxation (a), resulting in changes in the lattice spacing in z direction, $l_0 > l_1 > l_2$, and surface reconstruction (b).	23
Figure 2.11.	Changes in the electron potential $V(x)$ upon surface reconstruction.	24
Figure 2.12.	Three-dimensional systems for bulk material.	25

Figure 2.13.	Distribution of electron states in bulk material.	27
Figure 2.14.	Calculation of the number of states with the wavenumbers less than k .	28
Figure 2.15.	Density of states D_{3d} for free electrons in 3-dimensional system.	30
Figure 2.16.	Two-dimensional system (a) ; Distribution of electronics states (b) ; Dispersion relation $E(k)$ - k (c) ; Density of states D_{2d} for free electrons (d) .	31
Figure 2.17.	One-dimensional solid (a) ; The distribution of states can be visualized as lines parallel to the k_x axes in the three-dimensional k -space (b) ; The dispersion relations, along the k_x -axes the energy band $E(k_x, k_y, k_z)$ is quasi-continuous, but along the k_y - and k_z -axes only certain energies exist (c) ; The density of states along the k_x -axes is proportional to $E^{-1/2}$ (d) .	33
Figure 2.18.	Zero-dimensional solid (a) ; All states (k_x, k_y, k_z) are discrete points in the three-dimensional k -space (b) ; Only discrete energy levels are allowed (c) ; Density of states $D_{0d}(E)$ contains delta functions (d) .	34
Figure 2.19.	Free charge carriers in a bulk semiconductor and in a quantum dot.	37
Figure 2.20.	Absorption (solid lines) and emission (dotted lines) spectra of colloid CdSe quantum dots of different size. The absorption peak of 2.3/ 3.8/ 4.0/ 4.6 nm diameter nanocrystals are at 507/ 547/ 580/ 605 nm, respectively, corresponding to the green/yellow/orange/red colour; the fluorescence peaks are respectively at 528/ 570/ 592/ 637 nm.	38
Figure 2.21.	Stokes shift.	39
Figure 2.22.	Schematic illustration of a dark exciton in semiconductors.	39

- Figure 2.23. Band structure of a zinc blende CdS spherical cluster having $R = 15$ Å near the top of the valence band. 47
- Figure 2.24. Allowed electron levels of wurtzite CdS spherical cluster with $R = 15$ Å. 48
- Figure 2.25. Comparison with the experimental data for CdS. The tight-binding model results are shown as a solid line, and those of the EMA model by a dash line. The experimental data are given as square and triangle points. 51
- Figure 2.26. Ground-state energies for excitons in CdS microcrystallites as a function of radius calculated using the EBOM. The confining potentials for the electrons and holes assumed to be equal, are shown as: (---) curve for the Lippens and Lannoo tight-binding model with $V = \infty$; (-----) curve obtained using Kayanuma's model; (■) experimental results from Ekimov et al.; (○) experimental results from Wang and Herron. 52
- Figure 2.27. Two configurations of conductivity measurements: planar (a) and sandwich (b) structure. 53
- Figure 2.28. The schematic of interdigitated electrodes. 54
- Figure 2.29. Quantum mechanical tunnelling through a: (a) thick barrier; (b) thin barrier. 55
- Figure 2.30. Models of electron tunnelling for different barriers: (a) rectangular; (b) trapezoidal; (c) triangular. 56
- Figure 2.31. Schematic diagram of resonance tunnelling. 58
- Figure 2.32. Band diagram and current-voltage characteristics of a resonant tunnelling under different bias conditions. 58

Figure 2.33.	I-V characteristic of a resonance tunnelling structure with each peak corresponding to the energy matching conditions $eV=E_i$ ($i=1, 2, 3$).	59
Figure 3.1.	The sequence of layer by layer electrostatic deposition.	66
Figure 3.2.	A typical kinetic profile of QCM measurements for polyions adsorption.	68
Figure 3.3.	Optical absorbance comparison of 20 bilayer (PDDA/Poly S-119) films fabricated using different dipping times.	69
Figure 3.4.	Ellipsometry comparison of (PDDA/Poly S-119) films fabricated using different dipping times.	70
Figure 3.5.	UV/vis absorption spectra of PVP/PMA multilayer thin films.	71
Figure 3.6.	UV/vis absorption spectra of PDDA/C60 multilayer thin films.	71
Figure 3.7.	Ellipsometry comparison of (Poly R-478/PDDA) films dried in a stream of nitrogen after deposition of each monolayer (dried) and dried only for measurement purposes (nondried).	72
Figure 3.8.	UV/vis absorbance spectra of 50 bilayer (Poly R-478/PDDA) films dried in a stream of nitrogen after deposition of each monolayer (dried) and dried only for measurement purposes (nondried).	73
Figure 3.9.	Effect of drying on the layer interpenetration.	73
Figure 3.10.	UV/vis absorbance spectra of 30 bilayer (Poly R-478/PDDA) film before and after water submersion for 21 hours.	74
Figure 3.11.	Basic ESA schematic for the buildup of multilayer assemblies by consecutive adsorption of cationic polyelectrolytes and anionic nanoparticles.	76

Figure 3.12.	The absorption spectra of CdS formed in SiO ₂ by ion implantation at different implanted dose and bulk CdS [70]. The arrow indicates the increase in the implantation dose.	78
Figure 3.13.	PL, PL excitation, and optical absorption spectra of the low doped sample (a) and the high-doped (b) samples at 14 K.	79
Figure 3.14.	Schematics for the capping of a nanoparticle by alkanethiol molecules.	82
Figure 3.15.	Absorption spectra of CdS and ZnS taken at different times (from 0.02 to 3600 s) after mixing the reactants.	85
Figure 4.1.	The route of making colloid nanoparticles solution.	96
Figure 4.2.	Electrostatic self-assembly deposition cycle.	98
Figure 4.3.	Deposition of colloid nanoparticles CdS-SO ₃ ⁻ (a) and CdS-NH ₂ ⁺ (b).	99
Figure 4.4.	Deposition of polyelectrolyte films (a) and polyelectrolyte/nanoparticles sandwich structures: 1-P-1 (b), 2-P-2 (c), 3-P-3 (d).	102
Figure 4.5.	Excitation of electrons between molecular orbitals.	103
Figure 4.6.	Vibrational and rotational levels superimposed with the electronic levels.	104
Figure 4.7.	Absorption transitions between impurities and bands: (a) donor to conduction band; (b) valence band to acceptor; (c) valence band to donor; and (d) acceptor to conduction band.	105
Figure 4.8.	Basic principle of UV-Vis Spectrophotometry.	107
Figure 4.9.	Schematic diagram of Varian Cary 50 UV-Vis Spectrophotometer.	109
Figure 4.10.	Schematic of the ellipsometry experiment.	111
Figure 4.11.	Reflections and transmissions in multiple interfaces samples.	112

Figure 4.12. Ellipsometer Configurations.	115
Figure 4.13. Schematic of Variable Angle Spectroscopy Ellipsometry.	117
Figure 4.14. Graphical representation of wavevector matching.	118
Figure 4.15. A typical SPR curve of metal film showing the critical angle (θ_c) and the angle of incidence minimum (θ_0).	120
Figure 4.16. Experimental SPR curves for gold film, and those of LB films of calix-4-resorcinarene deposited on it. The number of monolayers is indicated on the corresponding curve. The inset presents the dependence of the resonance shift ($\Delta\theta_{SPR}$) on the thickness of the LB films.	121
Figure 4.17. Ellipsometry modeling process	122
Figure 4.18. Model of thin films on solid substrate.	123
Figure 4.19. The illustration of choosing guess values as close to the actual values as possible so that the algorithm can settle on a best fit instead of a local minima.	124
Figure 4.20. Total internal reflection ellipsometry set-up.	126
Figure 4.21. Schematic of Atomic Force Microscopy.	128
Figure 4.22. The most widely used form of cantilever deflection detection.	129
Figure 4.23. The effect of applied voltage on piezoelectric materials.	130
Figure 4.24. Non ideal behaviour of piezo materials: hysteresis (above) and creep (bottom).	130
Figure 4.25. Block diagram of an x-y closed loop scanner configuration.	131
Figure 4.26. Potential energy diagram of a probe/sample system.	132
Figure 4.27. Schematic of the contact mode AFM.	133
Figure 4.28. Schematic of the tapping mode AFM.	135

Figure 4.29.	Schematic of the non-contact mode AFM.	136
Figure 4.30.	Illustration of the particle size analysis at the selected height.	138
Figure 4.31.	Nanoscope IIIa AFM instrument.	139
Figure 4.32.	Mercury probe experimental set-up.	141
Figure 4.33.	The energy bandgap diagrams of luminescence for: direct bandgap (a) and indirect bandgap (b) materials.	142
Figure 4.34.	The principle of the electroluminescence set-up	144
Figure 4.35.	Electroluminescence experimental set-up.	145
Figure 5.1.	Figure 5.1. Absorption spectra of capping agents, CdS SO_3^- and CdS NH_2^+ colloid solutions (diluted 500x).	151
Figure 5.2.	Absorption spectra of ZnS SO_3^- and ZnS NH_2^+ colloid solution (diluted 500x).	152
Figure 5.3.	Gaussian fitting of the spectra of CdS- SO_3^- (a) and ZnS- SO_3^- (b) solutions. The experimental data (black line) was fitted using 5 Gaussian peaks (green line) and the result was shows by the red line.	154
Figure 5.4.	Absorption spectra of PAH and PSS solution (diluted 500x).	156
Figure 5.5.	UV-vis absorption spectra of PAH/ CdS- SO_3^- film. The numbers near respective spectra correspond to the number of polyelectrolyte/nanoparticle bilayers.	157
Figure 5.6.	UV-vis absorption spectra of PAH/ CdS- SO_3^- films. The numbers near respective spectra correspond to the number of polyelectrolyte/nanoparticle bilayers.	158
Figure 5.7.	UV-vis absorption spectra of PAH/ PSS/CdS- NH_2^+ film. The numbers near respective spectra correspond to the number of polyelectrolyte/nanoparticle bilayers.	158

- Figure 5.8. UV-vis absorption spectra of PAH/ ZnS-SO₃⁻ film. The numbers near respective spectra correspond to the number of polyelectrolyte/nanoparticle bilayers. 159
- Figure 5.9. UV-vis absorption spectra of PAH/ ZnS-NH₂⁺ films. The numbers near respective spectra correspond to the number of polyelectrolyte/nanoparticle bilayers. 160
- Figure 5.10. Gaussian fitting of the spectra of the first layer of CdS-SO₃⁻ (a) and the first layer of ZnS-SO₃⁻ (b). The experimental data (black line) was fitted using several Gaussian peaks (green line) and the result was shows by the red line. 161
- Figure 5.11. Alternative deposition of positively and negatively charged CdS (a) and ZnS (b) nanoparticles without intermediate layers of polyelectrolyte. 163
- Figure 5.12. Absorption spectra of polyelectrolyte/CdS nanoparticles structures.
 1 PAH/CdS SO₃⁻
 2 PAH/CdS SO₃⁻/PAH/PSS/CdS NH₂⁺
 3 PAH/CdS SO₃⁻/PAH/PSS/CdS NH₂⁺/PSS/PAH/CdS SO₃⁻
 4 PAH/CdS SO₃⁻/PAH/PSS/CdS NH₂⁺/PSS/PAH/CdS SO₃⁻
 /PAH/PSS/CdS NH₂⁺ 164
- Figure 5.13. Absorption spectra of polyelectrolyte/CdS nanoparticles structures.
 1 PAH/CdS SO₃⁻
 2 PAH/CdS SO₃⁻/PAH/PSS/CdS NH₂⁺
 3 PAH/CdS SO₃⁻/PAH/PSS/CdS NH₂⁺/PSS/CdS NH₂⁺
 4 PAH/CdS SO₃⁻/PAH/PSS/CdS NH₂⁺/PSS/CdS
 NH₂⁺/PSS/PAH/CdS SO₃⁻ 165
- Figure 5.14. Absorption spectra of polyelectrolyte/CdS nanoparticles structures.
 1 PAH/PSS/CdS NH₂⁺
 2 PAH/PSS/CdS NH₂⁺/ PSS/PAH/CdS SO₃⁻
 3 PAH/PSS/CdS NH₂⁺/ PSS/PAH/CdS SO₃⁻/PAH/PSS/CdS NH₂⁺
 4 PAH/PSS/CdS NH₂⁺/ PSS/PAH/CdS SO₃⁻/ PAH/PSS/CdS NH₂⁺
 PSS/PAH/CdS SO₃⁻ 166

- Figure 5.15. Absorption spectra of polyelectrolyte/CdS nanoparticles structures.
 1 PAH/PSS/CdS NH_2^+
 2 PAH/PSS/CdS NH_2^+ / PSS/PAH/CdS SO_3^-
 3 PAH/PSS/CdS NH_2^+ / PSS/PAH/CdS SO_3^- /PAH/CdS SO_3^-
 4 PAH/PSS/CdS NH_2^+ / PSS/PAH/CdS SO_3^- /PAH/CdS SO_3^-
 /PAH/PSS/CdS NH_2^+ 166
- Figure 5.16. Absorption spectra of polyelectrolyte/CdS nanoparticles structures.
 1 PAH/CdS SO_3^-
 2 PAH/CdS SO_3^- /CdS NH_2^+
 3 PAH/CdS SO_3^- /CdS NH_2^+ /PAH/CdS SO_3^- /CdS NH_2^+ 167
- Figure 5.17. Absorption spectra of polyelectrolyte/CdS nanoparticles structures.
 1 PAH/PSS/CdS NH_2^+
 2 PAH/PSS/CdS NH_2^+ / CdS SO_3^- 167
- Figure 5.18. Absorption spectra of mixed CdS and ZnS structures.
 1 PAH/CdS SO_3^-
 2 PAH/CdS SO_3^- /PAH/ZnS SO_3^-
 3 PAH/CdS SO_3^- /PAH/ZnS SO_3^- /PAH/CdS SO_3^-
 4 PAH/CdS SO_3^- /PAH/ZnS SO_3^- /PAH/CdS SO_3^- /PAH/ZnS SO_3^-
 5 PAH/CdS SO_3^- /PAH/ZnS SO_3^- /PAH/CdS SO_3^- /PAH/ZnS SO_3^-
 /PAH/CdS SO_3^- 168
- Figure 5.19. Typical $\psi(\lambda)$ and $\Delta(\lambda)$ ellipsometric spectra of a silicon substrate. 169
- Figure 5.20. Typical $\Delta(\lambda)$ (a) and $\Psi(\lambda)$ (b) ellipsometric spectra of a silicon substrate (1), and consecutively deposited layers on top: 1st layer of PAH (2), 1st layer of ZnS nanoparticles (3), 2nd layer of PAH (4), 2nd layer of ZnS nanoparticles (5). 170
- Figure 5.21. Ellipsometry fitting model for silicon/polyelectrolites/CdS (or ZnS). 171
- Figure 5.22. n and k curves obtained from the fitting for CdS (a) and ZnS (b). 175
- Figure 5.23. Typical $\psi(\lambda)$ and $\Delta(\lambda)$ TIRE spectra of a chromium/gold coated glass substrate. 176
- Figure 5.24. $\Delta(t)$ and $\psi(t)$ dependencies at 721.47 nm for the deposition of the 1st PAH layer (a) and the 2nd PAH layer (b). 177
- Figure 5.25. $\Delta(t)$ dependencies at selected wavelengths (shown near respective curves) for 1st CdS layer (a) 2nd CdS (b) 3rd CdS (c). 179

Figure 5.26.	$\Delta (t)$ dependencies at selected wavelengths (shown near respective curves) for 1 st ZnS layer (a) 2 nd ZnS (b) 3 rd ZnS (c).	180
Figure 5.27.	A typical set of $\Psi (\lambda)$ (a) and $\Delta (\lambda)$ (b) spectra for consecutive deposition of PAH /CdS films.	181
Figure 5.28.	A typical set of $\Psi (\lambda)$ (a) and $\Delta (\lambda)$ (b) spectra for consecutive deposition of and PAH/ZnS films.	182
Figure 5.29.	Ellipsometry fitting model for TIRE measurements.	183
Figure 5.30.	Tapping mode AFM images (1 μ m in size) of silicon.	186
Figure 5.31.	Roughness analysis of the AFM images of silicon.	187
Figure 5.32.	Tapping mode AFM images (1 μ m in size) of the first PAH layer.	187
Figure 5.33.	Roughness analysis of tapping mode AFM images (1 μ m in size) of the first PAH layer with different chosen areas: substrate (a) and film (b).	188
Figure 5.34.	Tapping mode AFM images (1 μ m in size) of consecutively deposited layers of: PAH (a), 1 st PSS (b), 1 st CdS-NH ₂ ⁺ (c), 2 nd PSS (d), 2 nd CdS-NH ₂ ⁺ (e), and 3 rd PSS (f).	190
Figure 5.35.	Section analysis of tapping mode AFM images (1 μ m in size) of the first CdS NH ₂ ⁺ layer.	191
Figure 5.36.	Particles analysis of the AFM image of the first CdS-NH ₂ ⁺ layer.	192
Figure 5.37.	Tapping mode AFM images (1 μ m in size) of consecutively deposited layers of: PAH (a), 1 st ZnS-SO ₃ ⁻ (b), 2 nd PAH (c), 2 nd ZnS-SO ₃ ⁻ (d), and 3 rd PAH (e).	193
Figure 5.38.	Surface roughness of CdS (a) and ZnS (b) multilayer as a function of number of layer.	195

Figure 5.39. The formation of aggregates of electrically charged nanoparticles by intercalation with polyelectrolytes.	196
Figure 5.40. Tapping mode AFM images (1 μ m in size) of CdS-NH ₃ ⁺ layer deposited from diluted colloid solutions: 100 times (a), 500 times (b).	197
Figure 5.41. Roughness analysis of tapping mode AFM image (1 μ m in size) of 500 times diluted CdS-NH ₃ ⁺ colloid solution monolayer film.	198
Figure 5.42. Particle analysis of tapping mode AFM image (1 μ m in size) of 500 times diluted CdS-NH ₃ ⁺ colloid solution monolayer film.	198
Figure 5.43. The effect of finite radius of the tip on the observed AFM features.	199
Figure 5.44. Typical DC I-V characteristics of ITO/(PAH/PSS) _N /Hg structure.	200
Figure 5.45. Typical DC I-V characteristics of ITO/(PAH/PSS) _N /Hg structure (a) and the same graph in semi-logarithmic scale (b).	201
Figure 5.46. The dependence of the current at 0.5 V on the number of polyelectrolyte layers in the ITO/(PAH/PSS) _N /Hg structure (a) and $\ln I$ vs thickness (W) (b).	203
Figure 5.47. Typical DC I-V characteristics (the voltage sweep range: - 0.5 to 1 V, step size: 5 mV) of PAH film compared to the films containing CdS (or ZnS) nanoparticles.	204
Figure 5.48. Typical DC I-V characteristics (the voltage sweep range: - 0.5 to 1 V, step size: 5 mV) of the films: polyelectrolyte/CdS/polyelectrolyte (a), and polyelectrolyte/ZnS/polyelectrolyte (b).	205

Figure 5.49.	Typical DC I-V characteristics of PAH/PSS/ZnS NH_2^+ /PSS/PAH, voltage sweep from 0 to -0.5 volt, step size 5 mV (a), a section of the graph zoomed in (b). The curves 1, 2, 3 and 4 correspond to consecutive measurements.	207
Figure 5.50.	Schematic diagram of nanoparticles charging.	208
Figure 5.51.	C-V characteristic of sandwich structures. (ITO/insulator/CdS /insulator/Hg) (a) and (ITO/insulator/ZnS /insulator/Hg) (b).	209
Figure 5.52.	G-V characteristic of sandwich structures (ITO/insulator/CdS /insulator/Hg) (a) and (ITO/insulator/ZnS /insulator/Hg) (b).	211
Figure 5.53.	C-f characteristic of sandwich structures (ITO/insulator/CdS /insulator/Hg) (a) and (ITO/insulator/ZnS /insulator/Hg) (b).	212
Figure 5.54.	Schematic diagram of electroluminescence experiment set-up.	213
Figure 5.55.	I-V measurements of the electroluminescence samples.	214
Figure 5.56.	The dark count level of the Hamamatsu instrument of averaged 22 photons per second.	215
Figure 5.57.	The electroluminescence for a sandwich structure of [PAH-(CdS-PAH) ₃] on TiO ₂ .	215
Figure 5.58.	The electroluminescence for a sandwich structure of [PAH-(CdS-PAH) ₃] on TiO ₂ with the voltage switch on and off.	216
Figure 5.59.	The electroluminescence for a sandwich structure of [PAH-(CdS-PAH) ₁₀] on ITO with different frequencies signal.	217
Figure 5.60.	Results of several tests of the electroluminescence for a sandwich structure of [PAH-(CdS-PAH) ₃] on TiO ₂ .	217
Figure 5.61.	The effect of step input voltage to EL intensity.	218
Figure 5.62.	The electroluminescence intensity as function of the input voltage.	219

Figure 5.63. The photon count for a sandwich structure of [PAH-(CdS-PAH) ₃] on ITO.	220
Figure 5.64. The photon count for a sandwich structure of 10 layers of CdS.	220
Figure 5.65. The photon count for a sandwich structure of 20 layers of CdS.	220
Figure 5.66. The electroluminescence intensity as function of number of layers.	221

LIST OF TABLES

Table 3.1.	The most common polyions used for ESA deposition.	67
Table 4.1.	Samples combination of nanoparticles (CdS and ZnS) and polyelectrolytes (PAH and PSS).	100
Table 5.1.	Energy gap, electron and hole effective masses for CdS and ZnS.	153
Table 5.2.	Energy gap and the radius of nanoparticles obtained by Gaussian fitting of the absorption spectra of CdS and ZnS solution.	155
Table 5.3.	Energy gap and the particles' size obtained by Gaussian fitting of the absorption spectra of CdS and ZnS films.	162
Table 5.4.	Ellipsometry data fitting for PAH/CdS-SO ₃ ⁻ films.	173
Table 5.5.	Ellipsometry data fitting for PAH/ZnS-SO ₃ ⁻ films.	173
Table 5.6.	TIRE data fitting for PAH/CdS SO ₃ ⁻ films.	184
Table 5.7.	TIRE data fitting for PAH/ZnS SO ₃ ⁻ films.	185
Table 5.8.	Summary of roughness parameters of polyelectrolyte/CdS films.	194
Table 5.9.	Summary of roughness parameters of polyelectrolyte/ZnS films.	194
Table 5.10.	Thickness and current values of polyelectrolyte layers (PAH/PSS).	202

INTRODUCTION

1.1. GENERAL INTRODUCTION

In the last decade, research on design and fabrication of nanostructured materials has rapidly grown and attracted much attention from many research groups [1]. Metal and semiconductor nanoparticles, particularly, have been generating continuous interest because of their unique electrical and optical properties [2, 3]. Various techniques have been developed, in order to prepare metal and semiconductor nanoclusters as dispersions in organic or inorganic media or as aggregates [4, 5]. Werner Kern and Klaus K. Schuegraf [6] classified the deposition techniques in three main groups: pure physical, pure chemical and physical-chemical methods. Physical methods, such as Molecular Beam Epitaxy (MBE), Metal-Organic Chemical Vapour Deposition (MOCVD) or Sputtering deposition, are much more complicated and expensive as compared to chemical methods.

Because of simplicity and economical reasons, chemical methods have rapidly grown as an alternative to physical methods to synthesise and deposit semiconductor nanoparticles. Various chemical techniques have been already developed such as chemical bath deposition [7, 8], Langmuir-Blodgett films [9-13], colloid synthesis [14, 15], reverse micelle [16, 17], core shell [18-20] and electrostatic self-assembly [21-65]. The latter method of electrostatic self-assembly (ESA) is particularly interesting, because it mimics the natural processes of molecular bonding, where the molecules adjust themselves to minimum thermodynamic conditions. The structures are stabilized by anion and cation groups as complementary units. The composition of each layer can be controlled by the incorporation of appropriately chosen molecules [25], and the

structure of each layer can be manipulated by adjusting the deposition parameters [21, 29, 35, 39]. As a result, a very good nanosized structures, as precise as MBE, could be produced at a much lower cost. Therefore, electrostatic self-assembly has been used for the deposition of ultrathin films containing different type of molecules such as charged polymers (polyions) [21-39], dyes [40-42], nanoparticles (metallic, semiconducting, magnetic, insulating) and clay nanoplates [43-55], and bio-objects (proteins, DNA, virus) [56-65].

Nanostructured II-VI semiconductor materials have been and still are the subject of an intensive study because of their chemical stability at room temperature compared to unstable III-V compounds; the range of bandgap energies that encompass the entire visible spectrum, and direct bandgap. By far, nanoparticles of cadmium sulfide (CdS) and zinc sulfide (ZnS) are the most studied systems among the semiconducting nanoparticles. The size dependent effect of these nanoparticles' optical and electronic properties have been studied experimentally and theoretically for possible application in photovoltaic and electroluminescence devices as well as other optoelectronics applications [66-72].

Although there are many publications on different methods of synthesis and different physical properties of CdS and ZnS nanoparticles such as optical absorption, luminescence, and electrical properties, the use of electrically charged CdS and ZnS nanoparticles, suitable for electrostatic self-assembly, is rather rare. The characterisation of CdS and ZnS or mixed of CdS-ZnS electrostatically assembled multilayer was not extensive. The study of optical properties of such nanostructure using spectroscopic ellipsometry (especially highly sensitive total internal reflection ellipsometry) has never been attempted.

In this study, CdS and ZnS nanoparticles were prepared by aqueous-phase synthesis and deposited on solid substrate using the electrostatic self-assembly

technique. The optical properties of these thin films were studied using UV-Vis spectroscopy and spectroscopic ellipsometry along with the electrical characterisation using the mercury probe, and atomic force microscopy (AFM) morphology study. The use of a nondestructive mercury contact (instead of traditional evaporated metal contacts) for electrical measurements in electrostatically deposited films was recently proposed by Nabok [73, 74] and established in the research group. This method allows the measurements of tunnelling current in ultrathin films containing CdS and ZnS nanoparticles which have not been attempted before.

1.2. AIMS AND OBJECTIVES

The main purposes of this research are to fabricate CdS and ZnS semiconductor nanostructures by low-cost electrostatic self-assembly technique, and to study morphology, optical and electrical properties of these materials with a view of possible applications in light-emitting devices.

The objectives of this research are:

1. To fabricate multilayers of CdS and ZnS thin films by using electrostatic self-assembly method.
2. To characterise the optical properties and to evaluate the thickness (d), refractive index (n) and extinction coefficient (k) parameters of CdS and ZnS nanostructures, by using UV-Vis spectrophotometry and Ellipsometry.
3. To study the morphology of CdS and ZnS nanostructures such as the uniformity, particles' size, and roughness of the thin films using AFM.
4. To investigate the electrical behaviour of the multilayered nanostructures using the mercury probe technique.
5. To measure the electroluminescence of the nanoparticles deposited onto solid substrates.

1.3. DISSERTATION OUTLINE

This dissertation is organized into six chapters.

Chapter 1 presents a general introduction to the thesis. It provides the background, motivation, aim and objectives of the research.

Chapter 2 presents the review of the theory of semiconductor nanostructures and their special properties due to high dispersity of nanocrystalline systems and quantum confinement. In this chapter, a basic theory of semiconductors is briefly introduced followed by the theoretical background of semiconductor nanostructure systems and their energy levels. Theoretical models of quantum confinement effects along with the optical and electrical properties in nanoparticles semiconductor were also reviewed.

Chapter 3 contains literature review of deposition and characterisation methods of CdS and ZnS films. The details of ESA process were discussed. The remaining part of the chapter presents the previous work on CdS and ZnS thin films using different depositions and characterisations methods.

Chapter 4 describes the theoretical background, procedure, and details of the experimental techniques for samples' preparation and investigation. It describes the details of the aqueous-phase synthesis of colloid semiconductor nanoparticles. The details of the substrates modification procedure and fabrication of CdS and ZnS multilayers using ESA method along with the experimental details of each characterisation method are also given there.

Chapter 5 contains the results and analysis of optical properties, morphology, electrical and electroluminescence characteristics of CdS and ZnS thin films.

Chapter 6 concludes this dissertation with the summary of all results obtained. In addition, the suggestions for further work in this area are made.

REFERENCES

1. Wilson M., et al. *Nanotechnology : basic science and emerging technologies*. Sydney: Chapman & Hall/CRC, 2002.
2. Alivisatos A. P. "Perspectives on the physical chemistry of semiconductor nanocrystals." *Journal of Physical Chemistry* 100 (1996): 13226-13239.
3. Yoffe A. D. "Low-dimensional systems: Quantum size effects and electronic properties of semiconductor microcrystallites (zero-dimensional systems) and some quasi-two-dimensional systems." *Advances in Physics* 51 (2002): 799-890.
4. Murray C. B., Norris D. J., and Bawendi M. G. "Synthesis and characterization of nearly monodisperse CdE (E = S, Se, Te) semiconductor nanocrystallites." *Journal of the American Chemical Society* 115 (1993): 8706-8715.
5. Kickelbick G. "Concepts for the incorporation of inorganic building blocks into organic polymers on a nanoscale." *Progress in Polymer Science* 28 (2003): 83-114.
6. Kern W., Schuegraf, Klaus K. 15 August 2007.
<http://www.williamandrew.com/pdf/1442_chapter.pdf>.
7. Dona J. M., and Herrero J. "Chemical bath codeposited CdS-ZnS film characterization." *Thin Solid Films* 268 (1995): 5-12.
8. Ramaiah Subba K., Pilkington R. D., Hill A. E., Tomlinson R. D., and Bhatnagar A. K. "Structural and optical investigations on CdS thin films grown by chemical bath technique." *Materials Chemistry and Physics* 68 (2001): 22-30.
9. Erokhin V., Facci P., Gobbi L., Dante S., Rustichelli F., and Nicolini C. "Preparation of semiconductor superlattices from LB precursor." *Thin Solid Films* 327-329 (1998): 503-505.
10. Erokhina S., Erokhin V., and Nicolini C. "Electrical properties of thin copper sulfide films produced by the aggregation of nanoparticles formed in LB precursor." *Colloids and Surfaces A: Physicochemical and Engineering Aspects* 198-200 (2002): 645-650.
11. Nabok A. V., Richardson T., Davis F., and Stirling C. J. M. "Cadmium sulfide nanoparticles in Langmuir-Blodgett films of calixarenes." *Langmuir* 13 (1997): 3198-3201.
12. Nabok A. V., Richardson T., McCartney C., Cowlam N., Davis F., Stirling C. J. M., Ray A. K., Gacem V., and Gibaud A. "Size-quantization in extremely small CdS clusters formed in calixarene LB films." *Thin Solid Films* 327-329 (1998): 510-514.
13. Nabok A. V., Iwantono B., Hassan A. K., Ray A. K., and Wilkop T. "Electrical characterisation of LB films containing CdS nanoparticles." *Materials Science and Engineering C* 22 (2002): 355-358.
14. Huang H., Dorn A., Bulovic V., and Bawendi M. G. "Electrically driven light emission from single colloidal quantum dots at room temperature." *Applied Physics Letters* 90 (2007).
15. Winter J. O., Gomez N., Gatzert S., Schmidt C. E., and Korgel B. A. "Variation of cadmium sulfide nanoparticle size and photoluminescence intensity with altered aqueous synthesis conditions." *Colloids and Surfaces A: Physicochemical and Engineering Aspects* 254 (2005): 147-157.

16. Hirai T., Sato H., and Komasaawa I. "Mechanism of Formation of CdS and ZnS Ultrafine Particles in Reverse Micelles." *Industrial & Engineering Chemistry Research* 33 (1994): 3262-3266.
17. Zhang J., Sun L., Liao C., and Yan C. "Size control and photoluminescence enhancement of CdS nanoparticles prepared via reverse micelle method." *Solid State Communications* 124 (2002): 45-48.
18. Kaltenpoth G., Himmelhaus M., Slansky L., Caruso F., and Grunze M. "Conductive core-shell particles: An approach to self-assembled mesoscopic wires." *Advanced Materials* 15 (2003): 1113-1118.
19. Liang Z., Susha A., and Caruso F. "Gold nanoparticle-based core-shell and hollow spheres and ordered assemblies thereof." *Chemistry of Materials* 15 (2003): 3176-3183.
20. Shih-Yuan Lu, Mei-Ling Wu, and Hsin-Lung Chen. "Polymer nanocomposite containing CdS-ZnS core-shell particles: Optical properties and morphology." *Journal of Applied Physics* 93 (2003): 5789-5793.
21. Lvov Y., Decher G., and Mohwald H. "Assembly, structural characterization, and thermal behavior of layer-by-layer deposited ultrathin films of poly(vinyl sulfate) and poly(allylamine)." *Langmuir* 9 (1993): 481-486.
22. Lvov Y., Haas H., Decher G., MÖhwald H., and Kalachev A. "Assembly of Polyelectrolyte Molecular Films onto Plasma-Treated Glass." *J. Phys. Chem.* 97 (1993): 12835-12841.
23. Lvov Y., Essler F., and Decher G. "Combination of polycation/polyanion self-assembly and Langmuir-Blodgett transfer for the construction of superlattice films." *Journal of Physical Chemistry* 97 (1993): 13773-13777.
24. Lvov Y. M. and Decher G. "Assembly of multilayer ordered films by alternating adsorption of oppositely charged macromolecules." *Crystallography Reports* 39 (1994): 628.
25. Decher G., Lvov Y., and Schmitt J. "Proof Of Multilayer Structural Organization In Self-Assembled Polycation-Polyanion Molecular Films." *Thin solid films* 244 (1994): 772-777.
26. Mao G., Tsao Y., Tirrell M., Davis H., Hessel V., and Ringsdorf H. "Self-assembly of photopolymerizable bolaform amphiphile mono-and multilayers." *Langmuir* 9 (1993): 3461-1470.
27. Tronin A., Lvov Y., and Nicolini C. "Ellipsometry and x-ray reflectometry characterization of self-assembly process of polystyrenesulfonate and polyallylamine." *Colloid and Polymer Science* 272 (1994): 1317-1321.
28. Hong J. D., Lowack K., Schmitt J., and Decher G. "Layer-by-layer deposited multilayer assemblies of polyelectrolytes and proteins: from ultra thin films to protein arrays." *Progress in Colloid & Polymer Science* 93 (1993): 98-102.
29. Schmitt J., Grunewald T., Decher G., Pershan P. S., Kjaer K., and Losche M. "Internal structure of layer-by-layer adsorbed polyelectrolyte films: A neutron and X-ray reflectivity study." *Macromolecules* 26 (1993): 7058-7063.
30. Sano M., Lvov Y., and Kunitake T. "Formation of ultrathin polymer layers on solid substrates by means of polymerization-induced epitaxy and alternate adsorption." *Ann. Rev. Material Science* 26 (1996): 153-187.

31. Hammond P. and Whitesides G. "Formation of Polymer Microstructures by Selective Deposition of Polyion Multilayers Using Patterned Self-Assembled Monolayers as a Template." *Macromolecules* 28 (1995): 7569- 7571.
32. Yoo D., Shiratori S., and Rubner M. "Controlling bilayer composition and surface wettability of sequentially adsorbed multilayers of weak polyelectrolytes." *Macromolecules* 31 (1998): 4309-4318.
33. Hoogeveen N., Stuart M. C., and Fleer G. Formation and stability of multilayers of polyelectrolytes." *Langmuir* 12 (1996): 3675-3681.
34. Sukhorukov G. B., MÖhwald H., Decher G., and Lvov Y. M. "Assembly of polyelectrolyte multilayer films by consecutively alternating adsorption of polynucleotides and polycations." *Thin Solid Films* 284 (1996): 220-223.
35. Decher G. and Schmitt J. "Fine-tuning of the film thickness of ultrathin multilayer films composed of consecutively alternating layers of anionic and cationic polyelectrolytes." *Progr. Colloid Polym. Sci.* 89 (1992): 160-164.
36. Serizawa T., Hashiguchi S., and Akashi M. "Stepwise Assembly of Ultrathin Poly (vinyl alcohol) Films on a Gold Substrate by Repetitive Adsorption/Drying Processes." *Langmuir* 15 (1999): 5363-5368.
37. Lvov Y., Ariga K., Onda M., Ichinose I., and Kunitake T. "A careful examination of the adsorption step in the alternate layer-by- layer assembly of linear polyanion and polycation." *Colloids and Surfaces A: Physicochemical and Engineering Aspects* 146 (1999): 337-346.
38. Elbert D. L., Herbert C. B., and Hubbell J. A. "Thin polymer layers formed by polyelectrolyte multilayer techniques on biological surfaces." *Langmuir* 15 (1999): 5355-5362.
39. Lowack K. and Helm C. A. "Molecular mechanisms controlling the self-assembly process of polyelectrolyte multilayers." *Macromolecules* 31 (1998): 823-833.
40. Cooper T. M., Campbell A. L., and Crane R. L. "Formation of polypeptide-dye multilayers by electrostatic self-assembly technique." *Langmuir* 11 (1995): 2713-2718.
41. Ariga K., Lvov Y., and Kunitake T. "Assembling alternate dye-polyion molecular films by electrostatic layer-by-layer adsorption." *Journal of the American Chemical Society* 119 (1997): 2224-2231.
42. Lvov Y., Yamada S., and Kunitake T. "Non-linear optical effects in layer-by-layer alternate films of polycations and an azobenzene-containing polyanion." *Thin Solid Films* 300 (1997): 107-112.
43. Kotov N. A., Dékány I., and Fendler J. H. "Layer-by-layer self-assembly of polyelectrolyte-semiconductor nanoparticle composite films." *Journal of Physical Chemistry* 99 (1995): 13065-13069.
44. Schmitt J. and Decher G. "Metal Nanoparticle/Polymer Superlattice Films: Fabrication and Control of Layer Structure." *Journal of Science* (1992): 257-508.
45. Schmitt J., Machtle P., Eck D., MÖhwald H., and Helm C. A. "Preparation and optical properties of colloidal gold monolayers." *Langmuir* 15 (1999): 3256- 3266.
46. Lvov Y., Ariga K., Onda M., Ichinose I., and Kunitake T. "Alternate assembly of ordered multilayers of SiO₂ and other nanoparticles and polyions." *Langmuir* 13, (1997): 6195-6202.

47. Liu Y., Wang A., and Claus R. O. "Layer-by-layer electrostatic self-assembly of nanoscale Fe₃O₄ particles and polyimide precursor on silicon and silica surfaces." *Applied Physics Letters* 71 (1997): 2265.
48. Caruso F., Lichtenfeld H., Giersig M., and Mohwald H. "Electrostatic self-assembly of silica nanoparticle-polyelectrolyte multilayers on polystyrene latex particles [4]." *Journal of the American Chemical Society* 120 (1998): 8523-8524.
49. Lvov Y., Ariga K., and Kunitake T. "Formation of ultrathin multilayer and hydrated gel from montmorillonite and linear polycations." *Langmuir* 12 (1996): 3038-3044.
50. Ichinose I., Tagawa H., Lvov Y., and Kunitake T. "Formation process of ultrathin multilayer films of molybdenum oxide by alternate adsorption of octamolybdate and linear polycations." *Langmuir* 14 (1998): 187-192.
51. Cassagneau T., Fendler J. H., and Mallouk T. E. "Optical and electrical characterizations of ultrathin films self-assembled from 11-aminoundecanoic acid capped TiO₂ nanoparticles and polyallylamine hydrochloride." *Langmuir* 16 (2000): 241-246.
52. Correa-Duarte M., Giersig M., Kotov N., and Liz-Marzan L. "Control of Packing Order of Self-Assembled Monolayers of Magnetite Nanoparticles with and without SiO₂ Coating by Microwave Irradiation." *Langmuir* 14 (1998): 6430- 6435.
53. Chang-Yen D. A., Lvov Y., McShane M. J., and Gale B. K. "Electrostatic self-assembly of a ruthenium-based oxygen sensitive dye using polyion-dye interpolyelectrolyte formation." *Sensors and Actuators, B: Chemical* 87 (2002): 336-345.
54. Fendler J. H. "Preparation and Utilization of Self-assembled Ultrathin Films Composed of Polyelectrolytes, Nanoparticles and Nanoplatelets." *Croatica Chemica Acta* 71 (1998): 1127-1137.
55. Ariga K., Lvov Y., Ichinose I., and Kunitake T. "Ultrathin films of inorganic materials (SiO₂ nanoparticle, montmorillonite microplate, and molybdenum oxide) prepared by alternate layer-by-layer assembly with organic polyions." *Applied Clay Science* 15 (1999): 137-152.
56. Cassier T., Lowack K., and Decher G. "Layer-by-layer assembled protein/polymer hybrid films: nanoconstruction via specific recognition." *Supramolecular Science* 5 (1998): 309-315.
57. Decher G., Lehr B., Lowack K., Lvov Y., and Schmitt J. "New nanocomposite films for biosensors: Layer-by-layer adsorbed films of polyelectrolytes, proteins or DNA." *Biosensors and Bioelectronics* 9 (1994): 677-684.
58. Lvov Y., Decher G., and Sukhorukov G. "Assembly of thin films by means of successive deposition of alternate layers of DNA and poly (allylamine)." *Macromolecules* 26 (1993): 5396-5399.
59. Tsukruk V., Rinderspacher F., and Bliznyuk V. "Self-assembled multilayer films from dendrimers." *Langmuir* 13 (1997): 2171-2176.
60. Caruso F., Niikura K., Furlong N., and Okahata Y. "Assembly of alternating polyelectrolyte and protein multilayer films for immunosensing." *Langmuir* 13 (1997): 3427-3433.
61. Caruso F., Furlong D. N., Ariga K., Ichinose I., and Kunitake T. "Characterization of polyelectrolyte-protein multilayer films by atomic force microscopy, scanning

- electron microscopy, and fourier transform infrared reflection-absorption spectroscopy." *Langmuir* 14 (1998): 4559-4565.
62. Ladam G., Schaaf P., Cuisinier F. J. G., Decher G., and Voegel J. C. "Protein adsorption onto auto-assembled polyelectrolyte films." *Langmuir* 17 (2001): 878-882.
 63. Lvov Y., Haas H., Decher G., Mohwald H., and Kalachev A. "Successive deposition of alternate layers of polyelectrolytes and a charged virus." *Langmuir* 10 (1994): 4232-4236.
 64. Lvov Y., Ariga K., Ichinose I., and Kunitake T. "Assembly of multicomponent protein films by means of electrostatic layer-by-layer adsorption." *Journal of the American Chemical Society* 117 (1995): 6117-6123.
 65. Lvov Y., Ariga K., Ichinose I., and Kunitake T. "Molecular film assembly via layer-by-layer adsorption of oppositely charged macromolecules (linear polymer, protein and clay) and concanavalin A and glycogen." *Thin Solid Films* 284 (1996): 797-801.
 66. Mitchell K.W., Fahrenbruch A. L., and Bube R. H. "Evaluation of the CdS/CdTe heterojunction solar cell." *Journal of Applied Physics* 48 (1977): 4365.
 67. Das S. K. and Morris G. C. "Preparation and characterisation of electrodeposited n-CdS/p-CdTe thin film solar cells." *Solar energy materials and solar cells* 28 (1993): 305-316.
 68. Britt J. and Ferekides C. "Thin-film CdS/CdTe solar cell with 15.8 % efficiency." *Applied Physics Letters* 62 (1993): 2851.
 69. Tang W. and Cameron D. C. "Electroluminescent zinc sulphide devices produced by sol-gel processing." *Thin Solid Films* 280 (1996): 221-226.
 70. Bol A. A., Ferwerda J., Bergwerff J. A., and Meijerink A. "Luminescence of nanocrystalline ZnS: Cu²⁺." *Journal of Luminescence* 99 (2002): 325-334.
 71. Nanda K. K., Sarangi S. N., and Sahu S.N. "Visible light emission from CdS nanocrystals." *Journal of Physics D: Applied Physics* 32 (1999): 2306-2310.
 72. Lakowicz J. R., Gryczynski I., Gryczynski Z., and Murphy C. J. Luminescence spectral properties of cds nanoparticles." *J. Phys. Chem. B* 103 (1999): 7613-7620.
 73. Nabok A. V. and Hassan A. K., Ray A. K., and Toldi G. N. "Electrical study of polyelectrolyte self-assembled films using mercury probe." *Materials Science and Engineering C* 22 (2002): 387-391.
 74. Nabok A. V., Massey J., Buttle S., and Ray A. K. "Study of electron tunnelling through thin polymer films using a mercury probe technique." *IEE Proceedings: Circuits, Devices and Systems* 151 (2004): 461-465.

2.1. INTRODUCTION TO SEMICONDUCTORS

Based on their conductivity, solid state materials are grouped into three classes: insulators, semiconductors and conductors. Semiconductors are materials that have conductivity values in between those of conductors and insulators; they are neither good conductors nor good insulators (shown in Figure 2.1).

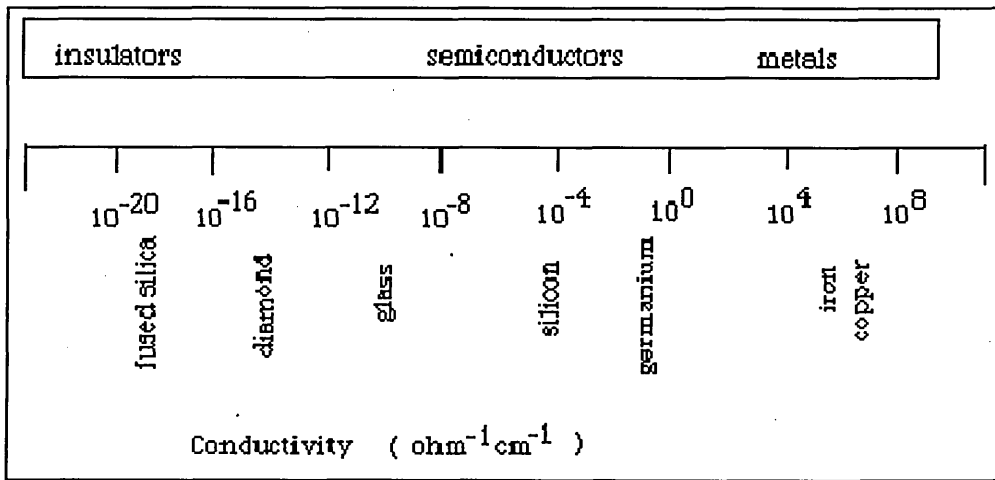


Figure 2.1. Conductivities of conducting, semiconducting and insulating materials [1].

The conductivity of a semiconductor is strongly dependent on temperature. For example, at very low temperatures, semiconductor behaves as an insulator, while at room temperature it has an appreciable electrical conductivity though much lower than a conductor. These characteristics make the semiconductor become the most important materials for electronic applications. These characteristics can be explained from their energy band diagram, shown in Figure 2.2.

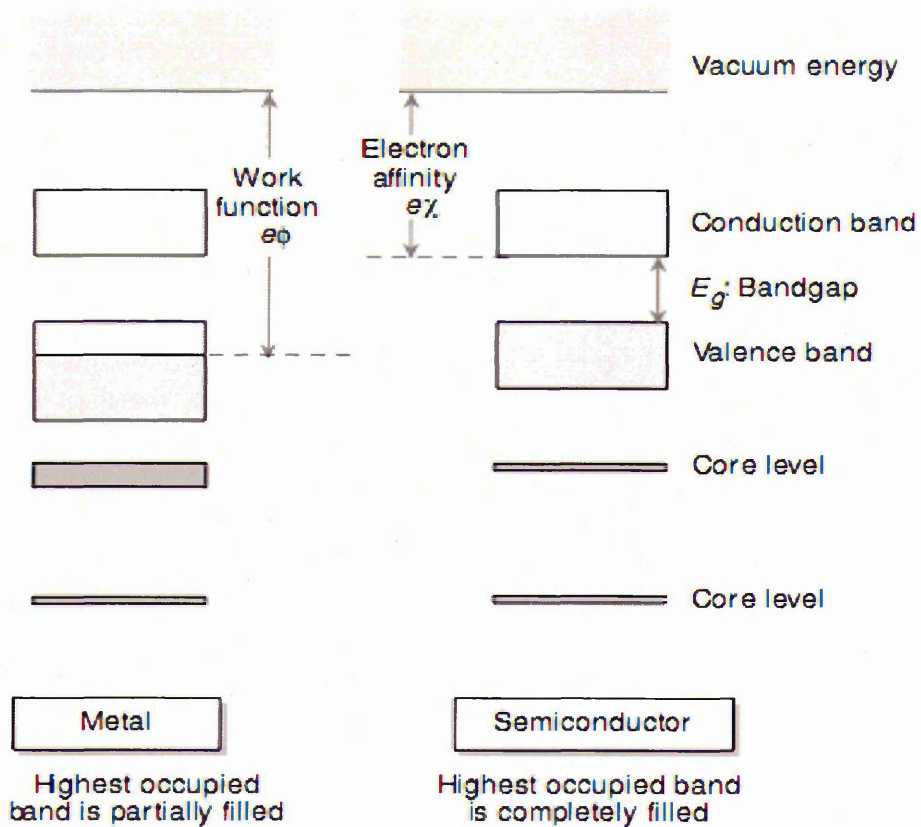


Figure 2.2. Schematic band diagrams for a metal and semiconductor (or insulator) [2].

As shown in Figure 2.2, the energy difference between the vacuum level and the highest occupied electronic state in metal is called the metal work function. In semiconductors, the band that filled with electrons at $T = 0 K$ is known as the valence band and the first unfilled band above the valence band is known as the conduction band. The energy between the vacuum level and the bottom of the conduction band gives an electron affinity.

Metals have a very high conductivity because of their partially filled valence bands. When an electrical potential (voltage) is applied, a large number of mobile charge carriers can be participated to move across the material, so that there is a net flow of electric current. In semiconductor, at $T = 0 K$, The valence band is filled with electrons and the conduction band is empty. At room temperature, the majority of electrons still occupy the valence band, but a small percentage of electrons are excited

to the conduction band and created positively charged holes in the valence band; both electrons and holes contribute to the conductivity. Therefore at high temperatures, these semiconductors are relatively good conductors.

In general, semiconductors are divided into two main classes: the elemental and compound semiconductors (as shown in Figure 2.3). The elemental semiconductors are usually found in group IV of the periodic table, while the compound semiconductors are formed from special combinations of group III and group V elements (called III-V semiconductors) or group II and group VI elements (called II-VI semiconductors). Majority of inorganic semiconductors are crystalline materials, in which the arrangement of the atoms or group of atoms is periodic and symmetric. The elemental semiconductors usually have a diamond-type crystal structure, while zinc-blende structure is typical for the compound semiconductors.

	III	IV	V	VI
II	Al	Si	P	S
Zn	Ga	Ge	As	Se
Cd	In	Sn	Sb	Te
Hg				

Figure 2.3. Elements found in elemental and compound semiconductors: group IV are elemental semiconductors; compound semiconductors can be formed by combining groups III and V or II and VI [3].

In the case of II-VI semiconductors, the compounds form a tetrahedral lattice structure where each atom *A* in a tetrahedral lattice site of *AB* compound is surrounded

symmetrically by four nearest neighbouring B atoms. In order to form this structure, the B atoms should occupy the corners of a tetrahedron with the A atom sit at its geometrical centre. Two possible structures can be formed by the combination of the tetrahedral sites. Figure 2.4 (a) shows the formation when the base triangles of the interpenetrating tetrahedrals are parallel and lined up normal to each other, while Figure 2.4 (b) shows the formation when the base triangles rotated at 60° about the normal to each other.

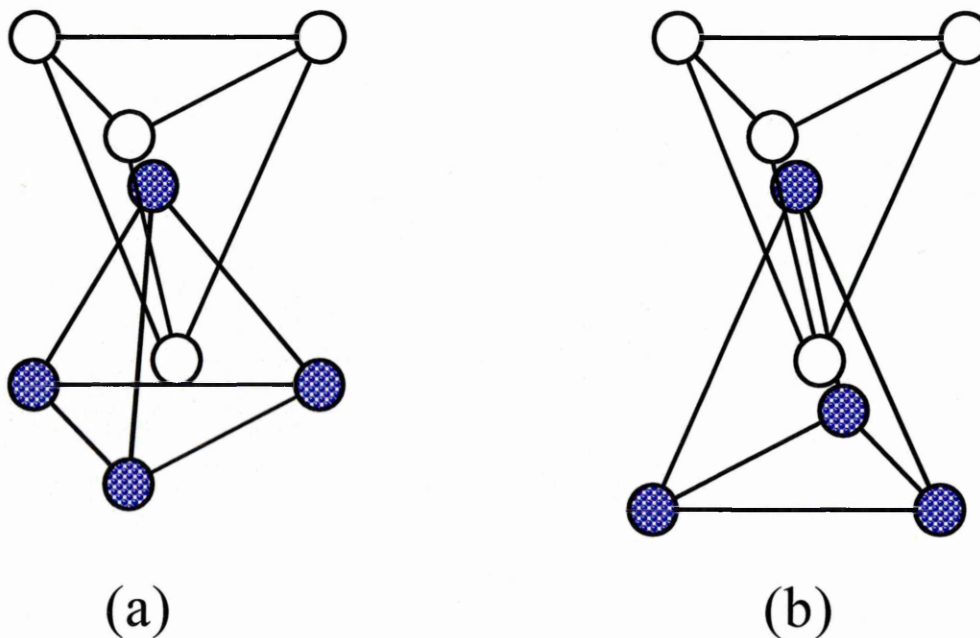


Figure 2.4. Two possible structures of tetrahedral sites for a compound: bases of tetrahedral parallel and in line vertically (a); bases of tetrahedral parallel and 60° out of line vertically (b) [4].

These two combinations of the tetrahedral lattice sites can form the two crystal structures: wurtzite and zinc blende. The first combination, as illustrated in Figure 2.4 (a), forms wurtzite crystal structure. This structure contains two interpenetrating close-packed hexagonal lattices, as shown in Figure 2.5, separated from each other by a distance $3/8c$ along the hexagonal c -axis (refers to the orientation of a_3). In ideal

wurtzite structure, where $|a| = |a_1| = |a_2|$, the nearest neighbour distance is $3/8c$ or $\sqrt{3}/8a$, which gives a c/a ratio of $\sqrt{8/3} = 1.632$ [2]. CdS, CdSe, ZnS, ZnSe, BeO, ZnO and MgTe have all been observed to take this wurtzite structure.

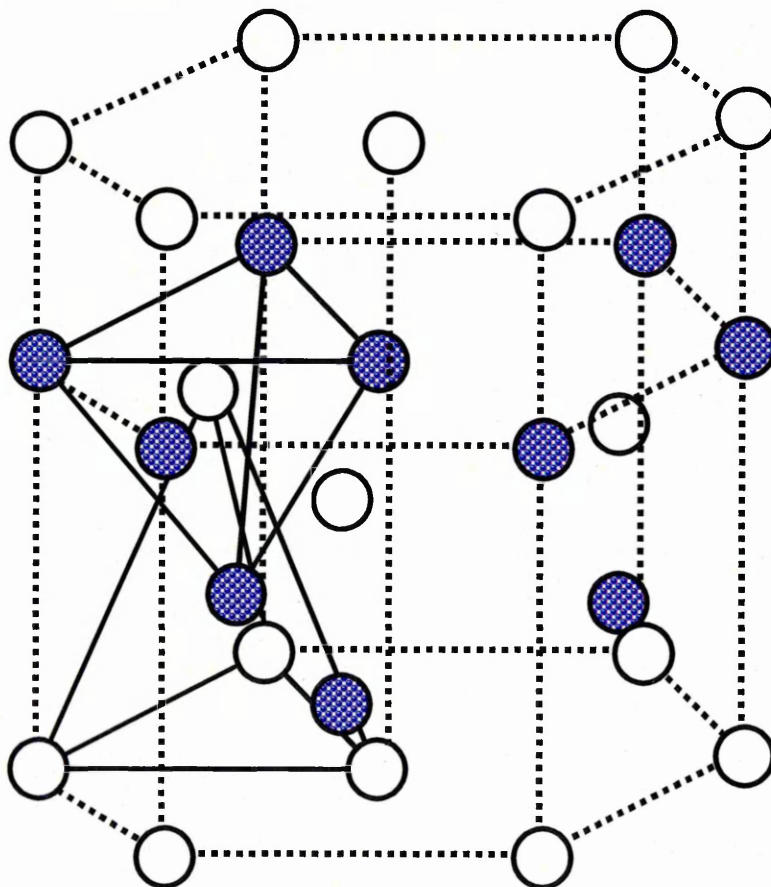


Figure 2.5. Wurtzite structure formed from tetrahedral sites [4].

The second combination (as shown in Figure 2.4 (b)) is related to the zinc blende structure which is included in cubic crystal class. This structure consists of two interpenetrating cubic close-packed lattices and derived from the diamond structure (see Figure 2.6), displaced each other by $1/4$ of the body diagonal. The nearest neighbour separation of this structure is $\sqrt{3}/4a$. The sulphides, selenides and tellurides of beryllium, zinc, cadmium and mercury have all been obtained with the zinc blende structure.

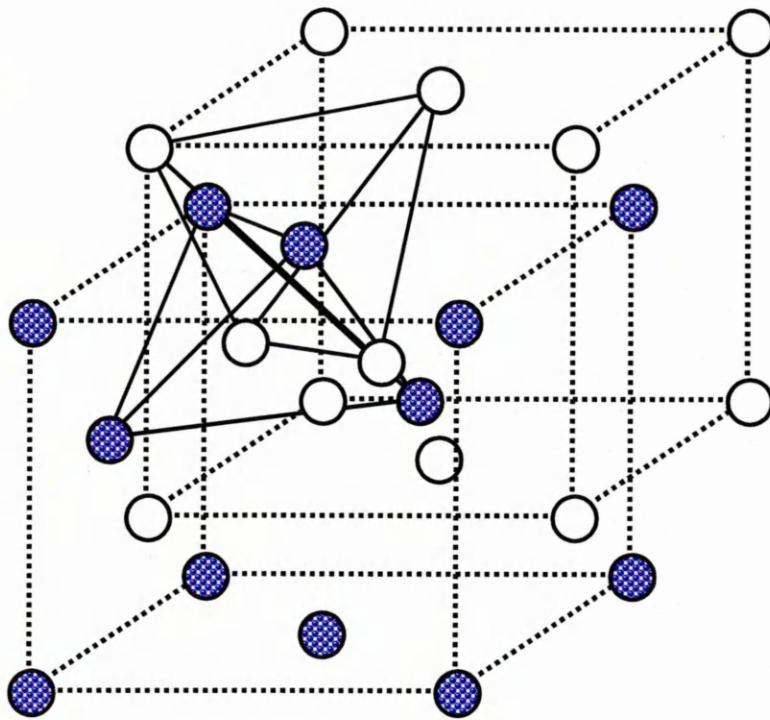


Figure 2.6. Crystallographic lattice of zinc blende structure [4].

2.1.1. Electrons in a crystal lattice

The behaviour of electrons in periodic crystalline lattices is different from free electron model. The E versus k diagrams for free electrons and electrons inside one-dimensional crystal are presented in Figure 2.7. The E versus k diagram for electrons in periodic crystalline lattices is generated from free electron model by using tight binding method.

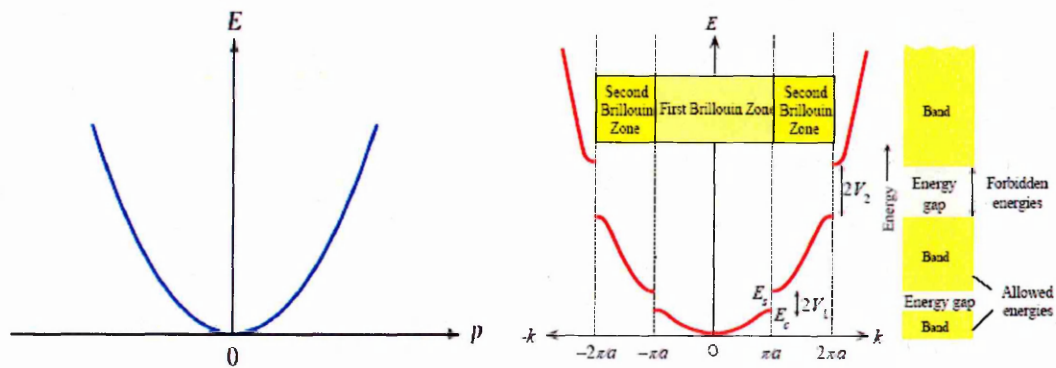


Figure 2.7. The E versus k diagram for: free electrons (a) and electron inside a one-dimensional crystal (b) [5].

In Figure 2.7 (b), there are discontinuities in the energy at $k = \pm n\pi/a$ where the waves suffer Bragg reflections in the crystal. There are energy gaps at these k values. Away from the critical k values, the behaviour is like that of a free electron, E increasing with k as $E = (\hbar k)^2/2m$.

In the region near the centre of the zone, near $k = 0$, the expression of $E(k)$ could be written as:

$$E = \left. \frac{dE}{dk} \right|_0 k + \frac{1}{2} \left. \frac{d^2E}{dk^2} \right|_0 k^2 + \frac{1}{6} \left. \frac{d^3E}{dk^3} \right|_0 k^3 + \dots \quad (2.1)$$

Since the curve is symmetric ($E(k) = E(-k)$), then equation (2.1) can be simplified as:

$$E \approx \frac{1}{2} \left. \frac{d^2E}{dk^2} \right|_0 k^2 \quad (2.2)$$

Therefore for small k ,

$$E \approx \frac{1}{2} \left. \frac{d^2E}{dk^2} \right|_0 k^2 \quad (2.3)$$

In other words, for small k the energy of electron in a semiconductor crystal has the same quadratic form as that for free electrons.

$$\frac{1}{2} \left. \frac{d^2E}{dk^2} \right|_0 k^2 = \frac{\hbar^2 k^2}{2m^*} \quad (2.4)$$

where m^* is the effective mass.

The effective mass can be rewritten as:

$$m^* = \frac{\hbar^2}{\left. d^2E/dk^2 \right|_0} \quad (2.5)$$

Since the effective mass m^* is affected by the potential in lattices, it will be different from the free electron, and would depend on how curved (or steep) the bands are around $k = 0$, as shown in Figure 2.8.

2.1.2. Direct and indirect semiconductors

According to the band structure, there are two types of semiconductors having direct and indirect band gaps (Figure 2.8). Direct band gap semiconductors have a minimum in the conduction band and a maximum in the valence band at the same k value ($k = 0$) in the (E, k) diagram, where E is the energy of an electron (or hole) and k is the wavevector.

As can be seen from Figure 2.8 (a), in a direct band semiconductor such as CdS, ZnS and GaAs, an electron in the conduction band can fall to an empty state in the valence band, emitting the energy difference E_g as a photon of light, in a process known as radiative recombination. The dispersion of photons is given by $k = n\omega/c$ (where n is the refractive index) and hence photons have wavevector which is relatively small in comparison to the Brillouin zone width $\sim \pi/a$. Thus, in order to conserve momentum, radiative recombination with the emission of photons can only involve transitions with $\Delta k \approx 0$. These transitions are vertical on an E vs k band diagram, and are known as direct transitions.

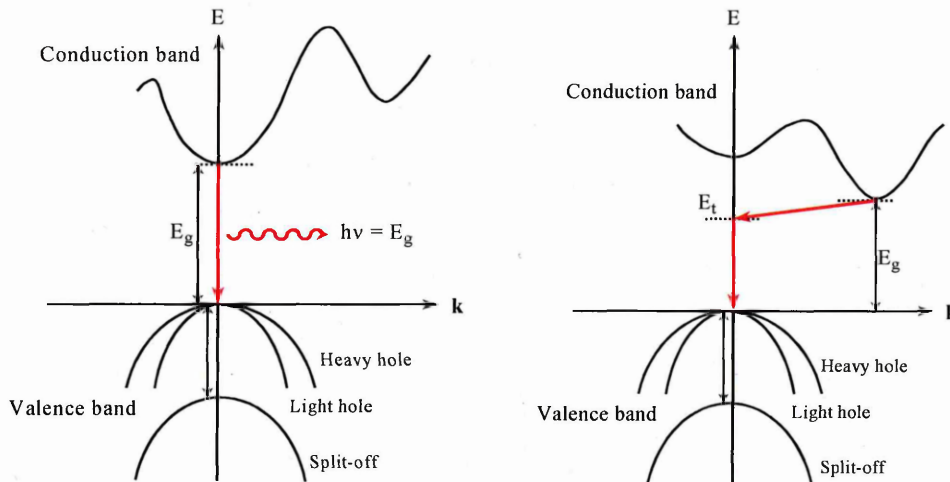


Figure 2.8. Direct electron transition in a direct band semiconductor with accompanied photon emission (a). Indirect electron transitions in an indirect semiconductor via defect level (b) [6].

On the other hand, indirect band gap semiconductors, such as silicon, germanium and GaP, have their valence band maximum at a different value of k than that of the conduction band minimum, shown in Figure 2.8 (b). An electron in the conduction band minimum cannot fall directly to the valence band maximum but must undergo a momentum change as well as changing its energy. In this case radiative recombination cannot occur without the assistance of some k -conservation mechanism. Scattering processes, such as phonon or impurity scattering, may provide such a mechanism by allowing radiative recombination to take place via a virtual state (E_i) in the forbidden gap, close to $k = 0$. In an indirect transition which involves a change in k , the energy is generally released as heat to the lattice rather than as an emitted photon.

2.1.3. Excitons in semiconductors and Bohr radius

Exciton is the term used to a bound state of an electron and a *hole*. Normally it is formed when a photon enters a semiconductor and excite an electron from the valence band into the conduction band leaving a hole behind. These electrons and holes attracted by the Coulomb force are called excitons. Excitons can move through the crystal and transport energy, but they do not transport charge because they are electrically neutral.

The natural physical separation between the electrons and holes varies for each material; the average distance is called the *Exciton Bohr Radius* (a_B). Because a free exciton is an electron-hole ($e-h$) pair, the natural spatial $e-h$ separation can be easily calculated by balancing the centripetal force on the electron to the Coulomb attraction force [7].

$$\frac{m_o v^2}{a_B} = \frac{e^2}{4\pi\epsilon_o a_B^2} \quad (2.6)$$

where m_o is the electron mass, v is the speed of electron, e is the electron charge, and ϵ_o is the permittivity of free space. By substituting Bohr postulate for angular momentum (L) to equation (2.6):

$$L = m_o v r = n \hbar, \quad (2.7)$$

where n is the quantum number and \hbar is reduced Planck's constant, exciton bohr radius could be defined as:

$$a_B = \frac{\epsilon \epsilon_o \hbar^2}{\mu e^2} \quad (\text{MKS}) \quad (2.8)$$

where μ is the reduced effective mass:

$$\frac{1}{\mu} = \frac{1}{m_e^*} + \frac{1}{m_h^*} \quad (2.9)$$

and ϵ is the dielectric constant of the crystal.

In a large semiconductor crystal, the Exciton Bohr Radius is small as compared to the crystal, and the exciton is free to move through the crystal (Figure 2.9) like a particle and transport energy, not charge. Then, when the electron and hole recombine, a photon is emitted, often at a wavelength different from that of the original photon.

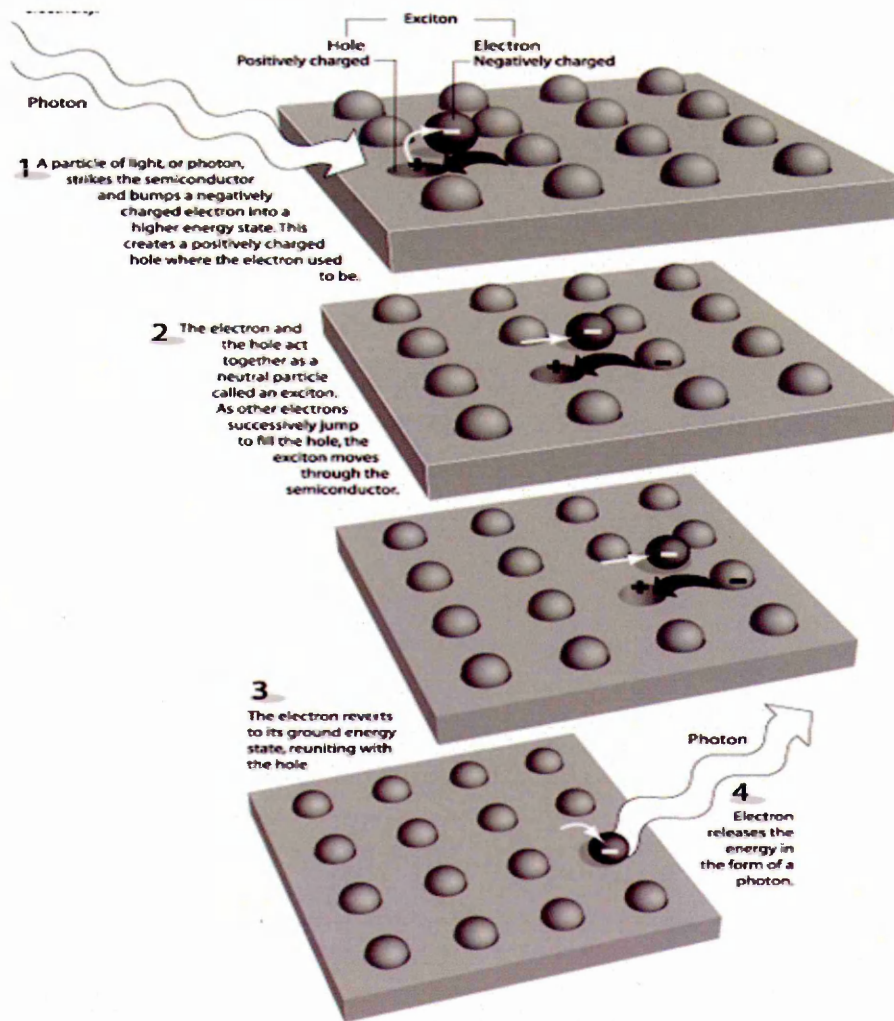


Figure 2.9. Exciton movement in the semiconductor crystal [8].

Based on their size relative to the interatomic or intermolecular distances in the material, excitons can be divided into two classes, **Mott-Wannier** excitons and **Frenkel** excitons [9]. **Mott-Wannier** excitons are typically observed in covalent semiconductors and insulators where the dielectric constant is large. Hence the Coulomb interaction between electrons and holes is reduced and electron-hole radius is much larger than the crystal lattice parameters. As a result, it is possible to attribute the electron and hole with the effective masses, m_e^* and m_h^* , which reflect the character of the valence and conduction bands within the crystal. Their binding energy is typically in the order of 0.1 eV.

In **Frenkel excitons**, typically seen in molecular or rare-gas crystals, where dielectric constant is very small, the Coulomb interaction between electrons and holes become very strong and the exciton radius tends to be smaller than the crystal lattice distances [6]. The binding energy of this **Frenkel exciton**, is typically on the order of 1.0 eV.

The energy levels $E_{n,K}$ of excitons created by the absorption of photons of appropriate wavelength are given by a simple hydrogenic model [10]:

$$E_{n,K} = E_g - \frac{\mu e^4}{2\hbar^2 \epsilon^2 n^2} + \frac{\hbar^2 K^2}{2(m_e^* + m_h^*)} \quad (2.10)$$

where n is the exciton quantum number, E_g is the bulk energy gap and $K = k_e - k_h$.

The second term in Equation (2.10) is associated with the exciton binding energy (E_b). Using Bohr's hydrogenic model, the ground state ($n = 1$) of the exciton binding energy for CdS ($\epsilon \sim 8.5$) can be expressed as:

$$E_b = \frac{e^2}{2\epsilon a_B} = \frac{\mu}{m_o} \times 13.6(eV) \quad (2.11)$$

Then, the general expressions for the exciton Bohr radii could be written as:

$$\begin{aligned} a_B(n) &= \frac{\epsilon \hbar^2}{\mu e^2} n^2 = 0.529 \frac{\epsilon}{\mu/m_o} n^2 (\text{\AA}) \\ &= \frac{7.2}{\epsilon E_{b(n=1)}} n^2 (\text{\AA}) \end{aligned} \quad (2.12)$$

The third term in Equation (2.10) is the kinetic energy term related to the centre-of-mass motion of the exciton, but this term is usually neglected for direct transitions where $K \approx 0$. Therefore equation (2.10) could be written in a simple form as

$$E(n) \approx E_g - \frac{E_b}{n^2}, \quad n = 1, 2, 3, \dots \quad (2.13)$$

2.2. SEMICONDUCTOR NANOSTRUCTURES

Semiconductor nanoparticles, also known as quantum dots or nanocrystals or nanoclusters, are a special class of semiconductor materials, which are typically built, from periodic groups of II-VI, III-V, or IV-VI materials. Their sizes are ranging from 2 to 10 nanometers in diameter, larger than individual atoms and molecules but much smaller than bulk solids. Hence their behaviours are also intermediate between macroscopic solids and that of atomic or molecular systems, obey neither absolute quantum chemistry nor laws of solid state classical physics. These different behaviours of nano-sized materials is believed due to two major phenomena. **First is the high dispersity of nanocrystalline systems.** As the size of a crystal is reduced to few nanometers, the ratio between the number of atoms at the surface and that in the crystal is increased. As the result, the physical and chemical properties, which are usually determined by the molecular structure of the bulk lattice, become dominated by the defect structure of the surface. **The second phenomenon, called size quantisation,** occurs noticeably only in metals and semiconductors. It arises because the size of nanoparticles is comparable to the de Broglie wavelength of charge carriers (i.e. electrons and holes). Due to the spatial confinement of the charge carriers, the valance and conduction bands split into discrete, quantized the electron levels.

2.2.1. High dispersity of nanocrystalline systems

High dispersity of nanocrystalline systems happens when the number of atoms at the surface is comparable to the number of atoms in the bulk of the crystalline lattice. As the size of a crystal is reduced, a fraction of atoms at the surface increases. For example, a cluster with 55 atoms will have 76 % of atoms at the surface; if it is constituted of 561 atoms only 45 % of those will be at the surface [7]. The role of surface atoms in electronic properties of nanoparticles becomes dominant. If an infinite

crystal is cleaved, as numerous studies indicate [11], both atomic and electronic structures of the solid experience dramatic changes at the surface. The most important phenomena are the surface relaxation and surface reconstruction (shown in Figure 2.10 (a) and (b)) both leading to changes of the atomic structure due to the surface energy minimization.

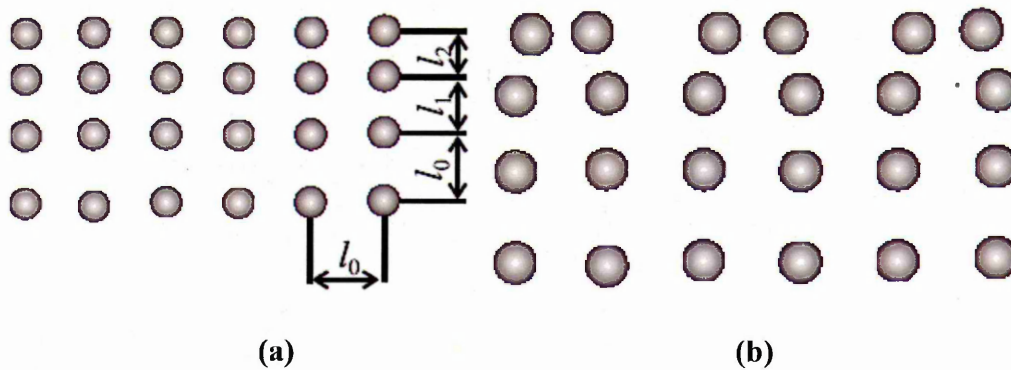


Figure 2.10. Schematic view of surface relaxation **(a)**, resulting in changes in the lattice spacing in z direction, $l_0 > l_1 > l_2$, and surface reconstruction **(b)** [11].

Changes in the atomic structure give rise to new features in the electronic structure. Usually new electronic states (or bands) appear, which are particularly important if they are formed in the semiconductor band gap. These states are spatially localized near the surface, so called surface states. The two different phenomena which would rise to the appearance of the surface states are breaking up the periodicity and changes in the arrangement of atoms at the surface (broken or dangling bonds) as shown in Figure 2.11.

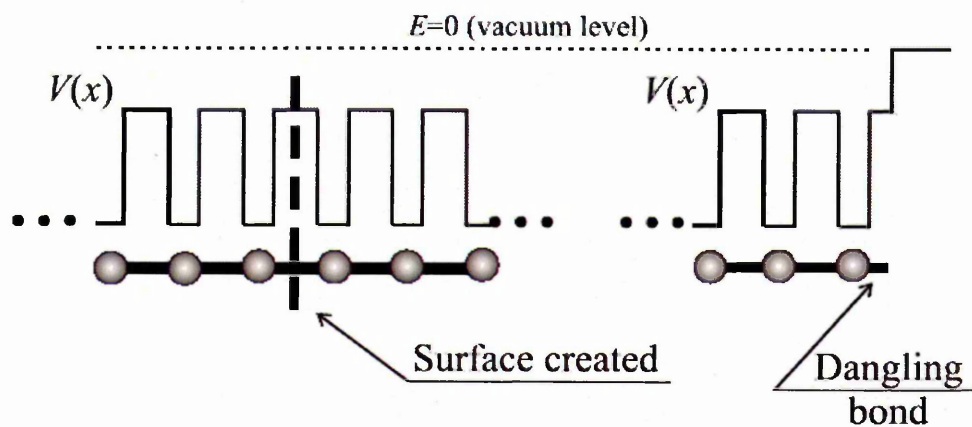


Figure 2.11. Changes in the electron potential $V(x)$ upon surface reconstruction [11].

The other phenomena observed when the crystal shrinks is the decrease in the melting temperature. In a wide variety of materials ranging from metals to semiconductors to insulators, a decrease in the melting temperature was observed with the decreasing particle size. For example, the melting point of CdS was shown to decrease from 1200 K for particles of a 4 nm radius to 600 K for particles of a 1.5 nm radius [7]. This behaviour could be explained by considering the factors that contribute to the total energy of a nanocrystal. The smaller the nanocrystal, the larger the contribution made by the surface energy to the overall energy of the system and thus the more dramatic the melting temperature decrease.

2.2.2. Quantum confinement

Quantum confinement (or size quantization) is a term for the splitting of the valance and conduction bands when the particles' size is comparable to the de Broglie wavelength. For semiconductors, the critical dimensions below which the quantization effects appear depend on the effective mass (m^*) of the charge carriers. It can be shown that both electrons and holes inside a semiconductor crystal respond to an electric field

almost as if they were free particles in vacuum, but with a different mass. The effective mass is usually stated in units of the mass of free electron in vacuum, m_e .

Since the quantisation depends on the spatial confinement conditions. Three different cases can be defined corresponding to the confinement in one, two, or three dimensions. The confinement in one-dimension leads to quantum films, in two-dimensions produces quantum wires, and finally, in three-dimensions produces quantum particles often called quantum dots.

2.2.2.1. Three-dimensional systems (bulk material)

To calculate the density of carriers in a semiconductor, firstly, the number of available states at each energy level should be defined. Since the number of energy levels is very large and dependent on the size of the semiconductor, the number of states per unit energy and per unit volume would be applied.

Let us consider a three-dimensional solid with the size dx , dy , dz containing N free electrons as shown in Figure 2.12.

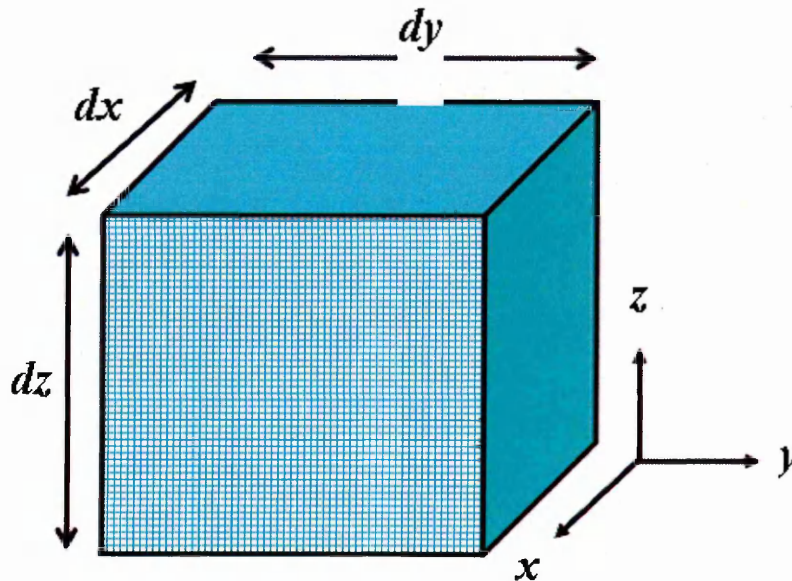


Figure 2.12. Three-dimensional systems for bulk material.

The electrons are moving freely with a velocity: $\vec{v}=(v_x, v_y, v_z)$. Assuming that the electrons are not localized and not bound to individual atoms, the interaction between the electrons, as well as, between the electrons and the crystal potential, can be neglected.

The kinetic energy of an individual electron is then defined as:

$$E_k = \frac{1}{2} m \vec{v}^2 = \frac{1}{2} m (v_x^2 + v_y^2 + v_z^2) \quad (2.14)$$

In solid state physics, the wavevector $\vec{k} = (k_x, k_y, k_z)$ of a particle is more frequently used instead of its velocity to describe the particle's state. Therefore, the linear momentum \vec{p} , which is directly proportional to the velocity \vec{v} of the electron, could be written as:

$$\vec{p} = m \vec{v} = \frac{h}{2\pi} \vec{k} \quad (2.15)$$

where h is the Planck constant.

An absolute value of $k = |\vec{k}|$, e.g. the wavenumber, is related to the electron wavelength through the de Broglie relation:

$$k = |\vec{k}| = \frac{2\pi}{\lambda} \quad (2.16)$$

From equation (2.14), (2.15) and (2.16), the kinetic energy E related to the wavenumber, k , could be written as:

$$E(k) = \frac{\hbar^2 k^2}{2m} \quad (2.17)$$

The calculation of the energy states for a bulk crystal is based on the assumption of an infinite periodic boundary conditions ($d \rightarrow \infty$) of solid. In this way, all possible electron states in the \vec{k} space are equally distributed and identical. Two electrons ($m_s = \pm \frac{1}{2}$) can

occupy each of the states $(k_x, k_y, k_z) = (\pm n_x dk, \pm n_y dk, \pm n_z dk)$, with $n_{x,y,z}$ is an integer number as shown in Figure 2.13.

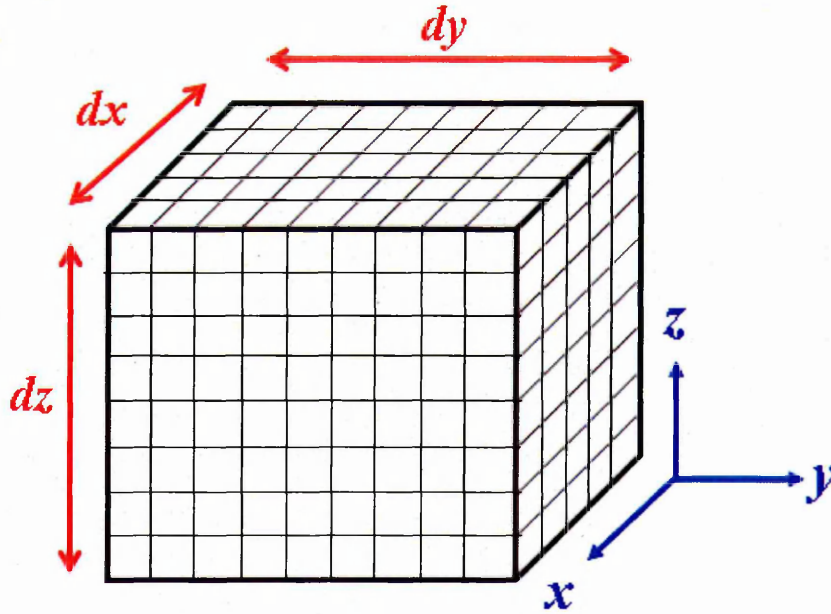


Figure 2.13. Distribution of electron states in bulk material.

Therefore, the solution of the stationary Schrödinger equation under such boundary conditions can be factorized into the product of three independent functions [12]:

$$\begin{aligned}\psi(x, y, z) &= \psi(x) \psi(y) \psi(z) \\ &= A \exp(ik_x x) \exp(ik_y y) \exp(ik_z z)\end{aligned}\quad (2.18)$$

Each function describes a free electron moving along one Cartesian coordinate. The solution of each function could be obtained by using "particle in the box" model. The Schrodinger equation for one-dimensional box is written as:

$$-\frac{\hbar^2}{2m} \frac{d^2 \Psi(x)}{dx^2} + V(x) \Psi(x) = E \Psi(x) \quad (2.19)$$

where $\Psi = A e^{-i(kx - \omega t)}$

The solutions of the equation (2.19), if $V(x) = 0$, are

$$\Psi = A \sin(k_x x) + B \cos(k_x x) \quad (2.20)$$

where A and B are to be determined.

The wavefunction must be zero at the infinite barriers of the well. At $x = 0$ the wavefunction must be zero so that only sine functions can be valid solutions and B must equal zero. At $x = L$, the wavefunction must also be zero yielding the following possible values for the wavenumber, k_x .

$$k_x = \frac{n\pi}{L}, n=1, 2, 3, .. \quad (2.21)$$

This calculation can now be repeated for y and z direction.

Each possible solution corresponds to a cube in k -space with the size $n\pi/L$ as indicated on Figure 2.14.

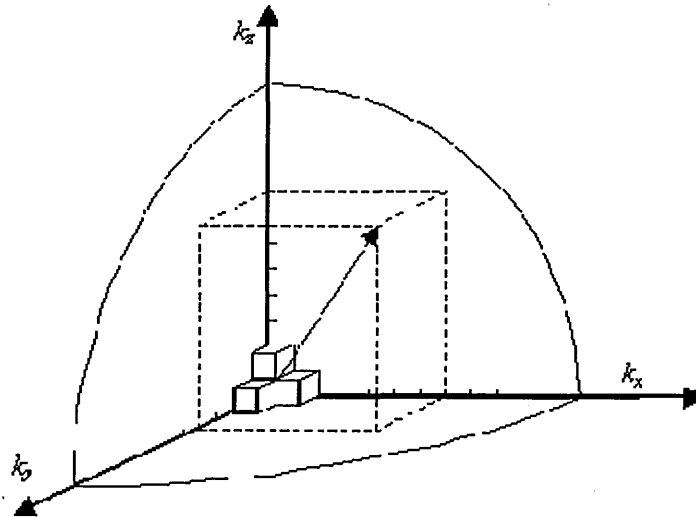


Figure 2.14. Calculation of the number of states with the wavenumbers less than k [13].

The total number of electrons with different values for k_x , k_y and k_z and with a magnitude of the wavevector less than k is obtained by calculating the volume of one eighth of a sphere with the radius k and dividing it by the volume corresponding to a single solution, $(\pi/L)^3$, yielding [13]:

$$N = 2 \times \frac{1}{8} \times \left(\frac{L}{\pi}\right)^3 \times \frac{4}{3} \pi k^3 \quad (2.22)$$

A factor of two is added to account for the two possible spins of electron for each solution.

The total number of electrons having wavenumbers smaller than k_{max} is:

$$N(k_{max}) = \int_0^{k_{max}} D_{3d}(k) dk \quad (2.23)$$

where D_{3d} is the density of states.

Then the density of states could be written as:

$$D_{3d}(k) = \frac{dN(k)}{dk} \quad (2.24)$$

The density of state per unit energy is defined as:

$$D_{3d}(E) = \frac{dN(E)}{dE} = \frac{dN(k)}{dk} \frac{dk}{dE} \quad (2.25)$$

By substituting equation (2.22) to (2.25), the density of states for a three-dimensional could be obtained as:

$$D_{3d}(E) = \left(\frac{L}{\pi}\right)^3 \pi k^2 \frac{dk}{dE} \quad (2.26)$$

From equation (2.17), $E(k)$ is proportional to k^2 and thus $k \approx \sqrt{E}$. Consequently,

$$\frac{dk}{dE} \approx \frac{1}{\sqrt{E}} \quad (2.27)$$

By substituting equation (2.27) to (2.26), the density of states per unit volume and per unit energy, $g_{3D}(E)$, is yielded as:

$$g_{3D}(E) = \frac{1}{L^3} \frac{dN}{dE} = \frac{8\pi\sqrt{2}}{h^3} m^{3/2} \sqrt{E}, \text{ for } E \geq 0 \quad (2.28)$$

The density of states is zero at the bottom of the quantum well. The same analysis also applies to electrons in a semiconductor. The minimum energy of the electron is the energy at the bottom of the conduction band, E_c , so that the density of states for electrons in the conduction band is given by:

$$g(E) = \frac{1}{L^3} \frac{dN}{dE} = \frac{8\pi\sqrt{2}}{h^3} m^{3/2} \sqrt{E - E_c}, \text{ for } E \geq E_c \quad (2.29)$$

The density of states is proportional to the square root of the energy as shown in Figure 2.15.

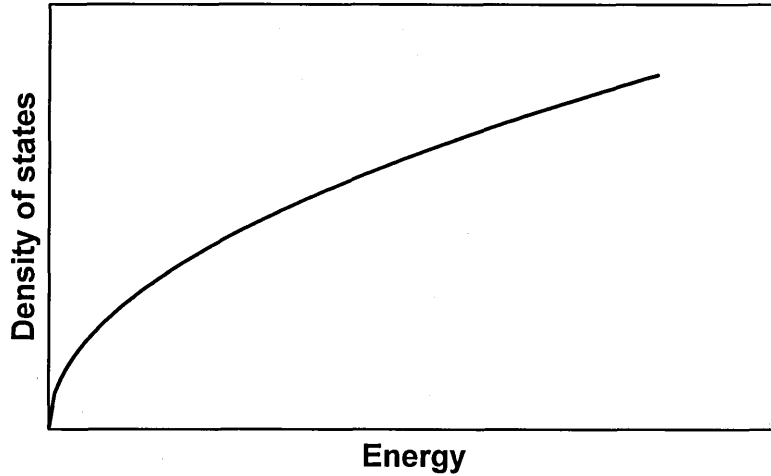


Figure 2.15. Density of states D_{3d} for free electrons in 3-dimensional system.

2.2.2.2. Two-dimensional systems

For two-dimensional systems, the solid is fully extended along the x and y directions, but the thickness along z -direction (dz) is only a few nanometers (see Figure 2.16 (a)). Free electrons can still move freely in the x - y -plane but movement in the z -direction is now restricted. The particle in a box model could be used again in this system and the solutions can be obtained by solving the one-dimensional Schrödinger equation for an electron in a potential $V(z)$, which is zero within the box but infinite at the borders. As can be seen in Figure 2.16 (c), the solutions are stationary waves with energies

$$E_{nz} = \frac{\hbar^2 k_z^2}{2m} = \frac{h^2 k_z^2}{8\pi^2 m} = \frac{h^2 n_z^2}{8m dz^2} \quad \text{with } n_z = 1, 2, 3, \dots \quad (2.30)$$

This is similar to states $k_z = n_z dk_z$ with $dk_z = \pi / dz$. Again, each of these states can be occupied at maximum by two electrons.

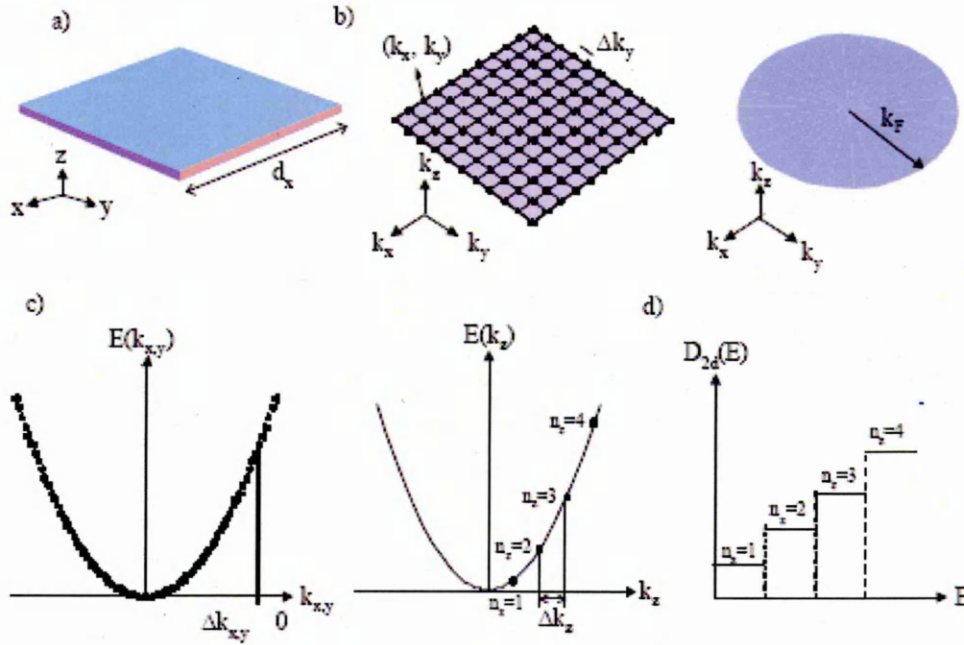


Figure 2.16. Two-dimensional system (a); Distribution of electronics states (b); Dispersion relation $E(k)-k$ (c); Density of states D_{2d} for free electrons (d) [14].

Now, the number of states is proportional to the area of the x - and y - plane. A square in x -and y - plane with size $n\pi/L$ is in a ring with the radius k and thickness dk . Therefore, the total number of electrons with different values for k_x and k_y and again, with a magnitude of the wavevector less than k is obtained by calculating the area of one fourth of a circle with the radius k and dividing it by the area corresponding to a single state, $(\pi/L)^2$, yielding:

$$N = 2 \times \frac{1}{4} \times \left(\frac{L}{\pi}\right)^2 \times \pi k^2 \quad (2.31)$$

Hence, the two-dimensional density of states could be obtained as:

$$D_{2d}(E) = \frac{dN(E)}{dE} = 2 \left(\frac{L}{2\pi}\right)^2 2\pi k \frac{dk}{dE} \quad (2.32)$$

And the density of states per unit volume and per unit energy, $g_{2D}(E)$, is yielded as:

$$g_{2D}(E) = \frac{1}{L^2} \frac{dN}{dE} = \frac{4\pi m}{h^2}, \text{ for } E \geq E_{min} \quad (2.33)$$

In two-dimensional materials the energy spectrum is still quasicontinuous, but the density of states now is a step function (see Figure 2.16 (d)).

2.2.2.3. One-dimensional systems (quantum wires)

Let us now consider the case in which the solid also shrinks along the second (y) dimension. Now electrons can only move freely in the x -direction, and their motion along the y - and z axes is restricted by the borders of the solid (see Figure 2.17 (a)). This system is called *quantum wire* or one-dimensional electron system (1DES). The states of a one-dimensional solid now can be obtained by methods analogous to those described for the three- and two-dimensional materials.

In the x -direction electrons can move freely, and again the concept of periodic boundary conditions could be applied. This gives a quasi-continuous distribution of states parallel to the k_x -axis and for the corresponding energy levels. Electrons are confined along the remaining directions and their states can be derived from the Schrödinger equation for a particle in a box potential.

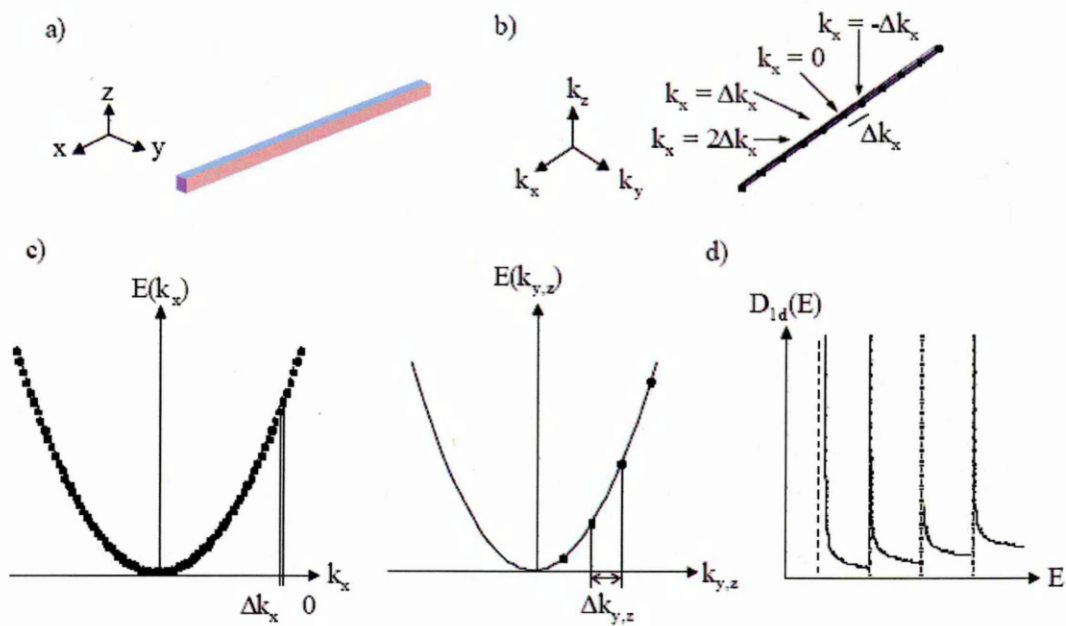


Figure 2.17. One-dimensional solid **(a)**; The distribution of states can be visualized as lines parallel to the k_x axes in the three-dimensional k -space **(b)**; The dispersion relations, along the k_x -axes the energy band $E(k_x, k_y, k_z)$ is quasi-continuous, but along the k_y - and k_z -axes only certain energies exist **(c)**; The density of states along the k_x -axes is proportional to $E^{-1/2}$ **(d)** [14].

All possible states are in lines parallel to the k_x -axis. Now, the number of states is proportional to the area of the x - and y - plane. The lines are separated by discrete intervals along k_y and k_z , but within one line the distribution of k_x states is quasi continuous, as shown in Figure 2.17 (c). The total number of states along the line is obtained by measuring the length of the line. The number of states is therefore proportional to $k = k_x$.

$$N = 2 \times \frac{1}{2} \times \left(\frac{L}{\pi} \right) \times k \quad (2.34)$$

Again, this yields discrete k_y and k_z -states. We can now visualize all possible states as lines parallel to the k_x -axis.

Hence, the density of state for a one-dimensional could be obtained as:

$$D_{1d}(E) = \frac{dN(E)}{dE} = \left(\frac{L}{\pi}\right) \frac{dk}{dE} \quad (2.35)$$

And the density of states per unit volume and per unit energy, $g_{1D}(E)$, is yielded as:

$$g_{1D}(E) = \frac{1}{L} \frac{dN}{dE} = \sqrt{\frac{2\pi m}{h^2}} \frac{1}{\sqrt{E - E_{min}}}, \text{ for } E \geq E_{min} \quad (2.36)$$

In one-dimensional systems, the density of states, as depicted in Figure 2.17 (d), has a $E^{-1/2}$ dependence and exhibits singularities near the band edges. Each of the hyperbolas contains a continuous distribution of k_x states, but only one discrete k_y - and k_z - state.

2.2.2.4. Zero-dimensional systems (quantum dots)

When charge carriers and excitations are confined in all three dimensions, the system is called quantum dot (see Figure 2.18).

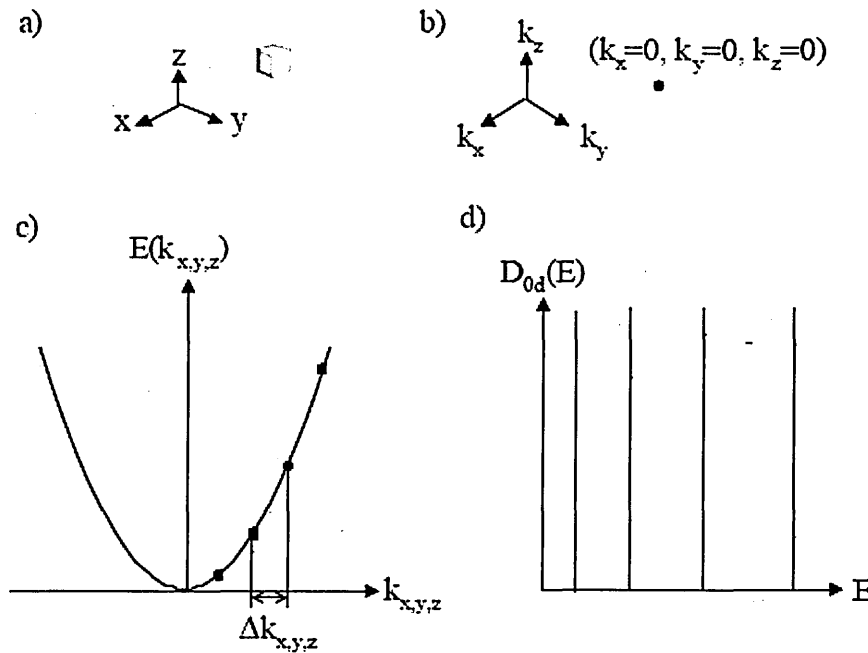


Figure 2.18. Zero-dimensional solid (a); All states (k_x, k_y, k_z) are discrete points in the three-dimensional k -space (b); Only discrete energy levels are allowed (c); Density of states $D_{0d}(E)$ contains delta functions (d) [14].

In a quantum dot, there are only discrete (k_x, k_y, k_z) -states in the k -space and each individual state in k -space can be represented by a point as shown in Figure 2.18 (b). The final consequence is that only discrete energy levels are allowed, which can be seen as delta-peaks in the distribution $D_{0d}(E)$, shown in Figure 2.18 (d).

2.3. ENERGY LEVELS IN A SEMICONDUCTOR QUANTUM DOT

The energy levels of a quantum dot can be estimated by using the particle-in-a-box model. The lowest energy for an electron in a one-dimensional potential well could be written as:

$$E_{\text{well},1D} = \frac{h^2}{8md^2} \quad (2.37)$$

where d is the width of the well and m is the electron mass.

As mentioned before, the charge carriers in a quantum dot are confined in all three dimensions, therefore this system can be described as an infinite 3-dimensional potential well. If the three-dimensional potential well is in a shape of a rectangular or a cube, then, the Schrödinger-equation can be solved independently for each of the three translational degrees of freedom. And the overall zero-point energy is simply the sum of the individual zero point energies for each degree of freedom:

$$E_{\text{well},3D(\text{cube})} = 3 \times E_{\text{well},1D} = \frac{3h^2}{8md^2} \quad (2.38)$$

If the three-dimensional potential well is assumed as a sphere of diameter d , then, the Schrödinger-equation can be solved by introducing spherical coordinates, and by separating the equation in the radial part and in the part that contains the angular momentum. The lowest energy level (with the angular momentum = 0) is then

$$E_{\text{well},3D(\text{sphere})} = \frac{h^2}{2md^2} \quad (2.39)$$

Theoretically, more confined charge carriers lead to a larger separation between the individual energy levels, as well as to a greater zero-point energy. Then, the zero-point energy for carriers that are confined into a sphere of diameter d , would be higher than that confined to a cube ($E_{well,2d(sphere)} > E_{well,2d(cube)}$) because a sphere simply has a smaller volume ($\pi/6 d^3$) than a cube (d^3).

In a semiconductor quantum dot, the size dependent energy gap, E_g (QD) consists of several terms; the bulk band gap energy, $E_{g(bulk)}$, the confinement energy for the carriers, E_{well} , and the Coulomb energy for electron hole interaction, E_{Coul} [10]:

$$E_{g(QD)} = E_{g(bulk)} + E_{well} + E_{Coul} \quad (2.40)$$

The second term in equation (2.29) could be written as:

$$E_{well} = E_{well(e^-)} + E_{well(h^+)}$$

or can be written as

$$E_{well} = \frac{\hbar^2}{2 \mu d^2} ; \quad \text{with } \frac{1}{\mu} = \frac{1}{m_e^*} + \frac{1}{m_h^*} \quad (2.41)$$

For large particles (bulk: $d \rightarrow \infty$) E_{well} reduces to zero.

An estimate of the Coulomb term yields

$$E_{Coul} = -1.8 \frac{e^2}{2 \pi \epsilon \epsilon_0 d} \quad (2.42)$$

This term can be quite significant, because the average distance between an electron and a hole in a quantum dot can be small.

Then, by inserting equations (2.41) and (2.42) into (2.40) we get:

$$E_g(dot) = E_g(bulk) + \frac{\hbar^2}{2 \mu d^2} - 1.8 \frac{e^2}{2 \pi \epsilon \epsilon_0 d} \quad (2.43)$$

Equation (2.43) shows that a quantum dot has energies larger than a bulk material. As mentioned before, bulk semiconductor states are quasi-continuous, and each point in the energy bands represents an individual state while, in a quantum dot,

the charges are confined to a small volume. Figure 2.19 illustrates the situation of charge carriers confined in an infinite potential well of width d . Here, the width d of the well potential corresponds to the diameter of the quantum dot. The only allowed states correspond to standing waves with zero amplitudes at the borders of the well. This leads to discrete energy levels. It is also shown that in a quantum dot, the ground state electrons have energies larger than that of a bulk material.

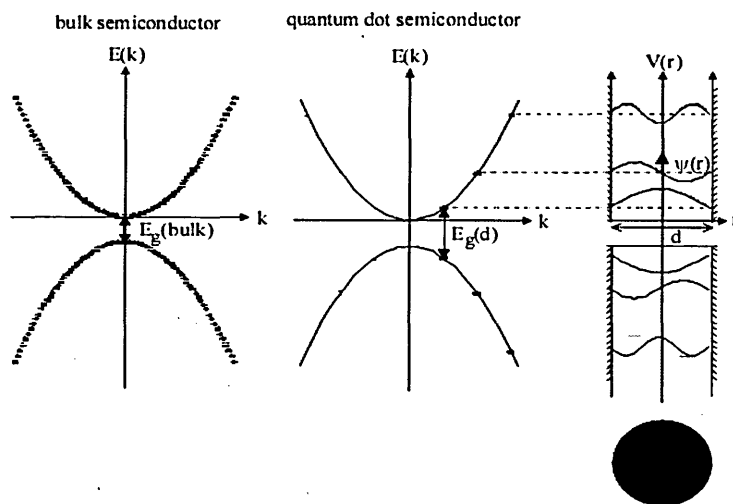


Figure 2.19. Free charge carriers in a bulk semiconductor and in a quantum dot [14].

2.4. OPTICAL PROPERTIES OF QUANTUM DOTS

The finite size of a quantum dot leads to an increase in the kinetic energy of confined quasi-particles and in turn shifts the electron-hole pair ground-state energy to higher values. This phenomenon, called blue spectral shift, directly affects the optical properties of quantum dots as compared to the corresponding bulk material. The blue spectral shift was observed for the first time in 1981 by Ekimov and Onushchenko when studying the optical properties of CuCl microcrystallites dispersed in a silicate glass [15]. In 1991, Ekimov reported the blue shift of exciton peaks for CuCl microcrystallites as the radius R changes from 310 Å to 20 Å [16].

Figure 2.20 shows the absorption and fluorescence of CdSe quantum dots having different size (diameter). The smaller quantum dots have their absorption spectrum, as well as their luminescence peaks, shifted to shorter wavelengths with respect to larger quantum dots and to the bulk material.

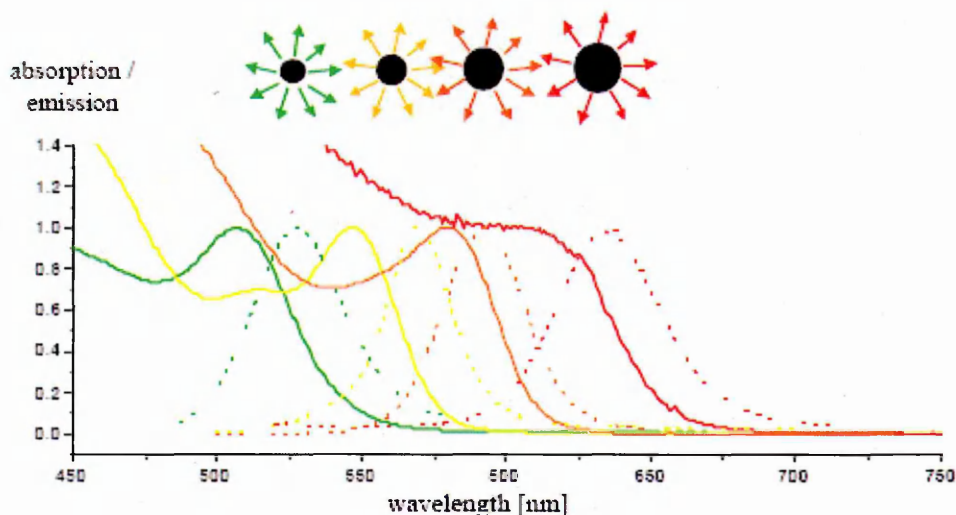


Figure 2.20. Absorption (solid lines) and emission (dotted lines) spectra of colloid CdSe quantum dots of different size. The absorption peak of 2.3/ 3.8/ 4.0/ 4.6 nm diameter nanocrystals are at 507/ 547/ 580/ 605 nm, respectively, corresponding to the green/yellow/orange/red colour; the fluorescence peaks are respectively at 528/ 570/ 592/ 637 nm [14].

The energy released upon exciton annihilation usually is too large to be dissipated by vibrational modes, so it is released in the form of emitted photons, instead [17]. The energy of light emitted from a quantum dot is smaller than the excitation energy. In other words, the wavelength of fluorescence is longer than that of the absorbed light, as shown in Figure 2.21, such red shift between the peak in the absorption spectrum and the corresponding emission peak is called **Stokes shift**.

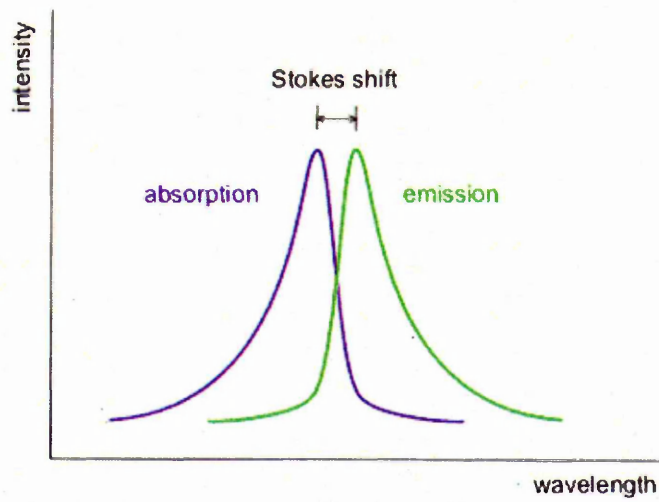


Figure 2.21. Stokes shift [18].

The Stokes shift phenomenon could be explained by examining the exciton structure in more detail [19-22]. More complex theoretical models and calculations show that the ground state of an exciton in a quantum dot has a total angular momentum equal to zero. In the dipole approximation, the creation of an exciton through absorption of a photon leads to an exciton state having angular momentum equal to ± 1 . This excited state relaxes rapidly to the lowest excited state or exciton $e-h$ ground state as shown in Figure 2.22, to a state with an angular momentum of ± 2 .

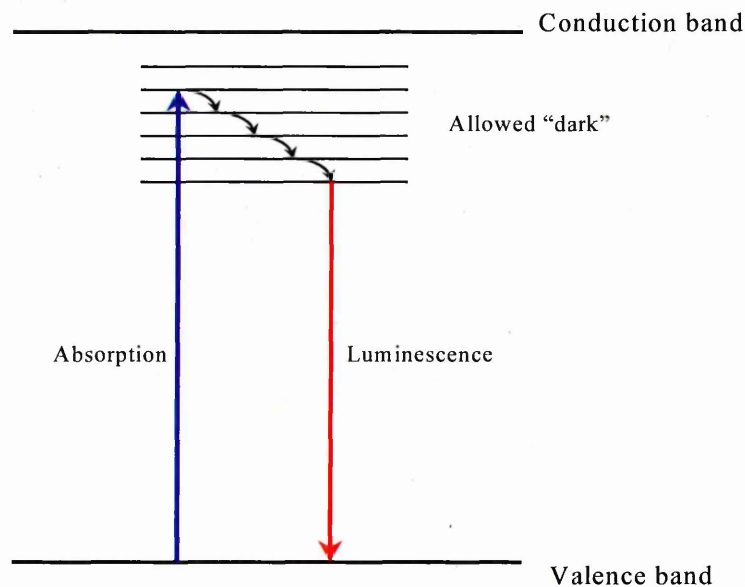


Figure 2.22. Schematic illustration of a dark exciton in semiconductors [23].

In the first order, this state cannot relax to the ground state with zero angular momentum by emitting a photon, because only transitions, that change the angular momentum by ± 1 , are allowed. Since no photon can be emitted in the first order, this state is called **dark exciton**. As a result, the decay time of the fluorescence is long and the fluorescence energy is red-shifted with respect to the absorption band edge energy (see Figure 2.20 and 2.21).

The dark exciton was first reported by Smotkin [24]. The evidence of this dark exciton state is supported by many experimental data, in particular by magnetic field dependent lifetime measurements [25] and electric field measurement [26, 27]. The position of the absorption spectrum and the luminescence peak are dependent on the average quantum dot size, and its width is correlated to the nanocrystals size distribution (see Figures 2.20). Consequently, the position of a maximum of the absorption and emission peaks, along with its width can be used to estimate the mean size and the size distribution of quantum dot.

2.5. THEORETICAL MODELS OF QUANTUM CONFINEMENT EFFECTS

The confinement of excitons in quantum dots is described by different theoretical models. There are four main theoretical models of quantum confinement which have been listed in [10] and [28]: effective mass approximation (EMA), empirical pseudo-potential method (EPM), semi-empirical tight binding (TB) approximation, and the effective bond orbital model (EBOM).

2.5.1. The effective-mass approximation (EMA) model

EMA, which was developed by Efros and Efros in 1982 [29], is widely used to interpret the variation of the band gap with the particles' size because of its simplicity. In this model, electrons and holes are confined in a spherical quantum dot with infinite

potential barriers having parabolical shape ($E \sim k^2$). Efros considered three possible situations with respect to the radius of quantum dots, R and Bohr radius, a_B :

(a) Weak confinement region where $R \gg a_B$, $R \gg a_e$, a_h and $a_B = a_e + a_h$

In this regime, the Coulomb term is the dominant energy. The exciton energy as the lowest-energy state is then shifted to higher energies due to the confinement, and this shift is proportional to $1/R^2$. The energy shift of the ground-state exciton is given approximately by:

$$\Delta E \approx \frac{\hbar^2 \pi^2}{2MR^2} \quad (2.44)$$

where M , the mass of the exciton, $M = m_e^* + m_h^*$, with m_e^* and m_h^* being the effective masses of the electrons and holes, respectively.

(b) Medium confinement region where $R \approx a_B$ and $a_h < R < a_e$

This regime is the common condition for very small microcrystallites. In this case the electron is quantized and the hole interacts with it through the Coulomb potential. a_e and a_h are given as:

$$a_e = \frac{\hbar^2 \epsilon}{m_e^* e^2} \quad (2.45)$$

$$a_h = \frac{\hbar^2 \epsilon}{m_h^* e^2} \quad (2.46)$$

where ϵ is the dielectric constant of the semiconductor materials and

$$a_B = \frac{\hbar^2 \epsilon}{\mu e^2} \quad (2.47)$$

The blue shift in the position of the optical absorption maximum is proportional to $\hbar^2/m_e^* R^2$.

(c) Strong confinement ($R \ll a_B$ or $R \ll a_h, a_e$)

In strong confinement regime, the confinement energy is dominated hence electrons and holes are quantized separately and should be viewed as individual particles with

only little spatial correlation between them. The Coulomb energy is relatively small and can be ignored or treated as a perturbation. The simple model gives the shift in energy as a function of crystallite size as

$$\Delta E \approx \frac{\hbar^2 \pi^2}{2\mu R^2} \quad (2.48)$$

where M is replaced by the reduced exciton mass μ , $\frac{1}{\mu} = \frac{1}{m_e^*} + \frac{1}{m_h^*}$

The model Hamiltonian used for electrons and holes in the EMA is [10, 28]:

$$H = -\frac{\hbar^2}{2m_e^*} \nabla_e^2 - \frac{\hbar^2}{2m_h^*} \nabla_h^2 + V(r_e) + V(r_h) - \frac{e^2}{\varepsilon |r_e - r_h|} \quad (2.49)$$

where m_e^* (m_h^*) is the electron (hole) effective mass, $V(r_e)$ ($V(r_h)$) is the potential experienced by the localized electron or hole, r_e (r_h) is the position coordinates of the electron (hole) in the solid, and ε is the dielectric constant.

Efros and Efros gave the solution of the equation for single-particle energies, termed as, excitation energy levels $E_{l,n}$:

$$E_{l,n} = E_g + \left(\frac{a_B}{R}\right)^2 \Phi_{l,n}^2 E_R = E_g + \frac{\hbar^2}{2\mu R^2} \Phi_{l,n}^2 \quad (2.50)$$

where $\Phi_{l,n}$ is the n^{th} root of the spherical Bessel function of l^{th} order, with $n = 1, 2, 3, \dots$, and $l = 0, 1, 2, \dots$, being respectively, the principal and orbital quantum numbers, and E_R is the bulk exciton Rydberg energy or binding energy.

For the lowest $1s$ excited state, $\Phi_{0,1} = \pi$, and then $\Phi_{0,1} = 3.14$, $\Phi_{1,1} = 4.49$ and $\Phi_{2,1} = 5.76$. Then for the ground state, the equation (2.50) can be rewritten as:

$$E_{l,n} = E_g + \frac{\hbar^2 \pi^2}{2\mu R^2} \quad (2.51)$$

In later treatments by Brus [30, 31] and Bawendi et al [32], the small attractive Coulomb interactions between electrons and holes are taken into account. They

developed a single-band effective-mass model with infinite confining potentials for electrons and holes outside the cluster. The Coulomb interaction can be written as

$$V = \frac{-e^2}{\epsilon|r_e - r_h|} + \text{small terms (polarization)} \quad (2.52)$$

Brus obtained an analytic approximation for the lowest $1s$ excited state for small R as [31]

$$E(R) = E_g + \frac{\hbar^2 \pi^2}{2 \mu R^2} - \frac{1.8 e^2}{\epsilon R} + \text{small term} \quad (2.53)$$

The first and the second terms are the same as in equation (2.51), while the third and the fourth terms are added for Coulomb interaction and polarisation at the surface, respectively.

Using equation (2.53), it is possible to analyse the importance of the various terms as a function of R . For large R , the exciton may form and the Coulomb term is more important than the kinetic energy. While in the case of small R , the confinement term dominates. However, there are significant limitations of this approach, particularly for small cluster sizes in the range of about 18 Å [10]. One problem is the assumption of a constant effective mass.

Kayanuma [33, 34] has extended the treatment of Brus, especially for direct-bandgap semiconductors, such as CdS, and obtained quite reasonable agreement with the experiment for large clusters. For strong confinement the ground-state energy is derived as [35]

$$E(R) = E_g + \frac{\hbar^2 \pi^2}{2 \mu R^2} - \frac{1.786 e^2}{\epsilon R} - 0.248 E_R \quad (2.54)$$

where $E_R = (13.606 m_0 / \mu \epsilon_2^2)$ is the value for the bulk semiconductor.

It was apparent that this model fits well to the experimental data for rather large particles, and the deviation from the measured values increased as the size decreased.

2.5.2. Empirical pseudo-potential method (EPM)

The concept of pseudo-potential was introduced for the first time in 1934 by E. Fermi, for high-lying atomic states [36]. This method became well-established in 1960's for calculating the electronic structure of bulk semiconductors [37-39]. Several groups have successfully used this method to calculate exciton energies, the band gap, and the band structure of II-VI (including CdS) and some III-V semiconductors quantum clusters [40, 41].

The method is based on the assumption that the core electrons are tightly bound to their nuclei, and the valence and conduction band electrons are influenced only by the remaining potential. Since the potential can be Fourier expanded in plane waves, an eigenvalue equation for $E(k)$ relationship can be established. Although the Fourier coefficients for the potentials are not known, they can be empirically determined for a given crystal by fitting the calculated crystal parameters to the experimental data for the band gaps at specific high-symmetry points that are derived from optical absorption experiments.

The energies of the electronic states in a crystal or clusters are described by the Schrödinger equation

$$H\Psi_{n,k}(r) = E_n(k)\Psi_{n,k}(r) \quad (2.55)$$

where H is the Hamiltonian, $\Psi_{n,k}$ are the wavefunctions, E_n are the corresponding eigenvalues, k is the wavevector quantum numbers of the wavefunctions and n is the band index.

Since electrons are interacting with the crystal lattice, an electronic band structure calculation is a many body problem, it is impossible to solve the Equation (2.55) for large clusters containing thousands of electrons. Several approximations, as a consequence, are made to formulate this many body problem into a numerical form. By using Philips-Kleinmann theorem, which provides a mean for the energy, the problem

of many body could be simplified into one electron like problem [38]. For this purpose, the crystal field potential experienced by the valence electrons is replaced by the pseudo-potential $V_p(r)$ to get the Hamiltonian:

$$H = -\frac{\hbar^2}{2m}\nabla^2 + V_p(r) \quad (2.56)$$

where

$$V_p(r) = \sum_{R,j} v_j(r - R - d_j) \quad (2.57)$$

where v_j is the atomic pseudo-potential of the j^{th} basis atom at a lattice site R , d_j is the position vector of the j^{th} basis atom relative to R , and the summation is over all lattice sites and all the basis atom j at each lattice site.

The atomic potentials v_j may then be expanded as plane waves of the reciprocal lattice vector G , $V_p(r)$ can then be written as

$$V_p(r) = \frac{1}{Nn_a} \sum_G \sum_{R,j} v_j(G) e^{iG \cdot (r - R - d_j)} \quad (2.58)$$

where G is the reciprocal-lattice vector, N is the number of lattice sites in the samples, and n_a is the number of basis atoms at each lattice site.

For zinc blende crystal structure, $n_a = 2$, $v_1(G) \neq v_2(G)$, and an extension of the above procedure for this structure yields

$$V_p(r) = \sum_G [V_S(G)S_S(G) + iV_A(G)S_A(G)] e^{iG \cdot r} \quad (2.59)$$

where the symmetric (V_S) and antisymmetric (V_A) form factors are given by

$$V_S(G) = \frac{1}{2}[v_1(G) + v_2(G)] \text{ and } V_A(G) = \frac{1}{2}[v_1(G) - v_2(G)] \quad (2.60)$$

and the symmetric (S_S) and antisymmetric (S_A) structure factors are given by

$$S_S(G) = \cos(G \cdot t_1) \text{ and } S_A(G) = \sin(G \cdot t_1) \quad (2.61)$$

with $t_1 = a_0(1/8, 1/8, 1/8)$, a_0 is the lattice constant.

In a hexagonal (wurtzite) crystal, there are four basis atoms and two different types at each lattice site. For this case, $n_a = 4$, and since atoms 1 and 3, and 2 and 4 are identical in the hexagonal lattice, the Equation (2.61) with the structure functions is defined as

$$S_S(G) = \cos(\sqrt{2}\pi G \cdot t_2) \cos\left(\frac{2\pi u_0 G_z}{\sqrt{3}}\right) \quad (2.62a)$$

$$S_A(G) = \cos(\sqrt{2}\pi G \cdot t_2) \sin\left(\frac{2\pi u_0 G_z}{\sqrt{3}}\right) \quad (2.62b)$$

where

$$t_2 = \left(\frac{1}{\sqrt{48}}, \frac{1}{12}, \frac{1}{\sqrt{6}} \right)$$

and $u_0 = 0.375$

The form factors are determined by a fitting procedure to experimental optical data, and this introduces the empirical character to the calculation. It is possible to calculate the energy levels of the valence electrons as a function of k when $V_p(r)$ is known.

In the case of clusters, the energy levels do not form bands but can be represented as a collection of all the discrete quantized levels in the first Brillouin zone. For a cubic cluster, the physical dimensions are reduced from all sides to get a cube of side L . The wave vectors of the quantized energy levels of this shaped cluster can be represented as

$$k = \frac{\pi}{L} (n_x, n_y, n_z) \quad (2.63)$$

where n_x, n_y, n_z are the quantum numbers of a particle in a box with infinite potentials at the boundaries.

In a spherical cluster having radius R , the wave vectors for the quantized energy levels are given by

$$k = \frac{\pi}{\sqrt{3}R} (n_x, n_y, n_z) \quad (2.64)$$

It is now possible to calculate the band structure at allowed k states to obtain the energy levels of the clusters. These simple models of a cluster give an adequate understanding of the effect of quantum confinement on the electronic structure of the clusters.

Figure 2.23 and 2.24 show the results of the band structure calculations for zinc blende CdS in a spherical cluster form having $R = 15 \text{ \AA}$ and $a_0 = 5.818 \text{ \AA}$. The calculations for a cubic CdS cluster of side $L = 30 \text{ \AA}$ show very similar results to that given in Figure 2.24. Furthermore, for both models, the top of the valence band and the bottom of the conduction band lie at the smallest k given by $(n_x, n_y, n_z) = 1$.

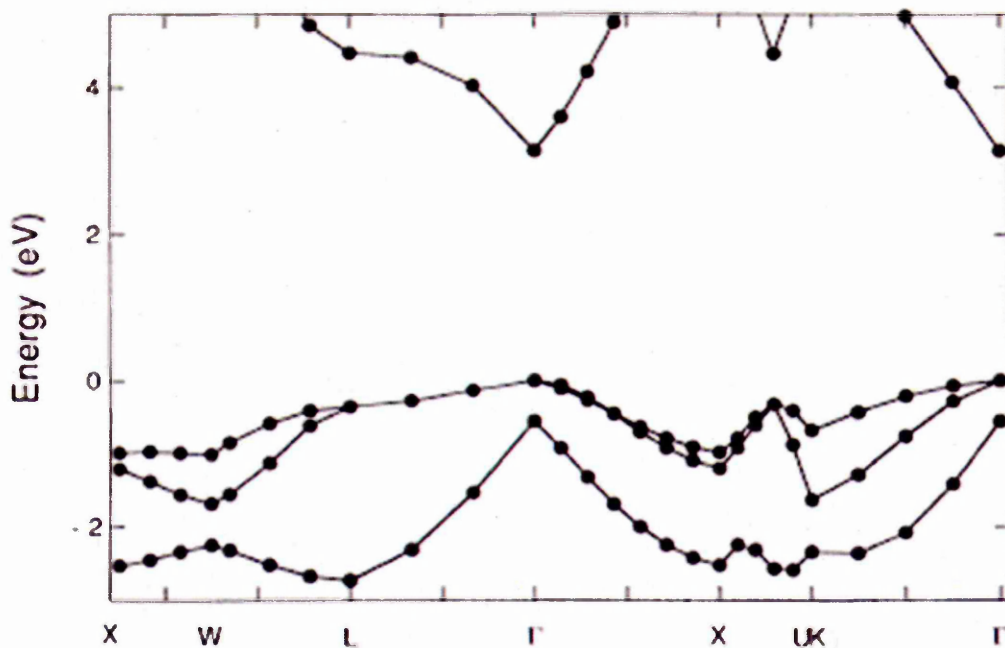


Figure 2.23. Band structure of a zinc blende CdS spherical cluster having $R = 15 \text{ \AA}$ near the top of the valence band [40].

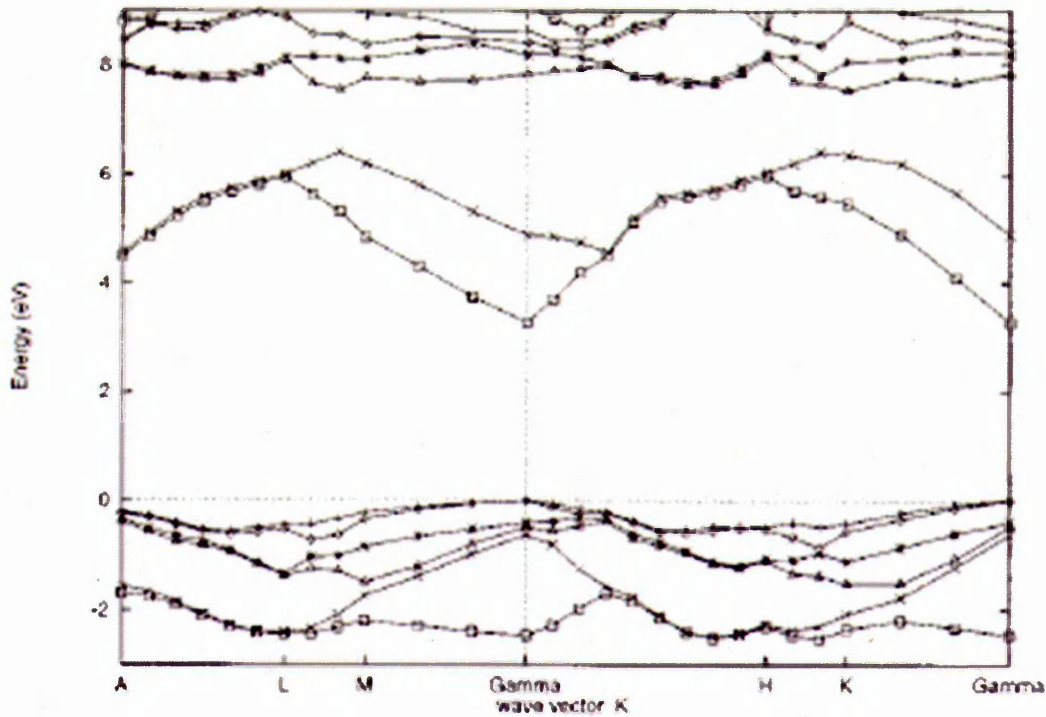


Figure 2.24. Allowed electron levels of wurtzite CdS spherical cluster with $R=15 \text{ \AA}$ [42].

Figure 2.24 shows the discrete energy levels of a $R = 15 \text{ \AA}$ wurtzite CdS cluster, modelled as a sphere of radius R . The exciton energies obtained using this calculation method are in agreement with the experiment for large clusters. This result differs from that of zinc blende CdS, which gives a good agreement with the experimental data for both large and small clusters. This indicates that small CdS clusters are more likely to have zinc blende structure rather than hexagonal. These results also indicate that the exciton energies in small clusters are sensitive to the crystal structure. The shape of the clusters has significant effect on the exciton energies. For example for zinc blende CdS clusters, the spherical shape gives better agreement with the experiment for all cluster sizes [42].

In order to obtain the exciton energies, E_x , the treatments by Brus [31] and Kayanuma [34] are used, which is

$$E_x = E_g - \frac{1.786e^2}{\epsilon_2 R} - 0.248E_{Ry} \quad (2.65)$$

where E_{Ry} , Rydberg energy is defined as:

$$E_{Ry} = \frac{\mu e^4}{2\epsilon_2^2 \hbar^2}$$

The third term in Equation (2.58), which is due to electron-hole correlation, is only 0.0171 eV and is of minor significance.

The EPM is also used to calculate the exciton energy for both bulk and cluster of CdS with hexagonal symmetry and $a_0 = 4.136 \text{ \AA}$. The band gap of hexagonal CdS crystal is found to be 2.52 eV [43], which is comparable to that of zinc blende CdS of 2.44 eV [44] and in good agreement with the experimental value of 2.5 eV [31, 34].

It is possible to estimate the number N of CdS molecules in the clusters using the calculated volumes of the unit cell and the cluster. With the volume of the unit cell is a_0^3 , the volume of the cluster is $4\pi R^3/3$, and there are four CdS molecules in one conventional unit cell. Hence,

$$N = \frac{16\pi R^3}{3a_0^3} \quad (2.66)$$

The values of $R = 5; 7.5; 10; 15;$ and 30 \AA , give $N = 13; 39; 89; 287;$ and 2297 , respectively. It would therefore seem that the empirical pseudo-potentials method gives reasonable values for exciton energies, even for clusters containing as few as 13 molecules. However, this method cannot work well for clusters smaller than 5 \AA . The calculations of the excited states of very small clusters would have to be carried out according to the traditional methods of electronic structure theory.

2.5.3. Semi-empirical tight-binding calculations

In the tight-binding model of electronic structures, single-electron wave functions are expanded in terms of atomic orbitals, centered around each atom, where R_{lm} and Y_{lm} are radial and spherical-harmonics functions in polar coordinates.

$$\Psi_{n,l,m}(r,\theta,\varphi) = R_{nl}(r)Y_{lm}(\theta,\varphi) \quad (2.67)$$

where n , l and m are the principal, angular-momentum and magnetic quantum numbers, respectively.

Lippens and Lannoo [45, 46] provided the procedure for calculating energy levels for wide-bandgap semiconductor clusters such as CdS. In the case of strong confinement, $R < a_B$, the ground-state energy $E(R)$ is taken as [10]

$$E(R) = E_g(R) + E_C(R) \quad (2.68)$$

where $E_g(R)$ is the crystallite bandgap energy and is a dominant term, while $E_C(R)$ is the Coulomb energy of the exciton and is a small correction term. The Coulomb energy for electron and hole in a spherical well of infinite depth ($V\infty$) is given by

$$E_C(R) = -\frac{e^2}{\epsilon_2 R} \left\langle \frac{R}{r} \right\rangle \quad (2.69)$$

where $\langle R/r \rangle = 1.786$, according to Brus [31], is the value averaged over the $1s$ wavefunctions. The average value of $E_C(R)$ can be calculated numerically. Lippens and Lannoo [46] have found a useful comparison of the calculated ground-state energies for the exciton of several II-VI semiconductors with zinc blende structures, using tight-binding and EMA procedures (see Figure 2.25).

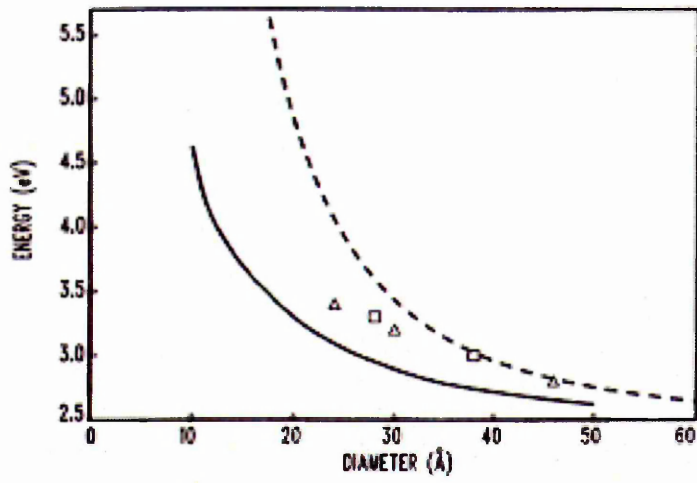


Figure 2.25. Comparison with the experimental data for CdS. The tight-binding model results are shown as a solid line, and those of the EMA model by a dash line. The experimental data are given as square and triangle points [45].

It can be seen that tight-binding model gives a slight underestimate of the exciton energy levels particularly for small crystals (less than 4 nm for CdS) as compared to EMA which gives higher values than experiment.

2.5.4. Effective bond order model (EBOM)

The bond-orbital model is basically a tight-binding model which uses bonding and antibonding orbitals as the basis: the tight-binding model for the valence bands and the EMA for the conduction bands. It is capable of taking into account the full band structure effect when a full set of bonding and antibonding orbitals is used, and a sufficient range of interactions between bond orbitals is considered. The bond orbital is defined as the proper linear combination of two atomic orbitals within a unit cell which best describe the valence-band states near the zone center. The interaction between the orbitals $|R, \alpha\rangle$ and $|R', \alpha'\rangle$ for a face-centered-cubic lattice is given by [47]:

$$\langle R, \alpha | H | R', \alpha' \rangle = E_p \delta_{R,R'} \delta_{\alpha,\alpha'} + \delta_{R'-R,\tau} \{ E_{xy} \tau_\alpha \tau_{\alpha'} (1 - \delta_{\alpha,\alpha'}) + [E_{xx} \tau_\alpha^2 + E_{zz} (1 - \tau_\alpha^2)] \delta_{\alpha,\alpha'} \} \quad (2.70)$$

where E_p is the on-site energy, E_{xx} , E_{xy} , and E_{zz} are three independent nearest neighbour interaction parameters, τ_α denotes the α component of the twelve nearest neighbour position vector.

This method has been used in an attempt to predict confined exciton energy levels in quantum dots in the diameter range of 10-80 Å [48-51]. The calculated ground state energies for excitons in CdS clusters in the strong-confinement regime is shown in Figure 2.26.

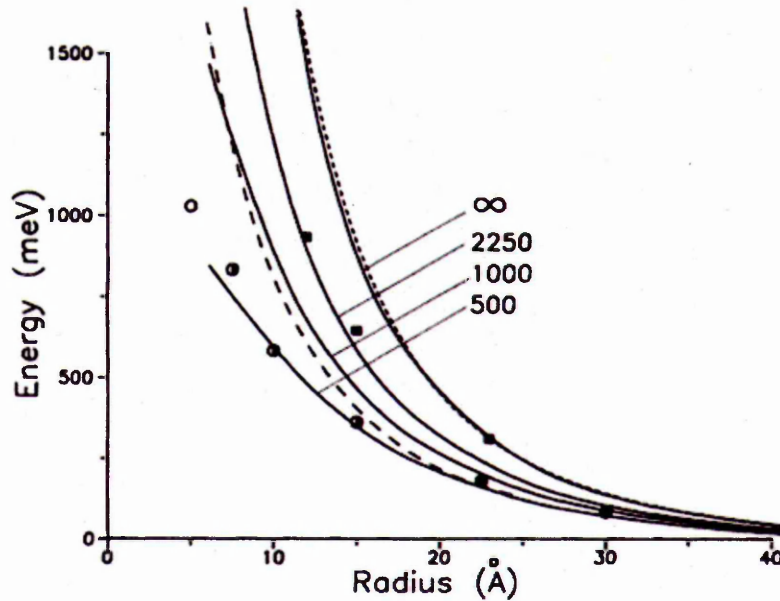


Figure 2.26. Ground-state energies for excitons in CdS microcrystallites as a function of radius calculated using the EBOM. The confining potentials for the electrons and holes assumed to be equal, are shown as: (---) curve for the Lippens and Lannoo tight-binding model with $V=\infty$; (-·-·-) curve obtained using Kayanuma's model; (■) experimental results from Ekimov et al.; (○) experimental results from Wang and Herron [48].

This figure shows that, just like EMA, the EBOM model also over-estimates the exciton energies, and the complicated procedure may be one of the limitations of this method.

2.6. ELECTRON TRANSPORT IN QUANTUM DOTS

In the current study of electrical properties of multilayered films containing II-VI semiconductor nanoparticles, several quantum mechanical effects can be considered. First of all, it is electron tunnelling through the potential barrier of different forms. Secondly, the phenomenon of resonant or assisted tunnelling should be considered in a multilayered film consisting of insulating and semiconducting layers. The following paragraphs described the basics of the mentioned above phenomena, as well as the description of electrical measurements in the planar and sandwich structures.

2.6.1. Conductivity of thin films

In general, the conductivity of thin films can be studied in two different configurations, parallel (in the film plane) and perpendicular (normal to the plane) to the substrate surface (as shown in Figure 2.27).

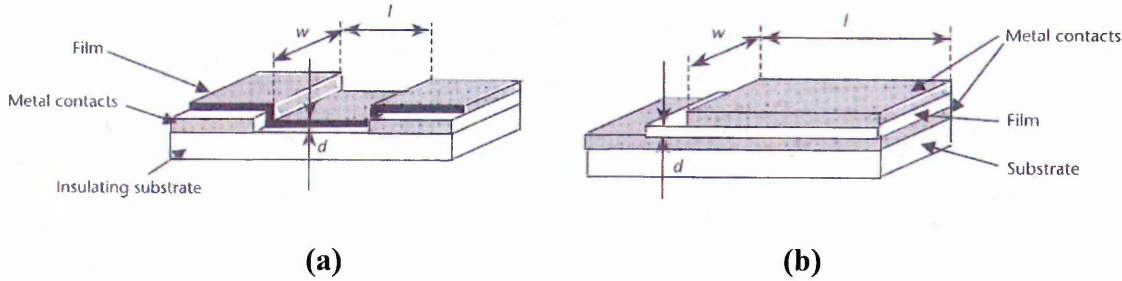


Figure 2.27. Two configurations of conductivity measurements: planar (a) and sandwich (b) structure [52].

In both cases, the conductivity is defined as:

$$\sigma = \frac{I}{V} \frac{l}{A} \quad (2.71)$$

where I is the current flowing through the sample, V is voltage applied to sample, l is distance between two electrodes, and A is the cross-section area of the sample.

In planar structures, l is the minimal distance between the electrodes, and A is the product of film thickness d and the electrode width w ($= d \times w$); while in sandwich structures, $l=d$ and A is the area of the electrodes overlap (see in Figure 2.27). From equation (2.71), the current could be written as:

$$I = \frac{A}{l} \sigma V = \frac{d w}{l} \sigma V \quad (2.72)$$

Since, in planar structures, l is much larger and A is much smaller as compared to the respective values in sandwich structures. Hence the measured current would be much smaller in planar structures while sandwich structures would have much larger electric field. In order to increase the measured current, planar interdigitated electrodes (shown in Figure 2.28) can be used.

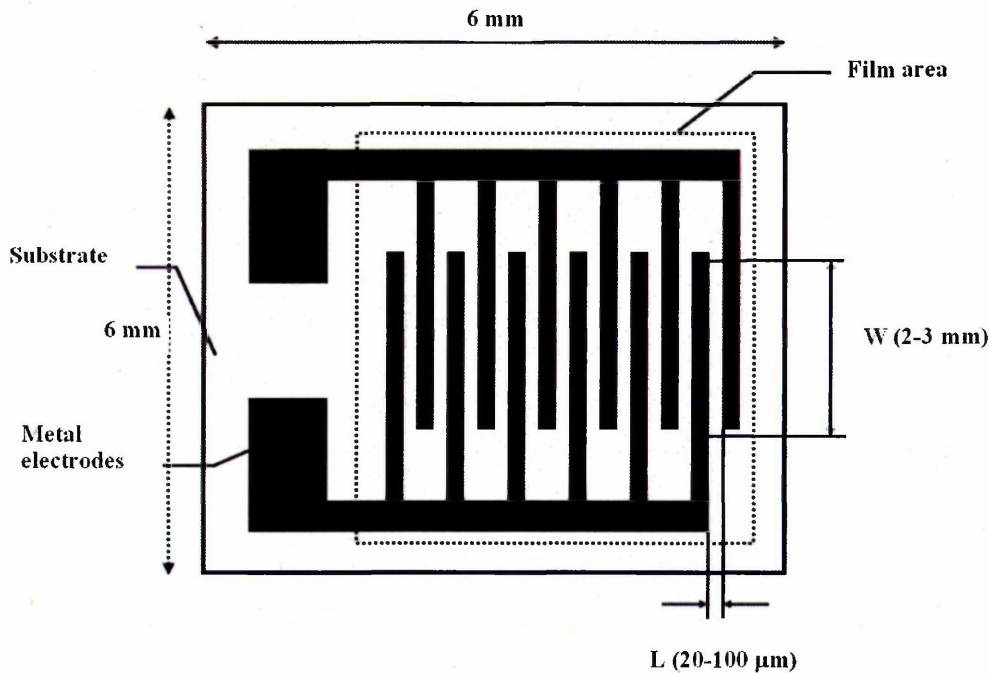


Figure 2.28. The schematic of interdigitated electrodes [52].

In this case, the equation (2.70) can be rewritten as:

$$I = \frac{n W d}{L} \sigma V \quad (2.73)$$

where n is the number of fingers ($n = 10-15$).

Then, the conductivity is given by:

$$\sigma = \frac{I}{V} \frac{L}{nWd} \quad (2.74)$$

2.6.2. Electron tunnelling in thin films

The theory of tunnelling appeared almost simultaneously with quantum mechanics. In classical mechanics, when the energy of a particle is less than the potential barrier, the particle, e.g. electron, will be reflected, since the electron cannot penetrate through the barrier. The quantum mechanics predicts the effect of particles penetration through the potential barrier of limited width and height even if the particles' total energy is less than the barrier height.

The wave nature of the electron allows the penetration through the barrier, since the electron wavefunction decays exponentially with the depth of penetration from the electrode-insulator interface.

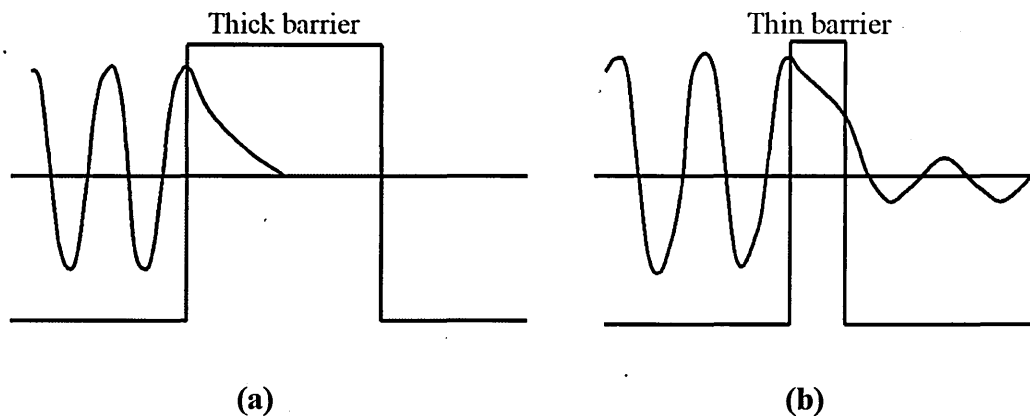


Figure 2.29. Quantum mechanical tunnelling through a: (a) thick barrier; (b) thin barrier

[53].

The wavefunction is equal to zero at the opposite interface for thick barriers (macroscopic thickness) as shown in Figure 2.29 (a). This means a zero probability of finding an electron on the other side of a barrier. In the case of very thin barriers (less

than 5 nm), the wavefunction has a nonzero value; therefore there is a finite probability that the electron can penetrate through the barrier (Figure 2.29 (b)). This phenomenon is referred as a quantum mechanical tunnelling (or tunnelling). Therefore the barrier transmission coefficient can be naturally considered as a ratio of the transmitted electrons probability flux density to that one of the incident electrons.

The general form of the transmission coefficient for the unidentified shape barrier was first used by Wentzel, Kramers and Brillouin [52].

$$T = T_0 \exp\left(-\frac{4\pi}{\hbar} \int_{x_1}^{x_2} 2m[\Phi(x) - E]^{1/2} dx\right) \quad (2.75)$$

where T_0 is the coefficient close to 1, m is the electron mass, and E is the electron energy.

This technique is known as WKB approximation or quasiclassical approximation method. There are three different types of barrier which can be considered in studying electron tunnelling, as shown in Figure 2.30.

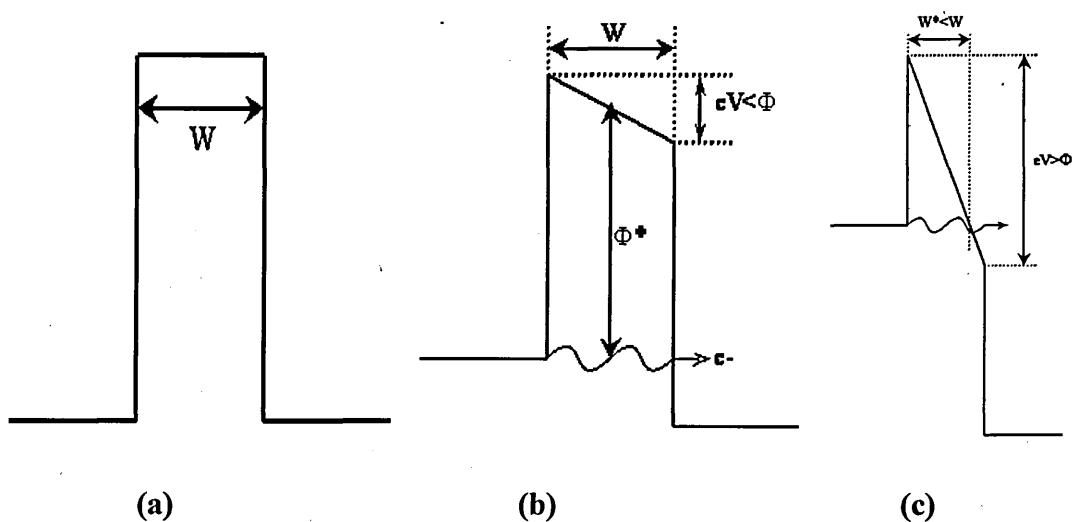


Figure 2.30. Models of electron tunnelling for different barriers: (a) rectangular; (b) trapezoidal; (c) triangular [54].

In the case of a rectangular barrier (see Figure 2.30. (a)), where

$$\Phi(x) = \begin{cases} 0, & \text{for } x < 0 \\ \Phi_0, & \text{for } 0 \leq x \leq W \\ 0, & \text{for } x > W \end{cases}$$

the transmission coefficient derived from Equation (2.75) is

$$T = T_0 \exp\left(-\frac{4\pi}{\hbar} [2m(\Phi_0 - E)]^{1/2}\right) \quad (2.76)$$

where Φ_0 is the barrier height.

When an external bias is applied, this rectangular barrier transforms to trapezoidal one (Figure 2.30 (b)), and the transmission coefficient of such barrier has become [52]

$$T = T_0 \exp\left(-\frac{8\pi W \sqrt{m} \left[\frac{\Phi_0^{3/2} - (\Phi_0 - eV_0)^{3/2}}{eV} \right]}{3\hbar}\right) \quad (2.77)$$

where W is the barrier thickness.

At a large applied bias, such barrier transforms to a triangular barrier (Figure 2.30 (c)), with the reduced thickness W^* [52]

$$T = T_0 \exp\left(\left[-\frac{8\pi W^* \sqrt{2m}}{\hbar}\right] \left[\frac{\Phi_0^{3/2}}{eV}\right]\right) \quad (2.78)$$

where $W^* = W \frac{\Phi_0}{eV}$

2.6.3. Resonance tunnelling

Resonant tunnelling refers to the tunnelling in which the electron transmission coefficient through a structure is sharply peaked at about certain energies. This phenomenon is a combination of two effects: electron tunnelling and size quantization.

Let us consider the structure of semiconductor quantum dot separated by thin insulating barrier and they are sandwiched between two metal electrodes (shown in Figure 2.31).

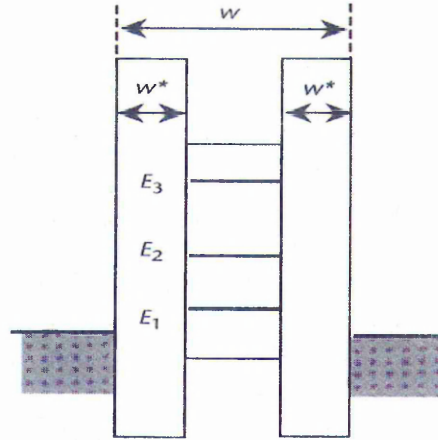


Figure 2.31. Schematic diagram of resonance tunnelling [52].

The region between the two semiconductors defines a virtual quantum well. The electrons can not penetrate through such complex barrier because the distance between metal electrodes (w) is large enough to reduce the probability of direct tunnelling to zero. However if electrons have the energy corresponding approximately to the virtual resonant energy level in the quantum well, the transmission coefficient is close to unity. Then the electron with this resonant energy can cross the barrier. It is illustrated in Figure 2.32.

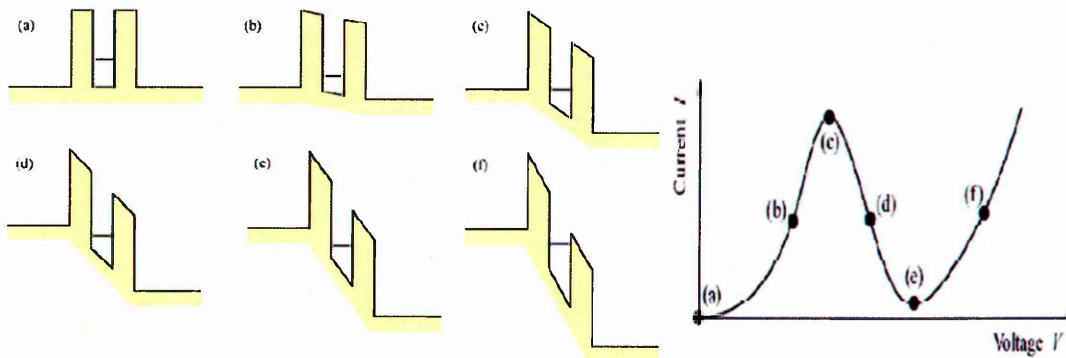


Figure 2.32. Band diagram and current-voltage characteristics of a resonant tunnelling under different bias conditions [55].

The band diagram of a virtual quantum well is shifted corresponding to the applied bias. When the Fermi level (E_F) in the source contact matches one of the energy level (E_i) in the quantum dot, resonance tunnelling will take place and reflected as a peak at the I-V characteristic. Figure 2.33 shows I-V characteristics with peaks corresponding to the energy levels of quantum well E_1 , E_2 , and E_3 .

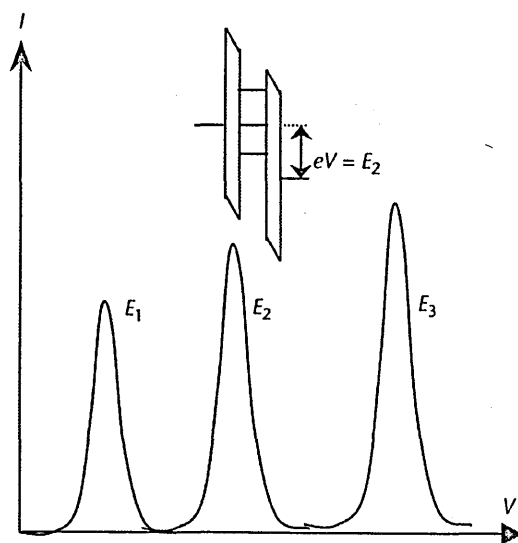


Figure 2.33. I-V characteristic of a resonance tunnelling structure with each peak corresponding to the energy matching conditions $eV=E_i$ ($i=1, 2, 3$) [52].

REFERENCES

1. "Scientific principles: conductors, insulators, and semiconductors." MAST. Dept. of Mat. Sci. and Eng. University of Illinois Urbana-Champaign. 15 August. 2007 <<http://matse1.mse.uiuc.edu/sc/prin.html>>.
2. Singh, Jasprit. *Electronic and optoelectronic properties of semiconductor structures*. New York: Cambridge University Press, 2002.
3. Neamen, Donald A. *Semiconductor physics and devices: basic principles*. 3rd ed. New York: McGraw-Hill Companies Inc., 2003.
4. Ray, B. *II-VI Compounds*. Oxford: Pergamon, 1969.
5. Sze, S. M. *Semiconductor Devices: Physics and Technology*. Singapore: John Wiley & Sons, 1985.
6. Kittel, Charles. *Introduction to solid state physics*. 7th ed. USA: John Wiley & Sons, Inc., 1996.
7. Rama J. and Pino R. "Physical chemistry: energy band theory and quantum confinement." 15 August. 2007 <http://www.meliorum.com/Meliorum_Technologies_Physical_Chemistry.pdf>.
8. "Moving light from here to there." 2 March 2004. University of Pittsburgh. 15 August 2007. <<http://www.umd.pitt.edu/rr/2002summer/summer2002exciton.html>>.
9. "Exciton." *Wikipedia: The Free Encyclopedia*. 28 July 2007. 15 August 2007 <<http://en.wikipedia.org/wiki/Exciton>>.
10. Yoffe, A. D. "Low-dimensional systems: Quantum size effects and electronic properties of semiconductor microcrystallites (zero-dimensional systems) and some quasi-two-dimensional systems." *Advances in Physics* 51 (2002): 799-890.
11. Krasheninnikov, Arkady V. *Lecture 12. Surfaces, STM and carbon nanotubes*, Lecture notes. 15 August 2007 <<http://beam.acclab.helsinki.fi/~akrashen/esctmp.html>>.
12. Ashcroft, N. W. and Mermin, N. D. *Solid State Physics*. USA: Saunders College Publishing, 1976.
13. Van Zeghbroeck, B. "Principles of Semiconductor Devices." 2004. 15 August 2007 <<http://ece.colorado.edu/~bart/book/book/contents.htm>>.
14. Parak W. J., Manna L., Simmel F. C., Gerion D., and Alivisatos P. "Chapter 2: Quantum dots." *Nanoparticles-from theory to applications*. Ed. G. Schmid. Wiley Verlag, 2004. 4-49.
15. Ekimov A. I. and Onushchenko A. A. "Quantum size effect in three-dimensional microscopic semiconductor crystals." *JETP Letters* 34 (1981): 345.
16. Ekimov A. I. "Optical Properties of Semiconductor Quantum Dots in Glass Matrix." *Physica Scripta* 39 (1991): 217-222.
17. Klimov V. I., McBranch D. W., Leatherdale C. A., and Bawendi M. G. "Electron and hole relaxation pathways in semiconductor quantum dots." *Physical Review B* 60 (1999): 13740-13749.

18. "Stokes shift." *Wikipedia: The Free Encyclopedia*. 10 January 2007. 15 August 2007 <http://en.wikipedia.org/wiki/Stokes_shift>.
19. Nirmal M., Norris D. J., Kuno M., Bawendi M. G., Efros A. L., and Rosen M. "Observation of the "Dark Exciton" in CdSe Quantum Dots." *Physical Review Letters* 75 (1995): 3728-3731.
20. Efros A. L., Rosen M., Kuno M., Nirmal M., Norris D. J., and Bawendi M. "Band-edge exciton in quantum dots of semiconductors with a degenerate valence band: Dark and bright exciton states." *Physical Review B* 54 (1996): 4843-4856.
21. Reboledo F. A., Franceschetti A., and Zunger A. "Dark excitons due to direct Coulomb interactions in silicon quantum dots." *Physical Review B* 61 (2000): 13073-13087.
22. Johnston-Halperin E., Awschalom D. D., Crooker S. A., Efros A. L., Rosen M., Peng X., and Alivisatos A. P. "Spin spectroscopy of dark excitons in CdSe quantum dots to 60 T." *Physical Review B* 63 (2001): 205309.
23. Yoffe A. D. "Semiconductor quantum dots and related systems: Electronic, optical, luminescence and related properties of low dimensional systems." *Advances in Physics* 50 (2001): 1-208.
24. Smotkin E. S., Lee C., Bard S., Champion A., Fox M. A., Mallouk T. E., Webber S. E., and White J. M. "Size quantization effects in cadmium sulfide layers formed by a Langmuir-Blodgett technique." *Chemical Physics Letters* 152 (1988): 265-268.
25. Nirmal M., Dabbousi B. O., Bawendi M. G., Macklin J. J., Trautman J. K., Harris T. D., and Brus L. E. "Fluorescence intermittency in single cadmium selenide nanocrystals." *Nature* 383 (1996): 802-804.
26. Chadderton L.T., Fitzgerald A. G., and Yoffe A. D. "Disordering of Defects in Single Crystals of Zinc Sulfide." *Journal of Applied Physics* 35 (1964): 1582.
27. Colvin V. L. "CdSe nanocrystals with a dipole moment in the first excited state." *Journal of Chemical Physics* 97 (1992): 730.
28. Marin J. L., Riera R., and Cruz S. A. "Confinement of excitons in spherical quantum dots." *J. Phys.: Condens. Matter*. 10 (1998): 1349-1361.
29. Efros Al L. and Efros A. L. "Interband absorption of light in a semiconductor sphere." *Soviet physics Semiconductors* 16 (1982): 772-775.
30. Brus L.E. "Electron-electron and electron-hole interactions in small semiconductor crystallites: the size dependence of the lowest excited electronic state." *The Journal of Chemical Physics* 80 (1984): 4403-4409.
31. Brus L. "Electronic wave functions in semiconductor clusters: Experiment and theory." *Journal of Physical Chemistry* 90 (1986): 2555-2560.
32. Bawendi M. G., Wilson W. L., Rothberg L., Carroll P. J., Jedju T. M., Steigerwald M. L., and Brus L. E. "Electronic structure and photoexcited-carrier dynamics in nanometer-size CdSe clusters." *Physical Review Letters* 65 (1990): 1623-1626.
33. Kayanuma Y. "Wannier exciton in microcrystals." *Solid state communications* 59 (1986): 405-408.
34. Kayanuma Y. "Quantum-size effects of interacting electrons and holes in semiconductor microcrystals with spherical shape." *Physical Review B* 38 (1988): 9797-9805.

35. Ekimov A. I., Efros A. L., and Onushchenko A. A. "Quantum size effect in semiconductor microcrystals." *Solid State Communications* 56 (1985): 921-924.
36. González, Salvador. "Empirical pseudopotential method for the band structure calculation of strained-silicon germanium materials." Diss. Arizona State University, 2001.
37. Phillips J.C. "Energy-Band Interpolation Scheme Based on a Pseudopotential." *Physics Review* 112 (1958): 685.
38. Phillips J.C. and Kleinman L. "New Method for Calculating Wave Functions in Crystals and Molecules." *Physics Review* 116 (1959): 287.
39. Kleinman L. and Phillips J.C. "Crystal Potential and Energy Bands of Semiconductors. III. Self-Consistent Calculations for Silicon." *Physics Review* 118 (1960): 1153.
40. Ramakrishna M. V. and Friesner R. A., "Exciton spectra of semiconductor clusters." *Physical Review Letters* 67 (1991): 629-632.
41. Franceschetti A. and Zunger A. "Direct Pseudopotential Calculation of Exciton Coulomb and Exchange Energies in Semiconductor Quantum Dots." *Physical Review Letters* 78 (1997): 915-918.
42. Tomasulo A. and Ramakrishna M. V. "Quantum confinement effects in semiconductor clusters. II." *The Journal of Chemical Physics* 105 (1996): 3612.
43. Wang Y. and Herron N. "Quantum size effects on the exciton energy of CdS clusters." *Physical Review B* 42 (1990): 7253-7255.
44. Fu H. and Zunger A. "InP quantum dots: Electronic structure, surface effects, and the redshifted emission." *Physical Review B* 56 (1997): 1496-1508.
45. Lippens P. E. and Lannoo M. "Calculation of the band gap for small CdS and ZnS crystallites." *Physical Review B* 39 (1989): 10935-10942.
46. Lippens P. E. and Lannoo M. "Optical properties of II-VI semiconductor nanocrystals." *Semiconductor Science and Technology* 6 (1991): A157-A160.
47. Chang Y. C. "Bond-orbital models for superlattices." *Physical review B* 37 (1988): 8215-8222.
48. Einevoll G. T. "Confinement of excitons in quantum dots." *Physics Review B* 45 (1992): 3410-3417.
49. Nair S. V., Ramaniah L. M., and Rustagi K. C. "Electron states in a quantum dot in an effective-bond-orbital model." *Physical Review B* 45 (1992): 5969-5979.
50. Ramaniah L. M. and Nair S. V. "Optical absorption in semiconductor quantum dots: A tight-binding approach." *Physical review B* 47 (1993): 7132-7139.
51. Sophia J. Sun and Yia-Chung Chang. "Modeling self-assembled quantum dots by the effective bond-orbital method." *Physical review B* 62 (2000): 13631-13640.
52. Nabok A. *Organic and inorganic nanostructures*. Artech House, Inc., 2005.
53. Petty M. C. *Langmuir-Blodgett Films: An Introduction*, Cambridge, UK: Cambridge University Press, 1996.
54. Iwantono. "Studies on Cadmium Sulphide nanoparticles formed by the Langmuir-Blodgett technique." Diss. Materials and Engineering Research Institute, Sheffield Hallam University, 2003.

55. "Resonant tunneling diode (RTD) structures." 15 August 2007
<www.ecse.rpi.edu/~schubert/Course-ECSE-6290%20SDM-2/1%20Resonant%20tunneling%20structures.pdf>.

ELECTROSTATIC SELF-ASSEMBLY DEPOSITION AND OTHER METHODS FOR II-VI NANOSTRUCTURES' FABRICATION (LITERATURE REVIEW)

3.1. INTRODUCTION

This chapter presents the literature review of the electrostatic self-assembly method and previous works on CdS and ZnS nanoparticles. History of ESA technique and their deposition process will be discussed in more detail including the types of polyelectrolytes and their adsorption kinetics. Several issues in the deposition process, such as dipping time, drying procedure, stability and uniformity of polyelectrolytes films, will be discussed. For the sake of comparison, several other techniques for the formation of CdS and ZnS nanostructures are presented along with their characterisations.

3.2. ELECTROSTATIC SELF-ASSEMBLY METHOD

Electrostatic self-assembly (ESA) method, also known as polyelectrolyte self-assembly or electrostatic layer-by-layer deposition is based on the alternating adsorption of molecular layers of oppositely charged polymers (anionic and cationic polyelectrolytes), where the electrostatic interaction between opposite charges is the driving force behind the multilayer build-up. As the result, a very good nanosized structures could be produced.

R. K. Iler [1] is the first person who introduced and proposed this process to deposited multilayered thin film. In 1966, he demonstrated the method by depositing the layers of negatively charged silica colloid and positively charged alumina fibrils. But

this technique was not in used until 1990s, when Decher and co-workers [2] at Gutenberg University in Mainz, Germany, extended the work of Iler to a new method of organizing thin films using layer-by-layer adsorption of polyelectrolytes and demonstrated optically transparent multilayer films of four different polyelectrolytes.

Since then, electrostatic self-assembly has been used for the deposition of ultrathin films containing different types of molecules such as charged polymers (polyions) [3-21], dyes [22-24], nanoparticles (metallic, semiconducting, magnetic, insulating) and clay nanoplates [25-37], and bio objects (proteins, DNA, virus) [38-47]. The composition of each layer can be controlled by the incorporation of appropriately chosen molecules [7], and the structure of each layer can be manipulated by adjusting the deposition parameters [3, 11, 17, 21]. This makes ESA thin films an excellent choice for use in a wide range of applications, such as conductive polymer [48], electronics applications (single electron devices, batteries, diodes) [49-51], sensing applications [52], magnetic imaging and information storage [53], solar cells [54], biologically active membranes [55] and LEDs [56-59].

3.2.1. ESA deposition process

In the standard ESA process, multilayered thin films can be deposited onto an electrically charged substrate by sequentially dipping it into solutions of polycations and polyanions. This process is shown schematically in Figure 3.1. Starting from a negatively charged substrate, the first layer can be deposited by simply dipping the substrate into a polycation solution. At this step, positively charged ionic groups of the polymer interact electrostatically with the substrate, resulting in a net positive surface charge of the film surface. The next step is rinsing the sample with water to wash out of non-bound polyion molecules. The samples are then dipped into polyanion solution to restore the negative surface charge followed by rinsing with water. This completes the

electrostatic self-assembly deposition cycle of polycation/polyanions sandwich unit onto the substrate. Such deposition routine can be repeated as many times as needed.

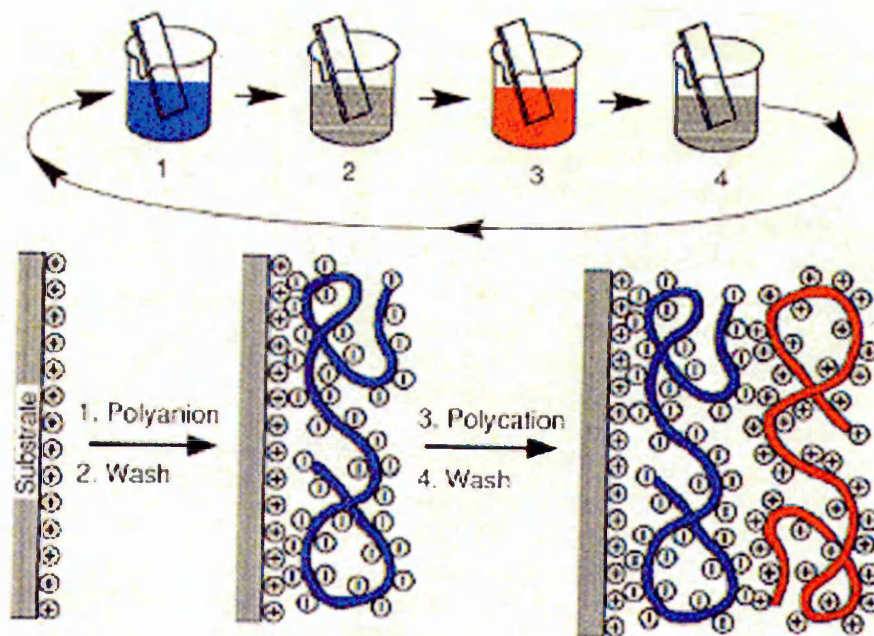
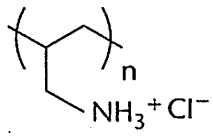
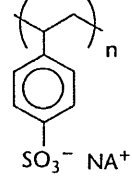
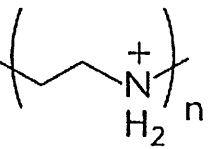
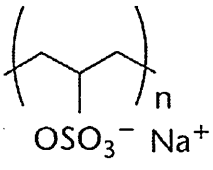
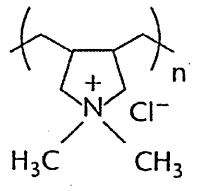


Figure 3.1. The sequence of layer by layer electrostatic deposition [60].

Polyions, either polyanions and polycations, usually exist in the form of salts, and can be dissolved in water or other polar solvents. The most common polyions used for ESA deposition, such as PSS, PVS, PDDA, and PEI are shown in Table 3.1. Typical molecular weight of polyelectrolytes is in the range of 50,000 - 200,000. In the solution with pH range from 3 to 9, they dissociate into the polymer chain containing ionized groups (either anionic or cationic) and counterions. The typical polyions concentrations used are about 1-2 mg/ml; the diluted polyions solution may result in a thinner film and may also need much longer deposition time. Lvov and Decher in 1994 reported that the variation in polyion concentration in the range from 0.1 to 5 mg/ml do not dramatically affect the layer thickness although the use of smaller concentrations down to 0.01 mg/ml has resulted in thinner films [45]. The thickness of polyanion/polycation layers depends on the compounds used and pH. The dependence of the polycation / polyanion

bilayer thickness on the ionic strength and on the variation of pH (for weak polyions) can be explained by partial neutralization of polyion side-groups which results in more coily conformation of polymer chains, as was analyzed by Rubner et al [14].

Table 3.1. The most common polyions used for ESA deposition

Polycations (MW = 50,000-70,000)		Polyanions (MW = 50,000-70,000)	
Poly(allylamine) hydrochloride (PAH)		Poly(styrenesulfonate) sodium salt (PSS)	
Poly(ethyleneimine) (PEI)		Poly(vinylsulphate) potassium salt (PVS)	
Poly(dimethyldiallyl-ammonium) chloride (PDDA)			

The multilayered ESA films usually are totally neutral, i.e. a stoichiometry of charged groups in neighboring polycation and polyanion layers has to be 1 : 1. It is confirmed for many polyelectrolyte combinations, such as PSS / PDDA or PSS / PEI, however for PSS / PAH, a deviation from 1 : 1 stoichiometry was found [15]. This is probably due to the incomplete dissociation of the polyions. It is difficult to control polyion dissociation, because it depends on a concentration and on the presence of oppositely charged compounds in solution [61].

3.2.2. Kinetic of polyions adsorption

In the deposition process, when the substrate is dipped into polyions solution, the polyelectrolyte molecules require a certain amount of time to move through the fluid, arrange themselves on the substrate and electrostatically bond to the surface. This time-dependent adsorption in ESA deposition has been investigated in [12, 19, 42] using quartz crystal microbalance (QCM) method.

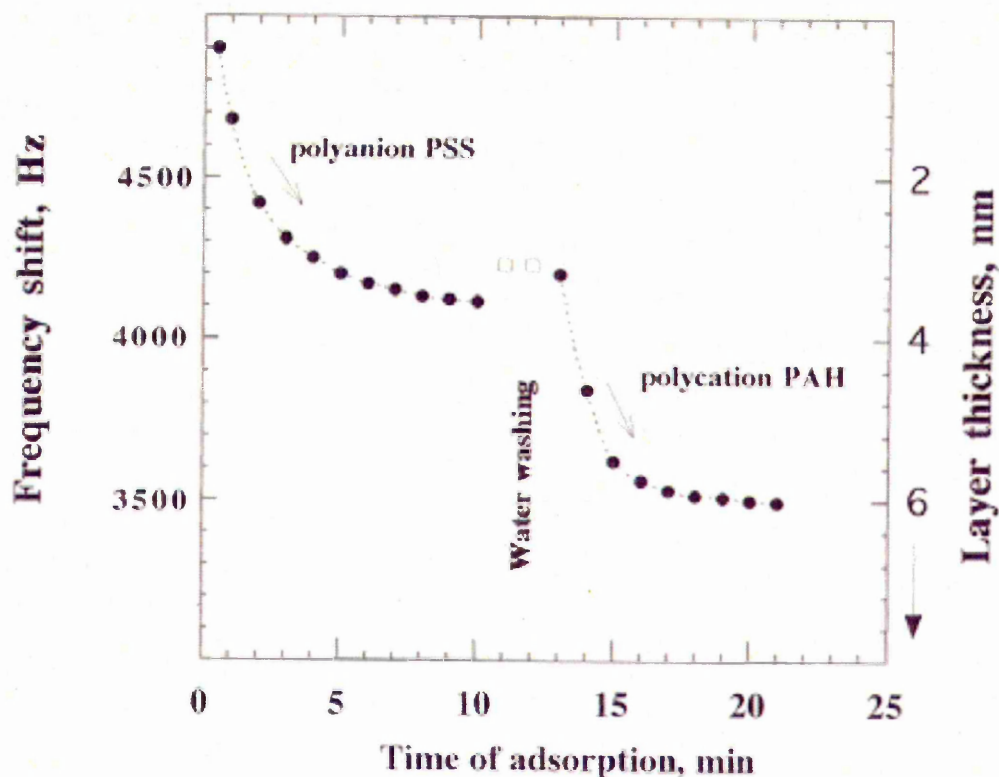


Figure 3.2. A typical kinetic profile of QCM measurements for polyions adsorption [60].

Typical kinetics of adsorption of PSS and PAH layers is shown in Figure 3.2. The fitting of the above data to exponential law yields the adsorption rates for PSS, $\tau = 2.5 \pm 0.2$ minutes and for PAH $\tau = 2.1 \pm 0.2$ minutes. This means that during the first 5 minutes 87 % of the material is adsorbed onto the charged substrate, and 95 % of full coverage is achieved after 8 minutes. In the majority of publications, adsorption times of 5 to 20 minutes are used [6]. Figure 3.2 also shows the effect of washing between subsequent deposition cycles. 1 - 2 minutes intermediate water-washing removes ± 10

% of weakly attached material from a polyion layer [19]. The importance of intermediate washing was analyzed in [15, 19].

K. L Cooper [62] studied the dependence of the film thickness of Poly S-119/PDDA on the dipping time using ellipsometry and UV/vis spectroscopy. It is shown in Figure 3.3 and 3.4 that the longer dipping time results in an increase in the layer thickness. At 20 minute dipping time, the increase in thickness is about 20 % higher as compared to 1 minute dipping; but the time required per bilayer is 20 times longer.

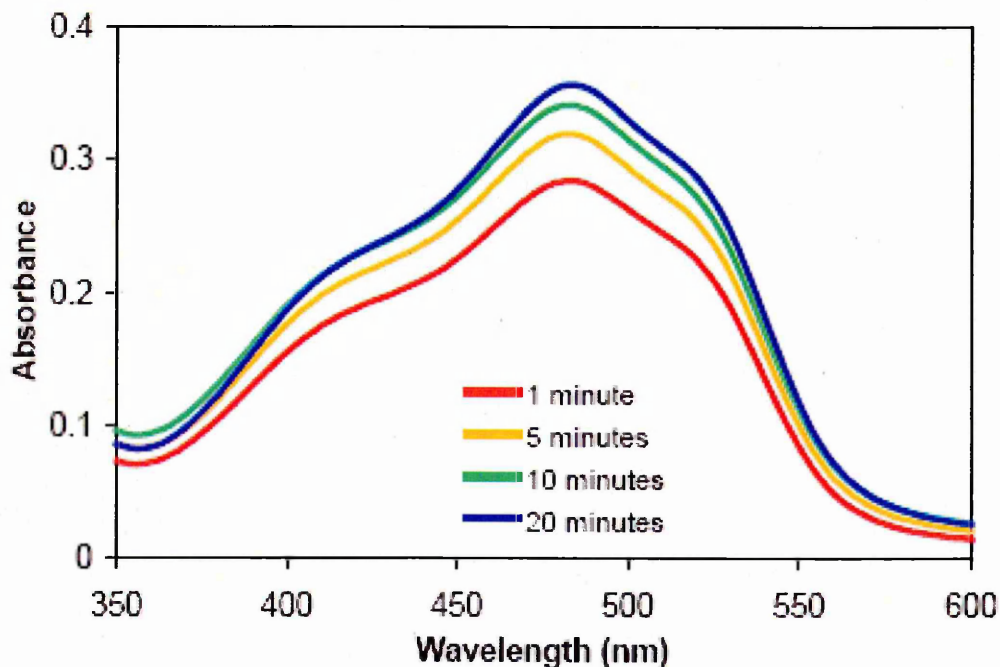


Figure 3.3. Optical absorbance comparison of 20 bilayer (PDDA/Poly S-119) films fabricated using different dipping times [62].

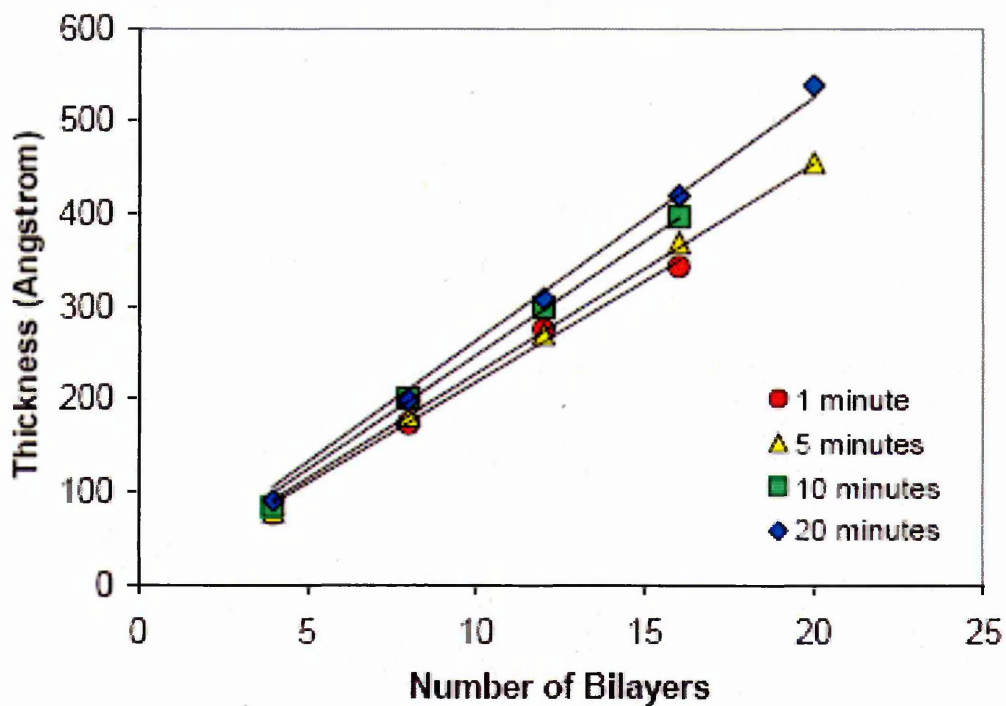


Figure 3.4. Ellipsometry comparison of (PDDA/Poly S-119) films fabricated using different dipping times [62].

The uniformity of ESA films growth has been investigated in [11]. Wei [63] demonstrated that the consecutive adsorption of layers using ESA is a stepwise and regular process. Figure 3.5 and 3.6 show the optical absorption spectra of PVP/PMA and PDDA/C60 multilayer assemblies for the layer numbers from 0 to 30, with the measurements taken for every 5 bilayers. Insets show the dependences of the optical density at the main absorption band (194 nm for PVP/PMA and 220 nm for PDDA/C60) versus the number of bilayers. The data points obey nearly perfect linear fit. The linear nature of the plots suggests that each adsorbed layer contributes an equal amount of material to the thin films. There are no shifts in the main absorption bands, which indicate that the films are uniform and no molecular aggregation occurred between the adjacent layers.

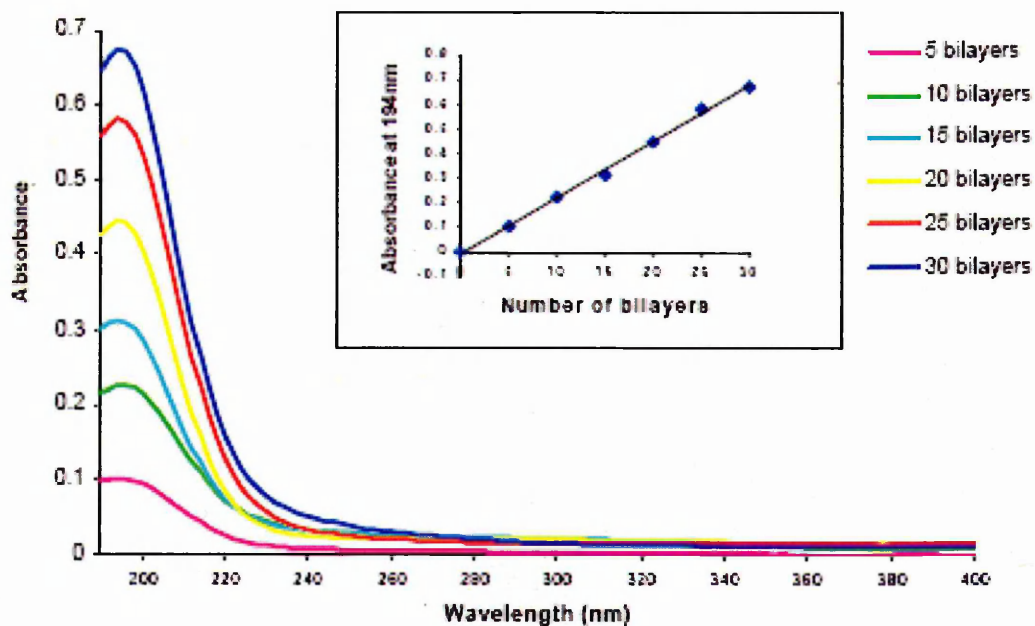


Figure 3.5. UV/vis absorption spectra of PVP/PMA multilayer thin films [63].

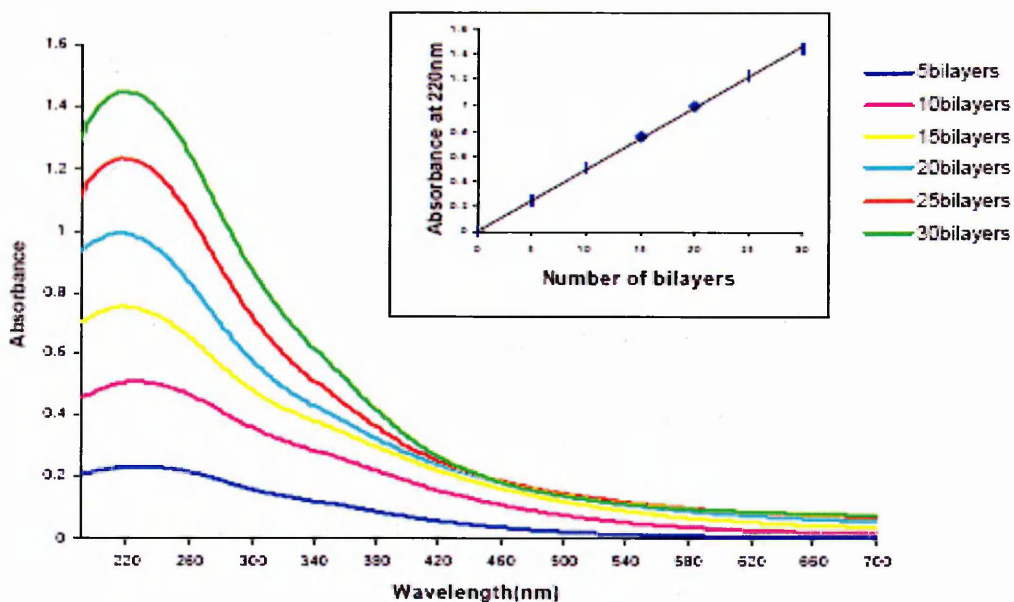


Figure 3.6. UV/vis absorption spectra of PDDA/C60 multilayer thin films [63].

It is found that the adsorption of the first 2-3 layers are usually non-linear [12, 41]. Tsukruk et al [41] explained this as an island-type adsorption of the first polyion layer on a weakly charged solid support. After several adsorption cycles, these islands

spread and cover the entire surface, and further multilayer growth will occur linearly.

That is why a longer time is recommended for the first few layers deposition.

As a part of deposition conditions study, the effect of periodic drying on the film characteristics has been investigated [7, 17, 19, 64]. Decher's group performed experiments on PSS/PAH films using X-ray reflectivity [7]; the results indicated that cyclic drying induced a periodic modulation in the film's electron density and reduced the interfacial width between monolayers, but did not affect either the total film thickness or individual bilayer thickness.

K. L Cooper [62] found that each bilayer in the dried film is thicker and more optically dense than that in the undried film (as shown in Figure 3.7 and 3.8). It was suggested that polyelectrolyte molecules in the undried sample were interpenetrated each other, and thus more density and the thickness became less than in dried films. This concept is illustrated in Figure 3.9.

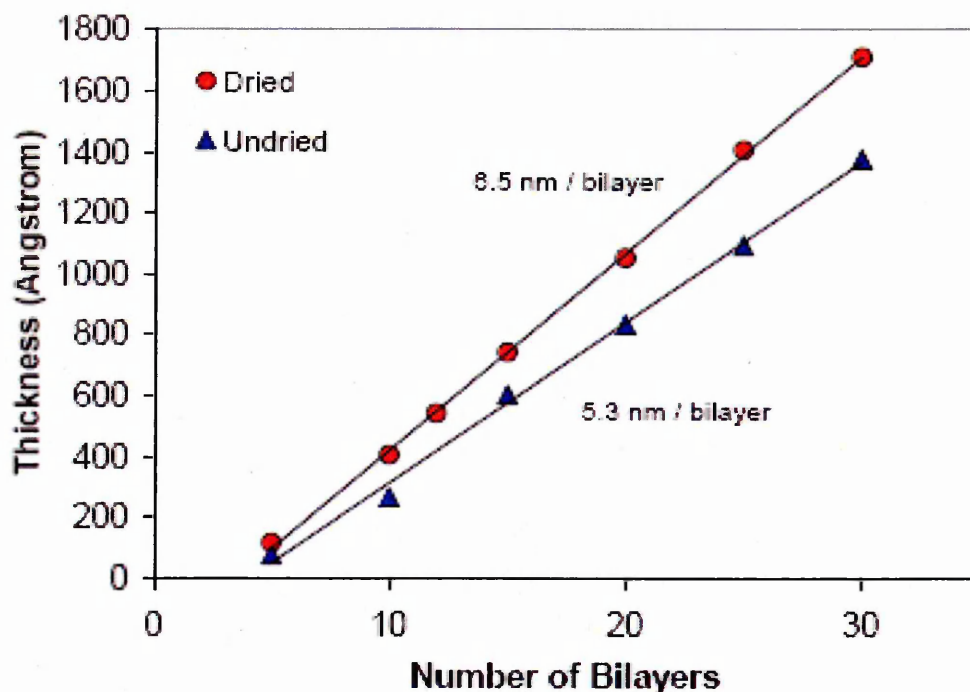


Figure 3.7. Ellipsometry comparison of (Poly R-478/PDDA) films dried in a stream of nitrogen after deposition of each monolayer (dried) and dried only for measurement purposes (nondried) [62].

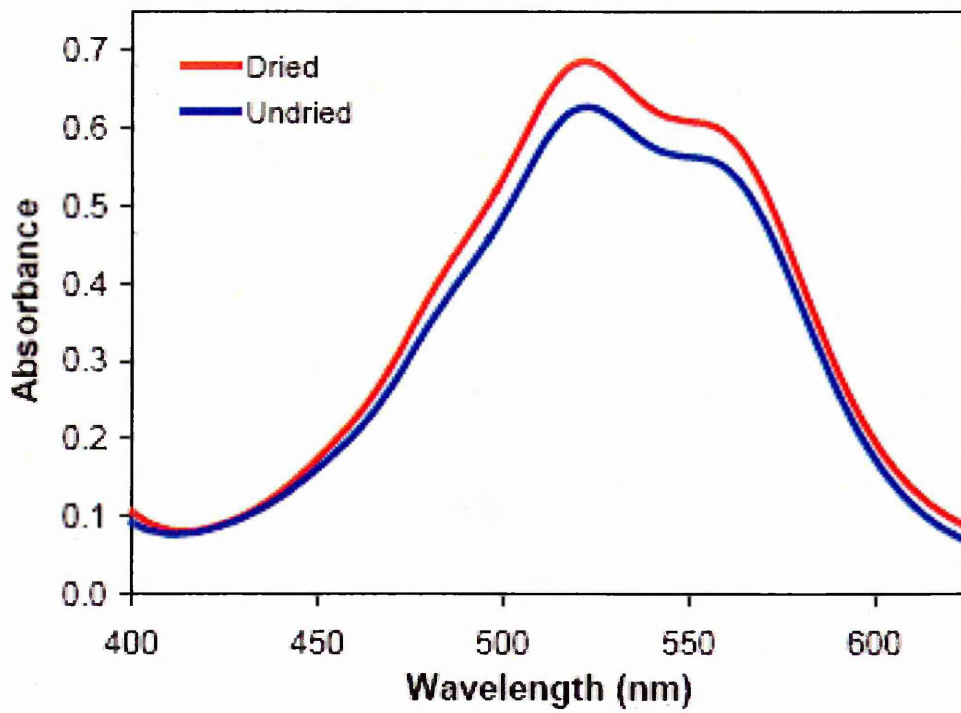


Figure 3.8. UV/vis absorbance spectra of 50 bilayer (Poly R-478/PDDA) films dried in a stream of nitrogen after deposition of each monolayer (dried) and dried only for measurement purposes (nondried) [62].

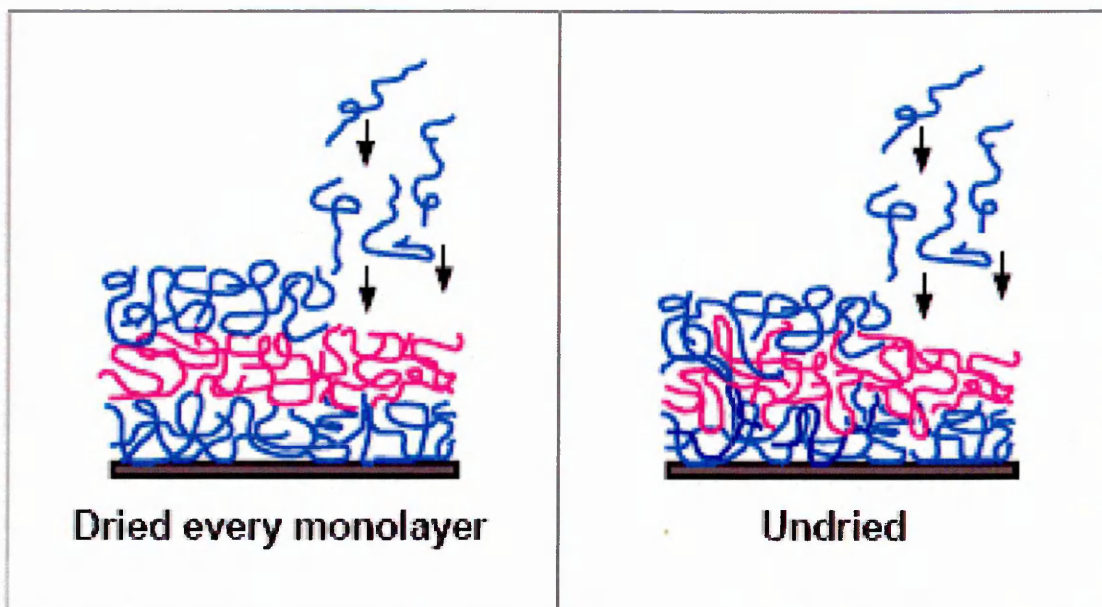


Figure 3.9. Effect of drying on the layer interpenetration [62].

The stability of ESA films was analysed in [6, 61]. A cooperative electrostatic interaction between the polycations and polyanions is strong and prevents the dissolution of the multilayers even in high ionic strength solvents. Figure 3.10 shows a negligible degradation of the absorbance spectra after 21 hours submersion in water.

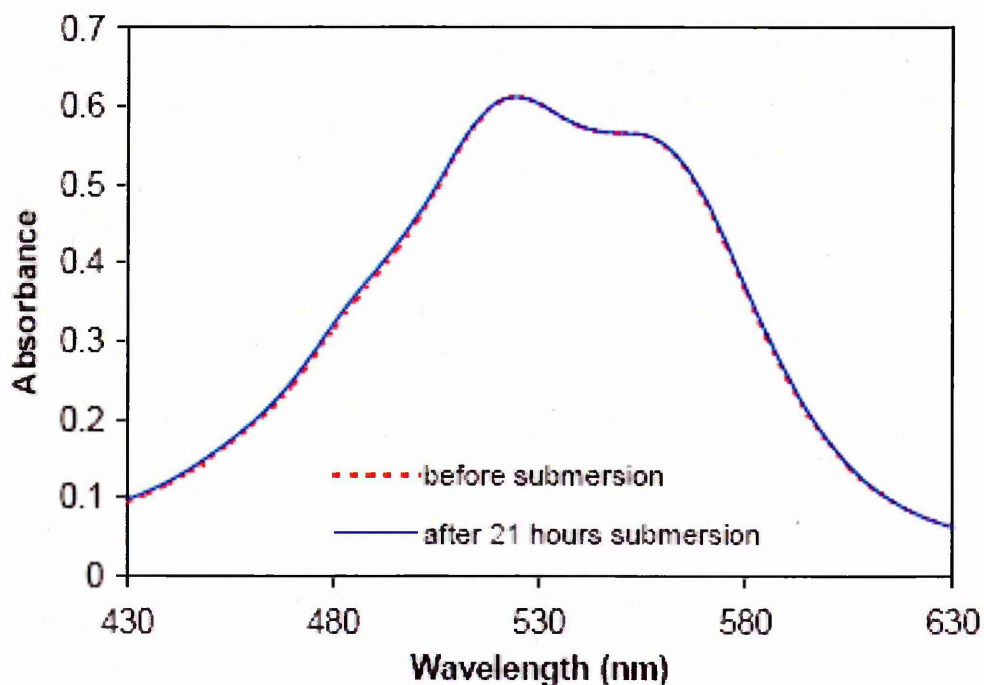


Figure 3.10. UV/vis absorbance spectra of 30 bilayer (Poly R-478/PDDA) film before and after water submersion for 21 hours [62].

In summary, comparing to other methods, ESA techniques have several advantages:

- Excellent molecular level uniformity which permits the fabrication of high quality films with homogenous properties (i.e. hydrophilicity/hydrophobicity and charge distribution).
- Independence from the substrate size or topology makes possible the ESA deposition on a variety of substrates of any size and complex shapes including implant organs or devices.

- The films have a good adhesion much higher than that in LB and spun films.
- ESA films are biocompatible.
- A large variety of materials such as polymers, organic macromolecules, proteins, inorganic nanoparticles, can be deposited with the ESA method.
- Multilayer thin films can be generated with almost no limit to the number of layers that can be generated.
- The process is environment-friendly, based on water solutions. The preparative procedure is simple, carried out in the open air and at room temperature, no elaborate instruments is required.
- The films are stable due to the minimum system energy obtained through self-rearrangement of molecules adsorbed on the surface.
- The ESA films have a defectless structure and therefore perfect for insulating and masking the surface.

The low speed of the film growth (one bilayer every 5-20 minutes) is a relative disadvantage of ESA technique. The other is the electrostatic anchoring of the first monolayer to substrate which depends on the surface charge and sometimes requires preliminary surface treatment using plasma or chemical modification (thiolation, silanization, oxidation, etc.).

3.2.3. Nanoparticles/ polyelectrolytes multilayers

As described earlier, inorganic particles of different nature, such as metallic, or semiconducting, can be incorporated into ESA films. The only requirement is to have polyelectrolytes and nanoparticles of opposite electrical charge. Therefore forces between nanoparticles and polyelectrolytes are primarily electrostatic, but they can also involve covalent and hydrogen bonding, π - π interactions, van der Waals attractions,

hydrophobic and epitaxial or other types of interactions. The schematic diagram of nanoparticles/polyelectrolytes multilayer is shown in Figure 3.11.

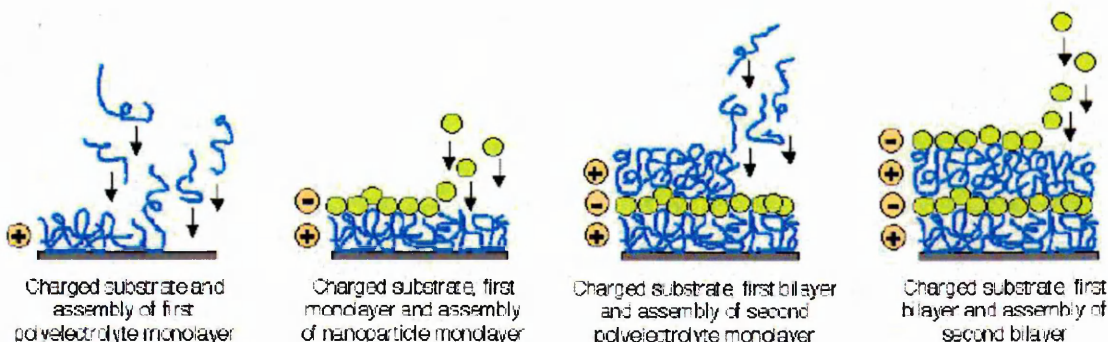


Figure 3.11. Basic ESA schematic for the buildup of multilayer assemblies by consecutive adsorption of cationic polyelectrolytes and anionic nanoparticles [62].

Some particles are naturally electrically charged. For example, oxide materials, such as SiO_2 , AlO_2 , TiO_2 , and SnO_2 , are negatively charged because of the hydroxide groups (OH^-) on their surface. The same applies to majority of metals, i.e. Al, Cu, Ti, Ag, and Fe; which are usually covered with a thin layer of native oxide. On the other hand, the electrical charge of nanoparticles can be formed by chemical modification. A typical example is the modification of gold nanoparticles with thiol-containing compound, which form short hydrocarbons containing a thiol-group on one end and, for example, $\text{SO}_3^- \text{Na}^+$ on the other end. This will form negatively charged particles, while thiol-amine compounds will form positively charged particles.

3.3. PREVIOUS WORK ON CdS AND ZnS NANOPARTICLES

By far, cadmium sulfide (CdS) and zinc sulfide (ZnS) are the most studied systems among of II-VI semiconductor materials due to their unique electrical and optical properties [murray93]. Various deposition techniques, both physical and chemical, such as: molecular beam epitaxy [65-69], ion implantation [70-72],

magnetron sputtering technique [73-75], electrochemical deposition [76-80], Langmuir-Blodgett (LB) films method [81-89], colloid synthesis [90-101], precipitation technique [102-105], and the reserve micelle method [106-108], have been used to deposit CdS and ZnS nanoparticles. In the next few paragraphs, some of these deposition techniques will be discussed in more detail.

Molecular Beam Epitaxy

The use of molecular beam epitaxy to grow single-crystalline layers of CdS and ZnS has been reported in the literature [65-68]. The films with thickness in the range of 2-7 μm were usually grown on top of buffer layers, such as InP (1 0 0), GaAs (1 1 1), and Si (1 0 0). Boieriu and coworker [66] grew CdS on CdTe (111) buffer layer on Si(100) or Si(111) substrates using MBE. The CdS layers have a wurtzite structure and are epitaxial on CdTe, with CdS [0110]//CdTe [112] and CdS([0001]//CdTe[111]). Auger electron spectroscopy and XPS have been used to determine the amount of S incorporated into CdTe at different values of the S pressure. The results indicate the formation of a $\text{CdTe}_{1-x}\text{S}_x$ layer, with x in the range of 5–8% for the sample studied by TEM.

In the case of ZnS, the luminescence peak at about 600 nm was observed from ZnS film grown on Si (1 0 0) using MBE and annealing at several temperatures of 190, 500, and 1000 °C [69].

Ion implantation technique

The average size in the range from 3.5 to 10 nm was recorded for CdS nanocrystals prepared by ion implantation [70]. The study shows that the particles' size depended on the ion dose and temperature of annealing post-treatment. As shown in Figure 3.12, the spectral shift towards larger wavelength for larger doses and higher

temperatures. X-ray diffraction (XRD) measurements performed on the samples after annealing post-treatment at 900°C identified the hexagonal phase of CdS.

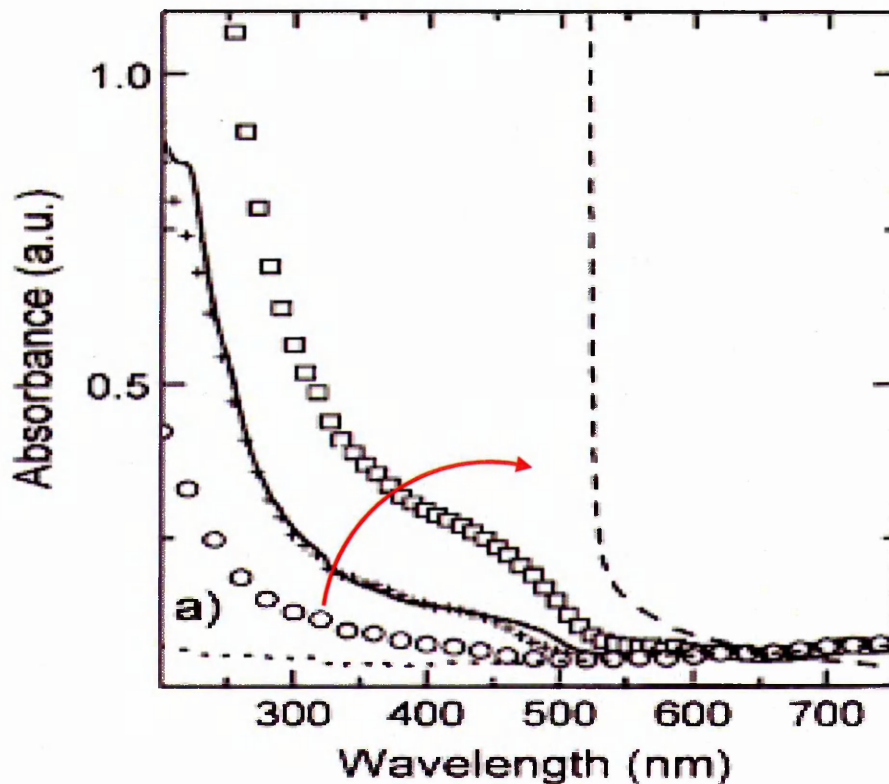


Figure 3.12. The absorption spectra of CdS formed in SiO₂ by ion implantation at different implanted dose and bulk CdS [70]. The arrow indicates the increase in the implantation dose.

The deposition of Mn doped ZnS using ion implantation was study by Ishizumi [71]. X-ray diffraction examination indicated that the ZnS nanocrystals are a mixture of hexagonal and cubic ZnS crystals. The far-field macro-PL spectra were presented in Figure 3.13.

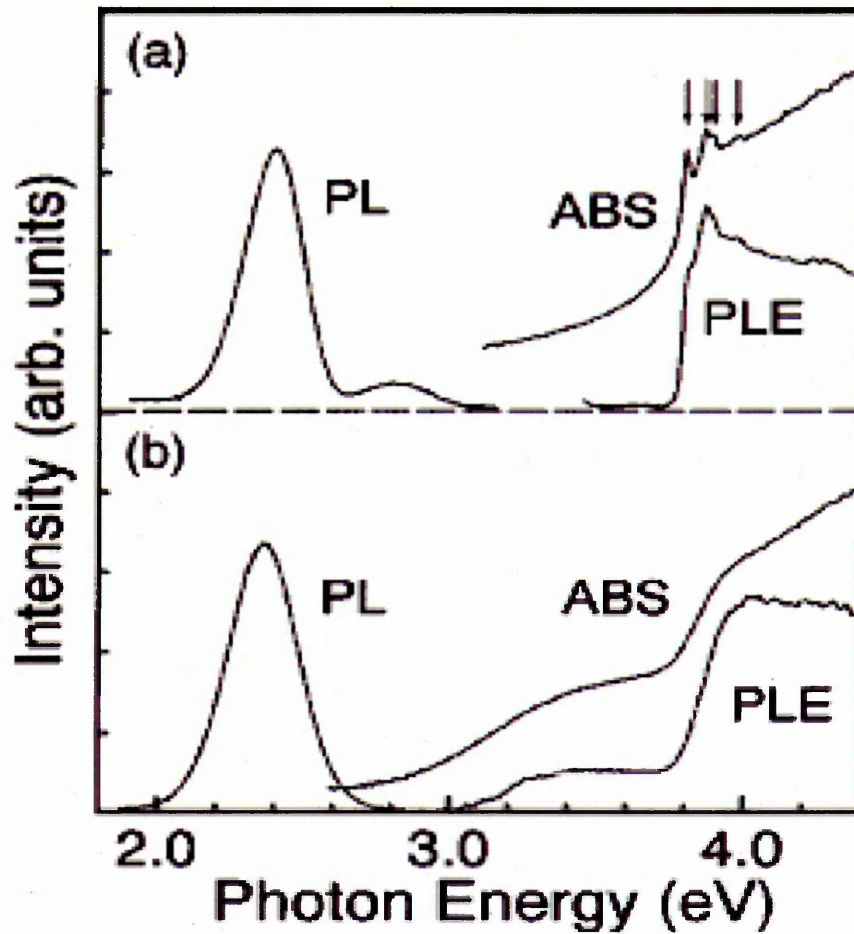


Figure 3.13. PL, PL excitation, and optical absorption spectra of the low doped sample (a) and the high-doped (b) samples at 14 K [71].

Magnetron sputtering technique

S. K. Mandal and coworker [75] are studied ZnS nanocrystals prepared by high pressure magnetron sputtering and found that films with different crystallite sizes and thickness could be obtained by varying the substrate temperature during deposition without sacrificing the blue shift. The films exhibited predominant zinc blende structure with intense diffraction rings for (111), (220) and (311) planes.

The other study using planar-magnetron-radio-frequency sputtering was done by Shao and co-worker [74]. They reported the fabrication of an 11.6% efficient

polycrystalline thin-film CdS/CdTe solar cell, deposited at 380 °C on soda-lime float-glass substrates coated with SnO₂:F. Much stronger photoluminescence and higher electrical conductivity are found in films and cells grown with unbalanced-field magnetrons.

Electrochemical technique

G. C. Morris and R. Vanderveen [76] deposited cadmium sulphide polycrystalline films on glass/indium tin oxide slides by periodic pulse electrolysis from aqueous solutions of cadmium chloride and sodium thiosulphate at 90° C. The properties of the films obtained were determined as functions of the deposition variables, such as cathodic voltage (V_c), anodic voltage (V_a), cathodic on time (t_c), anodic on time (t_a), deposition temperature, and solution concentrations of Cd²⁺ and S₂O₃²⁻. X-ray diffraction spectra and SEM showed that the hexagonal polycrystals were formed with the grain size of about 56 nm.

Zhang et al [79] were produced CdS nano-structures using electrochemical deposition on porous silicon (PS) as a substrate. AFM and SEM images show that the CdS deposit appeared to be a dense grain-like structure, each grain being of about 100 nm. These small nanoparticles are passivated with oxides on the surface and are responsible for green colour luminescence band centred at 530 nm.

For zinc containing compounds (ZnTe, ZnSe, ZnS), the electrodeposition from standard acidic aqueous solutions reveals to be more difficult [80]. It might be caused by the fact that the potential of zinc is more negative than that of cadmium by 0.36 V. The more negative deposition potential creates new problems due to the hydrogen evolution and parallel reactions of further reduction of chalcogenide elements.

D. Lincot [80] have recently shown that if the solution composition contains with the compound that dissolves the excess of elemental Se, for example sulfite ions SO_3^{2-} , it was possible to grow stoichiometric ZnSe.

Langmuir-Blodgett method

II-VI semiconductor quantum structures, including CdS, PbS, and ZnS nanostructures were also successfully formed within Langmuir-Blodgett (LB) films by exposing the LB films of respective metal salts to H_2S gas. Several compounds have been used as matrix materials, such as PMAO [81, 82], a variety of fatty acids [83-89], and calixarenes [86, 87, 89].

The blue shift is observed with respect to the bulk II-VI materials. The average size of CdS (less than 5 nm) was obtained and calculated from absorption spectra of the films. Direct observation techniques such as AFM, TEM and electron diffraction were performed on the CdS/calixarene acid and CdS/stearic acid LB films and confirmed the presence of CdS nanoparticles in LB films [89].

Aqueous colloid solutions

Stabilization of dispersed colloidal particles by surface treatments has been known for more than a century. There are two types of colloids, electrostatically and sterically stabilized [90]. The electrostatic stabilization is illustrated by a classical synthesis of 12-nm diameter gold particles. The method involves the reduction of an aqueous gold chloride solution by sodium citrate. The gold particles formed are stabilized by an electrical double layer (composed of bulky citrate ions, chloride ions, and the cations attracted to them) responsible for the Coulombic repulsions. There is a weak minimum in the van der Waals energy in the interparticle separation which approximately corresponds to the diameter of the stabilized gold nanoparticle. This

minimum (where the attractive van der Waals forces are overcompensated by the repulsive electrostatic interactions) is responsible for the electrostatic stabilization of the gold colloids in dispersions.

Steric stabilization is accomplished by adsorbing polymers and/or surfactants onto the surfaces of colloidal particles. Intertwining of the adsorbed polymers (and/or surfactant) in the interparticle space restricts the conformational motion (entropy effect) and increases the local polymer concentration (which has to be compensated by solvation osmotic effect) which, in turn, results in the stabilization of the particle.

Coating (capping or derivatization) by using surfactant molecules (capping agents), which form chemical bonds with the particles to stabilise and prevent them from the aggregation, provides an extremely useful method of nanoparticle stabilization. The choice of surfactants varies from case to case: molecules that bind too strongly to the surface of quantum dots are not suitable, as they would not allow the nanoparticles to grow. On the other hand, weakly coordinating molecules would yield large particles, or aggregates.

Some examples of suitable surfactants include alkane thiols (see Figure 3.14). Mercapto alcohols, mercaptocarboxylic acids, and thiophenol(s) have been shown to be highly suitable capping agents for CdSe, CdS, and ZnS nanoparticles [90, 91].

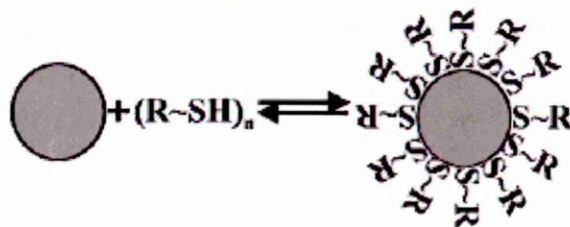


Figure 3.14. Schematics for the capping of a nanoparticle by alkanethiol molecules [90].

The colloid synthesis can be divided into two groups, non-aqueous and aqueous methods. In nonaqueous method, the capped nanoparticles were separated from the dispersing solvent, stored as dried powders (after precipitation), and redispersed on demand in a suitable solvent (polar solvent if the capping agent provides a hydrophilic surface and nonpolar solvent if the capping agent provides a hydrophobic surface) to form the same sized nanoparticles with the same degree of monodispersity. In 1990, Herron and coworkers successfully made CdS powder (non-aqueous method) by drying CdS solution capping with phenyl group (thiophenol) [92]. They have done chemical and NMR investigation along with the XRD and optical absorption to study the correlation between the cluster size and phenyl groups concentration. The size effects in CdS clusters were observed prominently for the radius 3 nm, which is the Bohr radius of exciton for this material.

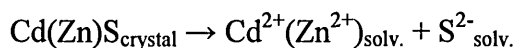
In aqueous synthesis method, there are two capping agents which are mostly used: thiolate [93, 94] and phosphate [95, 96] ligands. Since colloid nanoparticles are dispersed in solution, they can be produced in large quantities, and then can be transferred to any desired substrate. The size and shape of nanoparticles could be controlled by the composition of surfactant molecules and the time of growth of reaction [97-99].

Salata et al [100] prepared nanoparticulate CdS films for optoelectronic device applications by aqueous colloidal solutions method. The samples were deposited on ITO glass substrates utilizing a combination of the spin/dip coating techniques. The thickness of the CdS films varied from 50 to 200 nm. A typical diameter of the individual CdS nanoparticles was measured by high-resolution electron microscopy and it was found to be about 4 nm. Using similar technique, Sajinović et al [101] also formed 50 Å CdS quantum dots in a polystyrene matrix. Absorption onset of the CdS-Q-dots was blue shifted about 0.2 eV as compared to bulk CdS material. Using the

effective mass approximation model, the radius of CdS Q-dots was found to be 2.5 nm. X-ray diffraction measurements performed on the same sample gave a 4.5 nm diameter for CdS nanoparticles.

Precipitation technique

The earliest methods of II–VI quantum dots preparation were dated back to 1984 when Brus and coworkers [102] prepared uncapped and polymer-capped CdS and ZnS [103] nanoparticles (in size range 3–6 nm) by the arrested precipitation technique at room temperature involving the slow injection of the metal salt into a solution of ammonium or sodium sulfide in a suitable solvent (acetonitrile, methanol, or water). The success of the method relies on the ability to stop the crystal growth process immediately after the nucleation begins by controlling the equilibrium between the solid CdS (ZnS) and solvated metal ions in solution,



This can be achieved by selecting an appropriate reaction temperature or an appropriate solvent.

Nanda et al [104] also successfully formed thin films of CdS nanoparticles of different crystalline sizes by a precipitation technique using precursors as CdSO₄, thiourea and NH₄OH. The crystalline sizes in the range from 11 to 13 nm were found using AFM. The main absorption spectrum of the sample at room temperature was at 395 nm, giving an estimation of the band gap as 3.14 eV. The calculation gave the size of the particles to be in the range of 4 to 7.5 nm. XRD measurements of bulk CdS showed the presence of mixed cubic and hexagonal phases, whereas the nanocrystalline sample showed predominantly cubic phase.

Reverse micelle method

The mechanism of the formation of cadmium sulfide and zinc sulfide ultrafine particles in reverse micelles has been studied by Hirai [106], using sodium bis(2-ethylhexyl) sulfosuccinate (AOT)/isooctane as a reverse micellar solution. The particle formation process was followed by the change in UV-visible absorption spectra as shown in Figure 3.15. The absorption spectra were red shifted due to the increase of particles' diameter as a result of coagulation.

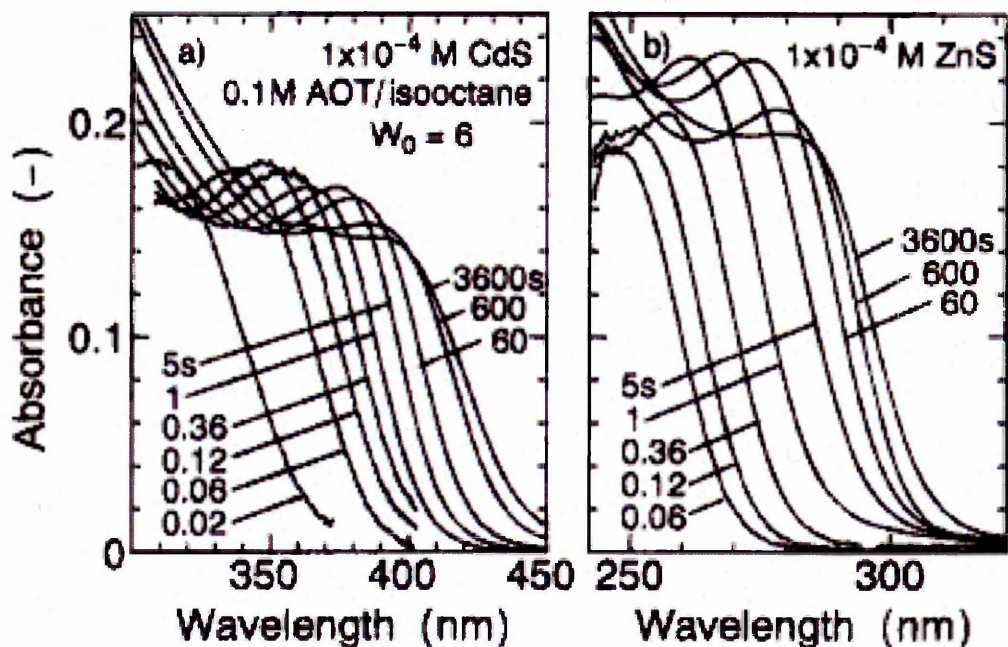


Figure 3.15. Absorption spectra of CdS and ZnS taken at different times (from 0.02 to 3600 s) after mixing the reactants [106].

In the other work by Yu et al [108] on CdS nanoparticles, TEM measurements showed that the particles' size were about 4 nm in diameter with a narrow size distribution and had the cubic zinc blend structure while UV-visible absorption spectra showed the main absorption at around 400 nm. The fluorescence spectra of the CdS nanoparticles exhibited broad emission bands at about 525 nm with the excitation at 417 nm.

REFERENCES

1. Iler R. K. "Multilayers of colloidal particles." *Journal of colloid and interface science* 21 (1966): 569-594.
2. Decher G., Hong J. D., and Schmitt J. "Buildup of ultrathin multilayer films by a self-assembly process. III: Consecutively alternating adsorption of anionic and cationic polyelectrolytes on charged surfaces." *Thin Solid Films* 210 (1992): 831-835.
3. Lvov Y., Decher G., and Mohwald H. "Assembly, structural characterization, and thermal behavior of layer-by-layer deposited ultrathin films of poly(vinyl sulfate) and poly(allylamine)." *Langmuir* 9 (1993): 481-486.
4. Lvov Y., Haas H., Decher G., MÖhwald H., and Kalacbev A. "Assembly of Polyelectrolyte Molecular Films onto Plasma-Treated Glass." *J. Phys. Chem.* 97 (1993): 12835-12841.
5. Lvov Y., Essler F., and Decher G. "Combination of polycation/polyanion self-assembly and Langmuir-Blodgett transfer for the construction of superlattice films." *Journal of Physical Chemistry* 97 (1993): 13773-13777.
6. Lvov Y. M. and Decher G. "Assembly of multilayer ordered films by alternating adsorption of oppositely charged macromolecules." *Crystallography Reports* 39 (1994): 628.
7. Decher G., Lvov Y., and Schmitt J. "Proof Of Multilayer Structural Organization In Self-Assembled Polycation-Polyanion Molecular Films." *Thin solid films* 244 (1994): 772-777.
8. Mao G., Tsao Y., Tirrell M., Davis H., Hessel V., and Ringsdorf H. "Self-assembly of photopolymerizable bolaform amphiphile mono-and multilayers." *Langmuir* 9 (1993): 3461-1470.
9. Tronin A., Lvov Y., and Nicolini C. "Ellipsometry and x-ray reflectometry characterization of self-assembly process of polystyrenesulfonate and polyallylamine." *Colloid and Polymer Science* 272 (1994): 1317-1321.
10. Hong J. D., Lowack K., Schmitt J., and Decher G. "Layer-by-layer deposited multilayer assemblies of polyelectrolytes and proteins: from ultra thin films to protein arrays." *Progress in Colloid & Polymer Science* 93 (1993): 98-102.
11. Schmitt J., Grunewald T., Decher G., Pershan P. S., Kjaer K., and Losche M. "Internal structure of layer-by-layer adsorbed polyelectrolyte films: A neutron and X-ray reflectivity study." *Macromolecules* 26 (1993): 7058-7063.
12. Sano M., Lvov Y., and Kunitake T. "Formation of ultrathin polymer layers on solid substrates by means of polymerization-induced epitaxy and alternate adsorption." *Ann. Rev. Material Science* 26 (1996): 153-187.
13. Hammond P. and Whitesides G. "Formation of Polymer Microstructures by Selective Deposition of Polyion Multilayers Using Patterned Self-Assembled Monolayers as a Template." *Macromolecules* 28 (1995): 7569- 7571.
14. Yoo D., Shiratori S., and Rubner M. "Controlling bilayer composition and surface wettability of sequentially adsorbed multilayers of weak polyelectrolytes." *Macromolecules* 31 (1998): 4309-4318.

15. Hoogeveen N., Stuart M. C., and Fler G. Formation and stability of multilayers of polyelectrolytes." *Langmuir* 12 (1996): 3675-3681.
16. Sukhorukov G. B., MÖhwald H., Decher G., and Lvov Y. M. "Assembly of polyelectrolyte multilayer films by consecutively alternating adsorption of polynucleotides and polycations." *Thin Solid Films* 284 (1996): 220-223.
17. Decher G. and Schmitt J. "Fine-tuning of the film thickness of ultrathin multilayer films composed of consecutively alternating layers of anionic and cationic polyelectrolytes." *Progr. Colloid Polym. Sci.* 89 (1992): 160-164.
18. Serizawa T., Hashiguchi S., and Akashi M. "Stepwise Assembly of Ultrathin Poly (vinyl alcohol) Films on a Gold Substrate by Repetitive Adsorption/Drying Processes." *Langmuir* 15 (1999): 5363-5368.
19. Lvov Y., Ariga K., Onda M., Ichinose I., and Kunitake T. "A careful examination of the adsorption step in the alternate layer-by-layer assembly of linear polyanion and polycation." *Colloids and Surfaces A: Physicochemical and Engineering Aspects* 146 (1999): 337-346.
20. Elbert D. L., Herbert C. B., and Hubbell J. A. "Thin polymer layers formed by polyelectrolyte multilayer techniques on biological surfaces." *Langmuir* 15 (1999): 5355-5362.
21. Lowack K. and Helm C. A. "Molecular mechanisms controlling the self-assembly process of polyelectrolyte multilayers." *Macromolecules* 31 (1998): 823-833.
22. Cooper T. M., Campbell A. L., and Crane R. L. "Formation of polypeptide-dye multilayers by electrostatic self-assembly technique." *Langmuir* 11 (1995): 2713-2718.
23. Ariga K., Lvov Y., and Kunitake T. "Assembling alternate dye-polyion molecular films by electrostatic layer-by-layer adsorption." *Journal of the American Chemical Society* 119 (1997): 2224-2231.
24. Lvov Y., Yamada S., and Kunitake T. "Non-linear optical effects in layer-by-layer alternate films of polycations and an azobenzene-containing polyanion." *Thin Solid Films* 300 (1997): 107-112.
25. Kotov N. A., Dékány I., and Fendler J. H. "Layer-by-layer self-assembly of polyelectrolyte-semiconductor nanoparticle composite films." *Journal of Physical Chemistry* 99 (1995): 13065-13069.
26. Schmitt J. and Decher G. "Metal Nanoparticle/Polymer Superlattice Films: Fabrication and Control of Layer Structure." *Journal of Science* (1992): 257-508.
27. Schmitt J., Machtle P., Eck D., MÖhwald H., and Helm C. A. "Preparation and optical properties of colloidal gold monolayers." *Langmuir* 15 (1999): 3256- 3266.
28. Lvov Y., Ariga K., Onda M., Ichinose I., and Kunitake T. "Alternate assembly of ordered multilayers of SiO₂ and other nanoparticles and polyions." *Langmuir* 13, (1997): 6195-6202.
29. Liu Y., Wang A., and Claus R. O. "Layer-by-layer electrostatic self-assembly of nanoscale Fe₃O₄ particles and polyimide precursor on silicon and silica surfaces." *Applied Physics Letters* 71 (1997): 2265.
30. Caruso F., Lichtenfeld H., Giersig M., and MÖhwald H. "Electrostatic self-assembly of silica nanoparticle-polyelectrolyte multilayers on polystyrene latex particles [4]." *Journal of the American Chemical Society* 120 (1998): 8523-8524.

31. Lvov Y., Ariga K., and Kunitake T. "Formation of ultrathin multilayer and hydrated gel from montmorillonite and linear polycations." *Langmuir* 12 (1996): 3038-3044.
32. Ichinose I., Tagawa H., Lvov Y., and Kunitake T. "Formation process of ultrathin multilayer films of molybdenum oxide by alternate adsorption of octamolybdate and linear polycations." *Langmuir* 14 (1998): 187-192.
33. Cassagneau T., Fendler J. H., and Mallouk T. E. "Optical and electrical characterizations of ultrathin films self-assembled from 11-aminoundecanoic acid capped TiO₂ nanoparticles and polyallylamine hydrochloride." *Langmuir* 16 (2000): 241-246.
34. Correa-Duarte M., Giersig M., Kotov N., and Liz-Marzan L. "Control of Packing Order of Self-Assembled Monolayers of Magnetite Nanoparticles with and without SiO₂ Coating by Microwave Irradiation." *Langmuir* 14 (1998): 6430- 6435.
35. Chang-Yen D. A., Lvov Y., McShane M. J., and Gale B. K. "Electrostatic self-assembly of a ruthenium-based oxygen sensitive dye using polyion-dye interpolyelectrolyte formation." *Sensors and Actuators, B: Chemical* 87 (2002): 336-345.
36. Fendler J. H. "Preparation and Utilization of Self-assembled Ultrathin Films Composed of Polyelectrolytes, Nanoparticles and Nanoplatelets." *Croatica Chemica Acta* 71 (1998): 1127-1137.
37. Ariga K., Lvov Y., Ichinose I., and Kunitake T. "Ultrathin films of inorganic materials (SiO₂ nanoparticle, montmorillonite microplate, and molybdenum oxide) prepared by alternate layer-by-layer assembly with organic polyions." *Applied Clay Science* 15 (1999): 137-152.
38. Cassier T., Lowack K., and Decher G. "Layer-by-layer assembled protein/polymer hybrid films: nanoconstruction via specific recognition." *Supramolecular Science* 5 (1998): 309-315.
39. Decher G., Lehr B., Lowack K., Lvov Y., and Schmitt J. "New nanocomposite films for biosensors: Layer-by-layer adsorbed films of polyelectrolytes, proteins or DNA." *Biosensors and Bioelectronics* 9 (1994): 677-684.
40. Lvov Y., Decher G., and Sukhorukov G. "Assembly of thin films by means of successive deposition of alternate layers of DNA and poly (allylamine)." *Macromolecules* 26 (1993): 5396-5399.
41. Tsukruk V., Rinderspacher F., and Bliznyuk V. "Self-assembled multilayer films from dendrimers." *Langmuir* 13 (1997): 2171-2176.
42. Caruso F., Niikura K., Furlong N., and Okahata Y. "Assembly of alternating polyelectrolyte and protein multilayer films for immunosensing." *Langmuir* 13 (1997): 3427-3433.
43. Caruso F., Furlong D. N., Ariga K., Ichinose I., and Kunitake T. "Characterization of polyelectrolyte-protein multilayer films by atomic force microscopy, scanning electron microscopy, and fourier transform infrared reflection-absorption spectroscopy." *Langmuir* 14 (1998): 4559-4565.
44. Ladam G., Schaaf P., Cuisinier F. J. G., Decher G., and Voegel J. C. "Protein adsorption onto auto-assembled polyelectrolyte films." *Langmuir* 17 (2001): 878-882.

45. Lvov Y., Haas H., Decher G., Mohwald H., and Kalachev A. "Successive deposition of alternate layers of polyelectrolytes and a charged virus." *Langmuir* 10 (1994): 4232-4236.
46. Lvov Y., Ariga K., Ichinose I., and Kunitake T. "Assembly of multicomponent protein films by means of electrostatic layer-by-layer adsorption." *Journal of the American Chemical Society* 117 (1995): 6117-6123.
47. Lvov Y., Ariga K., Ichinose I., and Kunitake T. "Molecular film assembly via layer-by-layer adsorption of oppositely charged macromolecules (linear polymer, protein and clay) and concanavalin A and glycogen." *Thin Solid Films* 284 (1996): 797-801.
48. Cheung J. H., Fou A. F., and Rubner M. F. "Molecular self-assembly of conducting polymers." *Thin Solid Films* 244 (1994): 985-989.
49. Feldheim D.L., Grabar K.C., Natan M.J., and Mallouk T.E. Electron transfer in Self-Assembled Polyelectrolyte/Metal Nanoparticle Heterostructures." *J. Am. Chem. Soc.* 118 (1996): 7640.
50. Cassagneau T. and Fendler J. H. "High density rechargeable lithium-ion batteries self-assembled from graphite oxide nanoplatelets and polyelectrolytes." *Advanced Materials* 10 (1998): 877-881.
51. Cassagneau T., Mallouk T. E., and Fendler J. H. "Layer-by-layer assembly of thin film zener diodes from conducting polymers and CdSe nanoparticles." *Journal of the American Chemical Society* 120 (1998): 7848-7859.
52. Liu Y., Wang A., and Claus R. "Molecular Self-Assembly of TiO₂/Polymer Nanocomposite Films." *J. Phys. Chem. B* 101 (1997): 1385.
53. Liu Y., Wang A., and Claus R. "Layer-by-layer electrostatic self-assembly of nanoscale Fe₃O₄ particles and polyimide precursor on silicon and silica surfaces." *Appl. Phys. Lett.* 71 (1997): 2265.
54. Oladeji I. O. and Chow, Lee. "Synthesis and processing of CdS/ZnS multilayer films for solar cell application." *Thin Solid Films* 474 (2005): 77-83.
55. Onda M., Lvov Y., Ariga K., and Kunitake T. "Sequential actions of glucose oxidase and peroxidase in molecular films assembled by layer-by-layer alternate adsorption." *Biotechnology and Bioengineering* 51 (1996): 163-167.
56. Fou A. C., Onitsuka O., Ferreira M., Rubner M. F., and Hsieh B. R. "Fabrication and properties of light emitting diodes based on self-assembled multilayers of poly (p-phenylene vinylene)." *J. Appl. Phys.* 79 (1996): 7501.
57. Onitsuka O., Fou A. C., Ferreira M., Hsieh B. R., and Rubner M. F. "Enhancement of light emitting diodes based on self-assembled heterostructures of poly (p-phenylene vinylene)." *J. Appl. Phys.* 80 (1996): 4067.
58. Mattoussi H. "Electroluminescence from heterostructures of poly (phenylene vinylene) and inorganic CdSe nanocrystals." *J. Appl. Phys.* 83 (1998): 7965.
59. Baur J. W., Kim S., Balandia P. B., Reynolds J. R., and Rubner, M.F. "Thin-film light emitting devices based on sequentially adsorbed multilayers of water-soluble poly (p-phenylene vinylene)." *Advanced Materials* 10 (1998): 1452-1455.
60. Lvov Y. M. "Thin film nanofabrication by alternate adsorption of polyions, nanoparticles and proteins." *Handbook for Surfaces and Interfaces Vol. 3 Nanostructured Materials*. Ed. H Nalwa. New York: Academic, 2001. p. 170-89.

61. Kabanov V. A. "Physicochemical basis and the prospects of using soluble interpolyelectrolyte complex." *Polymer science* 36 (1994): 143-156.
62. Cooper K. L. "Electrostatic Self-Assembly of Linear and Nonlinear Optical Thin Films." Diss. Virginia Polytechnic Institute and State University, Blacksburg, Virginia, 1999.
63. Weiwei Du. "Electrostatic Self-Assembly of Biocompatible Thin Films." Diss. Virginia Polytechnic Institute and State University, Blacksburg, Virginia, 2000.
64. Onda M., Lvov Y., Ariga K., and Kunitake T. "Molecularly flat films of linear polyions and proteins obtained by the alternate absorption method." *Jpn. J. Appl. Phys.* 36 (1997): 1608-1611.
65. Clark, A. H. and Unertl W. N. "MBE Growth of CuInSe₂ on CdS: Initial Stages." *Jpn. J. Appl. Phys.* 3 (1980): 3.
66. Boieriu P., Sporken R., Xin Y., Browning N. D., and Sivananthan S. "Wurtzite CdS on CdTe grown by molecular beam epitaxy." *Journal of Electronic Materials* 29 (2000): 718-722.
67. Suzuki S., Takazawa Y., Kumada H., Ishitani Y., and Yoshikawa A. "Optical characterization of hexagonal CdS layers grown on GaAs (111) by MBE: application of phase-shift-difference spectroscopy." *Physica status solidi(c)* 1 (1989): 657-661.
68. Tadokoro T., Ohta S. I., Ishiguro T., Ichinose Y., Kobayashi S., and Yamamoto N. "Growth and characterization of CdS epilayers on(100) GaAs by atomic layer epitaxy." *Journal of crystal growth* 130 (1993): 29-36.
69. McClean I. P. and Thomas C. B. "Photoluminescence study of MBE-grown." *Semicond. Sci. Tech.* 7 (1992): 1394-1399.
70. Desnica U.V., Gamulin O., Tonejc A., Ivanda M., and White C.W. "CdS nanocrystals formed in SiO₂ substrates by ion implantation." *Materials Science and Engineering C* 15 (2001): 105-107.
71. Ishizumi A. "Space-resolved photoluminescence of ZnS: Cu, Al nanocrystals fabricated by sequential ion implantation." *Applied Physics Letters* 84 (2004): 2397.
72. Bonafos C., Garrido B., Lopez M., Romano-Rodriguez A., Gonzalez-Varona O., Perez-Rodriguez A., Morante J. R., and Rodriguez R. "Structural and optical characterization of Mn doped ZnS nanocrystals elaborated by ion implantation in SiO₂." *Nuclear Instruments and Methods in Physics Research Section B: Beam Interactions with Materials and Atoms* 147 (1999): 373-377.
73. Hernández-Contreras H., Contreras-Puente G., Aguilar-Hernández J., Morales-Acevedo A., Vidal-Larramendi J., and Vigil-Galán O. "CdS and CdTe large area thin films processed by radio-frequency planar-magnetron sputtering." *Thin Solid Films* 403 (2002): 148-152.
74. Shao M., Fischer A., Grecu D., Jayamaha U., Bykov E., Contreras-Puente G., Bohn R. G., and Compaan A. D. "Radio-frequency-magnetron-sputtered CdS/CdTe solar cells on soda-lime glass." *Applied Physics Letters* 69 (1996): 3045.
75. Mandal S. K., Chaudhuri S., and Pal A. K. "Optical properties of nanocrystalline ZnS films prepared by high pressure magnetron sputtering." *Thin Solid Films* 350 (1999): 209-213.

76. Morris G. C. and Vanderveen R. "Cadmium sulphide films prepared by pulsed electrodeposition." *Solar Energy Materials and Solar Cells* 27 (1992): 305-319.
77. Schwarzacher W., Attenborough K., Michel A., Nabiyouni G., and Meier J. P. "Electrodeposited nanostructures." *Journal of Magnetism and Magnetic Materials* 165 (1997): 23-29.
78. Pasa A. A. and Schwarzacher W. "Electrodeposition of thin films and multilayers on silicon." *Physica Status Solidi (A) Applied Research* 173 (1999): 73-84.
79. Zhang P., Kim P. S., and Sham T. K. "XANES studies of CdS nano-structures on porous silicon." *Journal of Electron Spectroscopy and Related Phenomena* 119 (2001): 229-233.
80. Lincot, Daniel. "Electrodeposition of semiconductors." *Thin Solid Films* 487 (2005): 40-48.
81. Jin, J. and Li, L.S. and Tian, Y.Q. and Zhang, Y.J. and Liu, Y. and Zhao, Y.Y. and Shi, T.S. and Li, T.J. "Structure and characterization of surfactant-capped CdS nanoparticle films by the Langmuir-Blodgett technique." *Thin solid films* 327 (1998): 559-562.
82. Li, L.S. and Qu, L. and Wang, L. and Lu, R. and Peng, X. and Zhao, Y. and Li, T.J. "Preparation and Characterization of Quantum-Sized PbS Grown in Amphiphilic Oligomer Langmuir-Blodgett Monolayers." *Langmuir* 13 (1997): 6183-6187.
83. Erokhin, V. and Facci, P. and Carrara, S. and Nicolini, C. "Fatty acid-based monoelectron device." *Biosensors and Bioelectronics* 12 (1997): 601-606.
84. Erokhin V., Facci P., Gobbi L., Dante S., Rustichelli F., and Nicolini C. "Preparation of semiconductor superlattices from LB precursor." *Thin Solid Films* 327-329 (1998): 503-505.
85. Erokhina S., Erokhin V., and Nicolini C. "Electrical properties of thin copper sulfide films produced by the aggregation of nanoparticles formed in LB precursor." *Colloids and Surfaces A: Physicochemical and Engineering Aspects* 198-200 (2002): 645-650.
86. Nabok A. V., Richardson T., Davis F., and Stirling C. J. M. "Cadmium sulfide nanoparticles in Langmuir-Blodgett films of calixarenes." *Langmuir* 13 (1997): 3198-3201.
87. Nabok A. V., Richardson T., McCartney C., Cowlam N., Davis F., Stirling C. J. M., Ray A. K., Gacem V., and Gibaud A. "Size-quantization in extremely small CdS clusters formed in calixarene LB films." *Thin Solid Films* 327-329 (1998): 510-514.
88. Nabok A. V., Iwantono B., Hassan A. K., Ray A. K., and Wilkop T. "Electrical characterisation of LB films containing CdS nanoparticles." *Materials Science and Engineering C* 22 (2002): 355-358.
89. Iwantono. "Studies on Cadmium Sulphide nanoparticles formed by the Langmuir-Blodgett technique." Diss. Materials and Engineering Research Institute, Sheffield Hallam University, United Kingdom, 2003.
90. Fendler J.H. "Chemical self-assembly for electronic applications." *Chem. Mater.* 13 (2001): 3196-3210.
91. Marcus M. A., Flood W., Stiegerwald M., Brus L., and Bawendi M. "Structure of capped cadmium selenide clusters by EXAFS." *The Journal of Physical Chemistry* 95 (1991): 1572-1576.

92. Herron N., Wang Y., and Eckert H. "Synthesis and Characterization of Surface-Capped, Size-Quantized CdS Clusters Chemical Control of Cluster Size." *J. Am. Chem. Soc.* 112 (1990): 1322-1326.
93. Nosaka Y., Shigeno H., and Ikeuchi T. "Formation of polynuclear cadmium-thiolate complexes and CdS clusters in aqueous solution studied by means of stopped-flow and NMR spectroscopies." *J. Phys. Chem.* 99 (1996): 8317-8322.
94. Chen H. M., Huang X. F., Xu L., Xu J., Chen K. J., and Feng D. "Self-assembly and photoluminescence of CdS-mercaptopoacetic clusters with internal structures." *Superlattices and Microstructures* 27 (2000): 1-5.
95. Fojtik A., Weller H., Koch U., and Henglein A. "Photo-chemistry of colloidal metal sulfides. VIII: Photo physics of extremely small CdS particles: Q-state CdS and magic agglomeration numbers." *Berichte der Bunsengesellschaft für Physikalische Chemie* 88 (1984): 969-977.
96. Winter J. O., Gomez N., Gatzert S., Schmidt C. E., and Korgel B. A. "Variation of cadmium sulfide nanoparticle size and photoluminescence intensity with altered aqueous synthesis conditions." *Colloids and Surfaces A: Physicochemical and Engineering Aspects* 254 (2005): 147-157.
97. Murray C. B., Norris D. J., and Bawendi M. G. "Synthesis and characterization of nearly monodisperse CdE (E = S, Se, Te) semiconductor nanocrystallites." *Journal of the American Chemical Society* 115 (1993): 8706-8715.
98. Peng X., Manna L., Yang W., Wickham J., Scher E., Kadavanich A., and Alivisatos A. P. "Shape control of CdSe nanocrystals." *Nature* 404 (2000): 59-61.
99. Puentes, V. F. Krishnan K., and Alivisatos A. P. "Synthesis of colloidal cobalt nanoparticles with controlled size and shapes." *Topics in Catalysis* 19 (2002): 145-148.
100. Salata O. V., Dobson P. J., Sabesan S., Hull P. J., and Hutchison J. L. "Preparation of nanoparticulate CdS films suitable for opto-electronic device applications." *Thin Solid Films* 288 (1996): 235-238.
101. Sajinovic D., Saponjic Z. V., Cvjeticanin N., Cincovic M. M., and Nedeljkovic J. M. "Synthesis and characterization of CdS quantum dots-polystyrene composite." *Chemical Physics Letters* 329 (2000): 168-172.
102. Brus L.E. "Electron-electron and electron-hole interactions in small semiconductor crystallites: the size dependence of the lowest excited electronic state." *The Journal of Chemical Physics* 80 (1984): 4403-9.
103. Rossetti R., Ellison J. L., Gibson J. M., and Brus L. E. "Size effects in the excited electronic states of small colloidal CdS crystallites." *The Journal of Chemical Physics* 80 (1984): 4464.
104. Nanda K. K., Sarangi S. N., Mohanty S., and Sahu S. N. "Optical properties of CdS nanocrystalline films prepared by a precipitation technique." *Thin Solid Films* 322 (1998): 21-27.
105. Bredol M. and Merikhi J. "ZnS precipitation: morphology control." *Journal of Materials Science* 33 (1998): 471-476.
106. Hirai T., Sato H., and Komasaawa I. "Mechanism of Formation of CdS and ZnS Ultrafine Particles in Reverse Micelles." *Industrial & Engineering Chemistry Research* 33 (1994): 3262-3266.

107. Zhang J., Sun L., Liao C., and Yan C. "Size control and photoluminescence enhancement of CdS nanoparticles prepared via reverse micelle method." *Solid State Communications* 124 (2002): 45-48.
108. Yu Z., Degang F., Xin W., Juzheng L., and Zuhong L. "Optical and nonlinear optical properties of surface-modified CdS nanoparticles." *Colloids and Surfaces A: Physicochemical and Engineering Aspects* 181 (2001): 145-149.

EXPERIMENTAL METHODS

4.1. INTRODUCTION

This chapter describes the theoretical background, procedures, and details of the experimental techniques for sample preparation and investigation. The main deposition technique used was the electrostatic self assembly (ESA). Colloid solutions of electrically charged CdS and ZnS nanoparticles, which were suitable for ESA, were prepared by aqueous synthesis (described in section 4.2.1). The procedure of samples preparation along with the multilayer structure obtained were presented in sections 4.2.2 and 4.2.3. Sections 4.3 and 4.4 present the optical measurements using UV-Vis spectrophotometer Cary 50 from Varian and M2000 Ellipsometer from J. A. Woollam. Theoretical background, data analysis, and experimental procedures for both experimental techniques will be described in more detail including the technique of total internal reflection ellipsometry (TIRE). Atomic force microscopy deploying the Nanoscope IIIa from Digital Instrument (Veeco), which was used to observe the morphology of the films obtained, will be described in section 4.5. And section 4.6 will describe the mercury probe technique combined with Keithley 4200 semiconductor characterisation instrument and Hewlett Packard 4284 LCR meter to measure I-V and C-V. Section 4.7 presents the electroluminescence measurement using a Hamamatsu H7421 photon counter.

4.2. SAMPLES PREPARATION

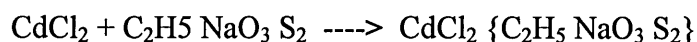
4.2.1. Preparation of CdS and ZnS colloid nanoparticles

In this work, the aqueous synthesis method was used to prepare electrically charged CdS and ZnS colloid nanoparticles, coated with organic shell containing either SO_3^- or NH_2^+ groups using thiolate ligand as a capping agent. All chemicals used are listed below:

- 184 mg of Cadmium chloride ($CdCl_2$, MW=183.31)
- 136 mg of Zinc Chloride ($ZnCl_2$, MW=136.28)
- 278 mg of Lead Chloride ($PbCl_2$, MW=278.1)
- 326 mg of Sodium 2-Mercaptoethane Sulphonate ($C_2H_5 NaO_3 S_2$, MW=164.18)
- 228 mg of Cysteamine Hydrochloride ($C_2H_7 NS$, MW=113.62)
- 78 mg of Sodium sulphate (Na_2S , MW=78.04)

All chemicals used were of high purity purchased from Sigma-Aldrich. All compounds were weighed and dissolved in 25 ml of Millipore water, having the resistance of no less than 18 M Ω .

In order to make $CdS SO_3^-$ colloid nanoparticles, firstly, the solution of Sodium 2-Mercaptoethane Sulphonate (0.08 M) was mixed with cadmium chloride solution (0.04 M). The Cd^{2+} and Cl^- ions would form complex bonding with sulphonated species.



And then when a sodium sulphide solution is added dropwise to the mixture while it is stirred (as shown in Figure 4.1), S^{2-} ions can exchange with Cl^- ions.

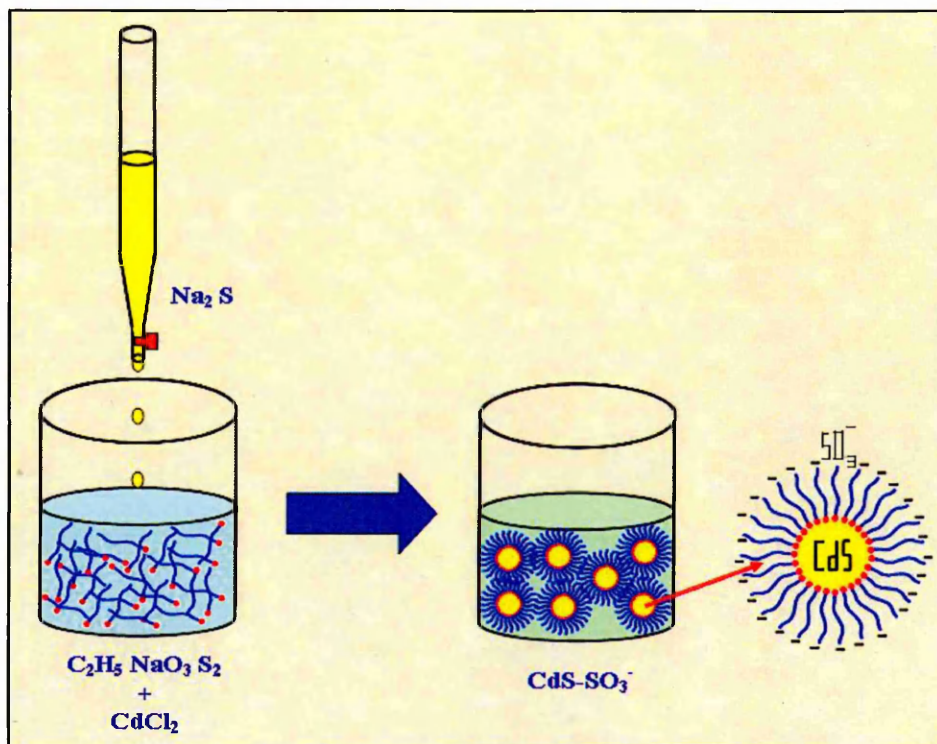
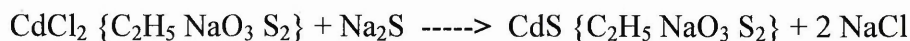


Figure 4.1. The route of making colloid nanoparticles solution.

This reaction is an equilibrium and theoretically reversible, however whereas CdCl_2 is soluble in water, CdS is not, so CdS particles begin to form. As the CdS forms, molecules of the thiol acid complex locate themselves on the surface of the forming particles, thereby preventing further reaction and aggregation, capping the particles and stabilising the colloid.



After a while a clear yellow colloid solution of CdS SO_3^- appeared.

Colloid nanoparticles of CdS NH_2^+ were made following the same routine but using cysteamine hydrochloride as a capping agent. The result is a cloudy yellow colloid solution of CdS NH_2^+ . Applying the similar routine, for ZnCl_2 , colloid solutions of ZnS SO_3^- and ZnS NH_2^+ nanoparticles were made. All processes were performed at room temperature.

4.2.2. Substrate modification procedures

In this study, glass (BDH super premium microscope slide), quartz, silicon and indium tin oxide (ITO from Pilkington), were used as solid substrates. To be suitable for electrostatic self-assembly deposition, the substrates need treatments to clean the surface and also to improve the surface charge. Glass and quartz microscope slides were cleaned in sulphuric/chromic acid mixture for 2 hours at room temperature, followed by extensive rinsing with ultrapure water. The substrates were then treated in 1% KOH solution in 60% ethanol, in the ultrasonic bath for 30 minutes, to make them negatively charged due to the presence of OH^- groups on the surface [1]. After rinsing for the second time with ultrapure water, those slides were dried in the stream of nitrogen.

The samples cut from silicon wafer and ITO sheets were soaked in a warm sulphuric/chromic acid solution for 2 hours and then rinsed extensively with ultrapure water, and dried with nitrogen gas.

4.2.3. Multilayer deposition procedures

The films of CdS and ZnS nanoparticles coated with either negatively (SO_3^-) or positively (NH_2^+) charged shells were deposited layer-by-layer onto electrically charged solid substrates using intermediate layers of either polycations, such as poly-allylamine hydrochloride (PAH), or, polyanions such as poly-styrene-sulfonate sodium salt (PSS) [2, 3]. Solutions of PAH and PSS were made by dissolving the respective polymers in ultrapure water to achieve the concentration of 2 mg/ml. Typical pH value of these solutions was 4.5.

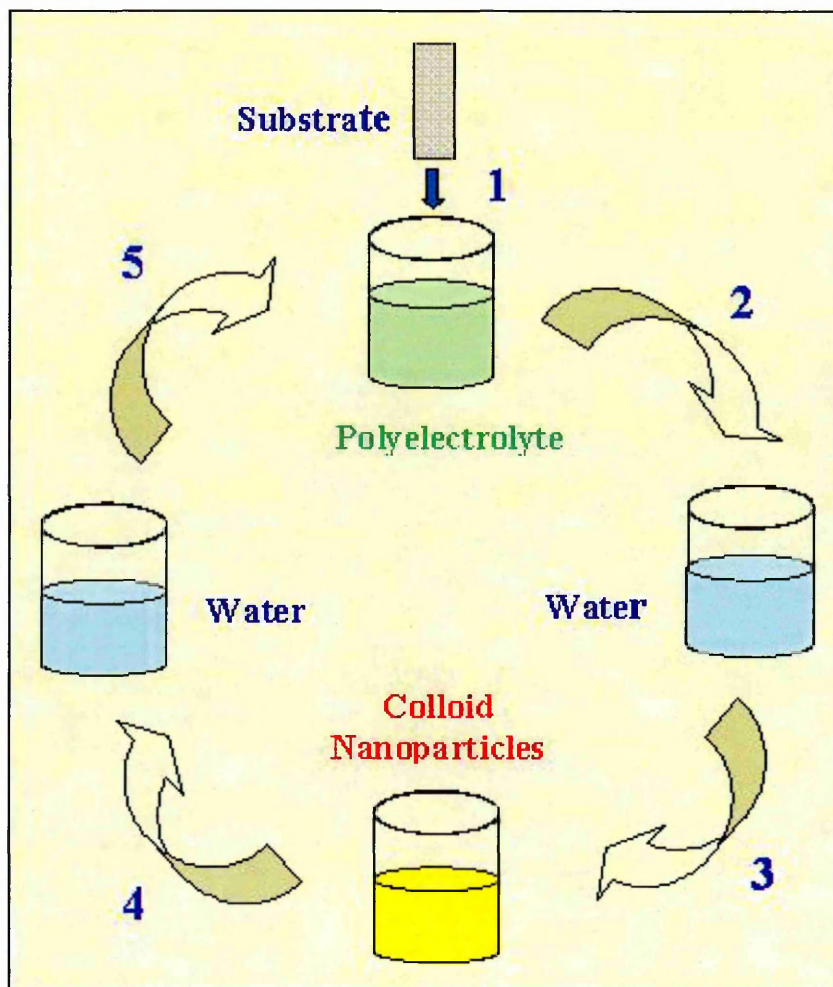


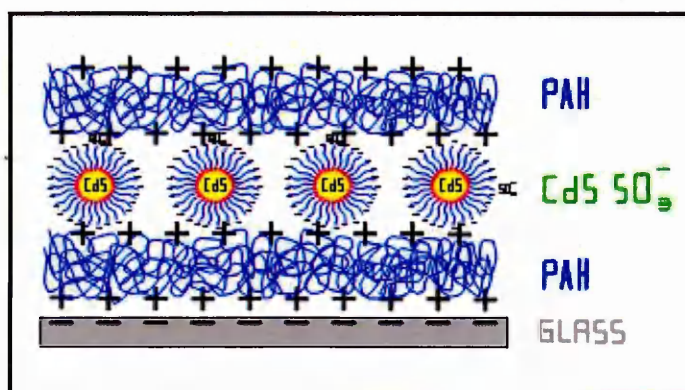
Figure 4.2. Electrostatic self-assembly deposition cycle.

The procedure of electrostatic self-assembly deposition is shown in Figure 4.2. Since the hydrophilic substrates are negatively charged, the film deposition began by immersing the substrate into the PAH solution at room temperature to adsorb a monolayer of polycation molecules, resulting in a positive surface charge of the film surface. After rinsing in Millipore water, the substrate was dipped into the solution of negatively charged nanoparticles to adsorb a monolayer, and restoring the negative surface charge. These operations complete the deposition cycle of polycation monolayer/nanoparticles sandwich unit. By repeating such cycles, multilayer films were self-assembled, as shown in Figures 4.3 (a) and (b). In the standard ESA process, the film surface remains wet through out all dipping steps.

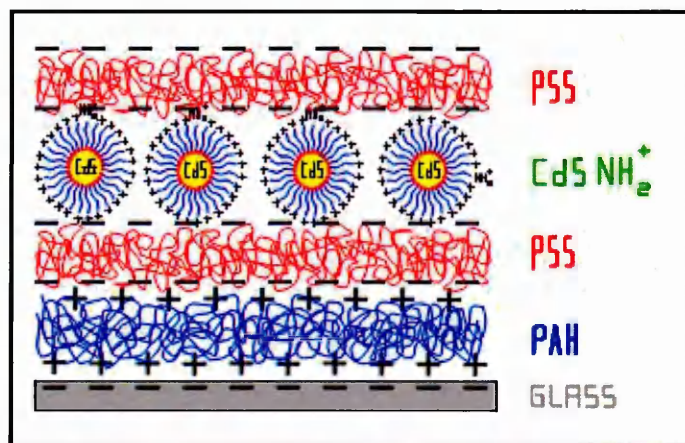
In this work, the films were deposited on different solid substrates, such as glass, quartz, ITO, silicon and gold, depending on the characterisation technique used. The details of samples preparation will be discussed in the following sections.

Samples for UV-Vis spectrophotometry measurements were deposited on glass and quartz slides. Multilayers of $CdS SO_3^-$ and $CdS NH_2^+$ nanoparticles were deposited on glass slides, while quartz substrates were used for $ZnS SO_3^-$ and $ZnS NH_2^+$ films, which have the main absorption band in the near UV range.

Multilayers of $CdS SO_3^-$ and $ZnS SO_3^-$ nanoparticles, were deposited by dipping the substrate consecutively into 1 M PAH solution and then into respective colloid solutions for 10 minutes in each, as shown in Figure 4.3 (a).



(a)



(b)

Figure 4.3. Deposition of colloid nanoparticles $CdS-SO_3^-$ (a) and $CdS-NH_2^+$ (b).

While Multilayers of $CdS NH_2^+$ and $ZnS NH_2^+$ nanoparticles, were prepared by dipping the substrate firstly into 1M solution of PAH for 20 minutes followed by consecutive dippings in 1M PSS solution and in respective colloid solutions for 10 minutes each, as shown in Figure 4.3 (b). All samples were thoroughly rinsed in Millipore water after each deposition step. Several combinations of nanoparticles (CdS and ZnS) and polyelectrolytes (PAH and PSS) were made as presented in table 4.1.

Table 4.1. Samples combination of nanoparticles (CdS and ZnS) and polyelectrolytes (PAH and PSS)

No	Type of Sample
1	Substrate-PAH- $CdS SO_3^-$ -PAH- $CdS SO_3^-$ -PAH
2	Substrate-PAH- $CdS SO_3^-$ -PAH-PSS- $CdS NH_2^+$ -PSS-PAH- $CdS SO_3^-$ -PAH
3	Substrate-PAH-PSS- $CdS NH_2^+$ -PSS- $CdS NH_2^+$ -PSS
4	Substrate-PAH-PSS- $CdS NH_2^+$ -PSS-PAH- $CdS SO_3^-$ -PAH-PSS-
5	Substrate-PAH- $ZnS SO_3^-$ -PAH- $ZnS SO_3^-$ -PAH
6	Substrate-PAH- $ZnS SO_3^-$ -PAH-PSS- $ZnS NH_2^+$ -PSS-PAH- $ZnS SO_3^-$ -PAH
7	Substrate-PAH-PSS- $ZnS NH_2^+$ -PSS- $ZnS NH_2^+$ -PSS
8	Substrate-PAH-PSS- $ZnS NH_2^+$ -PSS-PAH- $ZnS SO_3^-$ -PAH-PSS-
9	Substrate-PAH- $CdS SO_3^-$ -PAH- $ZnS SO_3^-$ -PAH

Samples for ellipsometry measurements were deposited onto two different substrates, silicon and chromium-gold coated slide. Chromium-gold coated slides were prepared using an Edwards evaporation unit by consecutive thermal evaporation of 3 nm of chromium (Cr) followed by the evaporation of 25-30 nm thick of gold (Au)

without breaking the vacuum of 2×10^{-5} Torr [6]. For standard (external reflection) ellipsometry, multilayers of CdS and ZnS thin films, like shown in Figure 4.3 (a and b), were deposited on pieces of silicon wafer and chromium-gold coated slide. While for TIRE measurements, the films were deposited on chromium-gold coated slides. The process of TIRE measurements will be described in more detail in section 4.4.4.

Atomic force microscopy measurements require small samples of approximately 1 cm by 1 cm in size. Basically, all kind of flat substrates could be used for AFM measurement; silicon and chromium-gold coated slides were used in this work. The thin film structures were the same as described in Figure 4.3 (a and b).

For electrical properties measurements (DC and AC measurements), two types of samples were prepared: **(i)** purely polyelectrolyte films consisting of different numbers (from 1 to 6) of consecutively deposited layers of PAH and PSS onto ITO coated glass slides (Figure 4.4 (a)), and **(ii)** composite layers of polyelectrolyte/semiconductor nanoparticles/polyelectrolyte deposited onto ITO coated glass slides (Figure 4.4 (b-d)). The number of polyelectrolyte layers and the type of CdS or ZnS colloids were varied in order to produce the structures 1-*P*-1 (Figure 4.4 b), 2-*P*-2 (Figure 4.4 c), and 3-*P*-3 (Figure 4.4 d), as well as 2-*P*-1, and 3-*P*-1, where the numbers 1, 2, and 3 indicate to the number of PAH or PSS layers on either side of the layer (*P*) of II-VI semiconductor nanoparticles (either CdS or ZnS). The dipping time in all solutions (PAH, PSS, CdS and ZnS colloid) was 30 minutes followed by thorough rinsing with pure Millipore water.

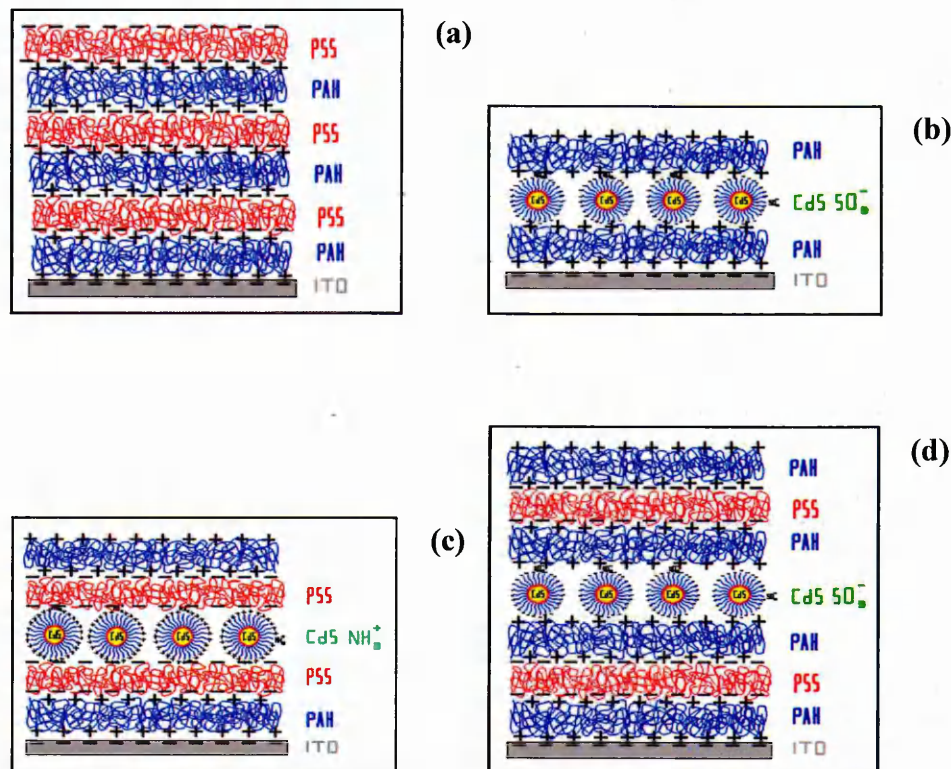


Figure 4.4. Deposition of polyelectrolyte films (a) and polyelectrolyte/nanoparticles sandwich structures: 1-P-1 (b), 2-P-2 (c), 3-P-3 (d).

Samples of electroluminescence measurements, with the structure shown in Figure 4.3 (a and b), were deposited on ITO. The films were coated only three quarter of the slides, as the remaining other quarter was used as an electric contact.

4.3. ABSORPTION SPECTRA MEASUREMENTS

Ultraviolet and visible (UV-Vis) absorption spectroscopy is based on the measurements of the attenuation of a beam of light after it passes through the sample or after reflection from the sample surface; this could be performed at a single wavelength or over an extended spectral range. The visible region of the spectrum (400-700 nm) has photon energies of 1.77 to 3.10 electron volt (eV), and the near ultraviolet region (out to 200 nm) extends this energy range to 10 eV. This spectral range has enough energy to

excite valence electrons to higher energy levels which correspond to higher molecular orbitals.

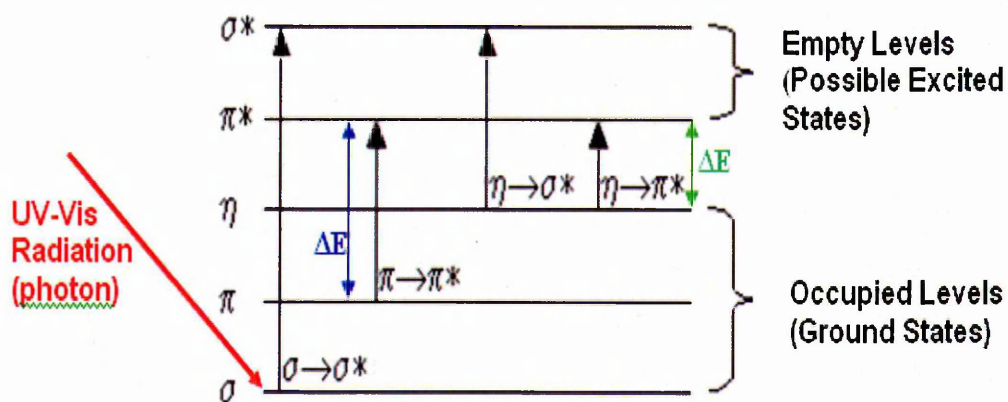


Figure 4.5. Excitation of electrons between molecular orbitals [4].

In Figure 4.5, a molecule in its ground state of electronic energy level can absorb a photon of light if the photon energy is equal to ΔE .

$$\Delta E = E_1 - E_0 = h\nu \quad (4.1)$$

where h is Planck's constant (6.626×10^{-34} Js), ν is the frequency of the radiation in Hz, and E_1 and E_0 are the excited and ground states of the molecule, respectively. The minimum photon energy required for absorption will be when E_0 corresponds to the highest occupied molecular orbital (HOMO) and E_1 to the lowest unoccupied molecular orbital (LUMO).

Theoretically, the transition could occur from various occupied to empty levels, but in reality, excitation only occurs between the two lowest energy transitions. Excitation from $\pi > \pi^*$ and $\eta > \pi^*$ levels are possible when UV-Vis excitation (range of 200-800 nm) is used [4, 5].

In general, UV-Vis spectra tend to be broaden due to the fact that vibrational and rotational levels of the molecular orbitals are superimposed with the electronic levels as

illustrated in Figure 4.6. This produces a combination of overlapping lines that appear as a continuous absorption bands in the UV-Vis spectrum.

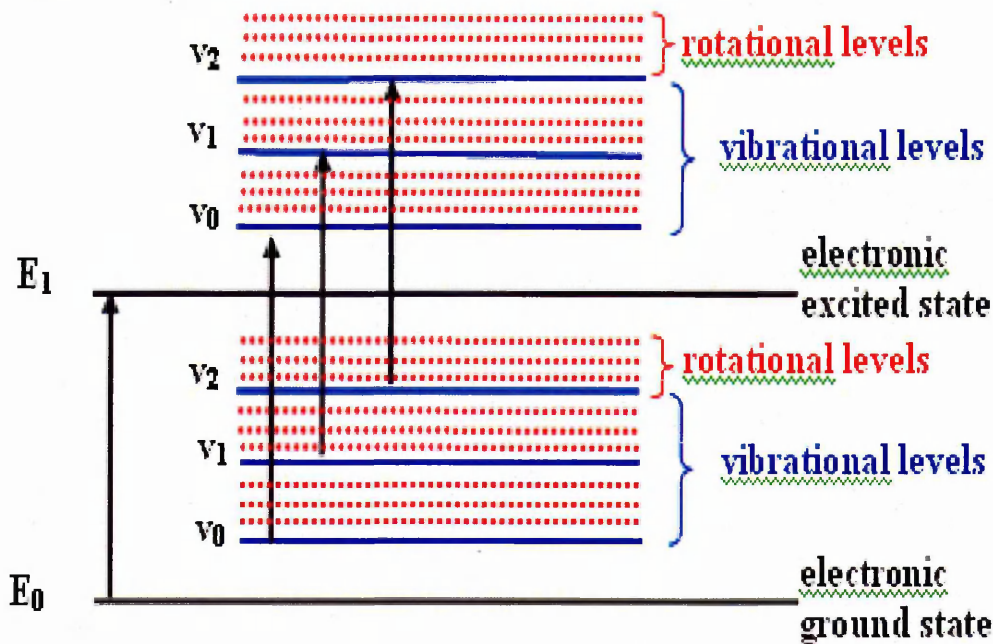


Figure 4.6. Vibrational and rotational levels superimposed with the electronic levels [4].

In the case of crystalline materials, such as semiconductors, all electron transitions, including band-to-band, excitons, subbands, between impurities, free carriers within a band, and also the resonances due to vibrational states of the lattice and of the impurities, contribute to the absorption processes and form the spectrum.

The transitions between a neutral donor and the conduction band or between the valence band and the neutral acceptor (Figure 4.7 (a) and (b)) can occur by the absorption of low energy photons. In this case, the energy of the photon must be at least equal to the ionization energy (E_i) of the impurity. The transitions between the valence band and an ionized donor or between an ionized acceptor and the conduction band occurs at photon energies given by $h\nu > E_g - E_i$, (Figure 4.7 (c) and (d)) [6].

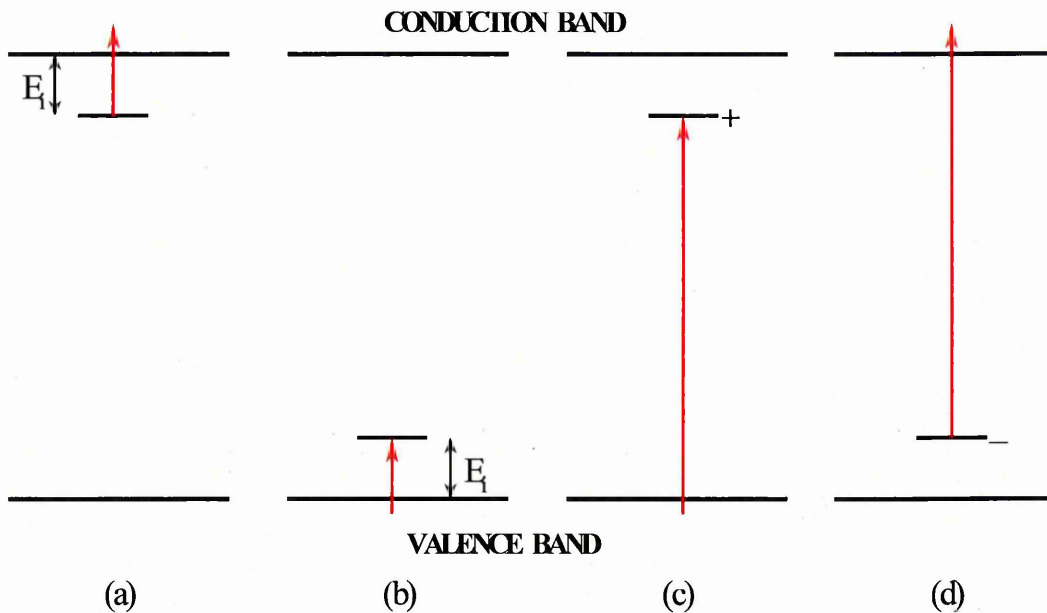


Figure 4.7. Absorption transitions between impurities and bands: **(a)** donor to conduction band; **(b)** valence band to acceptor; **(c)** valence band to donor; and **(d)** acceptor to conduction band [6].

The fundamental absorption referring to band-to-band or exciton transitions can be used to determine the energy gap of the semiconductor. However, the estimation of the energy gap from the “absorption edge” is not a straightforward process, since the electron transitions obey certain selection rules. The absorption transitions take place between two direct valleys where all the momentum-conserving transitions are allowed. Every initial state at E_i is associated with a final state at E_f

$$E_f = h\nu - |E_i| \quad (4.2)$$

In some materials, quantum selection rules forbid direct transitions without a change in the momentum. Momentum is conserved via a phonon (a quantum of lattice vibrations) interaction. Only phonons with the required momentum change are usable, although a broad spectrum of phonons is available.

As mentioned in **Chapter 2**, the formation of excitons usually appears as narrow peaks near the absorption edge of direct-gap semiconductors, or as steps in the

absorption edge of indirect-gap semiconductors. In direct-gap materials, the free excitons occur when the photon energy is $h\nu = E_g - E_x$ (E_x is the binding energy of exciton). Excitons can also be created by higher-energy photons, having excessive kinetic energy. In indirect-gap materials, phonon participation is needed to conserve the momentum. Therefore, an increase in absorption coefficient is obtained at

$$h\nu = E_g - E_p - E_x, \text{ for the transition with phonon absorption} \quad (4.3)$$

$$h\nu = E_g + E_p - E_x, \text{ for the transition with phonon emission} \quad (4.4)$$

where E_p is the phonon energy.

In semiconductors, optical absorption happens for photons with the energies smaller than the bandgap and also for photons with energies greater than the bandgap. As a result, there is a sharp increase in the absorption at energies close to the bandgap that manifests itself as an absorption edge in the UV-Vis spectrum. While the absorption edge is indicative of the location of the bandgap, the accurate estimation of the bandgap requires the use of the following formula.

For direct bandgap semiconductors [4]:

$$\alpha(\hbar\omega) \approx \frac{\sqrt{\hbar\omega - E_g}}{\hbar\omega} \quad (4.5)$$

where α is the absorption coefficient, $\hbar\omega$ is the energy of incident photons and E_g is the electronic bandgap of the semiconductor. E_g can be found as an intercept of the straight line obtained by plotting $(\alpha \hbar\omega)^2$ vs $\hbar\omega$.

While for indirect bandgap semiconductors [4]:

$$\alpha(\hbar\omega) \approx \frac{(\hbar\omega - E_g)^2}{\hbar\omega} \quad (4.6)$$

E_g is given by an the intercept of a straight line obtained by plotting $\sqrt{\alpha \hbar\omega}$ vs $\hbar\omega$.

4.3.1. Basic principles of UV-Vis spectrophotometry

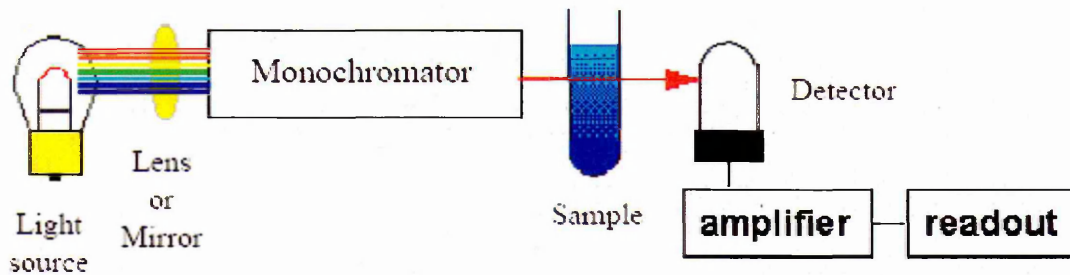


Figure 4.8. Basic principle of UV-Vis spectrophotometry [7].

As shown in Figure 4.8, the basic parts of a Ultraviolet-visible spectroscopy are a light source, a diffraction grating or monochromator to separate the different wavelengths of light, and, typically, a photodiode or CCD array as a detector. The instrument operates by passing a beam of light through the sample and measuring the attenuation of the intensity after it passes through. The intensity of light passing an absorbing material is reduced according to Beer's law:

$$I_t = I_o e^{-\alpha l} \quad (4.7)$$

where I_t is the measured intensity after passing through the material, I_o is the initial intensity, α is the absorption coefficient and l is the thickness of the material (in cm).

If the light reflection is taken into account, Equation (5.1) would be rewritten:

$$\frac{I_t}{I_o} = (1 - R^2) e^{-\alpha l} \quad (4.8)$$

where R is the reflectance. At normal incidence of light and transparent medium, R does not usually exceed 1% and thus can be neglected.

The absorbance (A) of the material is related to the logarithm of the I_o/I_t ratio [8, 9]:

$$A = \log \frac{I_o}{I_t} = \frac{\alpha \cdot l}{2.303} \quad (4.9)$$

where A is absorbance (ABS).

Hence the absorption coefficient (α) can be obtained from the experimental value of absorbance:

$$\alpha = \frac{2.303A}{l} \quad [\text{cm}^{-1}] \quad (4.10)$$

where the value of 2.303 is the change factor between \ln and \log . Then the extinction coefficient (k), which is defined as an imaginary part of the complex refractive index ($n^* = n - ik$) can be obtained as:

$$k = \frac{\alpha\lambda}{4\pi} \quad (4.11)$$

where λ is the wavelength of the light.

Absorption coefficient (α) and extinction coefficient (k), are characteristic optical parameters of the materials. In the case of thin films, they depend on the molecular spectra which consist of several spectral lines (bands) corresponding to electron transitions between the occupied and unoccupied electron levels of molecules. The absorption peak position, intensity and half-width of the band also depend on the structure of the molecular crystal. Therefore, UV-Visible spectra provide information about chemical contents and the structure of thin film.

4.3.2. UV-Vis spectrophotometer–Varian Cary 50

CARY 50, UV-Vis spectrophotometer, from Varian Australia Pty. Ltd., has a unique design as shown in Figure 4.9. A xenon flash lamp is used as a source of UV-Vis radiation which offers many advantages over traditional UV-Vis spectrophotometers. The xenon lamp flashes with the frequency of 80 Hz and data points are acquired during that short pulse of flash [10]. This reduces the exposure of the sample to the entire wavelength range and so reduces the degradation of photosensitive samples. As the light flashes from the xenon lamp are very intense, the Cary 50 can use a beam splitter

without the loss in the energy that causing excessive photometric noise. The beam splitter allows simultaneous reference beam correction, so peaks will not shift as the scan speed changes. This means that the wavelength shift errors associated with traditional scanning methods are eliminated.

The flashes also make Cary 50 immune from the room light. This allows the measurements of large samples with the lid off without affecting the result.

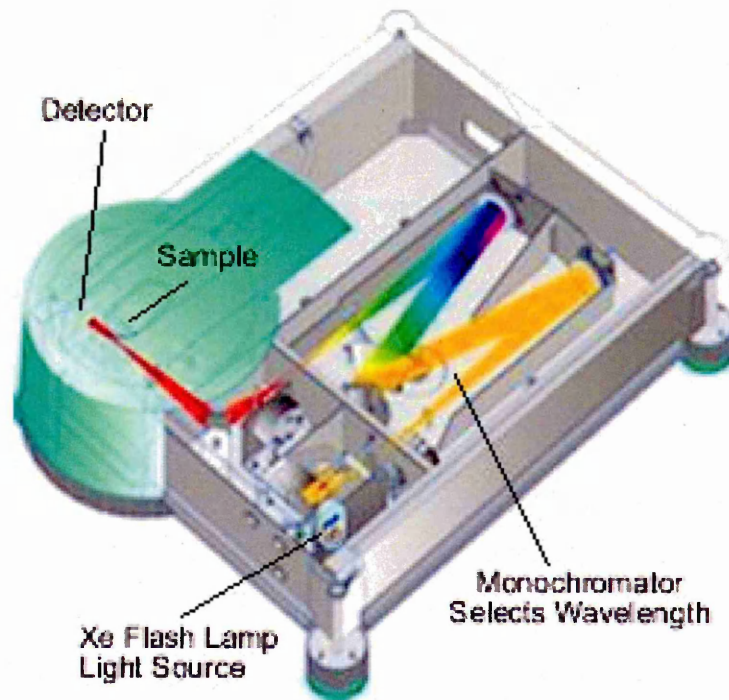


Figure 4.9. Schematic diagram of Varian Cary 50 UV-Vis spectrophotometer [11].

The maximum scan rate of Cary 50 is 24 000 nm per minute, that means, only take less than 3 seconds to scan the whole wavelength range of 190-1100 nm. This makes the measurements using Cary 50 very fast. It also can measure dense samples of up to 3 in Abs, so the liquid sample solutions do not need to be diluted so often. The Cary 50 is controlled by the new Cary WinUV software. This Windows based software features a modular design which makes it easy to use.

4.3.3. Procedure of UV-Vis spectrophotometry measurements

A Varian CARY 50, UV-vis spectrophotometer was used to determine the absorption spectra of CdS (or ZnS) colloid solutions and multilayer films deposited onto glass and quartz substrates. Firstly, for the absorption spectra of colloid solutions measurements, the wavelength range was set from 200 to 900 nm. Then the absorption measurements were carried out for an empty 2 ml quartz cuvette. The results were automatically saved by the software as a baseline. Then, CdS and ZnS nanoparticles colloid solutions were diluted: 100, 200, 500 and 1000 times. The absorption spectra of the solutions were measured by putting the solution into 2 ml quartz cuvette, mounted into a sample holder in the spectrophotometer. The results were saved as absorption of CdS and ZnS colloid solutions.

Secondly, the wavelength range, for absorption spectra measurement of multilayer films on solid substrates, was set to 300-900 nm for $CdS SO_3^-$ and $CdS NH_2^+$ nanoparticles, while $ZnS SO_3^-$ and $ZnS NH_2^+$ films were measured in the 200-800 nm range. Cleaned glass and quartz slides were measured as the respective baselines. Then the samples containing $CdS SO_3^-$, $CdS NH_2^+$, $ZnS SO_3^-$ and $ZnS NH_2^+$ nanoparticles, described in section 4.2.3.1, were measured. The values reported are the average of measurements taken at several locations on each sample.

4.4. ELLIPSOMETRY MEASUREMENTS

Ellipsometry is a powerful optical analytical technique for the investigation of the dielectric properties (complex refractive index or dielectric function) and thickness of thin films. As an optical technique, spectroscopic ellipsometry is non-destructive and non-contact.

4.4.1. Reflectance and Brewster angle

The basic theory of Ellipsometry was developed by Drude [12]. It involves the reflection of a plane polarised light from a solid surface (see Figure 4.10). In a simple case of one interface, when a plane polarised light is incident to the surface, some of the light is reflected and some is transmitted.

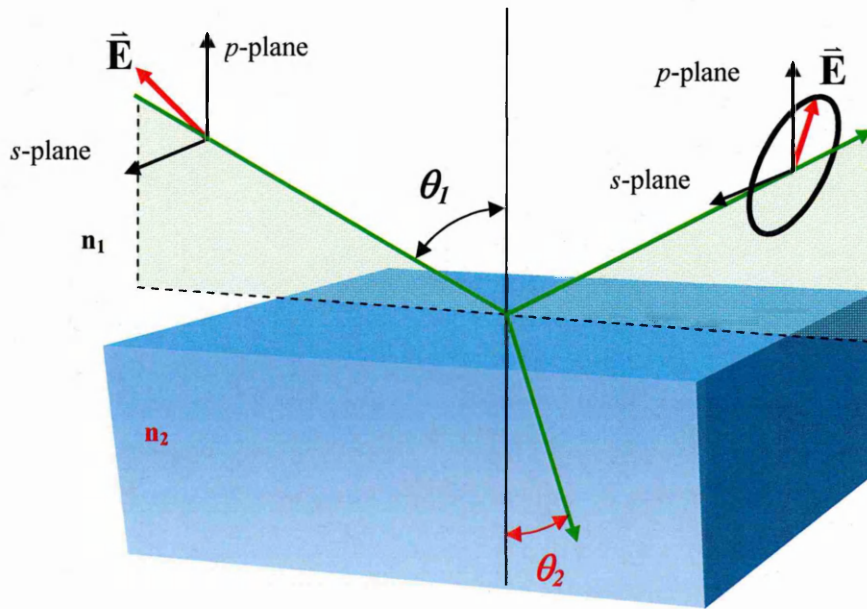


Figure 4.10. Schematic of the ellipsometry experiment.

Plane polarized wave can be decomposed into two components: one parallel to the plane of incidence defined as *p-component*, while *s-component* corresponding to the wave perpendicular to the plane of incidence. These two components reflect differently from the surface depending on the angle of incidence.

The Fresnel reflection coefficient r is the ratio of the amplitude of the reflected wave to the amplitude of the incident wave. The Fresnel reflection coefficients are different for *p* and *s* components, and can be obtained from electro-magnetic theory: [13-16]

$$R_p = \frac{E_p}{E_o} = \frac{n_2 \cos \theta_1 - n_1 \cos \theta_2}{n_2 \cos \theta_1 + n_1 \cos \theta_2} \quad (4.12)$$

$$R_s = \frac{E_s}{E_o} = \frac{n_1 \cos \theta_1 - n_2 \cos \theta_2}{n_1 \cos \theta_1 + n_2 \cos \theta_2} \quad (4.13)$$

where n_1 is the refractive index of the incidence medium, n_2 is the refractive index of the solid substrate, θ_1 is the angle of incidence on the sample, and θ_2 is the angle of refraction which can be related to θ_1 using Snell's law

$$n_1 \sin \theta_1 = n_2 \sin \theta_2 \quad (4.14)$$

Generally, at the Brewster angle, the R_p is at a minimum, so the difference between R_p and R_s is maximized.

In more complicated case where the system has multiple interfaces (see Figure 4.11), the light transmitted through the first interface can not be disregarded.

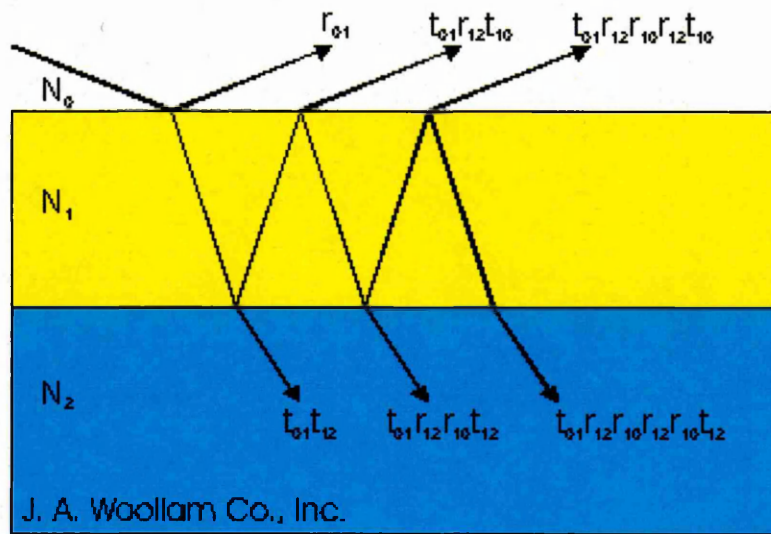


Figure 4.11. Reflections and transmissions in multiple interfaces samples [17].

The resultant reflected wave is made up of the light reflected directly from the first interface plus all of the secondary reflections on the interface between medium 1 and medium 2. Each successive transmission back into medium 1 is smaller than the incidence wave. The result of addition of the infinite series of partial waves has been derived by Azzam [15] as:

$$r_{tot} = r_{01} + t_{01}r_{12}t_{10}e^{-2i\beta} + t_{01}r_{12}^2r_{10}t_{10}e^{-2i\beta} + \dots \quad (4.15)$$

Reflection coefficients for p - and s - components of polarised light are given as:

$$R_p = \frac{r_{01}^p + r_{12}^p \exp(-i2\beta)}{1 + r_{01}^p r_{12}^p \exp(-i2\beta)} \quad (4.16)$$

$$R_s = \frac{r_{01}^s + r_{12}^s \exp(-i2\beta)}{1 + r_{01}^s r_{12}^s \exp(-i2\beta)} \quad (4.17)$$

where r_{12} is the Fresnel reflection coefficient for the interface between medium 1 and 2.

While the phase thickness, β , is given by:

$$\beta = 2\pi \left(\frac{d_1}{\lambda} \right) n_1 \cos \theta_1 \quad (4.18)$$

where d is the film thickness.

4.4.2. Delta (Δ) and Psi (Ψ)

The angles of Δ and Ψ are related to the ratio of the complex values R_p and R_s . Ψ represents the ratio of their magnitudes, and delta is the difference in their phase. If δ_1 is defined as the phase difference between the perpendicular and parallel components of the incident wave, and δ_2 as the phase difference between the same components for the outgoing wave. Then the change in *phase* difference between parallel and perpendicular components of the incident wave that occurs upon reflection, called Δ , could be defined as:

$$\Delta = \delta_1 - \delta_2 \quad (4.19)$$

While *Psi* (Ψ) is defined as:

$$\tan \Psi = \frac{|R_p|}{|R_s|} \quad (4.20)$$

These definitions lead us to the fundamental equation of ellipsometry: [14-16]

$$\tan \Psi \exp(i\Delta) = \frac{R_p}{R_s} \quad (4.21)$$

The changes on Δ and Ψ depend on the optical constants of the substrate (n_2, k_2), the angle of incidence θ , the optical constants of the film (n_1, k_1) and the film thickness d (see Figure 4.10). The optical constants of a material represented in the complex form is shown as

$$N = n - ik \quad (4.22)$$

where n is refractive index and k is extinction coefficient.

While n and k are defined as [17]:

$$n = \left\{ \frac{1}{2} \left[\varepsilon' + \left(\varepsilon'^2 + \frac{\sigma_c^2}{4\varepsilon^2 \omega^2} \right)^{\frac{1}{2}} \right] \right\}^{\frac{1}{2}} \quad (4.23)$$

and

$$k = \left\{ \frac{1}{2} \left[-\varepsilon' + \left(\varepsilon'^2 + \frac{\sigma_c^2}{4\varepsilon^2 \omega^2} \right)^{\frac{1}{2}} \right] \right\}^{\frac{1}{2}} \quad (4.24)$$

where $\varepsilon' = n^2 - k^2$, σ_c is conductivity of the material, ε is dielectric constant, and ω is the angular frequency of light ($\omega = 2 \pi f$, f is frequency). For conductive samples

$\frac{\sigma_c}{\varepsilon \omega} \ll 1$, and for dielectrics $\frac{\sigma_c}{\varepsilon \omega} \gg 1$.

4.4.3. J. A. Woollam Variable Angle Spectroscopic Ellipsometry (VASE) - M2000V

There are several types of ellipsometer configurations which have been developed and used for decades (Figure 4.12) [17, 18]. The first ellipsometer is called *null ellipsometer* because the measurements were obtained by adjusting the orientation of the polarizer, compensator, and analyzer so that the light incident on the detector is extinguished or "nulled". This type of ellipsometer is usually adjusted manually. Although this configuration is very accurate and has low systematic errors, its operation is slow and spectroscopic measurements are very difficult to make.

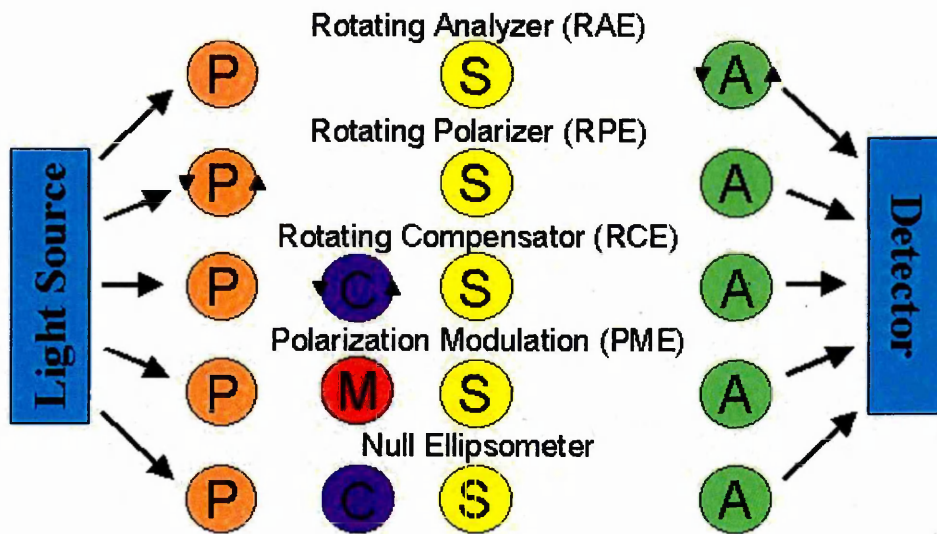


Figure 4.12. Ellipsometer configurations. [17]

The second configuration is *phase modulation ellipsometer* (PME). The main advantage of this configuration is a very fast data acquisition rate, (*theoretically* 10 milliseconds per point) because it uses a time dependent retarder that can operate at very high rates of ~50 kHz as a photo elastic modulator. The measurements are performed by adjusting the amplitude of the modulation at each wavelength at a time. In this case, the advantages of such high modulation rate are lost because of the limited mechanical speed at which the monochromator can change the wavelengths. These types of ellipsometers are also difficult to calibrate due to the temperature sensitivity of the modulator.

The modern configurations are *rotating polarizer ellisometry* (RPE) and *rotating analyzer ellisometry* (RAE). The operating characteristics of these configurations are very similar. Both of them are not using the retarding element. There are several advantages of using only polarizers:

- Polarizers are achromatic over a wide spectral range
- Polarizers are relatively easy to construct.
- Polarizers are relatively easy to align within a system.

However, there are several disadvantages of a system without a retarder (compensator):

- Sensitivity is lost when delta is near 0 or 180°
- One of the elements must be rotated at a speed that is typically limited from 10 to 60 Hz. This is usually not a problem because the time required to make one measurement with adequate signal to noise ratio is not fundamentally determined by the rotation speed unless the light source is very intense.

The latest configuration is rotating compensator ellipsometer (RCE). This configuration compensates for most of the disadvantages of the rotating element ellipsometry configurations. These advantages include: accurate measurements of the ellipsometric Δ and Ψ parameters over the complete measurement range ($\psi=0-90^\circ$, $\Delta=0-360^\circ$), no residual input or output polarizations sensitivity and the capability to directly measure depolarization effects. However RCE have only recently been constructed due to the perceived difficulty of constructing a mechanically rotatable compensator element that behaves ideally (retardance about 90°) over a wide spectral range. This special construction are used in new instruments from J. A. Woollam such as IR-VASE and the M-2000.

In this work, M-2000V, a variable angle spectroscopic ellipsometer (VASE) from J.A. Woollam. Inc, operating in the spectral range of 370-1000 nm, was used to obtain the dielectric parameters and the thickness of the films. M-2000 is a *rotating compensator ellipsometer* (RCE) with CCD array detection to provide fast and accurate ellipsometry measurements over a wide spectral range. As compared to conventional ellipsometry, M-2000 series offer several advantages such as flexibility, accuracy and fast measurement. The incidence angle could be adjusted at an angle near the Brewster angle for each sample, the measured Δ values are around 90°, where the sensitivity to the layer thicknesses and optical constants is the highest. The schematic diagram of M-2000V VASE is shown in Figure 4.13.

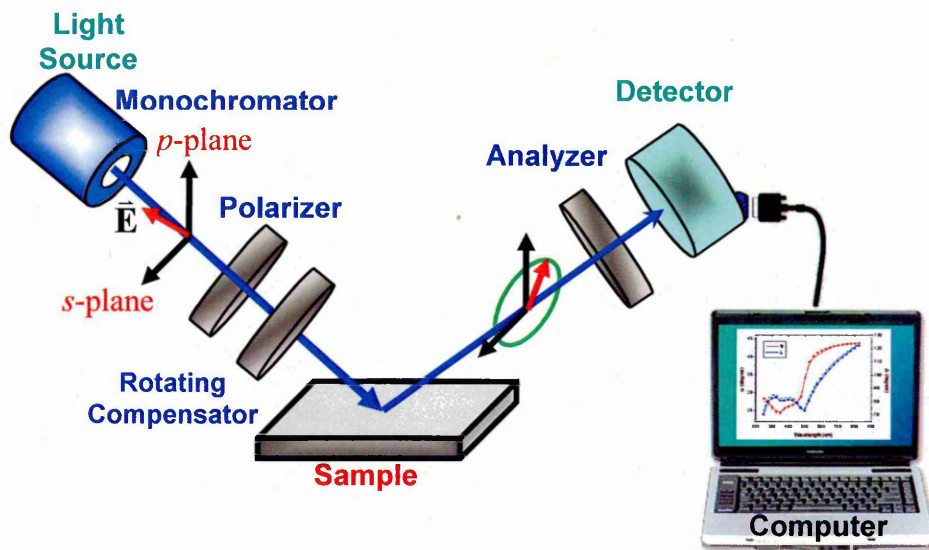


Figure 4.13. Schematic of Variable Angle Spectroscopy Ellipsometry.

The light from a *50 W quartz tungsten halogen lamp* (the wavelength range from 350 nm to 2 μm) is coupled to a *fiber optic cable* and passed through the *polarizer* to get linearly polarised light. A *monochromator* is placed before the sample to get monochromatic and low intensity light. This is important when studying photosensitive materials. The light intensity is low enough not to damage the samples. *The rotating compensator* is used to overcome Δ insensitivity caused by rotating element ellipsometer. It gives an accurate measurements of the ellipsometric Δ and Ψ parameters over the full measurements range, ($\psi = 0 - 90^\circ$, $\Delta = 0 - 360^\circ$). The light is reflected from the sample. The reflected light, in general, being elliptically polarised, is going through the second polarizing element, *analyzer*. Finally, the light is collected with a *diode array* which is specially designed to register the entire spectrum simultaneously.

4.4.4. Total internal reflection ellipsometry (TIRE)

TIRE appeared as a combination of spectroscopic ellipsometry with the SPR Kretschmann geometry of total internal reflection [19]. Total internal reflection is a situation in which light is completely reflected at an interface where the refractive index of the incident medium is larger than that of the reflecting medium. It happens when the incidence angle, Φ_i , is greater than the critical angle, Φ_C as defined by following equation:

$$\Phi_C = \sin^{-1} \frac{n_1}{n_0} \quad (4.25)$$

where n_0 is the refractive index of the first (incident) medium and n_1 is the refractive index of second medium.

When a thin layer of a noble metal (e.g. gold) is present at the interface between the two media, the oscillations of free electrons, called surface plasmons (SPs), are introduced. Surface plasmons propagate along the surface of the metal/dielectric interface, as shown in Figure 4.14.

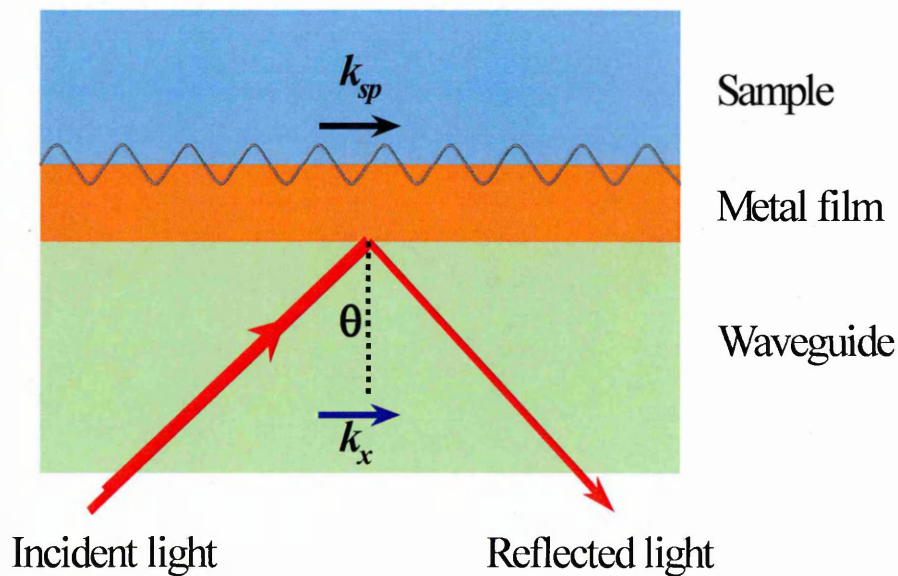


Figure 4. 14. Graphical representation of wavevector matching [20].

The frequency range of surface plasmons depend on the complex dielectric function of the metal (ϵ_m) and the dielectric function of the adjacent medium (ϵ_d), as shown by the following equation [21]:

$$k_{sp} = \frac{\omega}{c} \sqrt{\frac{\epsilon_m \epsilon_d}{\epsilon_m + \epsilon_d}} \quad (4.26)$$

where k_{sp} is the wave vector of the surface plasmon and (ω/c) is the wave vector of light in vacuum.

As shown by equation (4.26), surface plasmons can not be excited directly by light because they have a longer wave vector than the incident light ($k_{light} = \omega/c$). However, by using a prism or a grating coupler [22] at specific angle, the light wave vector could be modified to match the surface plasmons' wave vector. When the wave vector is matched, a substantial fraction of light energy is transferred to the plasmons in the metal film and causes the plasmons to resonate. As the result of this, the intensity of the reflected light is reduced. This phenomenon is called *Surface Plasmon Resonance (SPR)*, and that specific angle of incidence is called the surface plasmon resonance angle (θ_{spr}). The surface plasmon resonance angle mainly depends on the properties of the metal film, the wavelength of the incident light and the refractive index of the media on either side of the metal film [23, 24].

SPR technique is performed by scanning the angle of incidence and measuring the reflected light intensity. When the light is coupled to the samples, the momentum of the photons and plasmons can be described by vector functions having certain magnitudes and directions. Altering the angle of incidence would change the component of the wavevector parallel to the prism base, therefore only the x -component of wave vector parallel to the surface would be contributed to SPR curves. All the light which is not p -polarized will not contribute to the SPR and will increase the background intensity

of the reflected light. The reflection coefficient for p-polarized incident light is given by the formula:

$$r_p = E_r / E_i \quad (4.27)$$

where E_r is the electric field component of the light reflected from the interface, and E_i is the electric field component in the plane of incidence of the light transmitted through the interface. The light reflected from the interface can be calculated using the formula:

$$R_p = |r_p|^2 \quad (4.28)$$

The typical SPR curve of metal film is shown in Figure 4.15 as a reflectivity versus the incidence angle. As the angle increases to a critical angle (θ_c), the reflectivity reaches its maximum level close to 100 %. When the angle of incidence is further increased, the reflectivity is reduced and reached the minimum at θ_0 due to the SPR phenomenon.

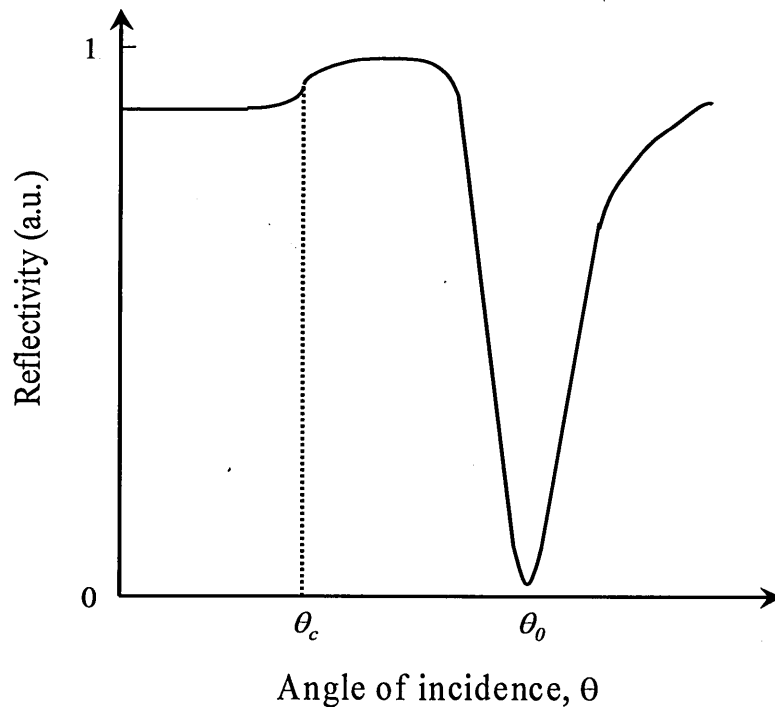


Figure 4.15. A typical SPR curve of metal film showing the critical angle (θ_c) and the angle of incidence minimum (θ_0) [24].

Both the position of the SPR minimum and the half-width of the SPR curve depend on the optical parameters (refractive index, and extinction coefficient) and thickness of metal film. The presence of a thin dielectric film on the metal surface would cause a shift of the surface plasmon dispersion curve to higher momentum. Consequently, the SPR curve will be shifted to higher angles and possibly broadened as shown for example in Figure 4.16 for calix-4-resorcinarene monolayers deposited onto gold film (A. Hassan and coworker [25]). This means that SPR is a surface sensitive technique and can be used for thin films characterization [25-27] and bio/chemical sensing [28-31].

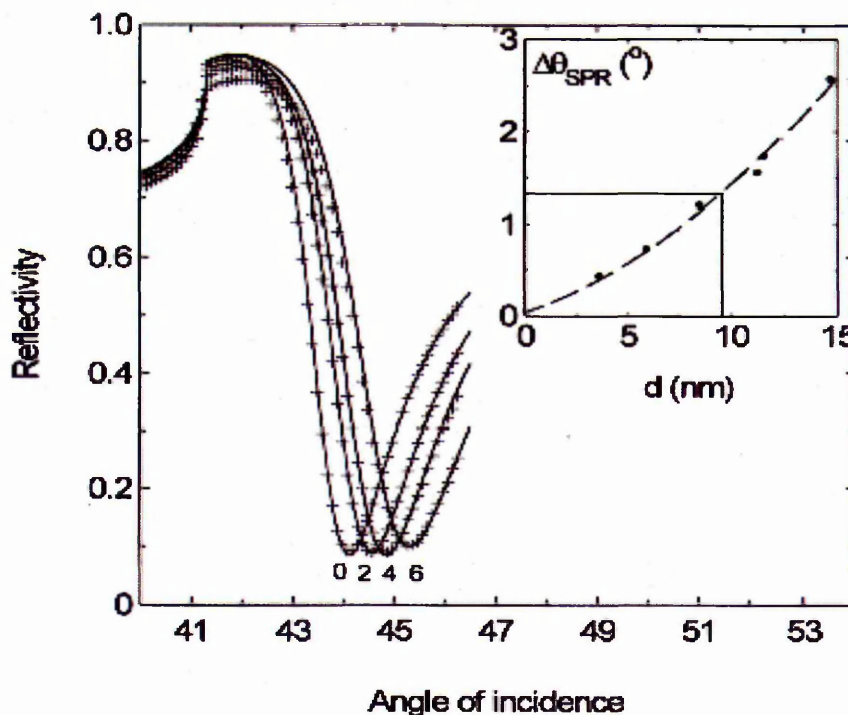


Figure 4.16. Experimental SPR curves for gold film, and those of LB films of calix-4-resorcinarene deposited on it. The number of monolayers is indicated on the corresponding curve. The inset presents the dependence of the resonance shift ($\Delta\theta_{SPR}$) on the thickness of the LB films [25].

By combining the advantages of SPR and ellipsometry, total internal reflection ellipsometry (or TIRE) offers two experimental parameters in comparison to only one in

SPR. The $\Psi(\lambda)$ spectra are similar to SPR curves, while the $\Delta(\lambda)$ spectra that represent the phase shift between p - and s - components is a new quantity that does not exist in SPR technique. A sharp drop in Δ near the resonance makes the TIRE method extremely sensitive to small changes in the optical parameters of the reflection system and even more sensitive than conventional ellipsometry. Arwin and coworkers showed that TIRE can lead to a substantial increase in the sensitivity [34]. The work of Nabok and coworkers also proved that TIRE have a ten fold higher sensitivity as compared to both standard ellipsometry and SPR, and therefore was successfully used in biosensing for the registration of low molecular weight toxins [32, 33].

4.4.5. Modelling and data analysis

As mentioned before, spectroscopic ellipsometry does not directly measure the film thicknesses or optical constants, instead it measures Ψ and Δ spectra for a particular sample. To extract useful information about the sample, normally, an analysis of ellipsometric Ψ and Δ data has to be performed step by step as shown in Figure 4.17.

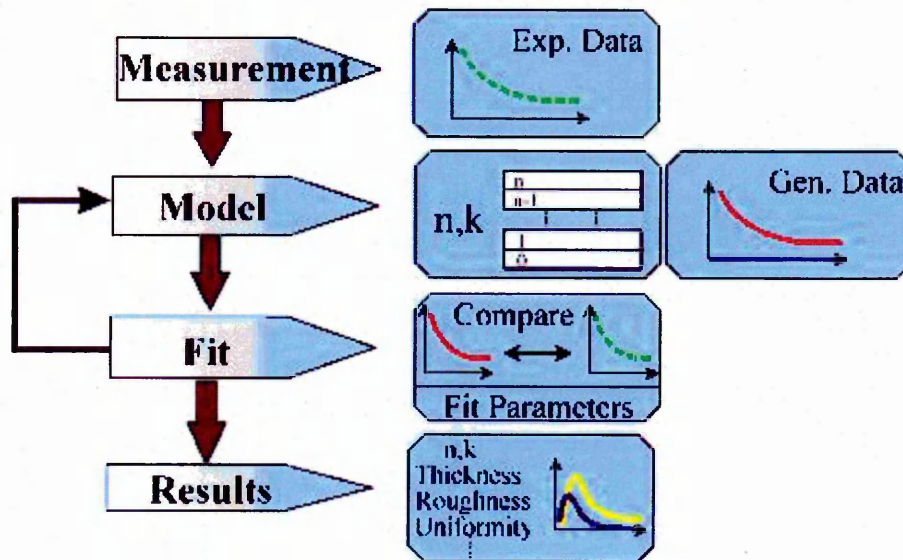


Figure 4.17. Ellipsometry modeling process [17].

The first step is to build a model for the optical structure of the sample. The model should include the substrate, one or more layers on top, and the medium, each characterised by optical constants values (n , k) and thicknesses (d). For example, Figure 4.18 shows a model for 2 layers of thin films on solid substrate. The model should start with the simplest one adding the complexity if required. The order of layers is also very important.

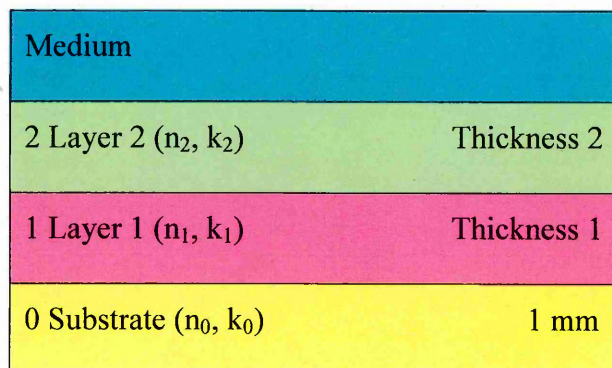


Figure 4.18. Model of thin films on solid substrate.

The next step, the best guess for n , k and d values should be entered and data must be generated from the model and then compared to the experimental data. Choosing the correct guess values is very important. Figure 4.19 shows that the error function has several minima in a multi-dimensional space of variable parameters. A wrong set of initial parameters may lead the search in a wrong direction resulting in finding the wrong minimum which is not adequate to the real system. In other words, if the guess values of the unknown parameters are too far off, the regression algorithm could give wrong values.

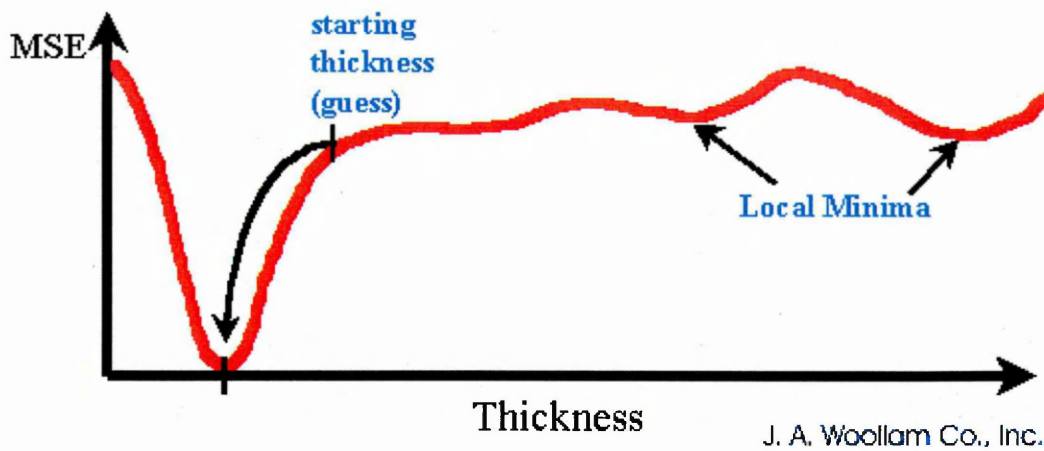


Figure 4.19. The illustration of choosing guess values as close to the actual values as possible so that the algorithm can settle on a best fit instead of a local minima [17].

The quality of the model fitting can be judged from the actual fitting curve and also from the mean squared error (MSE) value. WVASE32[®] uses a mean squared error (MSE) to quantify the difference between the experimental and calculated model data. The smaller MSE implies a better fit. The MSE is weighted by the error bars on each measured data point.

$$\begin{aligned}
 MSE &= \frac{1}{2N - M} \sum_{i=1}^N \left[\left(\frac{\Psi_i^{\text{mod}} - \Psi_i^{\text{exp}}}{\sigma_{\Psi_i}^{\text{exp}}} \right)^2 + \left(\frac{\Delta_i^{\text{mod}} - \Delta_i^{\text{exp}}}{\sigma_{\Delta_i}^{\text{exp}}} \right)^2 \right] \\
 &= \frac{1}{2N - M} \chi^2
 \end{aligned} \tag{4.29}$$

Using an iterative procedure (least-squares minimization), the unknown optical constants and/or thickness parameters are varied, and Ψ and Δ values are calculated using Fresnel equations. The calculated Ψ and Δ values, which match the experimental data the best, provide the optical constants and thickness parameters of the sample.

Once the fitting is complete, the resulting parameters must be evaluated for the sensitivity and possible correlation. To do this, the following steps can be taken:

- Compare the experimental data to the generated data.

- How low is the MSE? Can it be reduced further by increasing the model complexity?
- Are fitting parameters physically feasible?
- Perform fitting several times from different initial conditions.

To determine if the fitting parameters are physically correct, it is important to use some intuition with respect to the physics involved. For example:

- there should be no zero or negative thickness values.
- for insulators, generally, $k = 0$ and n must decrease with the increasing in λ .
- k can not be negative.

4.4.6. The procedure of ellipsometry measurements

4.4.6.1. External reflection ellipsometry

Before the measurements, the instrument was calibrated using a standard silicon wafer with the SiO₂ thickness of $1097 \pm 3 \text{ \AA}$ and refractive index of 1.462 ± 0.002 . The measurements were carried out in air, and the angle of incidence was set at 70° (near Brewster angle of silicon). Firstly, the measurements were carried out on a piece of bare silicon, showing typical ellipsometry spectra, $\psi(\lambda)$ and $\Delta(\lambda)$. The results were recorded as a blank substrate. Next, the same procedure was applied to the same silicon sample coated with thin films of polyelectrolytes and nanoparticles and the results were recorded. To determine the film thicknesses and optical constants of the films, a model layer was constructed for each set of experimental data, and the experimental $\psi(\lambda)$ and $\Delta(\lambda)$ spectra were fitted using WVASE32® software provided by J.A. Woollam Co. [14].

4.4.6.2. Total internal reflection ellipsometry

The TIRE experimental set-up was built on the basis of the J.A. Woollam M-2000V rotating analyser spectroscopic instrument; and contains a coupling prism, made of glass (BK7, $n=1.515$); and a 1.5 cm^3 cell [39, 40]. The schematic view of the system is presented in Figure 4.20. A beam from the light source (Tungsten lamp) was going through a monochromator and polarizer and then was refracted by 68° prism to a chromium/gold coated glass slide which was attached to the prism via index matching fluid (immersion oil). The choice of the prism depends on the type of medium used: 68° prism is recommended for aqueous media, while 45° prism should be used for measurements in gaseous media. The reflected beam, after passing through the analyser, was collected by photo detector. The cell attached to the gold layer, has inlet and outlet tubes allowing the injection of different solutions into the cell using the syringe.

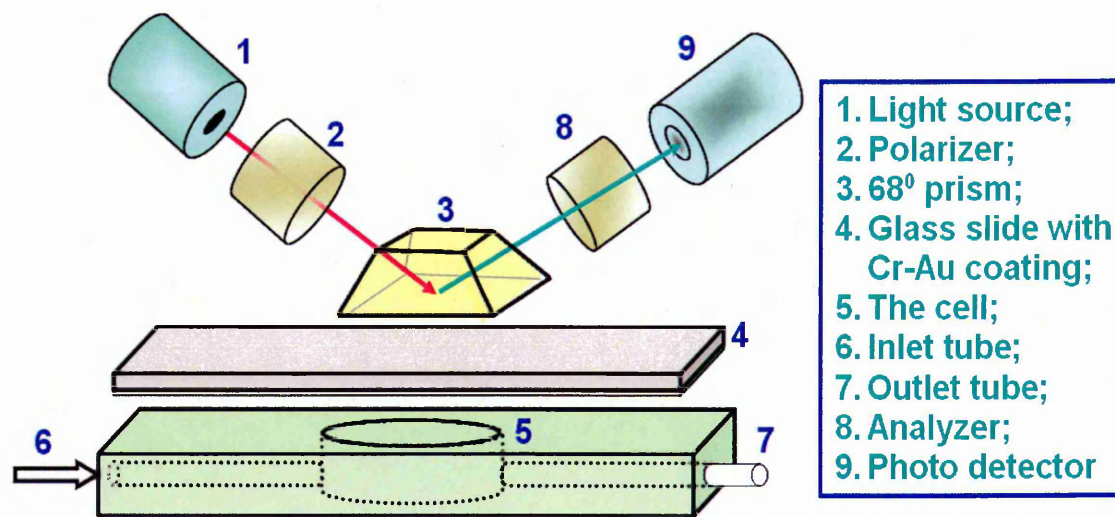


Figure 4.20. Total internal reflection ellipsometry set-up.

Both dynamic and static spectroscopic scans were performed. Firstly, pure water was carefully injected into the cell. The layer of gold should be soaked with water, without producing any bubbles. The measurements have to be taken after 5-10 minutes of stabilisation, the results were recorded for a blank substrate to obtain the initial

thickness of Chromium and gold layers. Afterwards, the cell has to be emptied followed by the injection of PAH solution, and the dynamic scan was performed for 30 minutes, by measuring a number of ψ and Δ spectra at a certain time interval. It has to be noted that the fitting of dynamic scan data is difficult because of unknown refractive index of the solution. The next step is rinsing the cell with ultrapure water, followed by measuring the spectra by normal spectroscopy scan. Then the colloidal $CdS SO_3^-$ (or $ZnS SO_3^-$) solution was injected into the cell for 30 minutes and the dynamic scan was performed. After rinsing, the spectra were measured again. The measurements of dynamic and static spectroscopic scans of multilayer films structure could be performed by repeating the procedures above.

4.5. ATOMIC FORCE MICROSCOPY MEASUREMENTS

The surface imaging technique of AFM is used to get information about film's morphology, such as, the uniformity, grain distributions or defect formation on the film surface. An AFM can image any surface, insulating or conducting without damaging the surface. A wide range of materials has been investigated using this technique including semiconductors, polymers, thin or/and thick film coatings, synthetic and biological membranes, metals and composites.

4.5.1. Basic principles

The first AFM was developed by Gerd Binnig, CF Quate and Christoph Gerber in 1985 [34, 35]. They used a cantilever made from a tiny diamond crystal glued onto one end of a gold foil strip to examine insulating surfaces. Lateral features as small as 300 Å were imaged. This first AFM used a scanning tunnelling microscope at the end of the cantilever to detect the bending of the lever [34, 36].

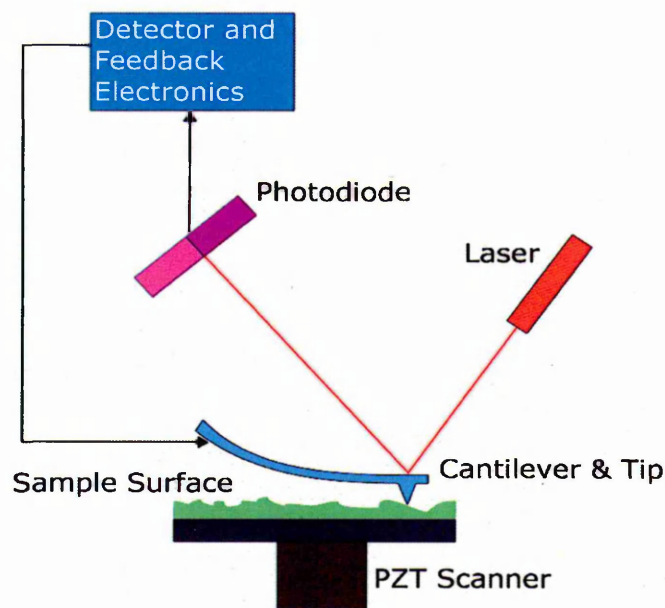


Figure 4.21. Schematic of Atomic Force Microscopy [37].

The schematic diagram of modern Atomic Force Microscopy (AFM) exploiting optical registration system is shown in Figure 4.21. AFM measures attractive or repulsive forces between the tip (probe) and the sample by sensing the atomic force interactions between them. The distance of the tip to the surface is controlled within the scale of a few angstroms within a range of chemical bonds. A constant force is maintained between the sample and the tip, as it follows the contours of the surface. There are three basic components of AFM: *force transducer*, *piezoelectric transducer* and *feedback control*.

Force Transducer is constructed to measure the force between the probe (tip) and the sample surface. The output was converted to the electronic signal and used in a feedback control system to maintain the force. In order not to break the probe, the force sensor must be able to measure very low force as low as 10 pN (picoNewtons). Several transducing techniques were often used, such as the optical beam deflection technique [12, 38], optical interferometry [39], laser diode feedback detection [40], and capacitive lever displacement [41]. The most popular optical beam deflection technique uses an

optical lever device which is easy in use and can achieve high resolution [42-44]. The optical lever operates by reflecting a laser beam from the back of the cantilever. The reflected beam is collected by a position sensitive detector (PSD) consisting of two side-by-side photodiodes. Angular displacement of the cantilever causes a twofold angular deflection of the laser beam, resulting in one photodiode would collect more light than the others. The difference between the photodiode signals, normalized by their sum which is proportional to the deflection of the cantilever, is collected by a differential amplifier as an output signal.

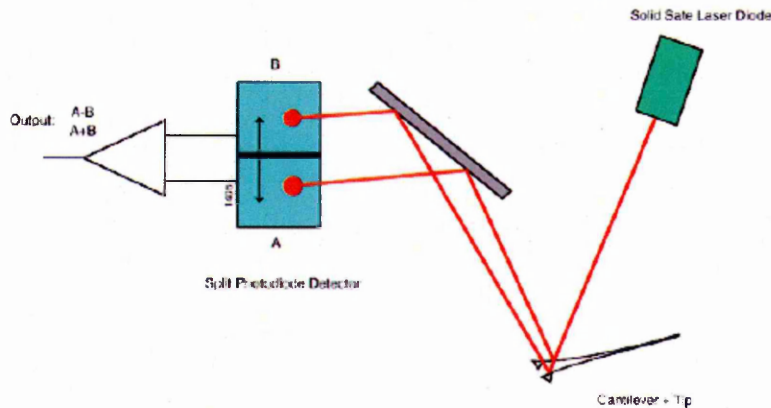


Figure 4.22. The most widely used form of cantilever deflection detection

Because the cantilever-to-detector distance generally measures thousands of times the length of the cantilever, the optical lever greatly magnifies the motion of the tip. Because of this approximately 2000-fold magnification, the optical lever detection can theoretically achieve a noise level of 10^{-14} m/Hz^{1/2} [38].

Piezoelectric transducer is electromechanical device that converts electrical potential into mechanical motion and vice versa. It expands and contracts proportionally to the applied voltage. The piezoelectric effect is reversible since mechanical deformations of the non centrocymetrical crystal cause the appearance of electrical charges and thus the electric potential. The magnitude of the dimensional changes

depends on the material, the geometry of the device, and the magnitude of the applied voltage (Figure 4.23).

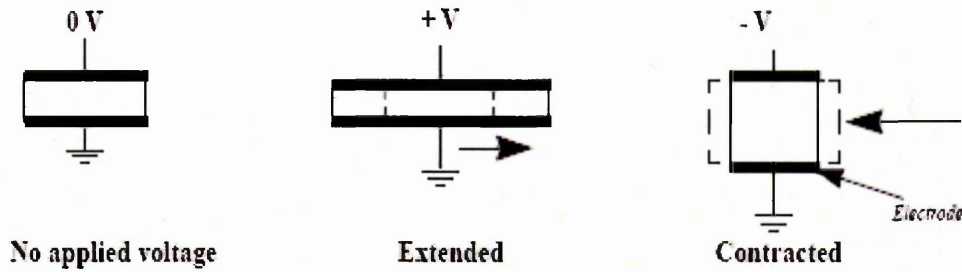


Figure 4.23. The effect of applied voltage on piezoelectric materials. [34]

In the AFM, piezoelectric material is used to construct the scanner tube. To be able to manipulate the sample and probe in three dimensions, the scanner is constructed by combining independently operated piezo electrodes for X, Y and Z into a single tube. Ideally, the piezoelectric ceramics would expand and contract in direct proportion to the driving voltage. However, piezoelectric materials have two primary non-ideal behaviours: *hysteresis* and *creep*.

Hysteresis is caused by the differences in the material properties and dimensions of each piezoelectric element which responds differently to an applied voltage as shown in Figure 4.24.

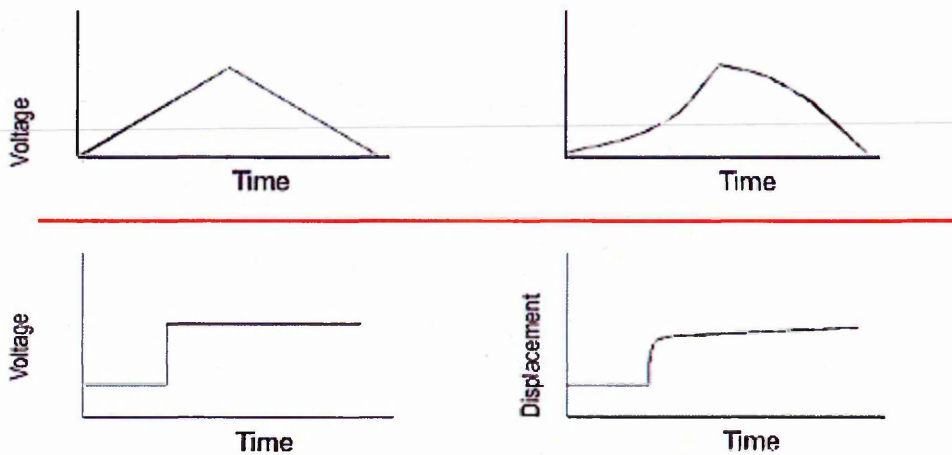


Figure 4.24. Non ideal behaviour of piezo materials: hysteresis (above) and creep (bottom) [44].

While *creep* occurs when the piezo material is subjected to a sudden impulse such as a voltage step function. When an offset DC voltage is applied, the piezo material will move the tip to the offset distance. However, it does not move all at once: it initially moves the majority of the offset distance quickly, and then slowly moves over the remaining distance (see Figure 4.24). These non-ideal behaviours must be corrected or they cause distortions in AFM images.

Feedback control is used to maintain a force between the probe and the surface. It operates by measuring the force between the surface and probe, then controlling a piezoelectric ceramic that establishes the relative position of the probe and surface. As the piezo material expands, the motion sensor measures the position of the probe and surface. Output from the motion sensor is used to correct the movement of the piezo.

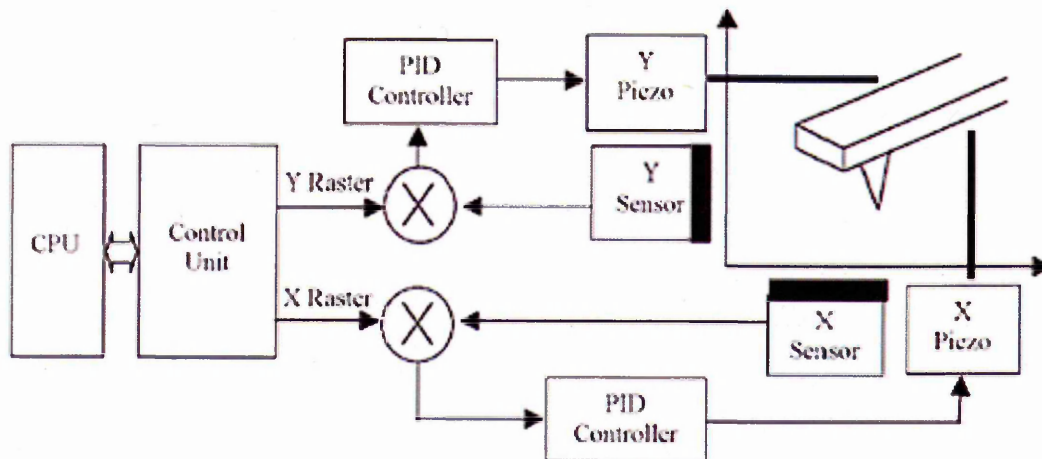


Figure 4.25. Block diagram of an x-y closed loop scanner configuration. [44]

The feedback system enables the piezoelectric scanner to maintain the tip operating at one of the two modes: *constant force* (to obtain height information), or *constant height* (to obtain force information). In *constant height mode*, during the scanning, the tip is maintained at a fixed height above the surface sample, hence the spatial variation of the cantilever deflection can be used directly to generate the topographic data set. In *constant-force mode*, the deflection of the cantilever,

responding to the topography, is used as an input to a feedback circuit that moves the scanner up and down in z-axis. By doing this, the total force applied by the cantilever to the sample is constant.

4.5.2. Imaging and measurements

As mentioned above, AFM operates by measuring attractive or repulsive forces between the tip and the sample. Two types of tip-surface interactions depending on the separation between the tip and the sample are shown in Figure 4.26. During close contact with the sample, the repulsive van der Waals forces would dominate the interaction with the tip. While long-range interaction, notably electric or magnetic forces, may dominate sample-tip interaction if the tip is far enough from the sample. Therefore AFM can operate in three main regimes: *contact mode*, *tapping mode*, and *non-contact mode*.

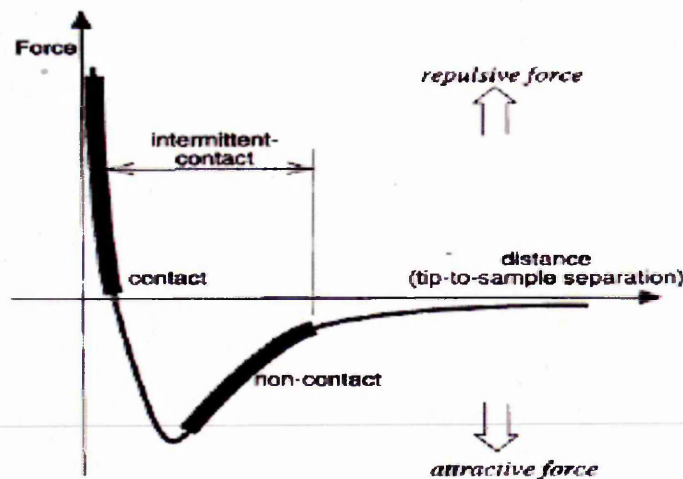


Figure 4.26. Potential energy diagram of a probe/sample system [34].

Contact mode is based on repulsive forces between the tip and the sample. In this mode, the tip contacts the surface either directly or through the adsorbed fluid layer on the sample surface. Electrostatic and/or surface tension forces from the adsorbed

fluid layer pull the scanning tip toward the surface but the repulsive force is set with a piezoelectric positioning element to drive the cantilever away from the sample surface. Hence the force between the tip and the sample remains constant. Force constants usually less than 1.0 N/m, resulting in forces ranging from nN to μN in an ambient atmosphere. The force could be calculated from Hooke's law:

$$F = -k \cdot x \quad (4.30)$$

where F is Force, k is spring constant and x is cantilever deflection.

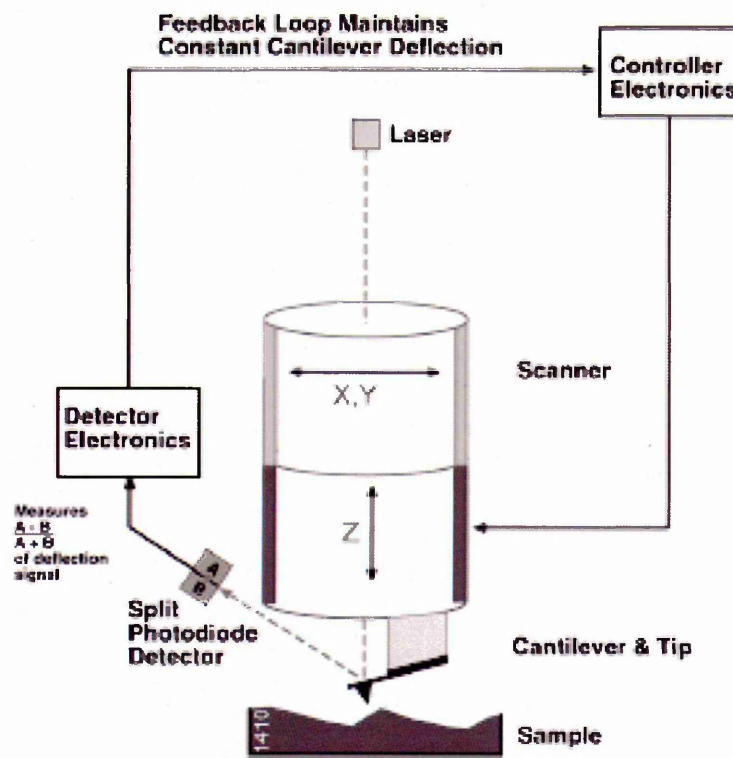


Figure 4.27. Schematic of the contact mode AFM [34].

The topographic data set of the sample surface is obtained from the vertical distance of scanner movement at each point (x, y). Advantages of the contact mode are:

- High scan speed
- Contact mode AFM is the only AFM technique which can obtain "atomic resolution" images.

- Rough samples with extreme changes in vertical topography can sometimes be scanned more easily in contact mode.

And the disadvantages are:

- Lateral (shear) forces can distort features of the image.
- The forces normal to the tip-sample interaction can be high in air due to capillary forces from the adsorbed fluid layer on the sample surface.
- The combination of lateral forces and high normal forces can result in the reduced spatial resolution and may damage soft samples (i.e., biological samples, polymers, organic film) due to scraping between the tip and the sample.

Tapping mode is the next most common mode and a key advance in AFM. In this mode, the tip is placed in contact with the surface to provide high resolution and then the tip is lifted off the surface to avoid dragging the tip across the surface. The piezoelectric crystal oscillates the cantilever at (or near) its resonant frequency (in the range of hundreds of kHz) with the amplitude from 20 nm to 100 nm. Then the oscillating tip is moved towards the surface until it begins to lightly touch (or tap) the surface. During scanning, the vertical oscillating tip alternately contacts the surface and lifts off, generally at a frequency of 50 kHz to 500 kHz. During the scanning, the feedback loop maintains a constant oscillation amplitude by maintaining a constant RMS of the oscillation signal acquired by the split photodiode detector (Figure 4.28). By maintaining a constant oscillation amplitude, a constant tip-sample interaction is maintained during imaging. The vertical position of the scanner at each (x, y) data point in order to maintain a constant *setpoint* amplitude is stored by the computer to form the topographic image of the sample surface.

cantilever's resonant frequency is decreased by the van der Waals forces and by other long range forces which extend above the surface. The decrease in resonant frequency causes the amplitude of oscillations to decrease. The feedback loop maintains a constant oscillation amplitude or frequency by vertically moving the scanner at each (x, y) data point until a "setpoint" amplitude or frequency is reached (Figure 4.29). The distance the scanner moves vertically at each (x, y) data point is stored by the computer to form the topographic image of the sample surface. This is a very difficult mode to operate in ambient condition with the AFM.

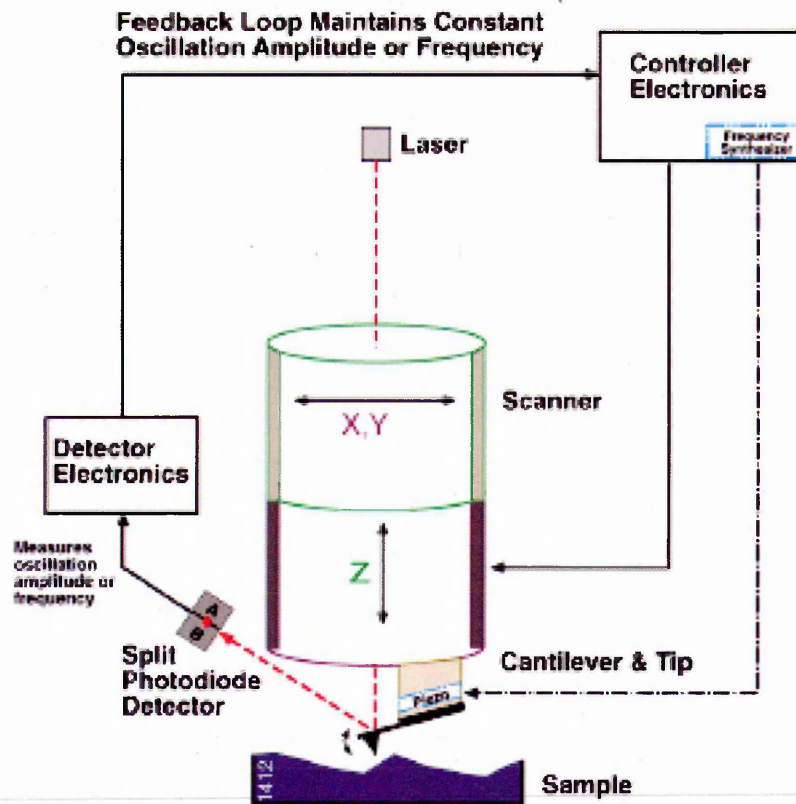


Figure 4.29. Schematic of the non-Contact mode AFM [34].

Advantage:

- No force exerted on the sample surface.

Disadvantages:

- Lower lateral resolution, limited by the tip-sample separation
- Slower scan speed than tapping or contact mode to avoid contacting the adsorbed fluid layer which results in the tip getting stuck.
- Non-contact mode usually works on extremely hydrophobic samples, where the adsorbed fluid layer is very thin. If the fluid layer is too thick, the tip becomes trapped in the adsorbed fluid layer causing unstable feedback and scraping the sample.

4.5.3. Quantitative analysis on AFM images

A great amount of information could be extracted from AFM images through visualization of the images which are stored in a computer as a three dimensional array of numbers. The array of numbers can be processed, displayed, analyzed and then reported by specialized image processing software. There are several ways of displaying images to make them more interesting to view by changing the display parameters using the software without changing the AFM data. Images could be displayed as either 2-dimensional or 3-dimensional projections. The 2-D image is shown in the x and y axis and the colour is used to depict the height. While 3-D image is displayed in the x, y and z axis as an interpretation of what the surface topography actually looks like. Often the scale on the x, y and z axis are not equal, which can make 3-D images misleading.

Line profile is the most common type of analysis made on AFM images. It is a two dimensional or cross section extracted from an AFM image. The line profile could be taken horizontally, vertically or at a specific angle. From a line profile, the distances between two points, as well as angle, may be calculated.

Surface roughness analysis is generally represented in terms of statistical deviation from the average height. The analysis generates a wide variety of statistics for surfaces, including classical roughness values, peak and summit (texture) data and

surface area calculations. Standard equations, which are typically used for these calculations, are:

$$S_R = \frac{1}{n} \sum_{j=1}^n |Z_j - \bar{Z}| \quad (4.31)$$

where S_R is surface roughness, Z_j is the height at specific point and \bar{Z} is the average height.

$$\bar{Z} = \frac{1}{n} \sum_{j=1}^n |Z_j| \quad (4.32)$$

Particle Analysis defines particles based on the height of pixel data. By setting the height threshold, the cross-section could be analysed. The particles are identified in an image by setting a certain height (threshold) as shown in Figure 4.30.

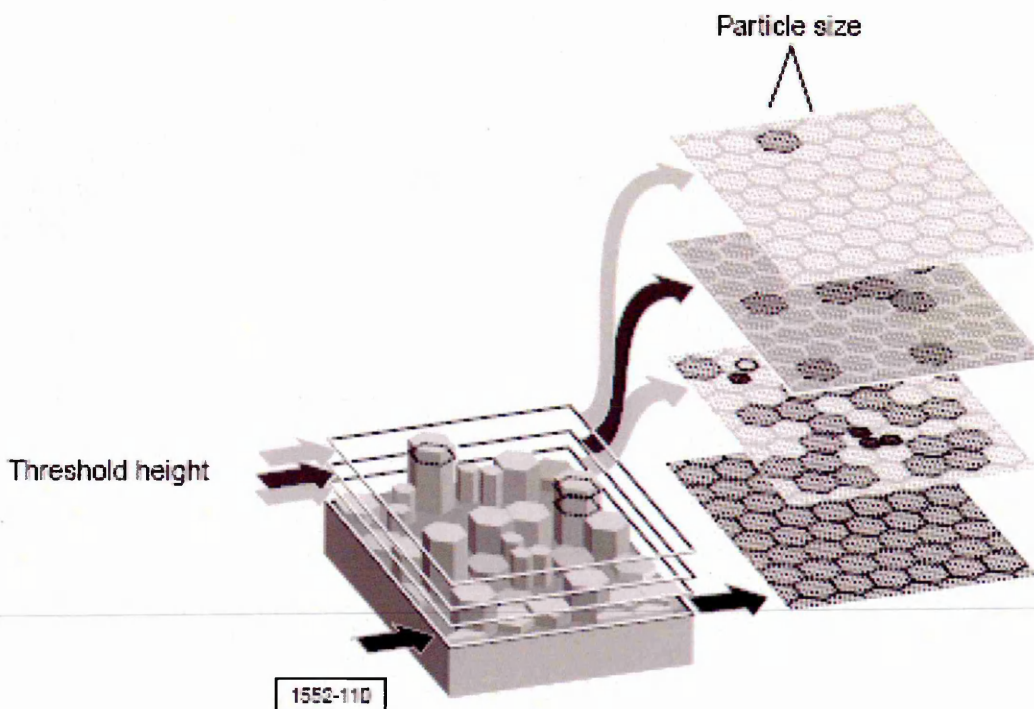


Figure 4.30. Illustration of the particle size analysis at the selected height [46].

Once the nanoparticles in the AFM image are identified they are automatically counted. Measurements on this analysis include: the mean area and standard deviation

of the particle sizes, the total number of particles, a correlation histogram, a bearing ratio curve and a depth histogram. The analyses could be done for a single particle or for a number of particles on the surface showing the statistical parameters and the distribution of particles as a function of any of the measured variables.

4.5.4. The procedure of AFM measurements

In this work, the CdS and ZnS nanoparticles thin films morphology was studied with atomic force microscopy (AFM) using the Digital Instruments Nanoscope IIIa instrument, from Veeco Metrology Group Inc.

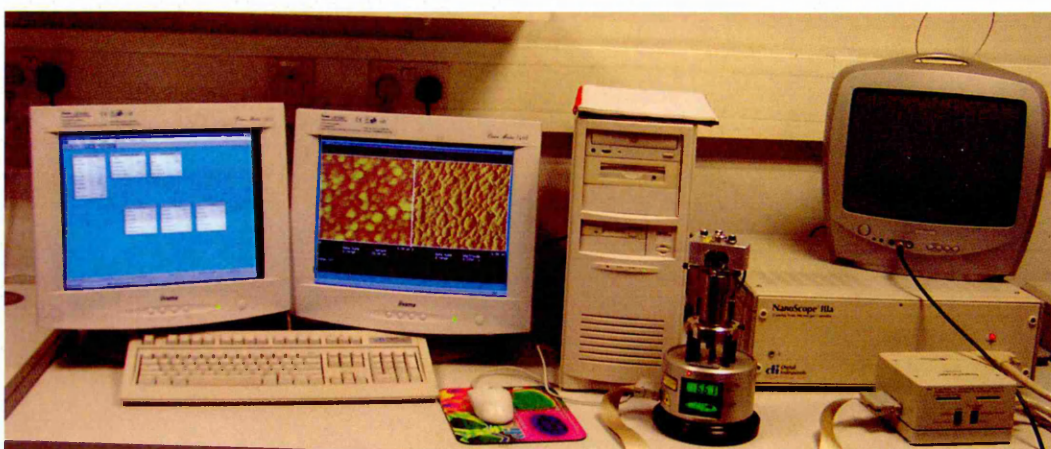


Figure 4.31. Nanoscope IIIa AFM instrument.

Thin films were deposited on small pieces of silicon, about 1 cm x 1 cm in size, and then mounted onto the AFM sample holder. The instrument was set for using E head for a small scanning area of maximum 15x15 μm . Tapping mode is chosen as a scanning technique due to its suitability for organic/polymer films. VEECO tapping mode cantilevers with the tip radius less than 10 nm (typically from 4-7 nm) having the oscillation frequency in the range from 300 to 500 kHz were used. Scanning was conducted at room temperature and ambient air. Technical parameters were set for scanning the area of 5 μm , 1 μm and 200 nm, with the scan rate of about 1 Hz. The

roughness, particle size, 2D and 3D images of scanning images were analysed using the Digital Instruments integrated image processing software, Nanoscope version 5.12 [46].

4.6. ELECTRICAL PROPERTIES STUDY USING MERCURY PROBE

Mercury probe technique has been used for many years to analyse semiconductor / insulator systems and to obtain the parameters such as permittivity, threshold voltage, interface trap density, impedance, substrate doping, oxide thickness and integrity, and low-dose ion implant doping profiles [47-51]. This precision technique provides rapid, convenient, and non-destructive measurements of semiconductor samples by probing sample with the mercury contact of a well-defined area.

In this work, this technique is used to counter the problems in studying electrical properties of composite films of metal sulfides (CdS and ZnS) and polyelectrolytes, in sandwich structures. The standard metal deposition methods (i.e. evaporation or sputtering) may cause the damage and give rise to short-circuits in thin films. While the mercury probe technique could be used without evaporating metal contact. However it does not always work for organic films. Because of a very high surface tension of about 485 mN/m at room temperature mercury could damage poorly adhesive organics films. Attempts to use a mercury probe for Langmuir-Blodgett and spun organic films were not successful; the mercury drop pulls the thin film on its surface and leaves a hole at the films underneath. But the same experiment on electrostatically self-assembled polyelectrolyte films of PAA/PSS deposited onto silicon wafers was successfully carried out by Nabok et. al. [52, 53] to measure I-V and C-V characterisation without damaging the films.

The schematic diagram of a mercury probe technique, similar to that used in [52], is shown in Figure 4.32. The micro-syringe complete with the stainless steel plunge was

modified and used here. The capillary tube filled with mercury was fixed to a holder. By pressing the stainless steel plunge, the mercury drop would appear at the bottom of the capillary tube. Then, the mercury drop was brought into contact with the sample surface using an adjustable microscopic stand. A microscope was used to observe the horizontal contact line between the mercury drop and sample surface. The diameter of the contact was measured using the micrometer scale in the microscope ocular.

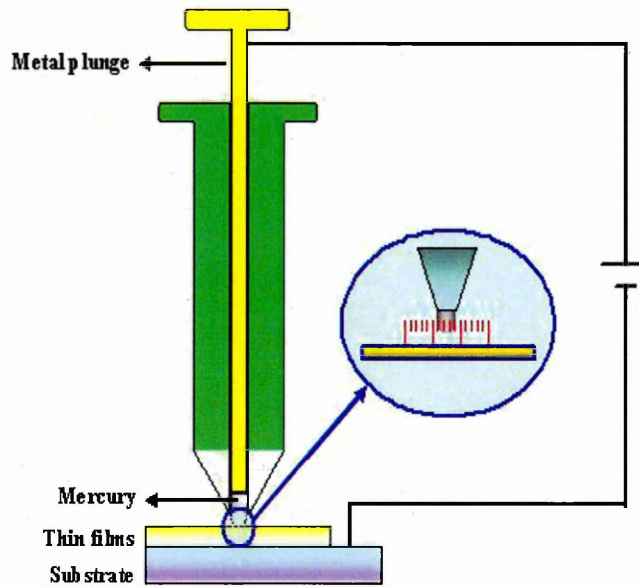


Figure 4.32. Mercury probe experimental set-up.

For both I-V and C-V measurement, the samples, as described in section 4.2.3.4, were deposited on ITO. The bias voltage was applied between an uncoated part of ITO and the mercury electrode.

4.6.1. I-V characterisation

DC current-voltage (I-V) characteristics were measured using Keithley 4200 Semiconductor Characterization System instrument. Parameters of the DC bias sweep were: the sweep range from - 0.5 to 0.5 V, and the step size of 5 mV. Some measurements were performed in the bias range from 0 to -0.5 V with the step of 5 mV.

Measurements were repeated several times on the same spot, as well as at different spots on the same sample.

4.6.2. C-V characterisation

C-V characteristic measurements were carried out by using Hewlett Packard 4284 A Precision LCR meter in a frequency range of 20 Hz- 1 MHz. The instrument was interfaced to computer via IEEE GPIB card and controlled by dedicated software. Parameters of bias sweep were: the bias range from - 0.5 to 0.5 V, and the step size of 10 mV. Measurements were repeated several times on the same spot, as well as at different spots on the same sample.

4.7. ELECTROLUMINESCENCE MEASUREMENTS

Luminescence is the emission of light by a material, usually a semiconductor, as a result of the recombination of electrons and holes. It occurs when an excited electron returns to the electronic ground state and releases their energy as a photon.

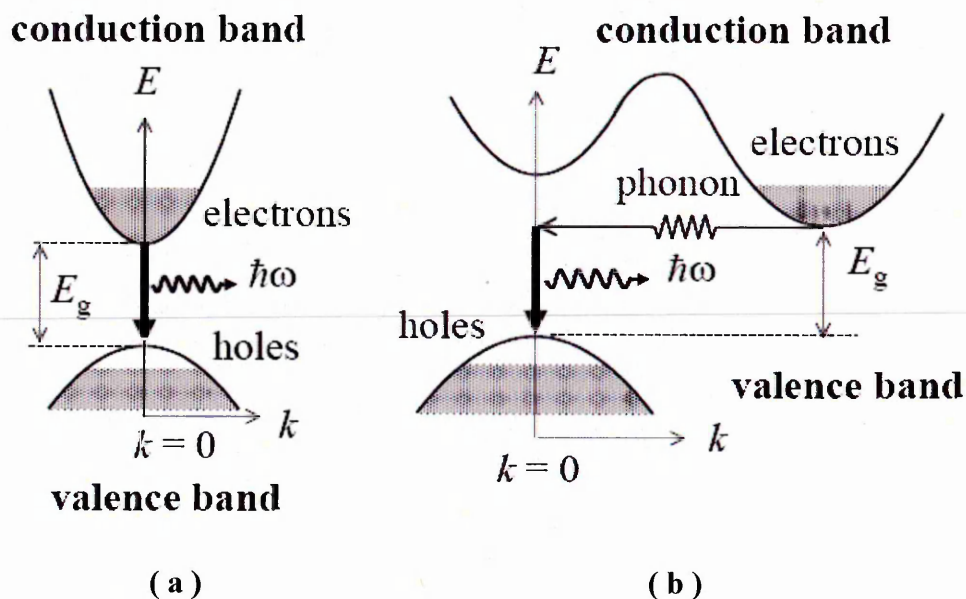


Figure 4.33. The energy bandgap diagrams of luminescence for: direct bandgap (a) and indirect bandgap (b) materials [54].

Figure 4.33 shows the energy bandgap of direct and indirect bandgap material for luminescence processes. In this picture, the excited electrons dwell in the conduction band (CB) after absorbing some energy and leave holes in the valence band (VB). Then, as the CB-electrons relaxes back into a VB-state and emit photons.

There are two excitation processes related to excite electrons from the ground state: optical (photoluminescence) and electrical (electroluminescence).

Photoluminescence occurs when a material absorbs light of a certain frequency and emits light at a specific frequency corresponding to the material's specific structure, composition and quality.

The other, *electroluminescence* is a phenomenon where a material emits light in response to an electric current passed through it. There are basically two distinct mechanisms of electroluminescence in solids: pure (intrinsic) excitation and charge injection [55]. In the intrinsic electroluminescence, thermal activation and the electric field liberate electrons from donor levels into the conduction band. Many of these conduction electrons are accelerated by the field until they collide with luminescent centres, ionizing them (i.e., ejecting electrons from their atoms).

For charge injection electroluminescence, a forward bias voltage is applied to a p-n junction semiconductor to provide a flow of electrons or holes, as shown on Figure 4.34.

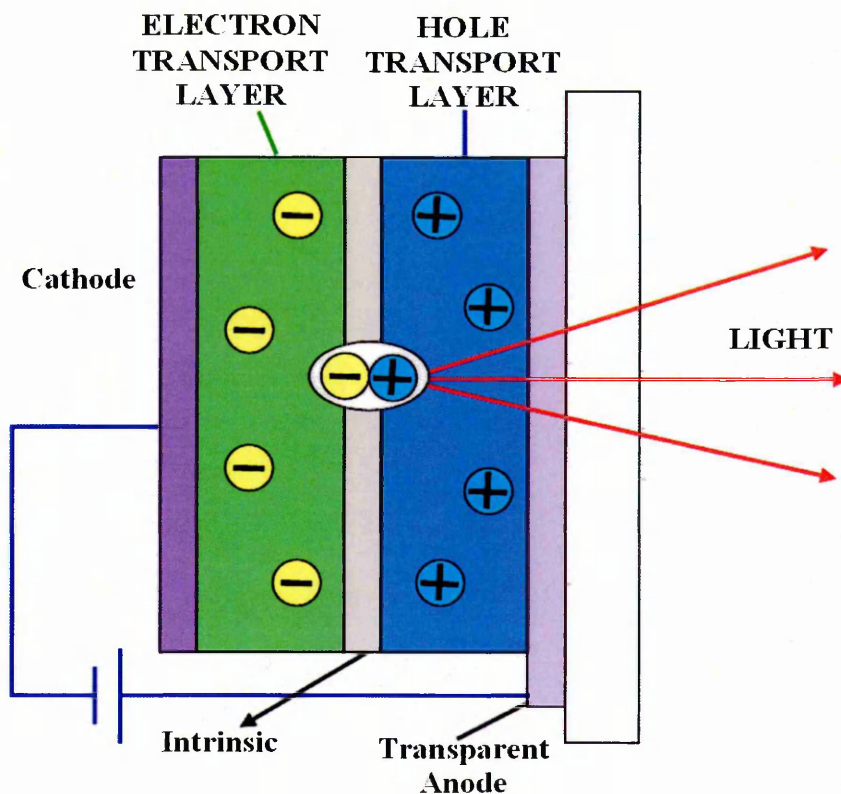


Figure 4.34. The principle of the electroluminescence set-up.

In both cases, the electrons lose energy when recombining with centres or positive holes accompanied by the emission of light.

Experiment Procedure

Electroluminescence measurements were carried out by using Hamamatsu H7421 photon counter. The instrument was interfaced to computer using a Hamamatsu M8784 Counting Board PCI card and controlled by Hamamatsu software. The samples, as prepared in section 4.2.3.3, were placed in the cell filled with electrolyte solution (sodium chloride 1 M) [56]. Then, voltage bias was applied to the samples as shown in Figure 4.35.

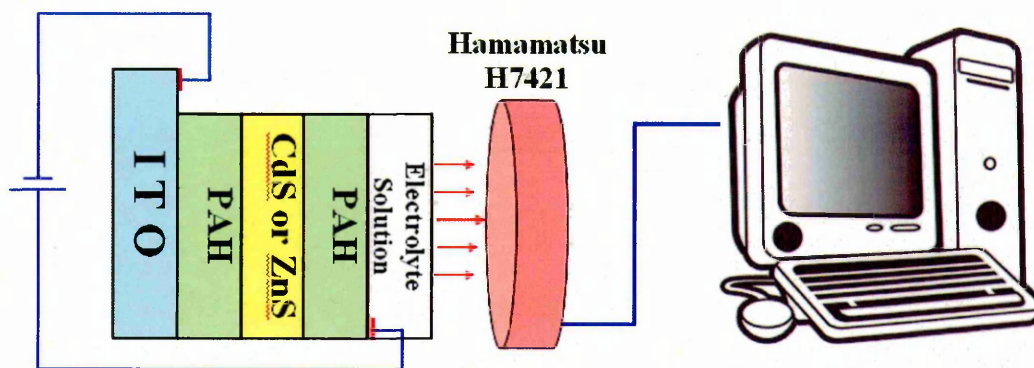


Figure 4.35. Electroluminescence experimental set-up.

Measurements were repeated several times on the same sample. All measurements were performed in a dark room. A special shielding was used to reduce the effect of weak light intensity emitted by electrical instruments or PC screen were used.

Because of a low intensity of electroluminescence in thin II-VI semiconductor/polyelectrolyte films, the spectral measurements of the electroluminescence were difficult to perform using the existing instrumentation.

REFERENCES

1. Nabok A. V., Hassan A. K., and Ray A. K. "Optical and electrical characterisation of polyelectrolyte self-assembled thin films." *Materials Science and Engineering C* 8-9 (1999): 505-508.
2. Lvov Y., Haas H., Decher G., Mohwald H., and Kalachev A. "Successive deposition of alternate layers of polyelectrolytes and a charged virus." *Langmuir* 10 (1994): 4232-4236.
3. Fendler J. H. "Self-assembled nanostructured materials." *Chemistry of Materials* 8 (1996): 1616-1624.
4. "UV-Vis Spectroscopy-Basic Theory." The Pennsylvania State University. 15 August 2007 <http://www.mri.psu.edu/mcl/techniques/uv-vis/basic_theory.asp>.
5. "UV-Vis Absorption Spectroscopy- Theoretical principles." Sheffield Hallam University. 15 August 2007 <<http://teaching.shu.ac.uk/hwb/chemistry/tutorials/molspec/uvvisab1.htm>>.
6. Pankove J. I. *Optical Processes in Semiconductors*. New Jersey: Prentice-Hall, Inc., 1971.
7. UV/Vis Spectrophotometer, 15 August 2007 <<http://www.mecasys.co.kr/kor/file/data/04/02/spectrometer.pdf>>.
8. Henderson, Brian. "Optical spectrometers." *Handbook of optics Volume II: Devices, measurements, and properties*. Ed. Michael Bass. New York: McGraw-Hill Inc., 1995.
9. Hof, Martin. "Basics of Optical Spectroscopy." *Handbook of Spectroscopy*. Ed. Günter Gauglitz and Tuan Vo-Dinh. Weinheim: Wiley-VCH Verlag GmbH & Co., 2003.
10. "Cary 50 UV-Vis spectrophotometer." 15 August 2007 <<http://www.varianinc.com/cgi-bin/nav?products/spectr/uv/cary50/cary50&cid=JNMPHHOMFO>>.
11. "Varian Cary 50." 15 August 2007 <http://faculty.kutztown.edu/betts/html/UV_Vis_Absorbance.htm#Varian>.
12. Schwartz G. C. and Srikrishnan K. V. *Handbook of semiconductor interconnection technology*. Boca Raton: CRC Press, 2006.
13. Tompkins H.G. *A user's guide to ellipsometry*. New York: Academic Press, 1993.
14. *Guide to Using WVASE32*. J. A. Woollam Co., Inc., 2002.
15. Azzam R. M. A. and Bashara N. M. *Ellipsometry and Polarized Light*. Elsevier Science Pub. Co., 1987.
16. Azzam R. M. A. "Ellipsometry." *Handbook of optics Volume II: Devices, measurements, and properties*. Ed. Michael Bass, New York: McGraw-Hill Inc., USA, 1995.
17. "Ellipsometry Tutorial." J.A. Woollam Co. Inc. 15 August 2007 <http://www.jawoollam.com/tutorial_1.html>.
18. Woollam J. A., Johs B., Herzinger C. M., Hilfiker J., Synowicki R., and Bungay C. L. "Overview of variable angle spectroscopic ellipsometer (VASE), Part I: Basic theory and typical applications." *Critical reviews of optical science and technology*,

19. Arwin H., Poksinski M., and Johansen K. "Total internal reflection ellipsometry: Principles and applications." *Applied Optics* 43 (2004): 3028-3036.
20. de Bruijn H. E., Altenburg B. S. F., Kooyman R. P. H., and Greve J. "Determination of thickness and dielectric constant of thin transparent dielectric layers using surface plasmon resonance." *Optical Communication* 82 (1991): 425.
21. Gordon J. G. and Swalen J. D. "The effect of thin organic films on the surface plasma resonance on gold." *Optics Communications* 22 (1977): 374.
22. Kretschmann E. and Raether H. "Radiative decay of non-radiative surface plasmons excited by light." *Z. Naturforsch. A* 23 (1968): 2135-2136.
23. van der Merwe P. A. *Surface plasmon resonance*. University of Oxford. 15 August 2007 <<http://users.path.ox.ac.uk/~vdmerwe/Internal/spr.PDF>>.
24. "SPR theory." March 2007. 15 August 2007 <<http://www.sprpages.nl/SPRtheory/SprTheory01.htm>>.
25. Hassan A. K., Ray A. K., Nabok A. V., Lucke A., Smith K., Stirling C. J. M., and Davis F. "Thin films of calix-4-resorcinarene deposited by spin coating and Langmuir-Blodgett techniques: determination of film parameters by surface plasmon resonance." *Materials Science and Engineering C* 8-9 (1999): 251-254.
26. Hassan A. K., Ray A. K., Nabok A. V., and Davis F. "Spun films of novel calix [4] resorcinarene derivatives for benzene vapour sensing." *Sensors and Actuators B* 77 (2001): 638.
27. Johnston K.S., Karlson S.R., Jung C. C., and Yee S. "New analytical technique for characterization of thin films using surface plasmon resonance." *Materials Chemistry and Physics* 42 (1995): 242-246.
28. Smith A. and Corn R. M. "Surface Plasmon Resonance Imaging as a Tool to Monitor Biomolecular Interactions in an Array Based Format." *Focal Point* 57 (2003): 320-332.
29. Mrksich M., Sigal G. B., and Whitesides G. M. "Surface Plasmon Resonance Permits in Situ Measurement of Protein Adsorption on Self-Assembled Monolayers of Alkanethiolates on Gold." *Langmuir* 11 (1995): 4383-4385.
30. Nelson S. G., Johnston K. S., and Yee S. S. "High sensitivity surface plasmon resonance sensor based on phase detection." *Sensors and Actuators B: Chemical* 35 (1996): 187-191.
31. Homola J. "Present and future of surface plasmon resonance biosensors." *Analytical and Bioanalytical Chemistry* 377 (2003): 528-539.
32. Nabok A.V., Tsargorodskaya A., Hassan A.K., and Starodub N.F. "Total internal reflection ellipsometry and SPR detection of low molecular weight environmental toxins." *Applied Surface Science* 246 (2005): 381-386.
33. Nabok A. V., Tsargorodskaya A., Holloway A., Starodub N. F., and Gojster O. "Registration of T-2 mycotoxin with total internal reflection ellipsometry and QCM impedance methods." *Biosensors and Bioelectronics* 22 (2006): 885-890.
34. *Scanning Probe Microscopy Training Notebook*, 2000, Digital Instruments/ Veeco Metrology Group Inc., Version 3.

35. Giessibl F. "Advances in Atomic Force Microscopy." *Reviews of Modern Physics* 75 (2003): 949-983.
36. Binnig G., Quate C. F., and Gerber C. "Atomic Force Microscope." *Physical Review Letters* 56 (1986): 930-933.
37. Atomic force microscope, 15 August 2007 <http://en.wikipedia.org/wiki/Atomic_force_microscope>.
38. Putman C. A. J., De Grooth B. G., Van Hulst N. F., and Greve J. "A detailed analysis of the optical beam deflection technique for use in atomic force microscopy." *Journal of Applied Physics* 72 (1992): 6-12.
39. Erlandsson R., McClelland G.M., Mate C.M., and Chiang S. "Atomic force microscopy using optical interferometry." *Journal of Vacuum Science & Technology A: Vacuum, Surfaces, and Films* 6 (1988): 266.
40. Sarid D., Iams D.A., Ingle J.T., Weissenberger V., and Ploetz J. "Performance of a scanning force microscope using a laser diode." *Journal of Vacuum Science & Technology A: Vacuum, Surfaces, and Films* 8 (1990): 378.
41. Goddenhenrich T., Lemke H., Hartmann U., and Heiden C. "Force microscope with capacitive displacement detection." *Journal of Vacuum Science* 8 (1990): 383.
42. Meyer G. and Amer N. M. "Novel optical approach to atomic force microscopy." *Applied Physics Letters* 53 (1988): 1045-1047.
43. Alexander S., Hellemans L., Marti O., Schneir J., Elings V., Hansma P. K., Longmiro M., and Gurley J. "An atomic-resolution atomic-force microscope implemented using an optical lever." *Journal of Applied Physics* 65 (1989): 164-167.
44. West P. *Introduction to Atomic Force Microscopy: Theory, Practice and Applications*. 15 August 2007 <<http://www.AFMUniversity.org>>.
45. Albrecht T.R., Grütter P., Horne D., and Rugar D. "Frequency modulation detection using high-Q cantilevers for enhanced force microscope sensitivity." *Journal of Applied Physics* 69 (1991): 668-673.
46. *NanoScope Command Reference Manual*, 2001, Digital instruments/Veeco Metrology Group, Inc., Version 5.12.
47. Tuck B. and Zahari M. D. "Electrical measurements on homogeneous diffused p-type InP." *J. Phys. D: Appl. Phys.* 10 (1977): 2473-2479.
48. Lederman A. "Vacuum Operated Mercury Probe for CV Plotting and Profiling." *Solid State Technology* 24 (1981): 123-126.
49. Paszkiewicz B. "Impedance spectroscopy analysis of AlGaIn/GaN HFET structures." *Journal of crystal growth* 230 (2001): 590-595.
50. Groner M. D., Elam J. W., Fabreguette F. H., and George S. M. "Electrical characterisation of thin Al₂O₃ films grown by atomic layer deposition on silicon and various metal substrates." *Thin solid films* 413 (2002): 186-197.
51. Popov V. M., Klimenko A. S., and Pokanevich A. P. "Investigation of electrically active defects in Si-based semiconductor structures." *Materials science and engineering B* 91-92 (2002): 248-252.

52. Nabok A. V. and Hassan A. K., Ray A. K., and Toldi G. N. "Electrical study of polyelectrolyte self-assembled films using mercury probe." *Materials Science and Engineering C* 22 (2002): 387-391.
53. Nabok A. V., Massey J., Buttle S., and Ray A. K. "Study of electron tunnelling through thin polymer films using a mercury probe technique." *IEE Proceedings: Circuits, Devices and Systems* 151 (2004): 461-465.
54. Fox A.M., *Luminescence*. Lecture notes. 15 August 2007 <http://www.mark-fox.staff.shef.ac.uk/PHY475/phy375_notes_5.pdf>.
55. Piper W. W. and Williams F. E. "Theory of Electroluminescence." *Physical Review* 98 (1955): 1809-1813.
56. Tsargorodskaya A., Nabok A.V., and Ray A.K. "Study of electroluminescence in porous silicon for sensing applications." *IEE Proc.-Circuits Devices Syst.* 150 (2003): 355-360.

RESULTS AND DISCUSSION

5.1. INTRODUCTION

This chapter presents all of the experimental data, calculations, and discussions. First of all, the data obtained from UV-Vis spectrophotometer and spectroscopic ellipsometry are discussed. The optical properties of the films are presented, examined, and discussed in section 5.2. The nanoparticles' size is calculated from the absorption spectra and compared to the results of ellipsometry fitting. Section 5.3 presents the tapping mode AFM images, as films' morphology study. Roughness and particles analysis are explored for the investigation of the films' surface and structures. DC and AC electrical characteristics are discussed in section 5.4 while electroluminescence measurements are presented in section 5.5.

5.2. OPTICAL PROPERTIES OF CdS AND ZnS NANOPARTICLES

5.2.1. Absorption spectra measurements

5.2.1.1. Absorption spectra of the colloid and polyion solutions

The observation of the blue spectral shift of the optical absorption edge for the nanoparticles in comparison with the respective bulk values is a typical experimental confirmation of nanoparticles' presence. Figure 5.1 and 5.2 show typical absorption spectra of CdS and ZnS colloid nanoparticles solutions. The main absorption band at about 410 nm appears for both SO_3^- and NH_2^+ groups of CdS colloid nanoparticles as shown in Figure 5.1.

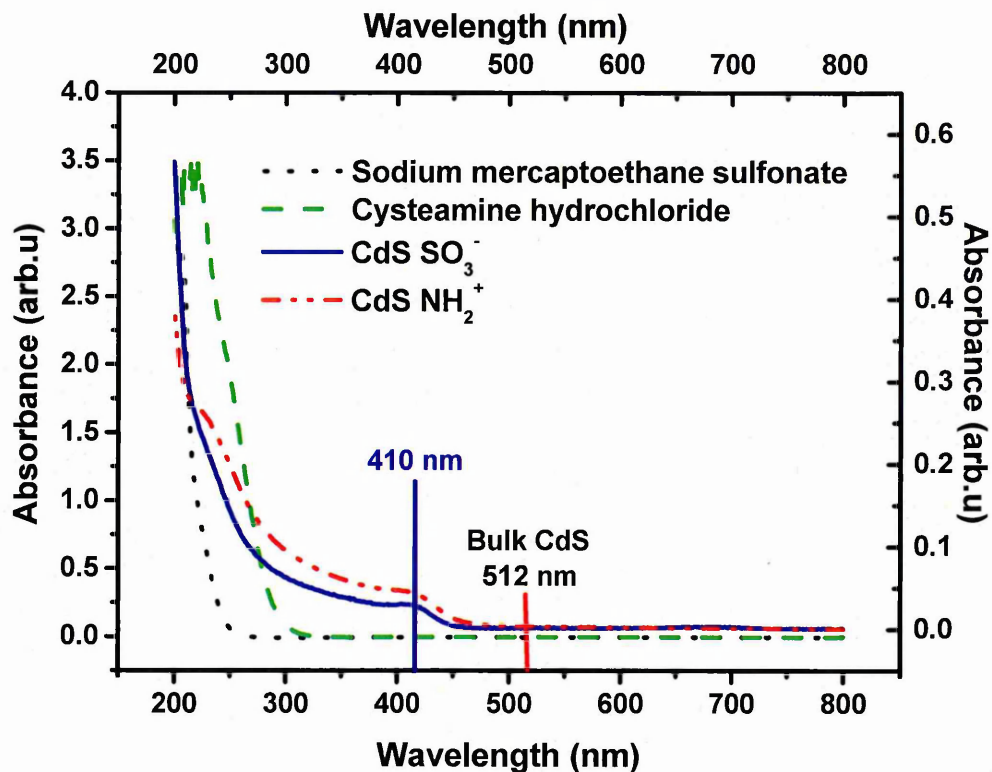


Figure 5.1. Absorption spectra of capping agents, CdS SO_3^- and CdS NH_2^+ colloid solutions (diluted 500x).

Both absorption bands are blue shifted as compared to the absorption band of bulk CdS at 512 nm. It can be seen that the capping agents, sodium mercapto sulfonate and cysteamine hydrochloride, do not contribute to the main absorption of nanoparticles. As mentioned before, this spectral shift confirms the presence of CdS nanoparticles. Since the absorption edges of both CdS SO_3^- and CdS NH_2^+ are located relatively at the same wavelength, it also means that their particles sizes are relatively the same for both colloid solutions.

As shown in Figure 5.2, the absorption peaks for both ZnS SO_3^- and ZnS NH_2^+ colloid solutions are also located at relatively the same wavelength of about 295 nm. Both of them are also blue shifted as compared to the absorption band of bulk ZnS at 335 nm.

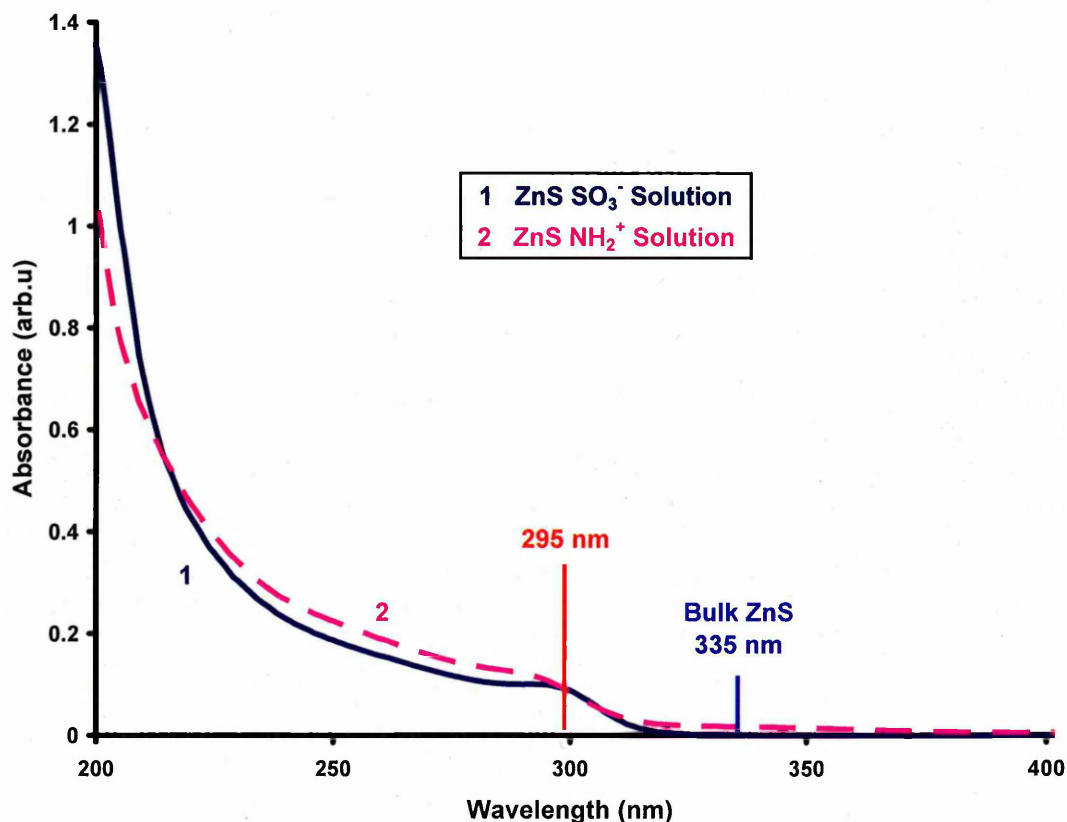


Figure 5.2. Absorption spectra of ZnS SO_3^- and ZnS NH_2^+ colloid solution (diluted 500x).

The size of CdS and ZnS nanoparticles can be evaluated from the blue shift of the absorption bands with respect to the band gap value of bulk CdS as a consequence of quantum confinement effect. In this work, the radius of semiconductor clusters is calculated using Efron's equation for the energy spectrum in nanoparticles of direct band gap semiconductors, having parabolic $E(k)$ dispersion. It is assumed that the particles' radius is smaller than Bohr exciton radius. Hence, in the case of strong confinement, (refer to Chapter 2, Equation 2.50) [1].

$$E_{(n,l)} = E_g + \frac{\hbar^2}{2\mu R^2} \phi_{(n,l)}^2 \quad (5.1)$$

where E_g is the band gap for bulk semiconductors, μ is the reduced effective mass of exciton, $\frac{1}{\mu} = \frac{1}{m_e^*} + \frac{1}{m_h^*}$, and $\phi_{(n,l)}$ are the roots of Bessel functions (for the ground state $\phi_{(0,1)} = \pi$).

The values of energy gap and electron (hole) effective mass, for both CdS and ZnS are obtained from ref. 2 as presented in Table 5.1.

Table 5.1. Energy gap, electron and hole effective masses for CdS and ZnS [2].

Parameter	CdS	ZnS
Energy gap (E_g) at 300 K	2.42 eV	3.68 eV
Electron effective mass (m_e^*)	0.21 m_e	0.25 m_e
Hole effective mass (m_h^*)	0.8 m_e	0.6 m_e

The values of $E_{n,l}$ can be found from the exact positions of the absorption peaks. To do that, the Gaussian fitting of absorption spectra re-plotted in energy coordinates was performed similar to ref. [3]. The results are shown in Figure 5.3 (a) and (b). The observed energy dispersion may reflect the combination of the size distribution of nanoparticles and the presence of higher index energy levels of size quantization, that is why only the first maximum (in each spectrum) corresponding to the ground state level was chosen for further analysis. The values of $E_{n,l} = 3.04$ eV (for CdS) and 4.19 eV (for ZnS) were found for the respective positions of the first absorption bands in Figure 5.3.

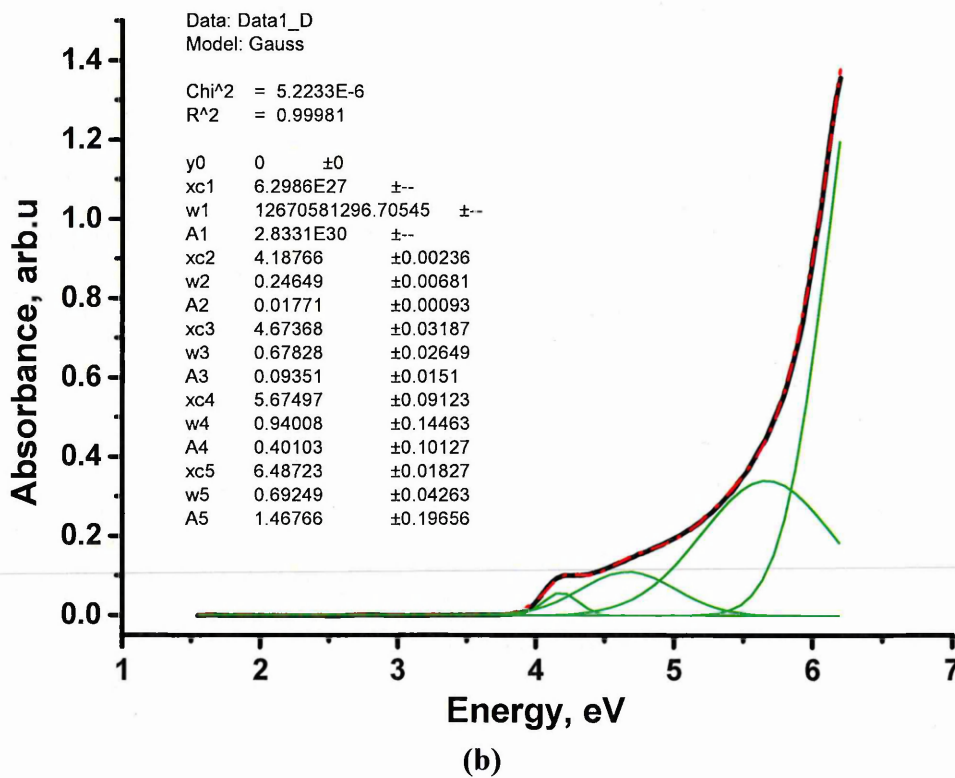
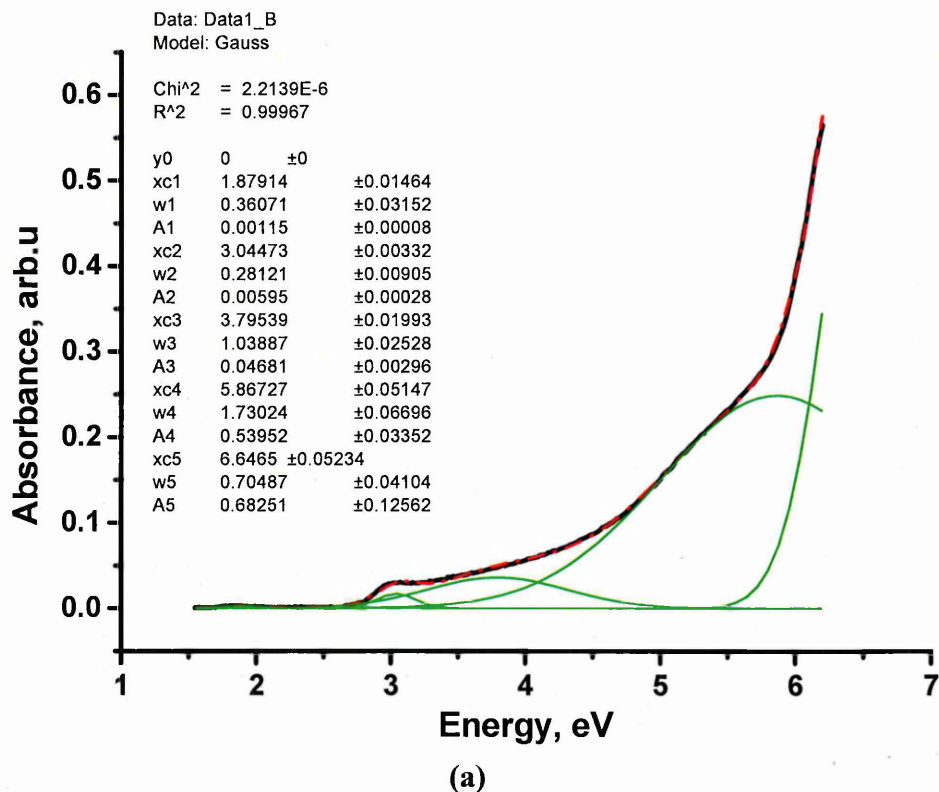


Figure 5.3. Gaussian fitting of the spectra of CdS-SO₃⁻ (a) and ZnS-SO₃⁻ (b) solutions.

The experimental data (black line) was fitted using 5 Gaussian peaks (green line) and the result was shows by the red line.

Using the data presented in Table 5.1 and the energy gap obtained from the Gaussian fitting, the particles' radius can be calculated using Equation (5.1) and the results are presented in Table 5.2.

Table 5.2. Energy gap and the radius of nanoparticles obtained by Gaussian fitting of the absorption spectra of CdS and ZnS solution.

Solution of	E (eV)	ΔE (eV)	Radius (nm)
CdS SO_3^-	3.04 ± 0.0033	0.62	1.91 ± 0.01
CdS NH_2^+	2.98 ± 0.0020	0.56	2.01 ± 0.01
ZnS SO_3^-	4.19 ± 0.0024	0.51	2.05 ± 0.01
ZnS NH_2^+	4.22 ± 0.0074	0.54	1.99 ± 0.03

Table 5.2 shows that the radius of nanoparticles for both CdS and ZnS colloid solutions were relatively the same of about 2 nm, which is smaller than their respective Bohr radii of 3 nm for CdS and 2.2 nm for ZnS [1].

As mentioned in Chapter 4, in this work, PAH and PSS are used as polyanion and polycation respectively. Therefore, their absorption spectra were also measured and shown in Figure 5.4. It is shown that PAH have peaks at 235 nm while PSS at 222 nm and 260 nm. The peak at 222 nm most likely corresponds to the absorption by benzene rings of PSS [4].

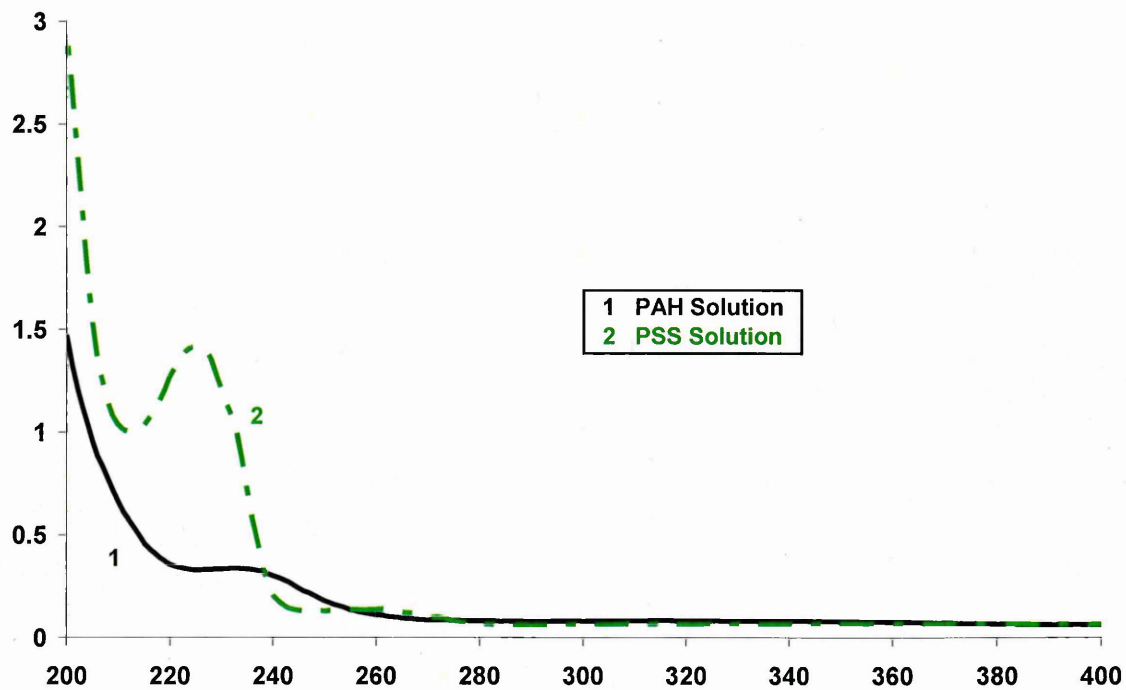


Figure 5.4. Absorption spectra of PAH and PSS solution (diluted 500x).

5.2.1.2. Absorption spectra of CdS and ZnS nanoparticles embedded in organic films

CdS nanoparticles films

As mentioned in Chapter 4, several structures of multilayer films were made and measured with UV-Vis spectroscopy. Typical absorption spectra of CdS nanoparticles embedded in organic films of PAH (for CdS SO_3^-) and PSS (for CdS- NH_2^+) are shown in Figures 5.5, 5.6 and 5.7. All of them show monotonous increase in the absorption intensity, with the increase in the number of layers, which reflects the consistency of electrostatic deposition.

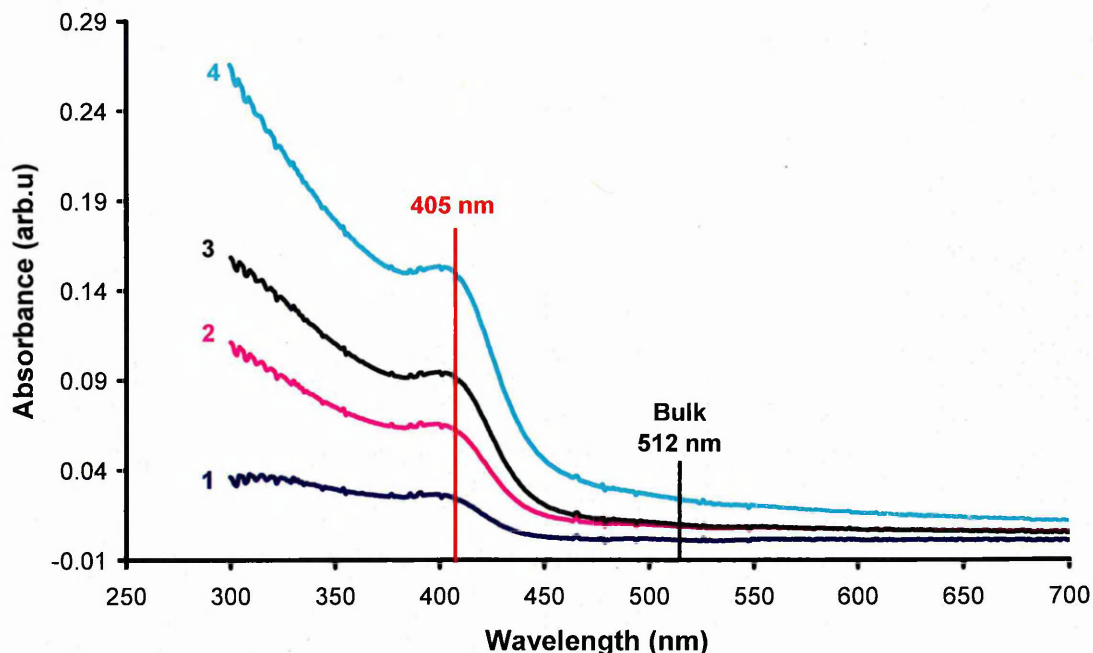


Figure 5.5. UV-vis absorption spectra of PAH/ CdS-SO₃⁻ film. The numbers near respective spectra correspond to the number of polyelectrolyte/nanoparticle bilayers.

Figure 5.5 shows the absorption spectra of CdS nanoparticles deposited on glass slide, the absorbance increases gradually and shows the absorption edge at about 405 nm which is blue shifted from the absorption bands of 512 nm for bulk CdS. This is believed to be due to the effect of quantum confinement in the nanoparticles since the polyions (PAH and PSS) possess no absorption at those wavelengths.

Figure 5.6 and 5.7 show, respectively, the UV-vis absorption spectra of CdS-SO₃⁻ and CdS-NH₂⁺ films, deposited on quartz slides. The main absorption bands are found at 405 nm for both of them. It also clearly shows the presence of the second peaks at about 230 nm and 226 nm, respectively. These peaks may correspond to the second quantum level ($n = 1$) in CdS nanoparticles. The adsorption peaks of PAH and PSS may also contribute to the absorption in this spectral range.

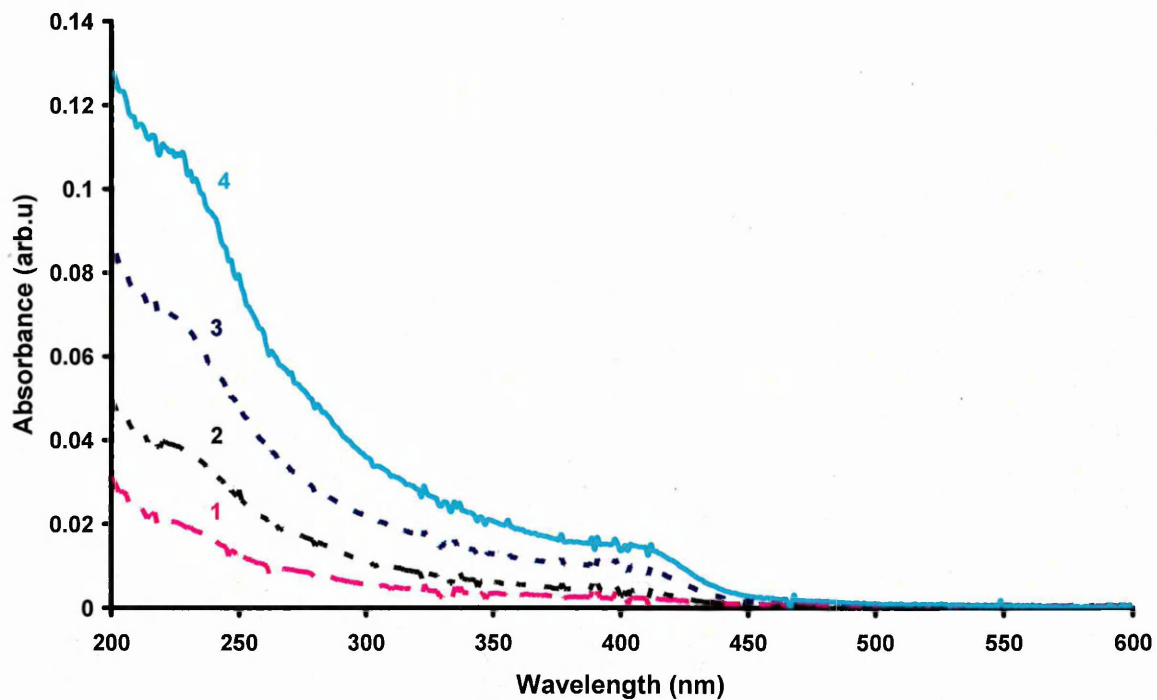


Figure 5.6. UV-vis absorption spectra of PAH/ CdS-SO₃⁻ films. The numbers near respective spectra correspond to the number of polyelectrolyte/nanoparticle bilayers.

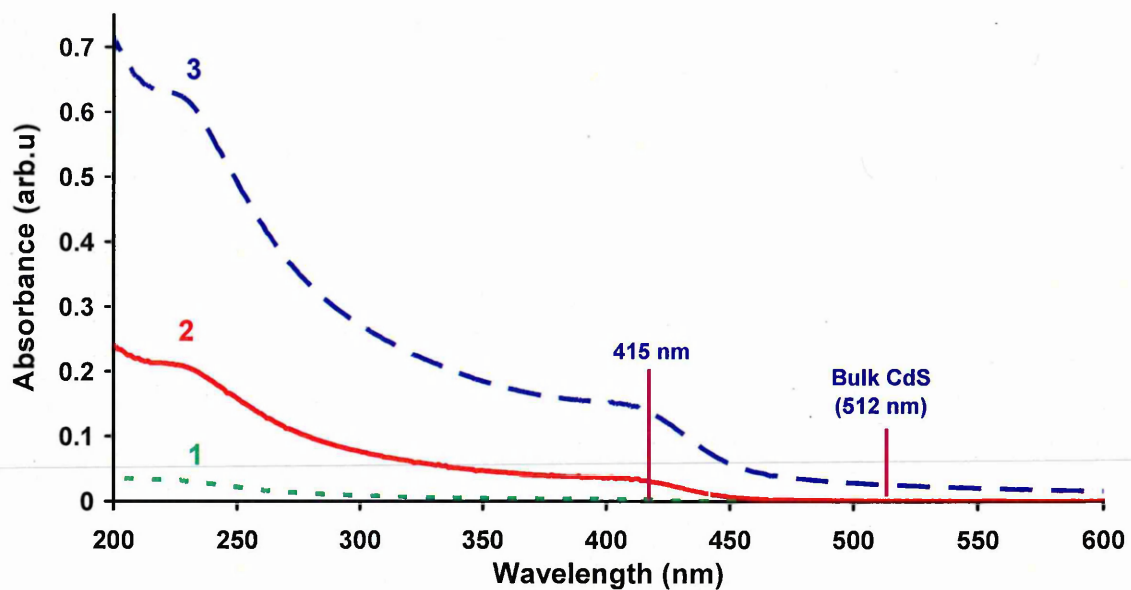


Figure 5.7. UV-vis absorption spectra of PAH/ PSS/CdS-NH₂⁺ film. The numbers near respective spectra correspond to the number of polyelectrolyte/nanoparticle bilayers.

The comparison with the solution spectra given in Figure 5.1 shows that the main absorption bands of CdS colloid solution occur at relatively longer wavelengths as compared to the absorption of electrostatically self-assembled films of CdS. The difference is believed to be due to the effect of the medium e.g. water or polyelectrolyte. The interaction of charged nanoparticles with highly polar water molecules is presumably larger than that with polyions, so that the absorption bands are slightly more red shifted in aqueous solutions.

ZnS nanoparticles films

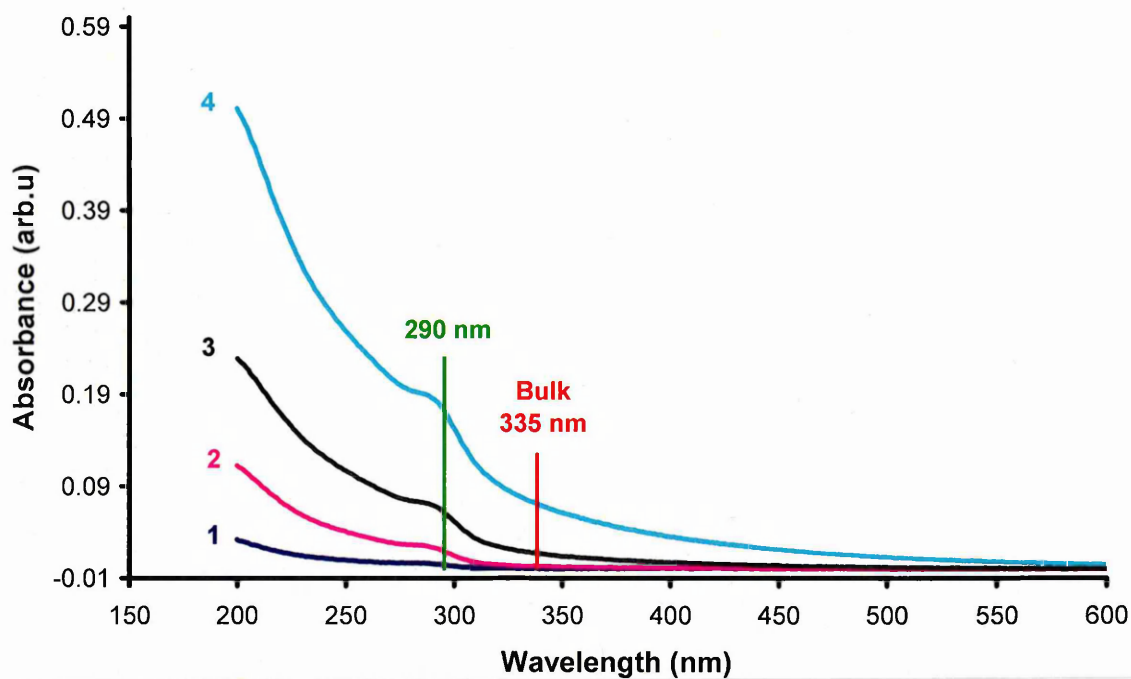


Figure 5.8. UV-vis absorption spectra of PAH/ ZnS-SO₃⁻ film. The numbers near respective spectra correspond to the number of polyelectrolyte/nanoparticle bilayers.

Similar features are observed for ZnS nanoparticles absorption spectra. Figure 5.8 and 5.9 show the absorption spectra of ZnS nanoparticles, both of SO₃⁻ and NH₂⁺ groups respectively, embedded in organic films. The main absorption bands are

recorded at the same wavelength of about 290 nm, both of them are blue shifted from the absorption band of 335 nm for bulk ZnS material. They are also slightly different as compared to their solutions spectra.

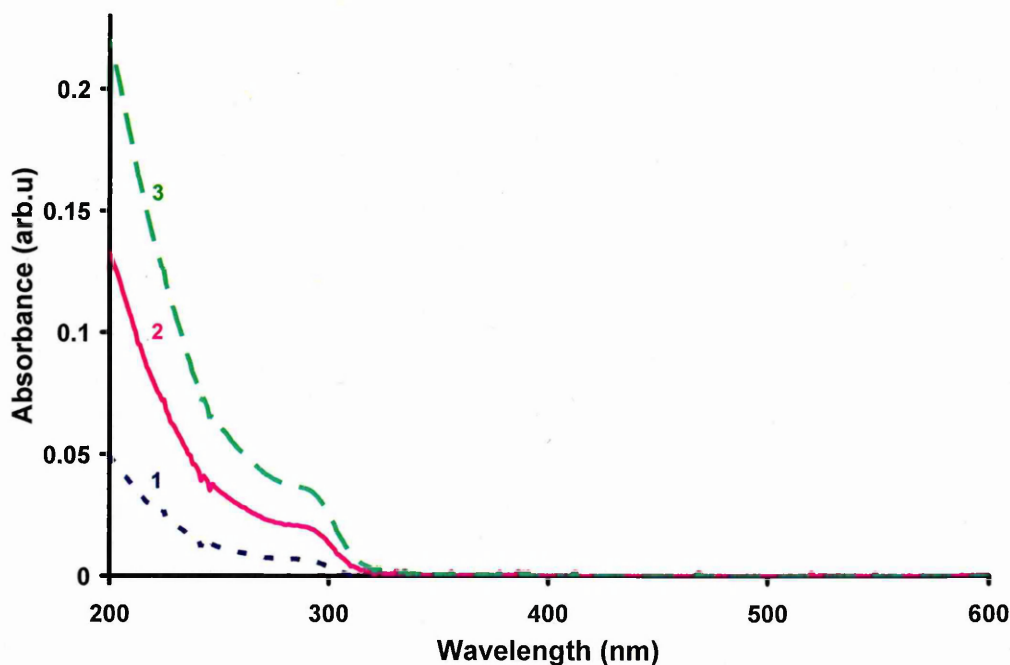
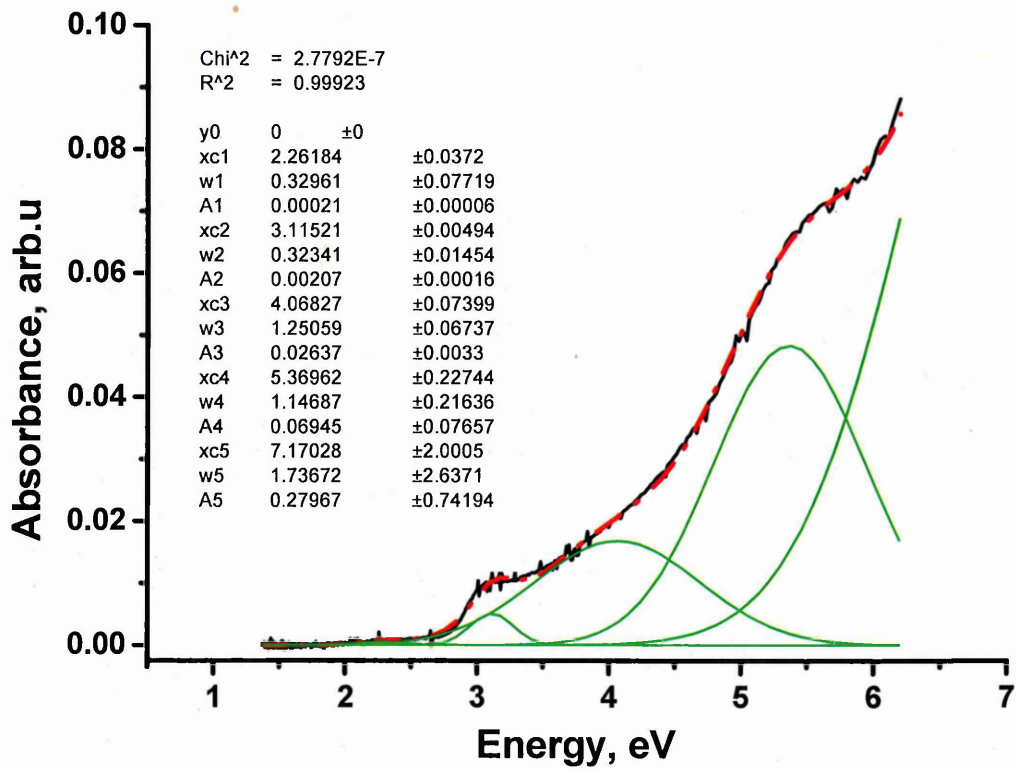


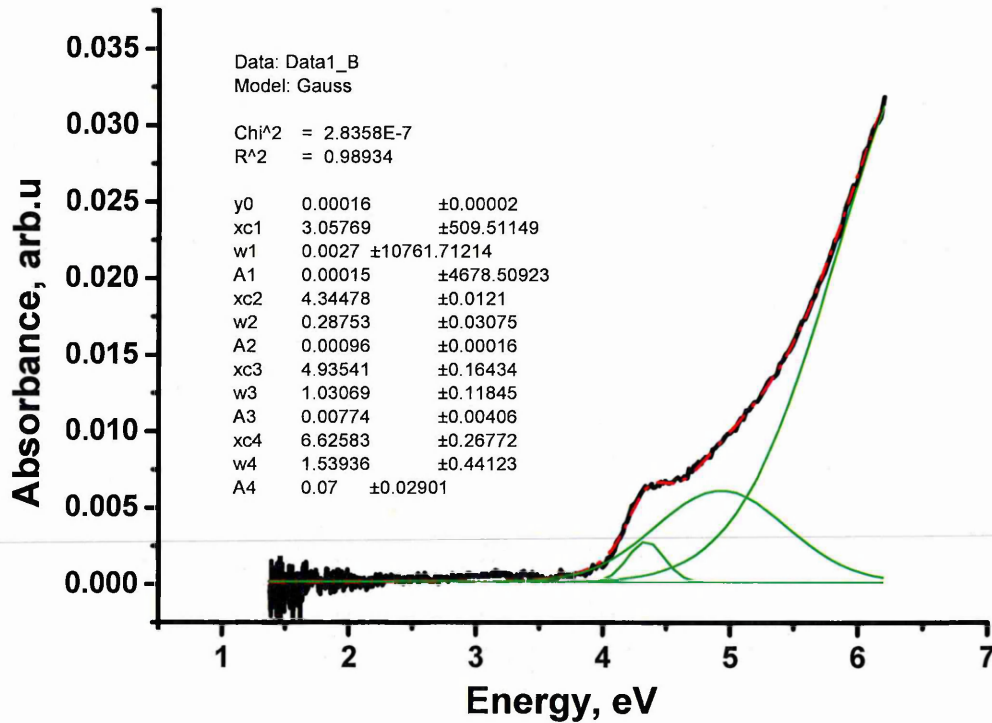
Figure 5.9. UV-vis absorption spectra of PAH/ ZnS-NH₂⁺ films. The numbers near respective spectra correspond to the number of polyelectrolyte/nanoparticle bilayers.

Although the CdS and ZnS nanoparticles were embedded in organic films, the thin films could not be assumed as two-dimensional (2D) system of clusters as in the case of nanoparticles in LB films. In our case, CdS and ZnS nanoparticles have spherical shape and separated individually because of the shell (capping agents). Therefore the Efron approximation in Equation (5.1) is used to calculate the radius of CdS and ZnS nanoparticles embedded in thin films.

The energy gap ($E_{n,l}$) of CdS and ZnS nanoparticles embedded in organic films were found from the Gaussian fitting performed in Figure 5.10 (a) and (b).



(a)



(b)

Figure 5.10. Gaussian fitting of the spectra of the first layer of CdS-SO₃⁻ (a) and the first layer of ZnS-SO₃⁻ (b). The experimental data (black line) was fitted using several Gaussian peaks (green line) and the result was shown by the red line.

Using the data in Table 5.1 and energy gap obtained from the Gaussian fitting, the calculated values of CdS and ZnS particle size are summarized in Table 5.3.

Table 5.3. Energy gap and the particles' size obtained by Gaussian fitting of the absorption spectra of CdS and ZnS films.

	E_1 (eV)	ΔE_1 (eV)	R_1 (nm)	E_2 (eV)	ΔE_2 (eV)	R_2 (nm)
CdS SO_3^-	3.12 ± 0.0048	0.7	1.79 ± 0.01	5.37 ± 0.2274	2.95	1.61 ± 0.12
CdS NH_2^+	3.08 ± 0.0020	0.66	1.85 ± 0.01	5.15 ± 0.3932	2.73	1.67 ± 0.24
ZnS SO_3^-	4.34 ± 0.0121	0.66	1.80 ± 0.03	-	-	-
ZnS NH_2^+	4.38 ± 0.0074	0.7	1.74 ± 0.02	-	-	-

The radius of nanoparticles yield for both CdS and ZnS films were relatively the same, about 1.8 nm. As was suggested earlier, the peak in Figure 5.10 (a) may correspond to the second energy level in the CdS quantum dot. The calculation of second peaks using Equation (5.1) gives the values of the particles' radii of 1.61 and 1.67 nm which is close to the values obtained from the first peaks within the experimental error. This is a good evidence that the second peaks belong to the energy ladder of the size quantisation. ZnS containing films having their spectra shifted further in the UV range do not show the absorption peak corresponding to the second energy level. More accurate determination of the particles' size could be achieved if the contribution of PAH (or PSS) layers to the absorption spectra was taken into account.

The combinations of positively and negatively charged nanoparticles

It has to be noted that the role of polyelectrolyte layers is very important for a successful deposition. The attempts of alternative deposition of layers of anion and cation modified nanoparticles without intermediate polyelectrolyte layers have failed

due to the peeling of the first layer during the attempted deposition of the second layer (as shown in Figure 5.11). This was most likely because of a poor adhesion of the first layer of nanoparticles to the substrate.

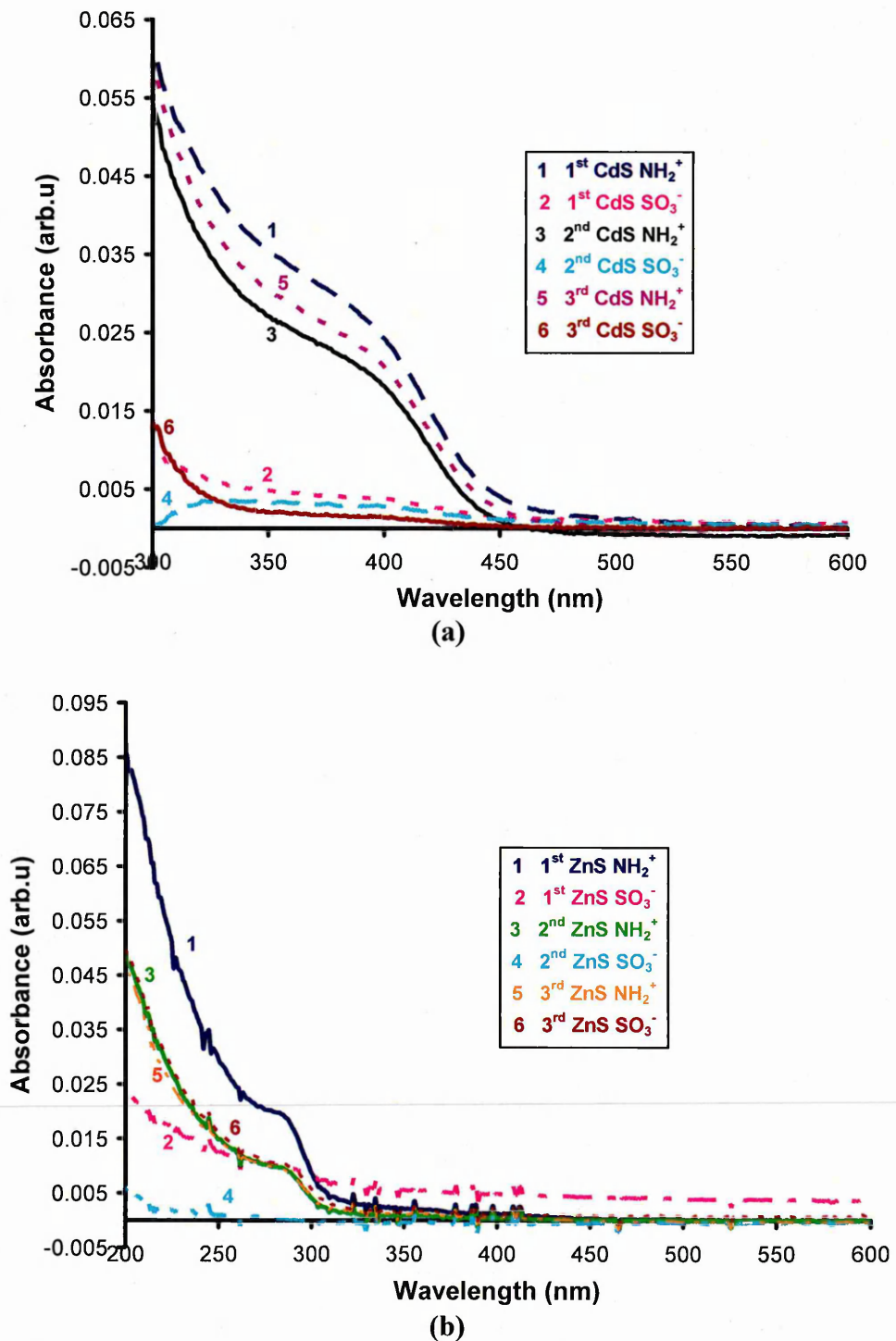


Figure 5.11. Alternative deposition of positively and negatively charged CdS (a) and ZnS (b) nanoparticles without intermediate layers of polyelectrolyte.

Figure 5.11 (a) shows the deposition of positively and negatively charged CdS nanoparticles without polyelectrolyte as an alternate layer. The first layer of CdS NH_2^+ was successfully deposited (dark blue line) on the substrate. The first layer (Pink line), CdS SO_3^- , gave lower absorbance intensity which indicates much thinner film. In other words, the first layer was partially peeled off. When the second layer of CdS NH_2^+ was deposited, the intensity was increased again and reduced as the second layer of CdS SO_3^- was deposited. The same thing happened when the third layers was deposited. A similar phenomenon is observed for the deposition of ZnS nanoparticles (see Figure 5.11 (b)).

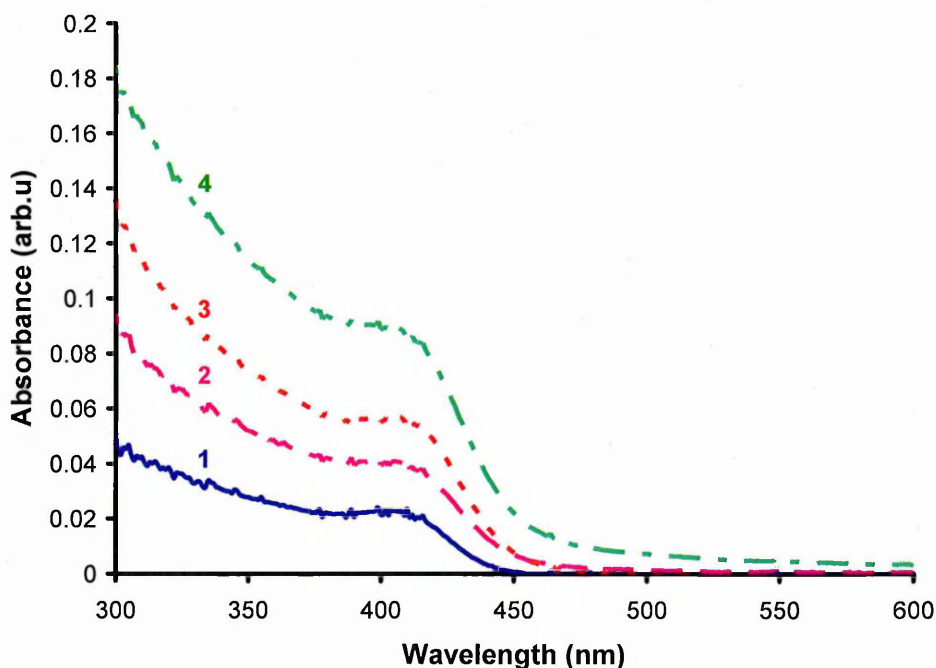


Figure 5.12. Absorption spectra of polyelectrolyte/CdS nanoparticles structures.

- 1 PAH/CdS SO_3^-
- 2 PAH/CdS SO_3^- /PAH/PSS/CdS NH_2^+
- 3 PAH/CdS SO_3^- /PAH/PSS/CdS NH_2^+ /PSS/PAH/CdS SO_3^-
- 4 PAH/CdS SO_3^- /PAH/PSS/CdS NH_2^+ /PSS/PAH/CdS SO_3^- /PAH/PSS/CdS NH_2^+

In contrast to that if the intermediate polyelectrolyte layers were used, the deposition of alternatively charged nanoparticles was successful as shown in Figure 5.12 to Figure 5.17. Figure 5.12 shows the absorption spectra of CdS with P-S-P-P-N structures, where *P* is polyions (PAH or PSS), *S* is negatively charged nanoparticles

(SO_3^- group), and N is positively charged nanoparticles (NH_2^+ group). As can be seen, the films were well deposited layer by layer. The first layer was PAH and then CdS SO_3^- was deposited followed by PAH and PSS layers before CdS NH_2^+ deposition. The third nanoparticles layer, CdS SO_3^- was deposited after PAH and PSS layers and the fourth was CdS NH_2^+ again. This demonstrates the successful deposition of positively and negatively charged CdS colloid nanoparticles in the same films.

Figure 5.13 shows the same sequence for first and second layer as in Figure 5.12 but the third nanoparticles layer was CdS NH_2^+ and the fourth layer was CdS SO_3^- . Despite some inconsistency, the absorption intensity is proportional to the number of layers which also reflects the successful deposition of positively and negatively charged CdS colloid nanoparticles in the same films.

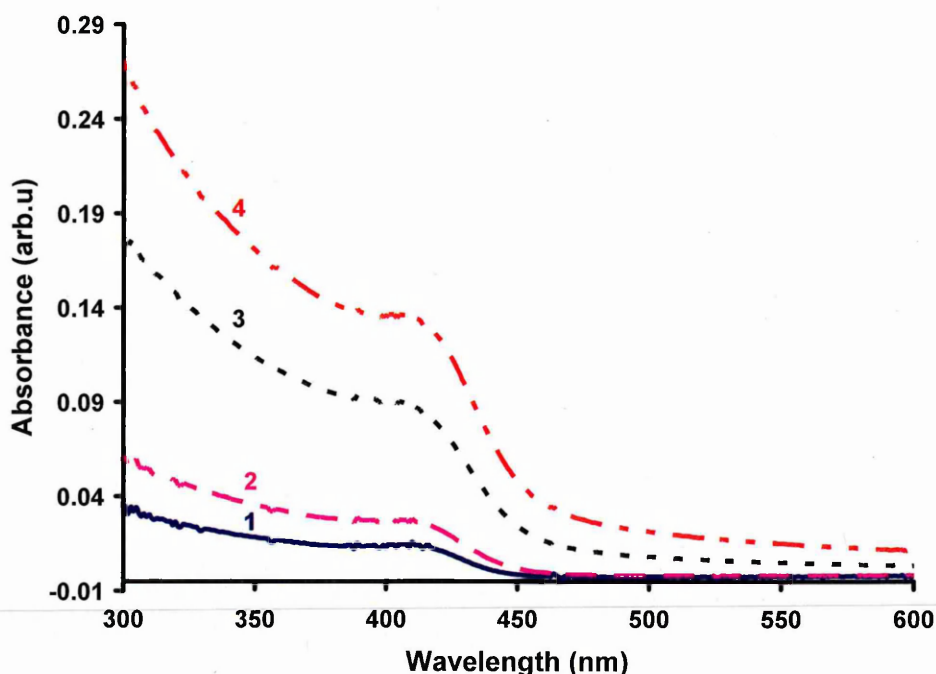


Figure 5.13. Absorption spectra of polyelectrolyte/ CdS nanoparticles structures.

- 1 PAH/ CdS SO_3^-
- 2 PAH/ CdS SO_3^- /PAH/PSS/ CdS NH_2^+
- 3 PAH/ CdS SO_3^- /PAH/PSS/ CdS NH_2^+ /PSS/ CdS NH_2^+
- 4 PAH/ CdS SO_3^- /PAH/PSS/ CdS NH_2^+ /PSS/ CdS NH_2^+ /PSS/PAH/ CdS SO_3^-

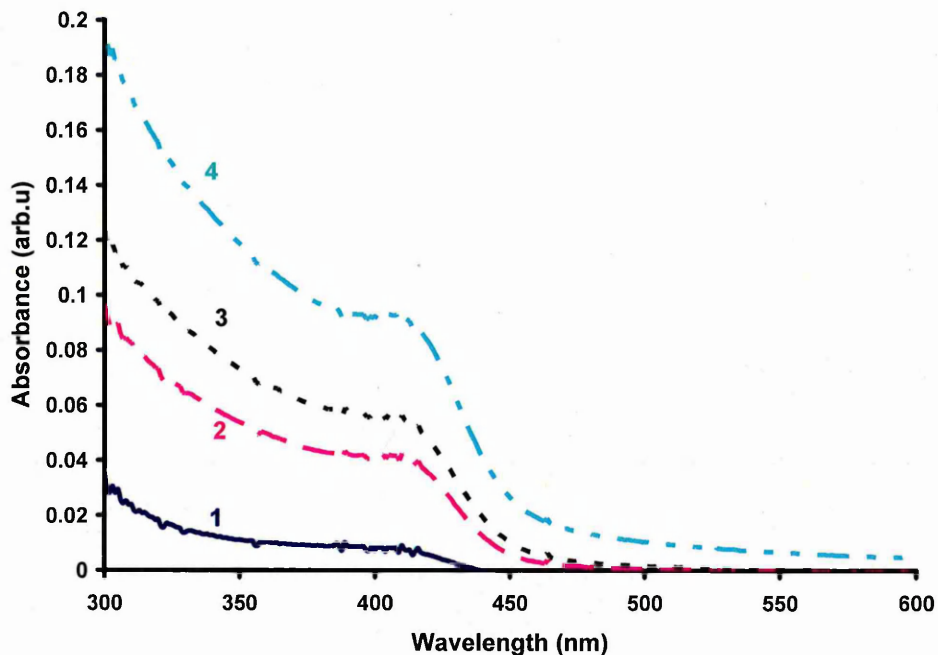


Figure 5.14. Absorption spectra of polyelectrolyte/CdS nanoparticles structures.

- 1 PAH/PSS/CdS NH_2^+
- 2 PAH/PSS/CdS NH_2^+ / PSS/PAH/CdS SO_3^-
- 3 PAH/PSS/CdS NH_2^+ / PSS/PAH/CdS SO_3^- /PAH/PSS/CdS NH_2^+
- 4 PAH/PSS/CdS NH_2^+ / PSS/PAH/CdS SO_3^- / PAH/PSS/CdS NH_2^+ / PSS/PAH/CdS SO_3^-

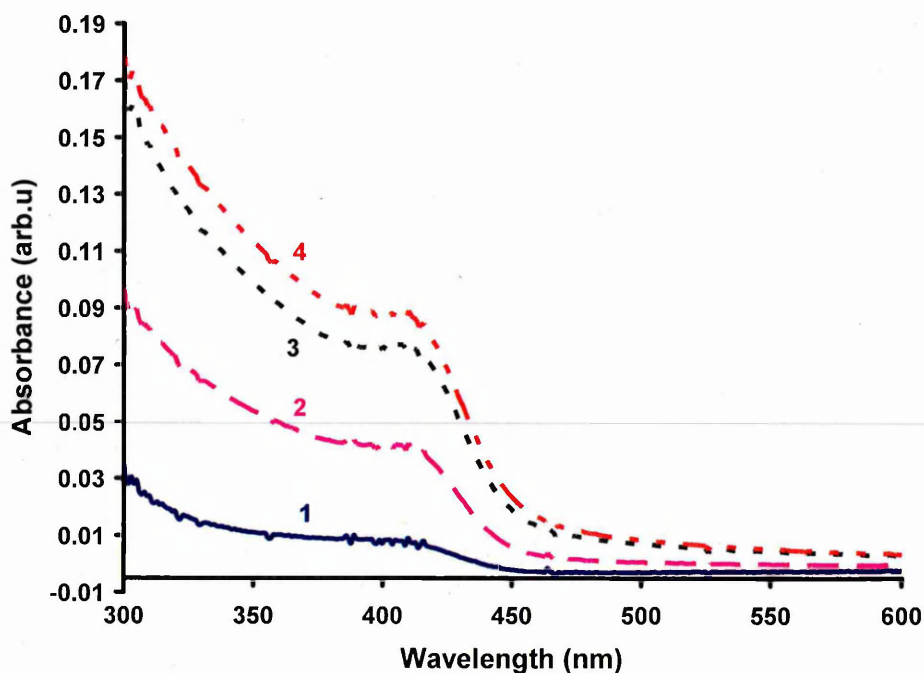


Figure 5.15. Absorption spectra of polyelectrolyte/CdS nanoparticles structures.

- 1 PAH/PSS/CdS NH_2^+
- 2 PAH/PSS/CdS NH_2^+ / PSS/PAH/CdS SO_3^-
- 3 PAH/PSS/CdS NH_2^+ / PSS/PAH/CdS SO_3^- /PAH/CdS SO_3^-
- 4 PAH/PSS/CdS NH_2^+ / PSS/PAH/CdS SO_3^- /PAH/CdS SO_3^- /PAH/PSS/CdS NH_2^+

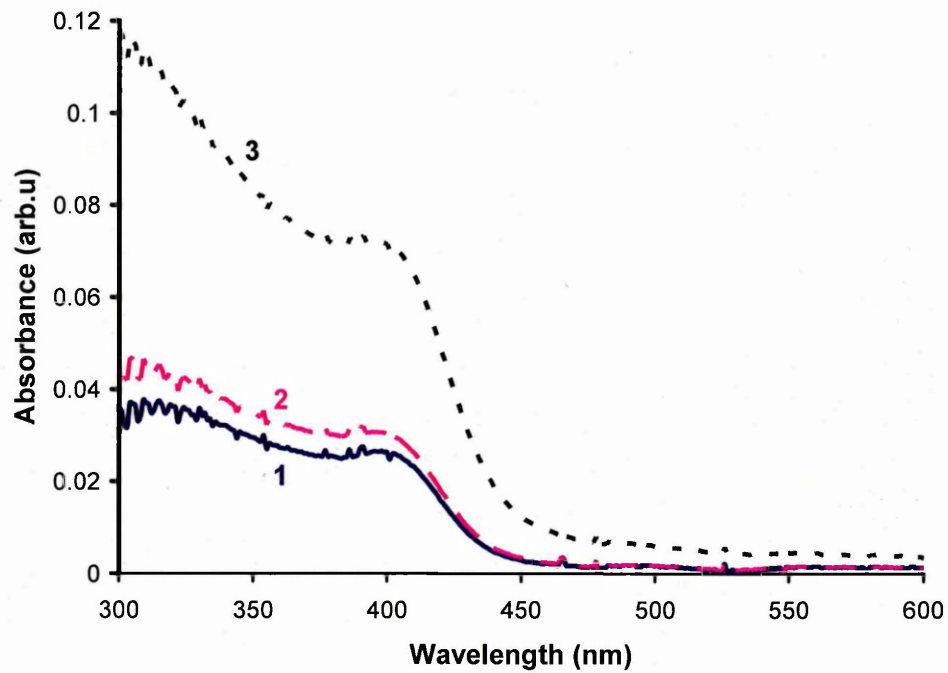


Figure 5.16. Absorption spectra of polyelectrolyte/CdS nanoparticles structures.

- 1 PAH/CdS SO_3^-
- 2 PAH/CdS SO_3^- /CdS NH_2^+
- 3 PAH/CdS SO_3^- /CdS NH_2^+ /PAH/CdS SO_3^- /CdS NH_2^+

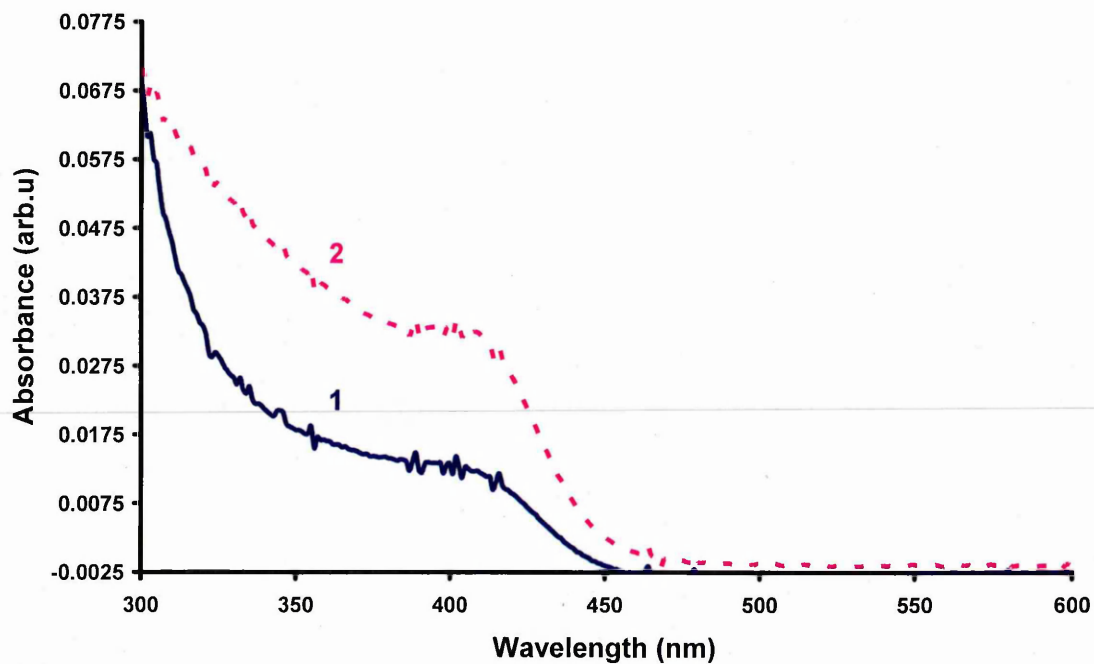


Figure 5.17. Absorption spectra of polyelectrolyte/CdS nanoparticles structures.

- 1 PAH/PSS/CdS NH_2^+
- 2 PAH/PSS/CdS NH_2^+ /CdS SO_3^-

A different deposition sequence, started with positively charged CdS NH_2^+ which was deposited after PAH and PSS, followed by the deposition of PAH and CdS SO_3^- , shown in Figure 5.14 and 5.15, proved to be successful as well.

The attempt to directly deposit positively and negatively charged nanoparticles were also successful (as shown in Figure 5.16 and 5.17) if using polyions between the nanoparticles bilayers. Figure 5.16 shows the deposition of positively charged nanoparticles directly after negatively charged nanoparticles without an alternating layer of polyelectrolytes. The deposition of positively charged nanoparticles followed by negatively charged nanoparticles without an alternating layer of polyelectrolytes is shown in Figure 5.17. Both results show the increase in absorption intensity which reflects the increase in films thicknesses although some inconsistency was observed in Figure 5.16.

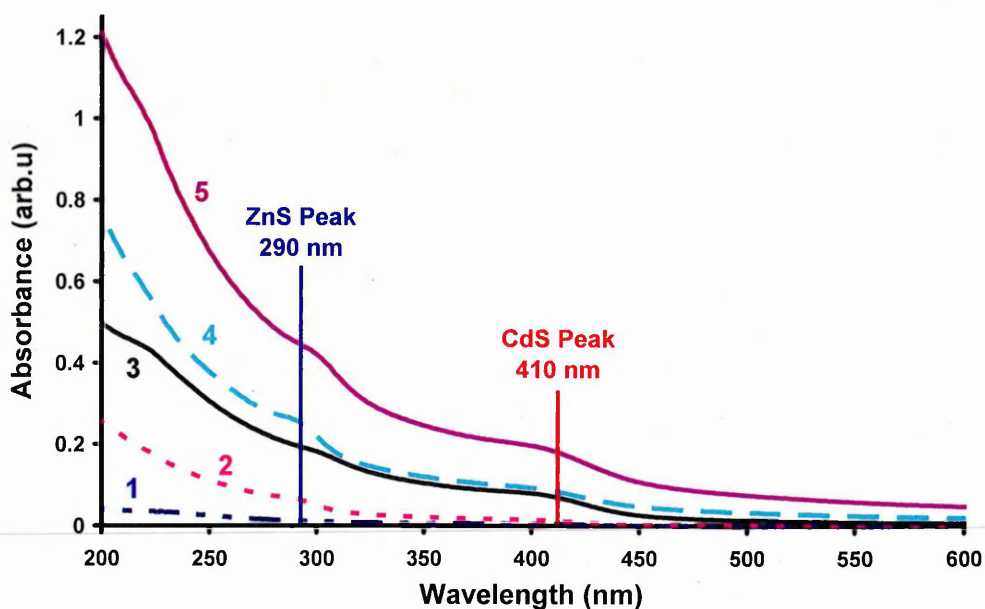


Figure 5.18. Absorption spectra of mixed CdS and ZnS structures.

- 1 PAH/CdS SO_3^-
- 2 PAH/CdS SO_3^- /PAH/ZnS SO_3^-
- 3 PAH/CdS SO_3^- /PAH/ZnS SO_3^- /PAH/CdS SO_3^-
- 4 PAH/CdS SO_3^- /PAH/ZnS SO_3^- /PAH/CdS SO_3^- /PAH/ZnS SO_3^-
- 5 PAH/CdS SO_3^- /PAH/ZnS SO_3^- /PAH/CdS SO_3^- /PAH/ZnS SO_3^- /PAH/CdS SO_3^-

The alternated CdS and ZnS sandwich structure, (PAH/CdS/PAH/ZnS)_N, was also successfully deposited, as illustrated by the absorption spectra in Figure 5.18. The first layers of CdS SO₃⁻ was deposited after PAH layer followed by another PAH and then ZnS SO₃⁻ layer. The absorption spectra clearly show two peaks, one at 290 nm corresponding to ZnS, and the other at 410 nm corresponding to CdS nanoparticles.

5.2.2. Ellipsometry measurements

The optical properties of polyelectrolyte/nanoparticles films were studied with spectroscopic ellipsometry. Two different configurations of ellipsometry measurements were used: (i) traditional external reflection ellipsometry and (ii) rather novel method of total internal reflection ellipsometry (TIRE).

5.2.2.1. External reflection ellipsometry

The external reflection ellipsometry measurements carried out on a bare silicon show typical ellipsometric spectra of $\psi(\lambda)$ and $\Delta(\lambda)$ (see in Figure 5.19).

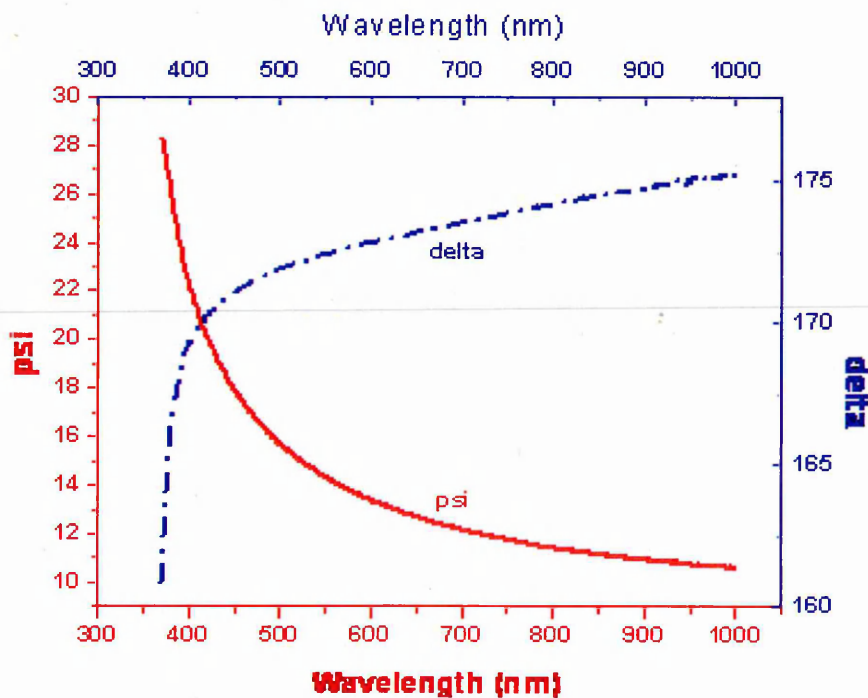
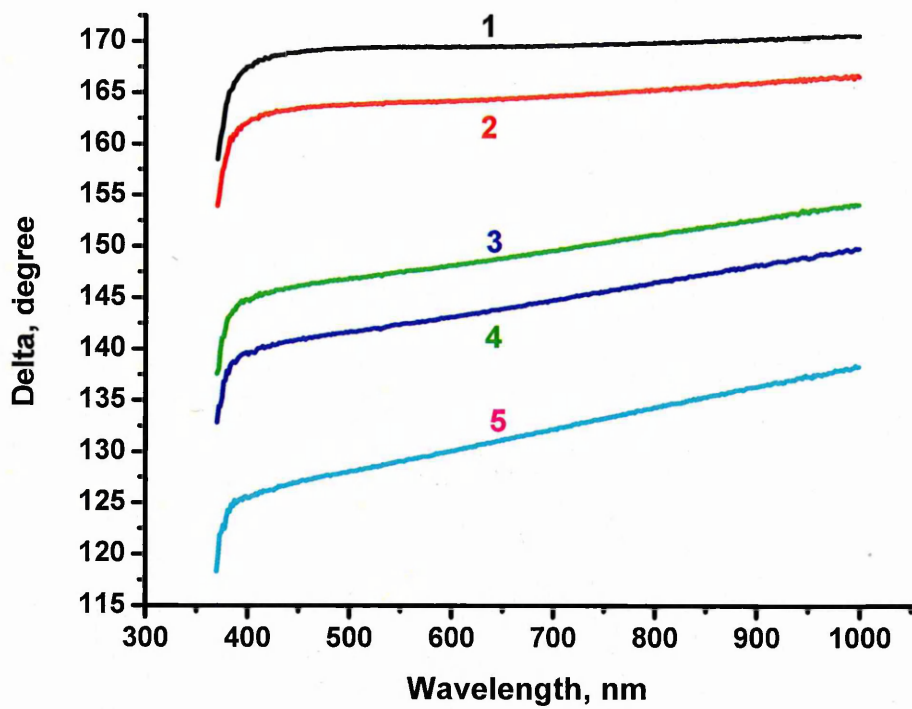
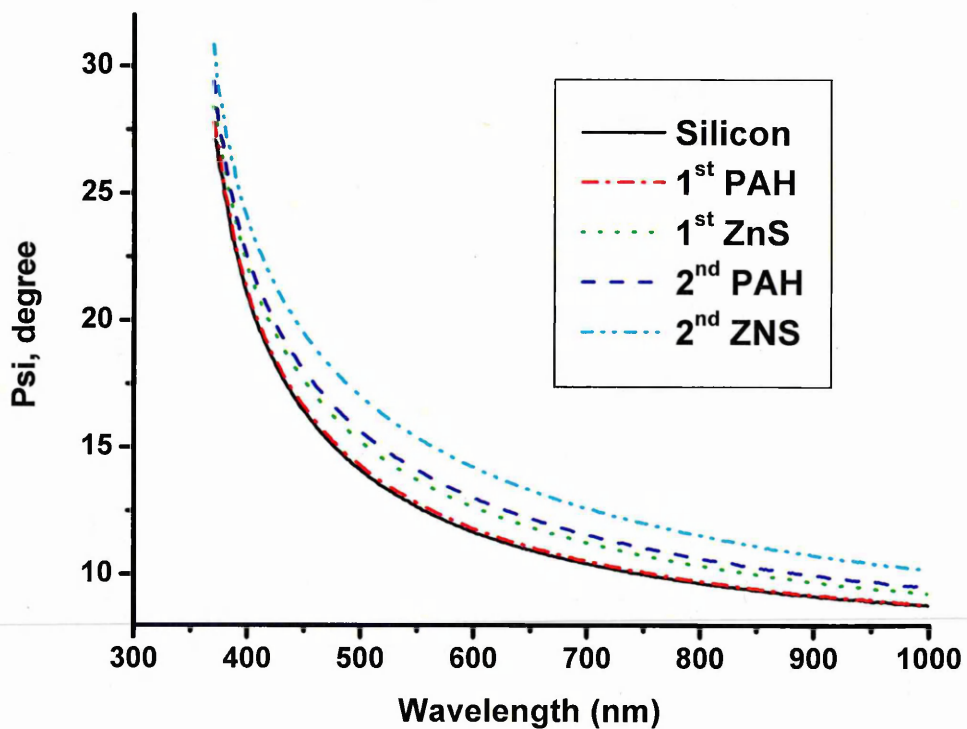


Figure 5.19. Typical $\psi(\lambda)$ and $\Delta(\lambda)$ ellipsometric spectra of a silicon substrate.



(a)



(b)

Figure 5.20. Typical $\Delta(\lambda)$ (a) and $\Psi(\lambda)$ (b) ellipsometric spectra of a silicon substrate (1), and consecutively deposited layers on top: 1st layer of PAH (2), 1st layer of ZnS nanoparticles (3), 2nd layer of PAH (4), 2nd layer of ZnS nanoparticles (5).

The measurements of the same silicon substrate coated with thin films of polyelectrolytes and nanoparticles confirmed the consistent film growth as shown in Figure 5.20. The series of $\Delta(\lambda)$ spectra show their consecutive shift downwards after each layer being deposited, which corresponds to the increase in the film thickness. The deposition of polyelectrolyte causes a small shift (curves 1 and 2; 3 and 4) while larger shift is caused by nanoparticles deposition (curves 2 and 3; 4 and 5). This indicates that nanoparticles layers are much thicker than polyelectrolyte layers. The series of $\psi(\lambda)$ spectra show much smaller shift in the opposite direction (upwards) after each deposition as compared to $\Delta(\lambda)$ spectra, which corresponds mostly to the increase of the film's refractive index. The larger shifts are caused by nanoparticles deposition which have a significant refractive index difference as compared to the polyelectrolyte.

Fitting of the experimental $\psi(\lambda)$ and $\Delta(\lambda)$ ellipsometric spectra using WVASE@ J.A. Woollam software allowed the extraction of optical parameters, such as the thickness (d), refractive index (n), and extinction coefficient (k) of all consecutively deposited layers. A multilayer model used for ellipsometry fitting, shown in Figure 5.21, consists of Si substrate, SiO₂ layer representing a very thin (2-3 nm) film of native oxide, polyelectrolyte films of either PAH or PSS represented by the Cauchy model, and the layers of either CdS or ZnS nanoparticles.

Medium (air)	
3 CdS or ZnS (n_2, k_2)	Thickness 3
2 Cauchy (n_1)	Thickness 2
1 SiO ₂	Thickness 1
0 Si (substrate)	1 mm

Figure 5.21. Ellipsometry fitting model for silicon/polyelectrolytes/CdS (or ZnS).

The parameters of all layers were obtained by fitting the spectra for consecutively deposited layers and fixing the previously obtained parameters for the layers below. Firstly, the substrate was silicon with fixed thickness of 1 mm. Then the model layer of SiO₂ was added and the thickness was fitted. When the thickness was obtained, the parameters were fixed and the next layer of cauchy was added. Cauchy model is deployed for the fitting of the adsorbed organic and bio-material layers, in this case polyelectrolyte (PAH or PSS). The dispersion function is described by the following equation [6]:

$$n = A + B/\lambda^2 + C/\lambda^4 \quad (5.2)$$

$$k(\lambda) = \alpha e^{\beta(12400(\frac{1}{\lambda} - \frac{1}{\gamma}))}$$

where A , B , C are constants, λ is the wavelength, α is the extinction coefficient, β is the exponential factor, and γ is the band edge. Each of these parameters except for the band edge can be defined as fit parameter in the cauchy dialog box. The values $A_n = 1.415$, $B_n = 0.01$ and $C_n = 0$ were fixed during the fitting. This gives the value of the refractive index of 1.445 at $\lambda = 633$ nm, which is typical for polyelectrolytes. For the layers of CdS (or ZnS) nanoparticles the model files of respective bulk materials were used, and all three parameters d , n , and k were varied during fitting. The default medium (air) was used everywhere.

The results of fitting are summarized in Tables 5.4 and 5.5, and the file names of models chosen from the WVASE32® library are shown near respective layers. Although the whole spectra of n and k were obtained, only the values at 633 nm are shown.

Table 5.4. Ellipsometry data fitting for PAH/CdS-SO₃⁻ films

Model Layer	<i>d</i> (nm)	<i>n</i> (at 633 nm)	<i>k</i> (at 633 nm)
Si (<i>Si_gel.mat</i>)		3.867	0.02
SiO ₂ (<i>SiO2.mat</i>)	5.99 ± 0.03	1.46	0
PAH (<i>CAUCHY.mat</i>)	1.94 ± 0.03	1.49	0
1 st CdS (<i>CDSO.mat</i>)	4.94 ± 0.04	2.28	0.74
PAH (<i>CAUCHY.mat</i>)	2.12 ± 0.02	1.54	0
2 nd CdS (<i>CDSO.mat</i>)	12.84 ± 0.02	1.82	0.74

Table 5.5. Ellipsometry data fitting for PAH/ZnS-SO₃⁻ films

Model Layer	<i>d</i> (nm)	<i>n</i> (at 633 nm)	<i>k</i> (at 633 nm)
Si (<i>Si_gel.mat</i>)		3.867	0.02
SiO ₂ (<i>SiO2.mat</i>)	3.53 ± 0.05	1.46	0
PAH (<i>CAUCHY.mat</i>)	1.96 ± 0.06	1.49	0
1 st ZnS (<i>ZNS.mat</i>)	5.24 ± 0.03	2.29	0.78
PAH (<i>CAUCHY.mat</i>)	2.24 ± 0.01	1.49	0
2 nd ZnS (<i>ZNS.mat</i>)	5.53 ± 0.06	2.29	0.78

The obtained thicknesses of nanoparticle layers of around 5 nm for both CdS and ZnS were yielded from the fitting. These values correspond well to the size of particles evaluated from UV-vis spectral data if an additional thickness of the organic shell is taken into account. The obtained larger thickness of the 2nd layer of CdS nanoparticles (in Table 5.4) is most likely due to the aggregation of nanoparticles.

The obtained values of *n* for both CdS and ZnS were a little bit smaller than respective values of bulk materials (2.475 for CdS and 2.364 for ZnS) possibly due to the contribution of the organic shell. These could be seen in Figure 5.22 which presented the whole spectra of *n* and *k* curves for both CdS and ZnS nanoparticles. As

compared to the reference materials (provided in the software), the dispersion curve for the refractive index of CdS obtained from the fitting has relatively the same shape but shifted downward which caused smaller n values for the whole spectra. The obtained $k(\lambda)$ spectra of both CdS and ZnS films resemble the respective absorption spectra with the characteristic blue shift to the main absorption band as compared to the bulk materials. The whole $k(\lambda)$ spectra were shifted upwards and thus gives larger k values' for nanoparticles as compared to bulk materials.

The values of k at 633 nm obtained from the experimental data fitting (see Table 5.4 and 5.5) are much higher than the respective values for bulk materials (0.0186 for CdS and 0.0077 for ZnS). This may be attributed to the substantial increase in the oscillator strength due to the effect of quantum confinement [5]. The obtained values of refractive index for polyelectrolyte layers of 1.49 - 1.54 are quite typical for PAH and PSS films, while the thickness of around 2 nm is slightly larger than reported previously [2], which may be caused by inhomogeneous coating.

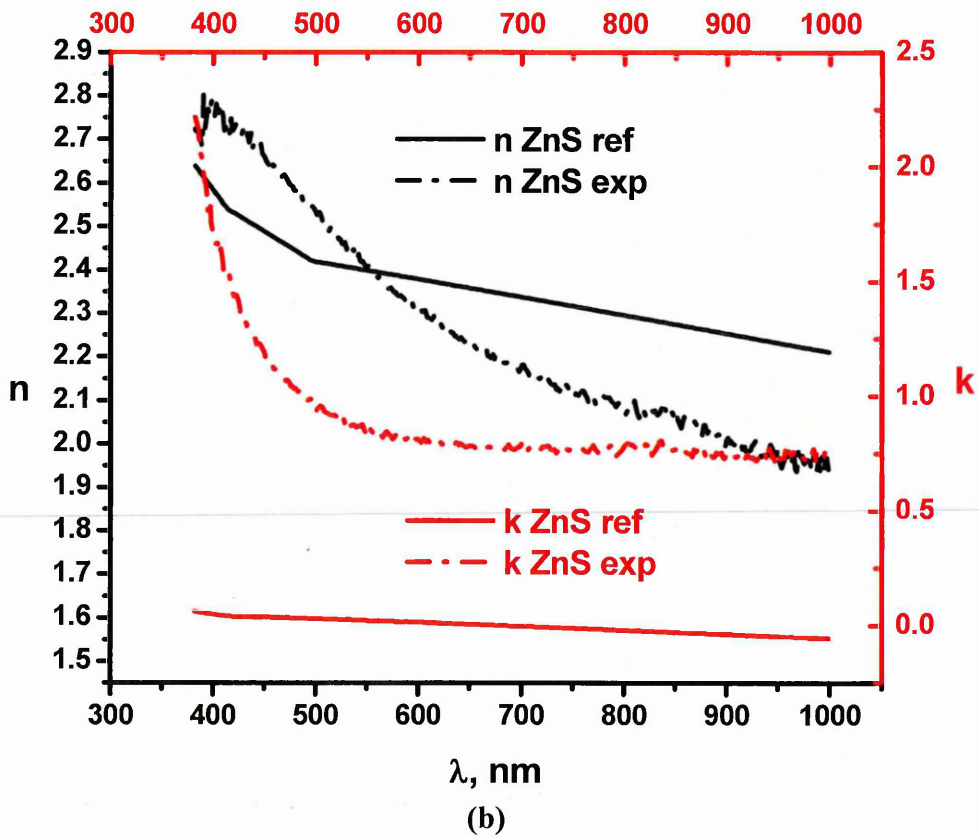
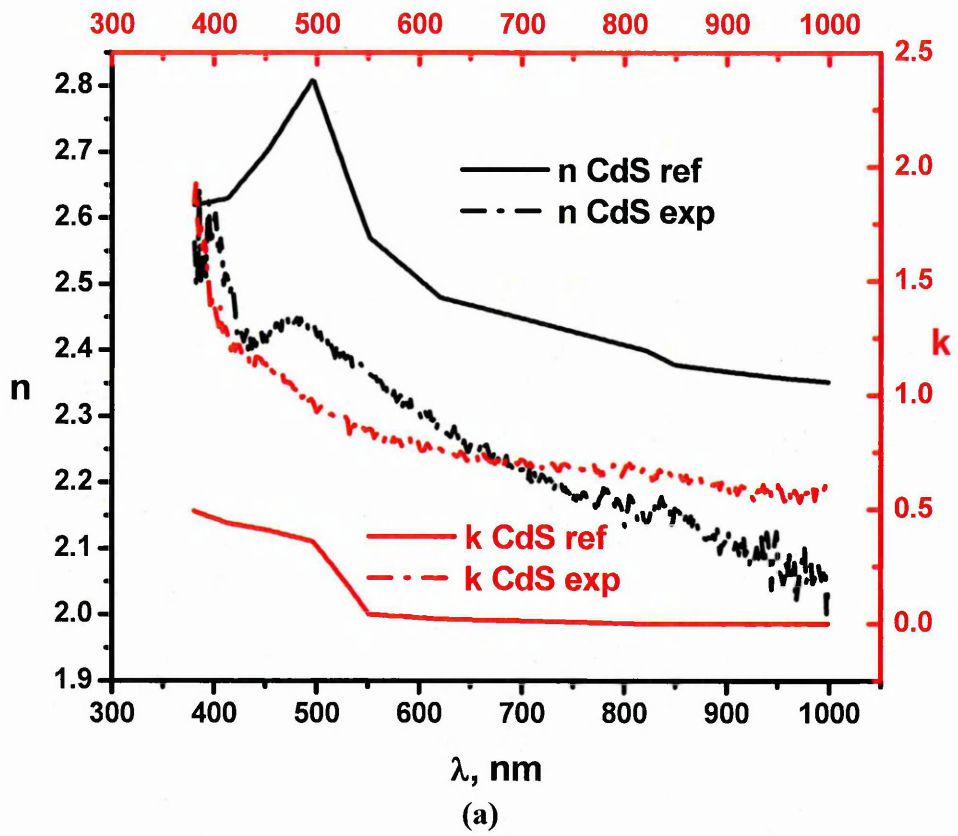


Figure 5.22. n and k curves obtained from the fitting for CdS (a) and ZnS (b).

5.2.2.2. Total internal reflection ellipsometry

Typical TIRE spectra of $\psi(\lambda)$ and $\Delta(\lambda)$ are shown in Figure 5.23. The $\psi(\lambda)$ spectrum resembles SPR curves, which is quite obvious, since both dependencies $\psi(\lambda)$ (in TIRE) and $R(\theta)$ (in SPR) represents the R_p Fresnel's amplitude. At the same time, the $\Delta(\lambda)$ spectra in the TIRE method represent the phase shift between p - and s -components, which is a new quantity that does not exist in the SPR method. The phase changes sharply from 270° down to 90° near the plasmon resonance, which makes $\Delta(\lambda)$ spectrum extremely sensitive to any small changes in the optical parameters of the reflection system.

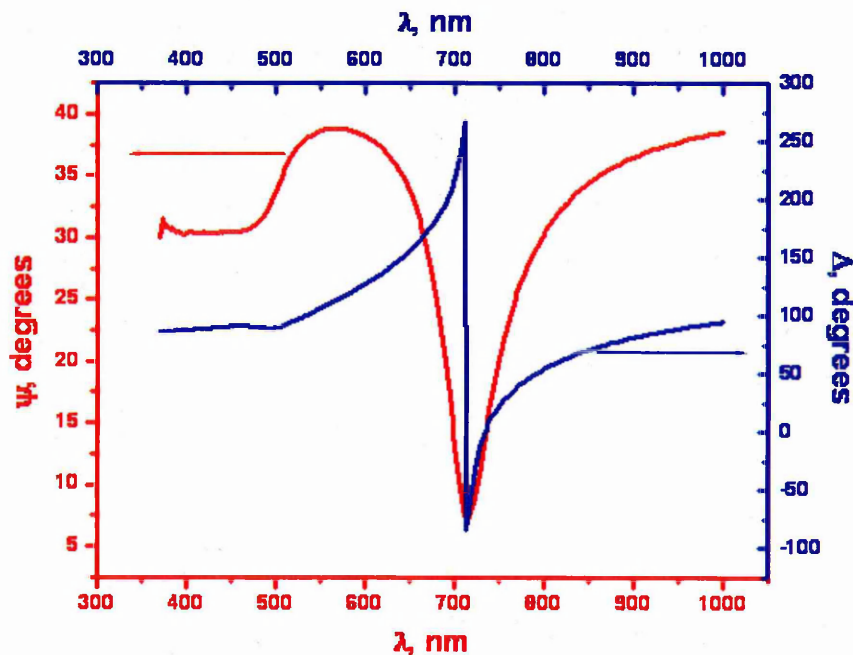


Figure 5.23. Typical $\psi(\lambda)$ and $\Delta(\lambda)$ TIRE spectra of a chromium/gold coated glass substrate.

In TIRE experiments, the ellipsometric angles $\psi(\lambda)$ and $\Delta(\lambda)$ were recorded dynamically for a certain period of time (15–40 min). The time dependences of either $\psi(\lambda)$ and $\Delta(\lambda)$ were obtained at the wavelength of 721.47 nm (see Figure 5.23) which was

chosen near the vertical drop in the $\Delta(\lambda)$ spectra. Typical $\Delta(t)$ and $\psi(t)$ dependencies at 721.47 nm for the first and second PAH layers are shown in Figure 5.24 (a) and (b).

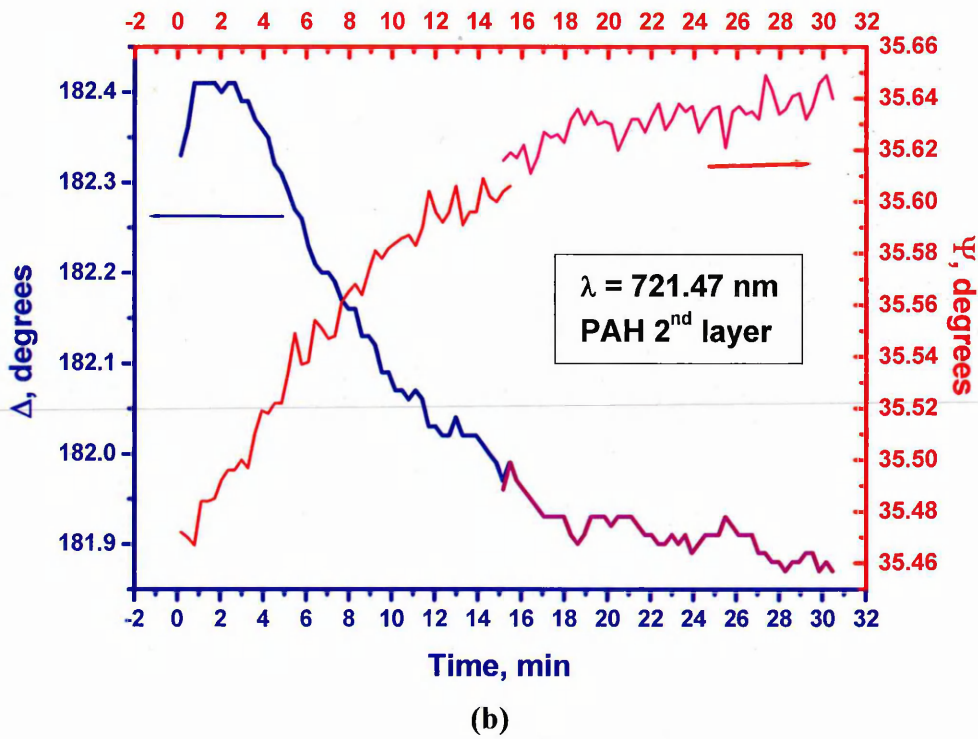
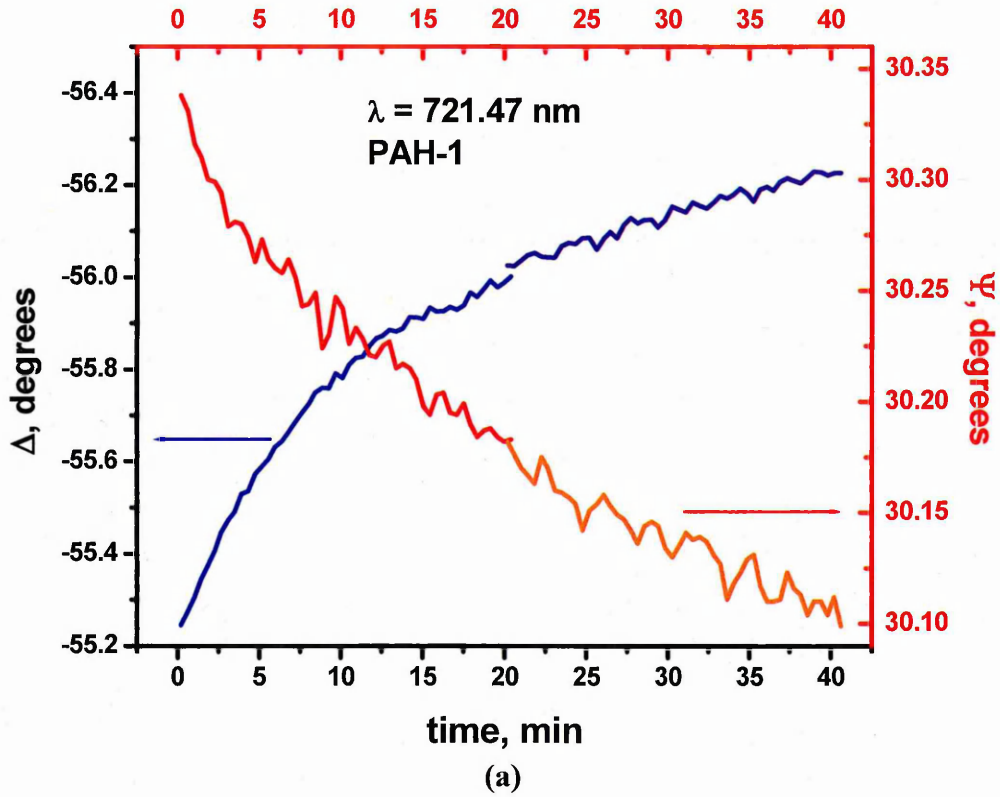
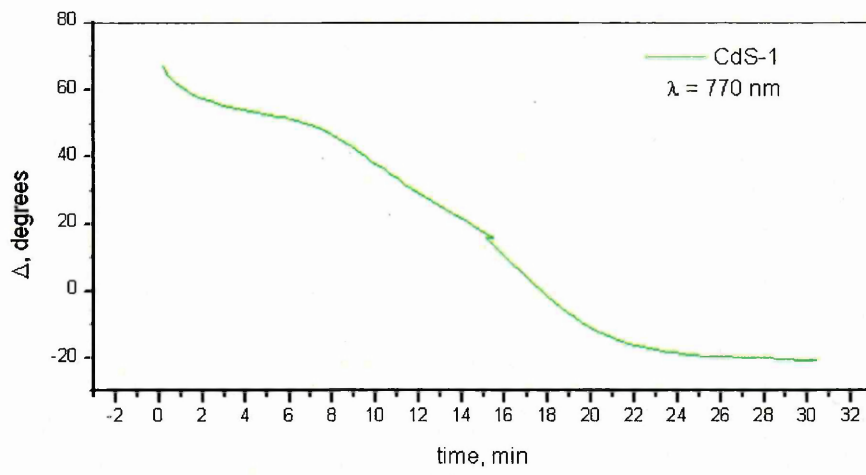


Figure 5.24. $\Delta(t)$ and $\psi(t)$ dependencies at 721.47 nm for the deposition of the 1st PAH layer (a) and the 2nd PAH layer (b).

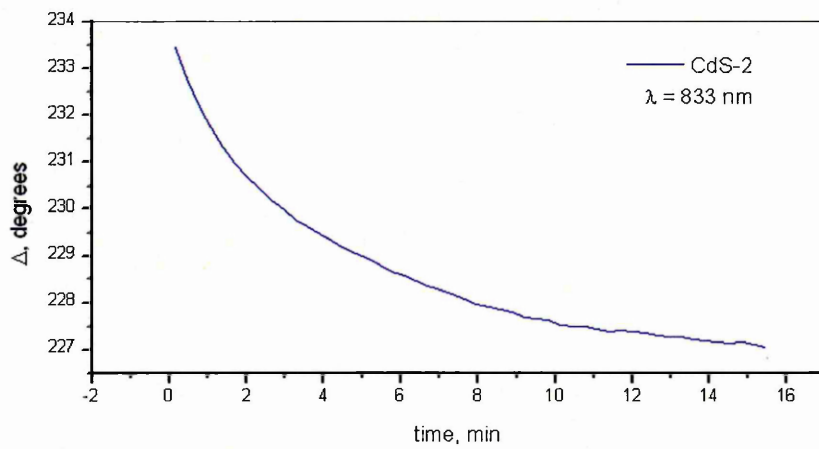
For the first PAH layer, $\Delta(\lambda)$ shows a quick increase during the first 10 minutes and then almost saturated after 35 minutes, as shown in Figure 5.24 (a). The saturation of the second PAH layer is reached much faster, in 24 minutes. This means that the adsorption of the second layer is much faster than the first layer. As a conclusion, a longer time is recommended for the deposition of the first few layers.

The dynamic scan during CdS nanoparticles deposition shows quite complex adsorption kinetics. For the first layer of CdS nanoparticles, there was a trend of saturation at about 4-5 minutes followed by a further decrease and the final saturation after 28 minutes (see Figure 5.25 (a)). This could be explained by a combination of the initial 2D adsorption of CdS nanoparticles on the PAH layer followed by the formation of 3D aggregates of CdS nanoparticles intercalated with PAH. In contrast, the adsorption of the second and third layers of CdS is more straightforward (see Figure 5.25 (b) and (c)), since it is most likely to occur in 3D PAH intercalated structures. The saturation was reached much faster, in 15 and 12 minutes, respectively.

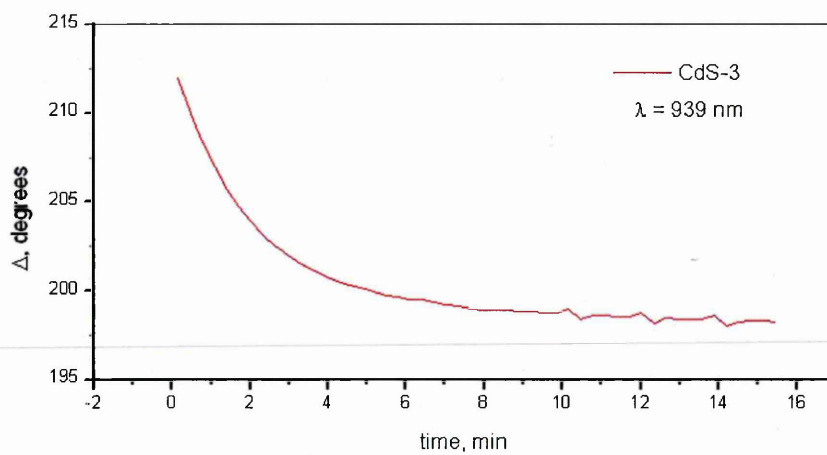
The same condition was observed during the deposition of ZnS nanoparticles as shown in Figure 5.26. For the first layer of ZnS nanoparticles, after initial decrease in Δ , the second stage of adsorption was observed at about 10-15 minutes; the final saturation was reached after about 30 minutes. The saturation of the second and the third layers of ZnS were reached much faster, in 15 and 14 minutes, respectively.



(a)



(b)



(c)

Figure 5.25. $\Delta(t)$ dependencies at selected wavelengths (shown near respective curves) for 1st CdS layer (a) 2nd CdS (b) 3rd CdS (c).

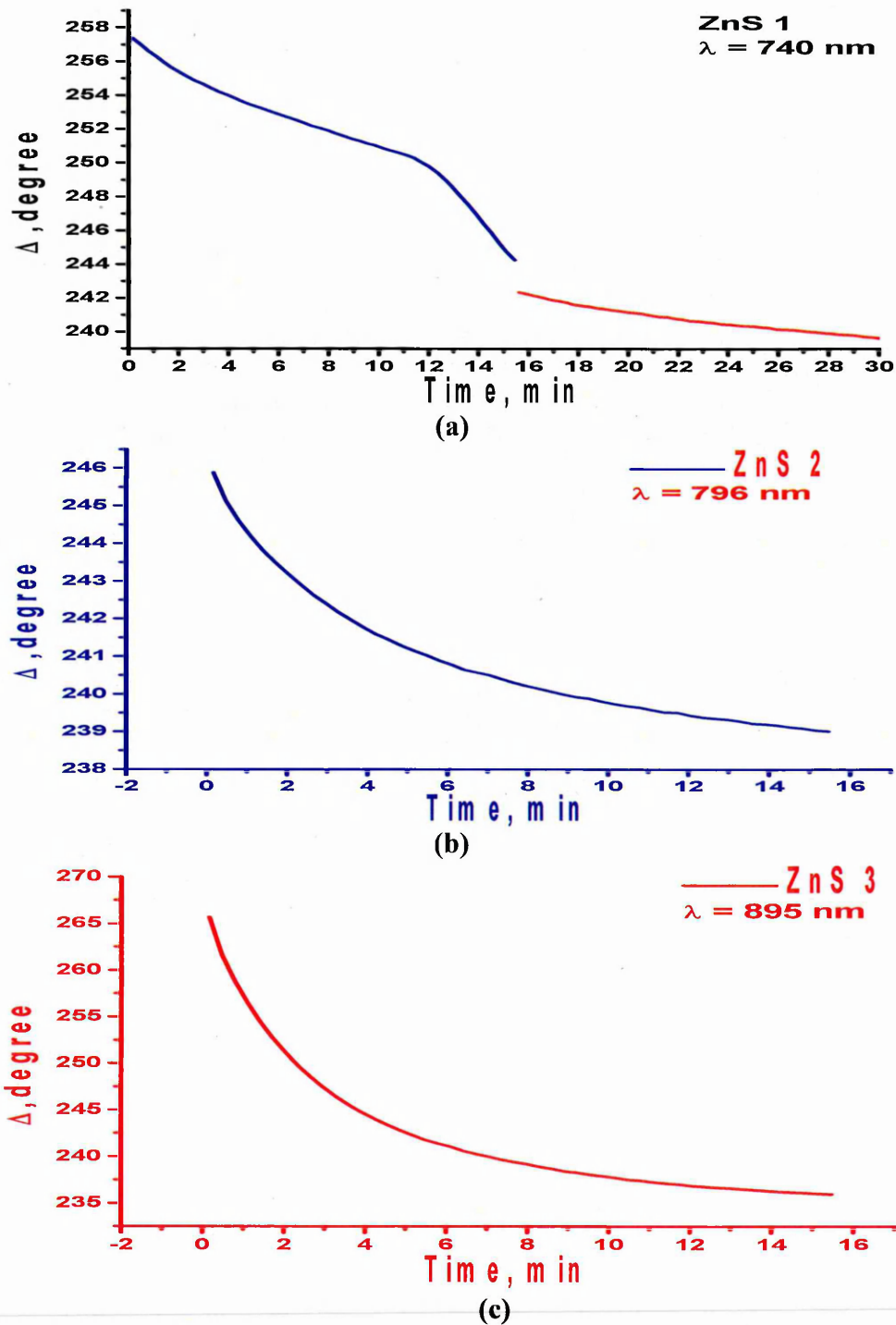


Figure 5.26. $\Delta(t)$ dependencies at selected wavelengths (shown near respective curves) for 1st ZnS layer (a) 2nd ZnS (b) 3rd ZnS (c).

Typical set of TIRE $\Psi(\lambda)$ and $\Delta(\lambda)$ spectra of consecutive adsorption of PAH and CdS (or ZnS) nanoparticles is shown in Figure 5.27 and 5.28. All stages of adsorption can be clearly seen, with the spectral shift corresponding to the thickness of

adsorbed material. Adsorption of CdS and ZnS nanoparticles which have the largest shift of $\Psi(\lambda)$ and $\Delta(\lambda)$ spectra means the layer of CdS and ZnS were much thicker than the polyelectrolyte layer.

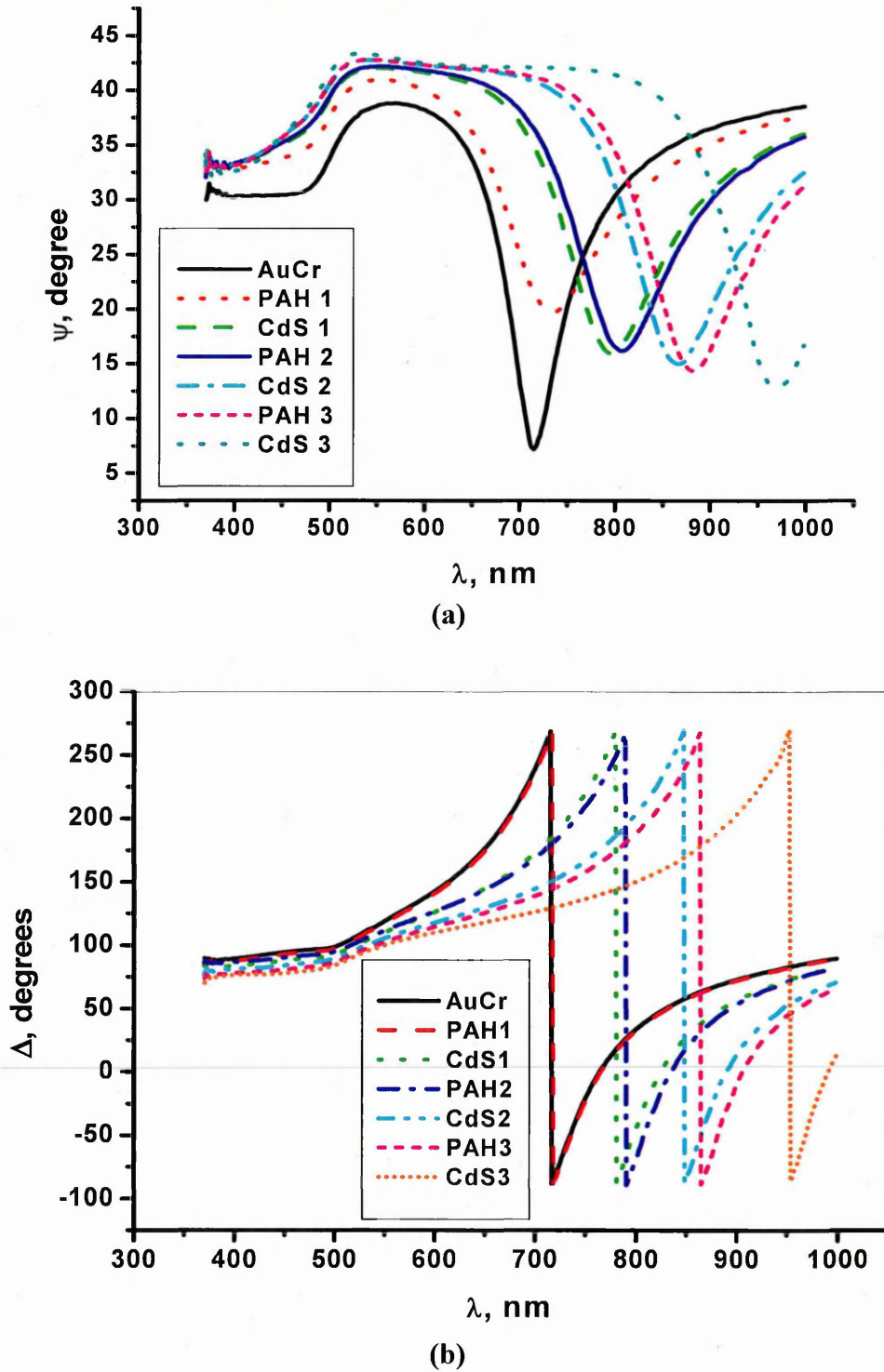
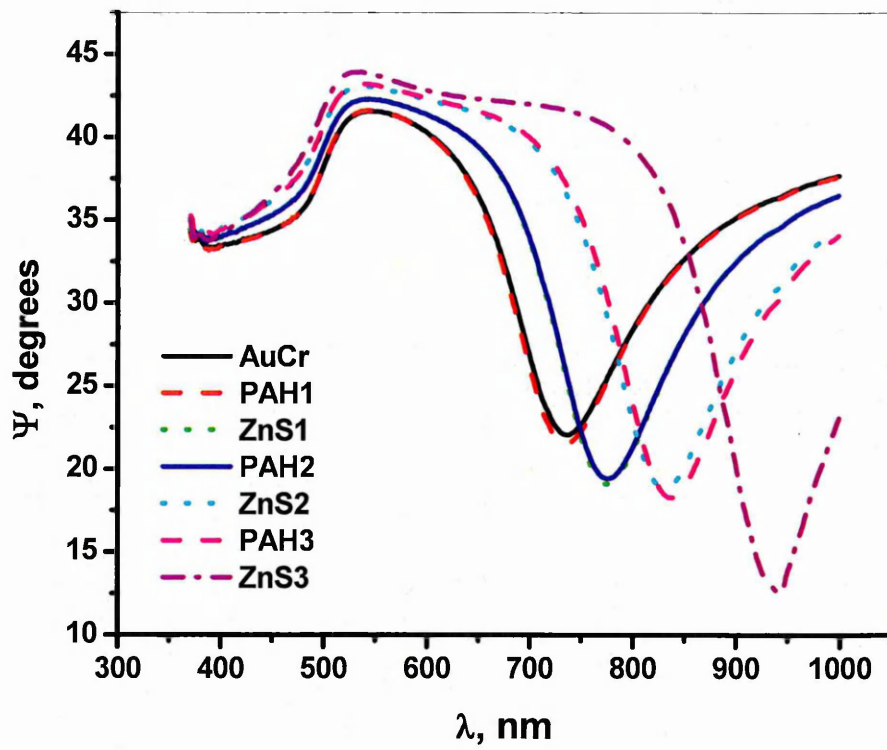
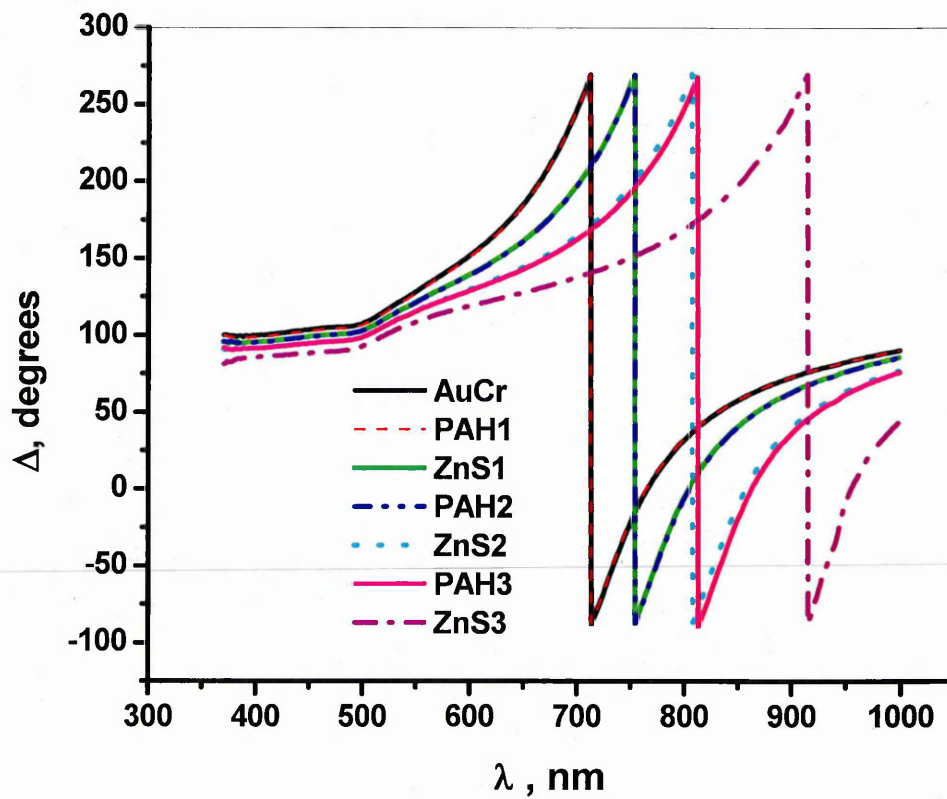


Figure 5.27. A typical set of $\Psi(\lambda)$ (a) and $\Delta(\lambda)$ (b) spectra for consecutive deposition of PAH /CdS films.



(a)



(b)

Figure 5.28. A typical set of $\Psi(\lambda)$ (a) and $\Delta(\lambda)$ (b) spectra for consecutive deposition of AuCr and PAH/ZnS films.

The fitting model for TIRE is different from that in standard ellipsometry measurements. The sequences are reversed since the light is incident from the glass prism. As shown in Figure 5.29, the model starts with BK7 (glass) acting as the ambient, then Chromium/gold layer, polyelectrolyte films of either PAH or PSS represented by Cauchy model, the layers of either CdS or ZnS nanoparticles mixed with PAH (EMA model) and finally the substrate e.g. water in this case, with the fixed thickness of 10 mm.

AMBIENT: BK7 (medium)	
3 Cr/Au	Thickness 1
2 Cauchy (n_1)	Thickness 2
1 CdS (or ZnS)	Thickness 3
0 water (substrate)	10 mm

Figure 5.29. Ellipsometry fitting model for TIRE measurements.

Fitting of the experimental $\psi(\lambda)$ and $\Delta(\lambda)$ spectra was carried out using the above model. Firstly, the parameters (thickness d , refractive index n , extinction coefficient k) of Cr/Au layer were found by fitting the respective $\psi(\lambda)$ and $\Delta(\lambda)$ data for bare Cr/Au coated glass. The optical properties of the first polyelectrolyte layers were determined by fitting respective $\psi(\lambda)$ and $\Delta(\lambda)$ spectra using the Cauchy model, while parameters for Cr/Au were fixed. For the fitting of following layers, the EMA (effective medium approximation) model was used instead of Cauchy model, while the parameters for Cr/Au were fixed.

The effective medium approximation (EMA) model was chosen because of the assumed aggregation of CdS (or ZnS) nanoparticles by intercalation with PAH and the subsequent formation of mixed PAH/semiconductor layers. It allows the calculation of

optical constants of mixtures of a number of materials (two in our case). In this work, we used the Bruggemann EMA to model a wide range of mixed materials. The Bruggemann EMA requires the numerical solution of the following equation [6]

$$f_A \frac{\epsilon_A - \epsilon}{\epsilon_A + 2\epsilon} + f_B \frac{\epsilon_B - \epsilon}{\epsilon_B + 2\epsilon} + f_C \frac{\epsilon_C - \epsilon}{\epsilon_C + 2\epsilon} = 0 \quad (5.3)$$

where ϵ is the effective complex dielectric function of the mixture, f_A , f_B , and f_C are the volume fractions of each material, and ϵ_A , ϵ_B , and ϵ_C are the complex dielectric functions of each material.

The summaries of optical properties for both polyelectrolyte/CdS and polyelectrolyte/ZnS are presented in Table 5.6 and 5.7.

Table 5.6. TIRE data fitting for PAH/CdS SO₃⁻ films

Model Layer	d, nm	Δd, nm	n*	k*	Comments
AMBIENT: bk7					
Cr/Au	32.041	-	0.442	2.961	
Cauchy (PAH-1)	1.836	1.836	1.3759	0	A=1.351; B=0.01; C=0
EMA-1 (PAH-1/CdS-1)	9.386	7.550	1.8041	0.1069	PAH: 68.59% CdS: 31.41%
EMA-2 (+ PAH-2)	10.027	0.641	1.7846	0.0810	PAH: 68.59% CdS: 31.41%
EMA-3 (+ CdS-2)	17.597	7.57	1.8235	0.1178	PAH: 80.0% CdS: 20.0%
EMA-4 (+ PAH-3)	19.418	1.821	1.8838	0.1618	PAH: 78.74% CdS: 21.26%
EMA-5 (+ CdS-3)	26.193	6.775	1.8984	0.1984	PAH: 76.06% CdS: 23.94%
Water	10 mm	-	1.3369	0	

Table 5.7. TIRE data fitting for PAH/ZnS SO₃⁻ films

Model Layer	d, nm	Δd, nm	n*	k*	Comments
AMBIENT: bk7					
Cr/Au	30.984	-	0.3799	3.0753	
Cauchy (PAH-1)	1.836	1.836	1.357	0	A=1.351; B=0.01; C=0
EMA-1 (PAH-1/ZnS-1)	11.918	10.082	1.505	0.030	PAH: 81.66% CdS: 18.34%
EMA-2 (+ PAH-2)	12.650	0.732	1.497	0.0280	PAH: 80.65% CdS: 19.35%
EMA-3 (+ ZnS-2)	25.411	12.761	1.517	0.0267	PAH: 78.765% CdS: 21.235%
EMA-4 (+ PAH-3)	26.997	1.586	1.513	0.0258	PAH: 77.15% CdS: 22.85%
EMA-5 (+ ZnS-3)	39.444	12.447	1.5698	0.0418	PAH: 76.90% CdS: 23.10%
Water	10 mm	-	1.3369	0	

The thickness of CdS and ZnS layers of about 7 nm and 12 nm, respectively, were obtained. These values appear to be several times larger than particles' size obtained from the calculation using Efron approximation, and thus confirm the suggestion of the formation of three-dimensional aggregates of semiconductor nanoparticles intercalated with the polyelectrolyte. As can be seen from Table 5.6 and 5.7, the values of n in EMA layers (EMA 1, 3, and 5) increase with the number of deposited nanoparticles layers and decrease when polyelectrolyte were deposited (EMA 2 and 4). The values of k are also tended to increase when nanoparticles were deposited. Those trends in n and k changes are, however, not consistent; deviations from the main trend were observed most likely due to inhomogeneity of the deposited layers.

5.3. MORPHOLOGY STUDY USING ATOMIC FORCE MICROSCOPY

In order to examine the morphology of the multilayered films, the AFM study was carried out on the same types of films deposited on silicon (refer to Chapter 4, section 4.2.3.1). Typical tapping mode AFM images of bare silicon is presented in Figure 5.30. The image shows that the silicon surface has the maximum height of about 2 nm.

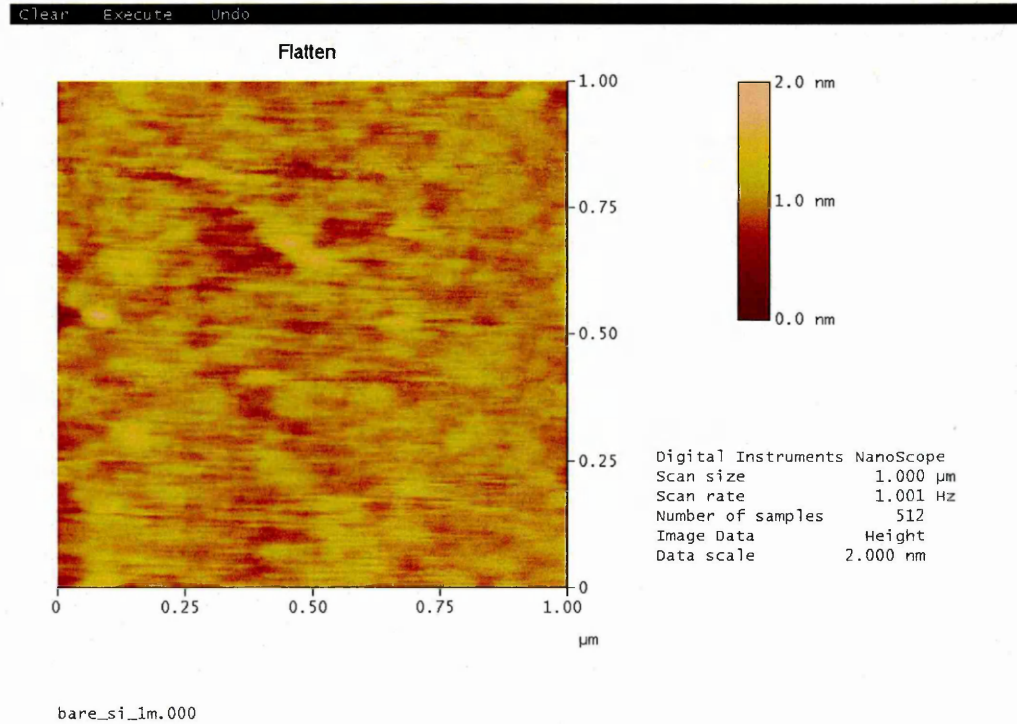


Figure 5.30. Tapping mode AFM images (1 μm in size) of silicon.

To obtain the average height of the surface, roughness analysis software was used. The results is presented in Figure 5.31. The yielded root means square (RMS) roughness of 0.15 nm indicates that the silicon surface is quite flat. The chosen area in the image was illustrated by square line in the image and the roughness statistic was shown.

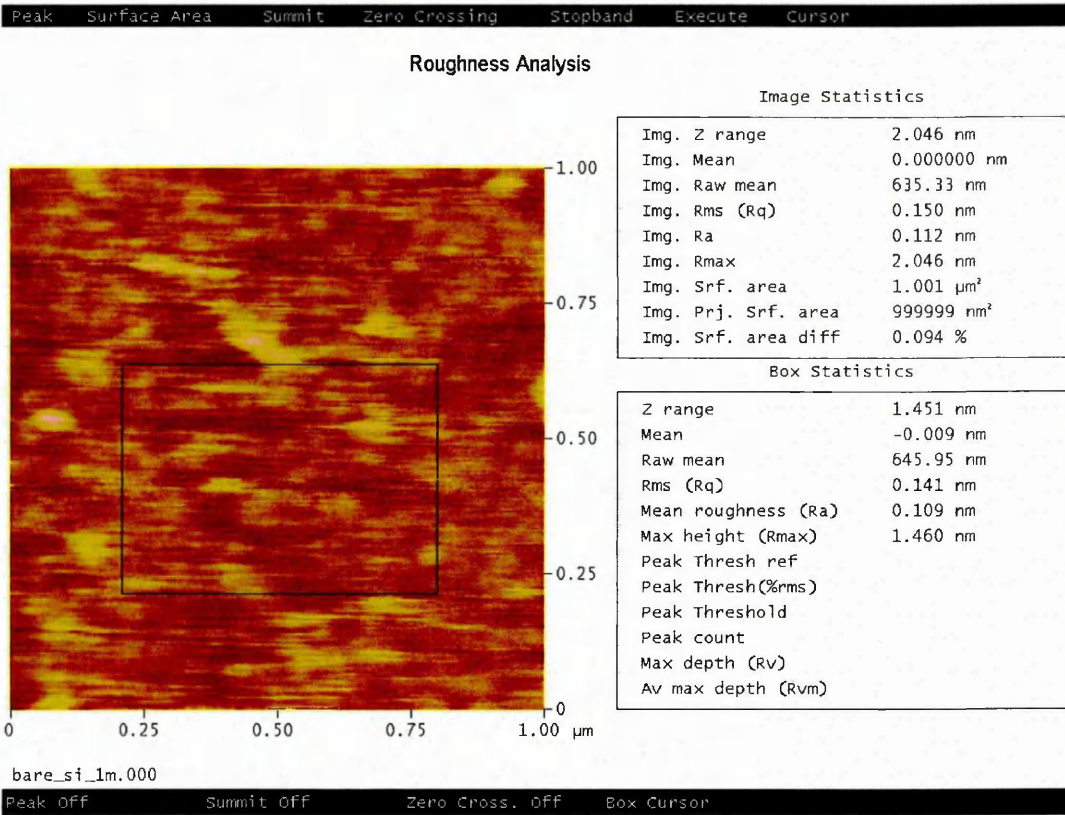


Figure 5.31. Roughness analysis of the AFM images of silicon.

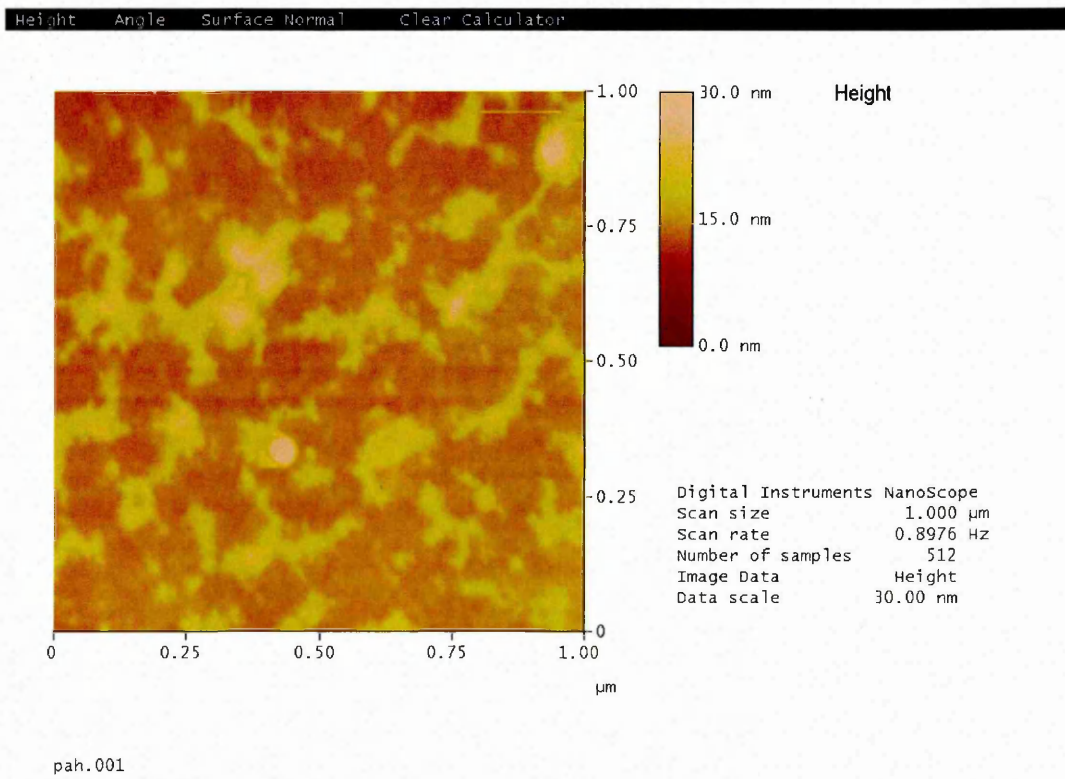
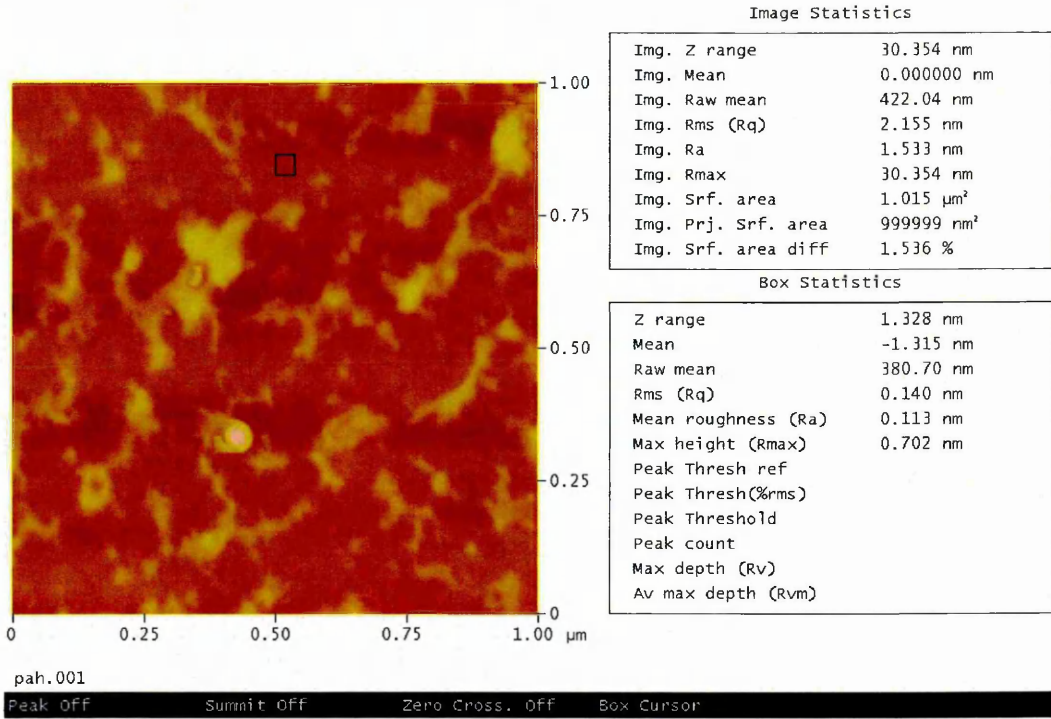


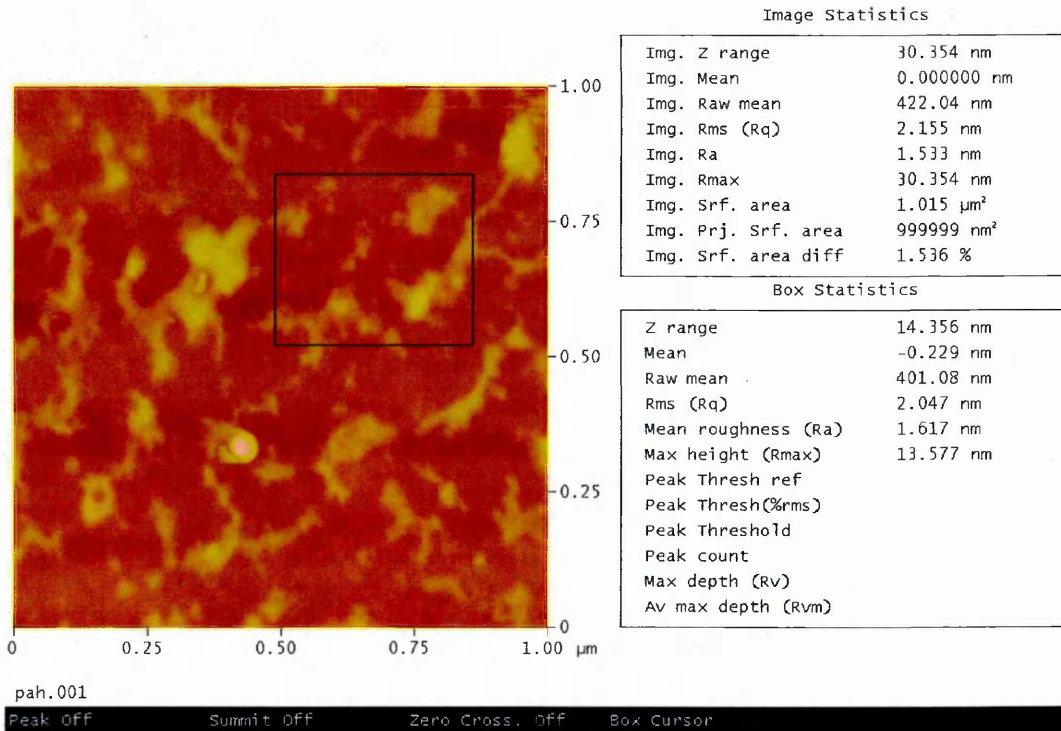
Figure 5.32. Tapping mode AFM images (1 μm in size) of the first PAH layer.

Roughness Analysis



(a)

Roughness Analysis



(b)

Figure 5.33. Roughness analysis of tapping mode AFM images (1μm in size) of the first PAH layer with different chosen areas: substrate (a) and film (b).

After the first layer of PAH was deposited, the successful adsorption can be seen from the increase of height to a maximum value of 30 nm (see in Figure 5.32). The image shows that the PAH layer was deposited in a certain areas and not covering the substrate homogeneously.

The roughness analysis of the image, presented in Figure 5.33 (a), clearly shows that the small chosen area at the lowest height gives RMS roughness of about 0.14 nm. This value is the same as RMS roughness of the silicon (substrate). If the chosen area was enlarged to include the PAH layer, the RMS roughness is increased to 2.047 nm (see Figure 5.33 (b)).

Typical tapping mode AFM images of consecutively deposited layers of polyelectrolytes and colloid nanoparticles are shown in Figures 5.34. All the images are scanned in area of $1\mu\text{m} \times 1\mu\text{m}$.

The first PAH layer (see Figure 5.34 (a)) shows a patchy and inhomogeneous pattern. The next layer of PSS seems to have adsorbed onto PAH layer and may be partly on the substrate and gave much more homogeneous coating. However it can be seen that aggregates in grainy pattern have began to form. After the first layer of CdS- NH_2^+ was deposited, the CdS nanoparticles were distributed randomly across the films while the maximum thickness suddenly increased to 100 nm and the aggregates became bigger. The thickness value did not change for the next two layers but the next deposition steps show further aggregation of CdS nanoparticles.

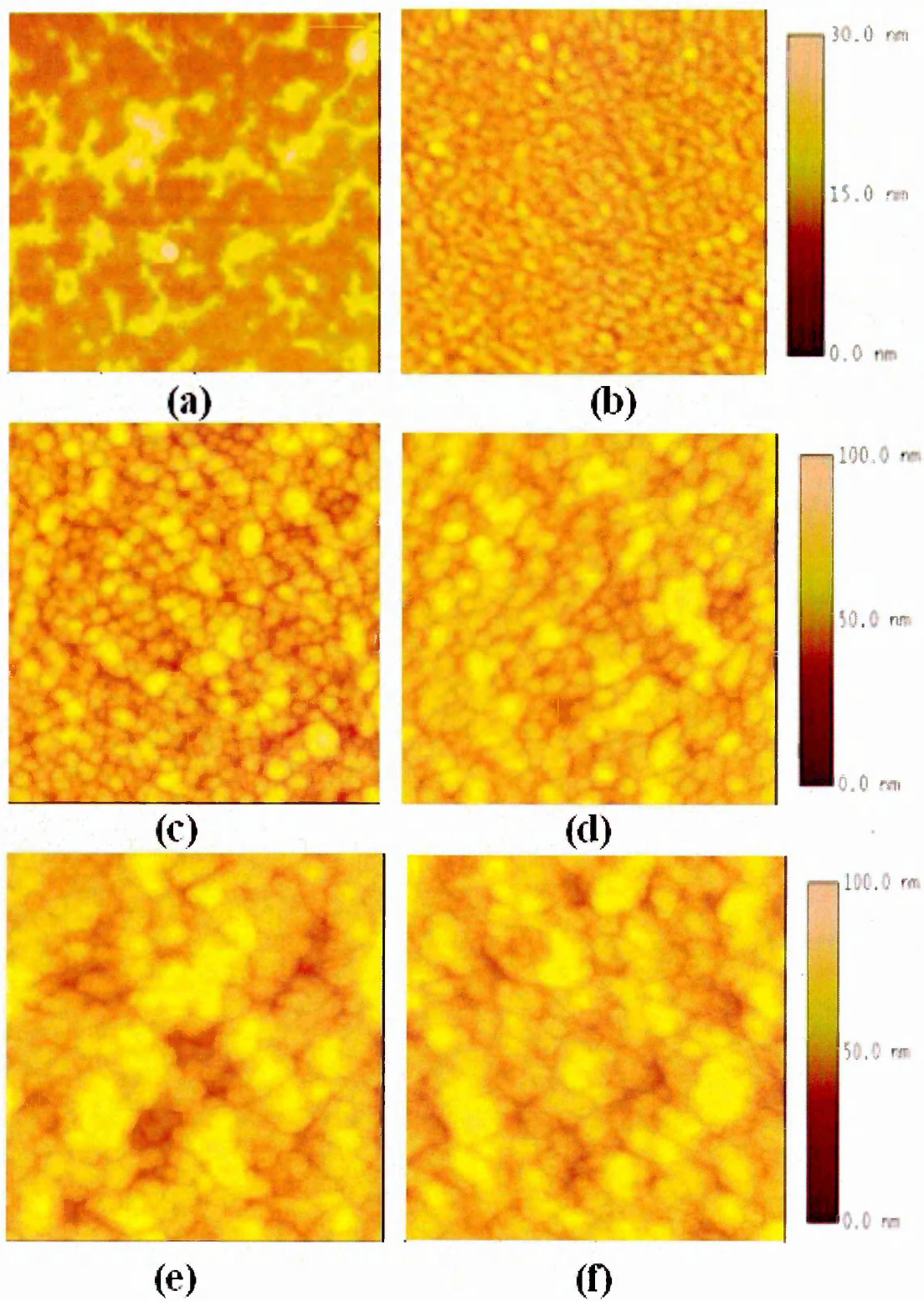


Figure 5.34. Tapping mode AFM images ($1\mu\text{m}$ in size) of consecutively deposited layers of: PAH (a), 1st PSS (b), 1st CdS-NH₂⁺ (c), 2nd PSS (d), 2nd CdS-NH₂⁺ (e), and 3rd PSS (f).

The section analysis reveals aggregates of nanoparticles of up to 50 nm in size as shown in Figure 5.35.

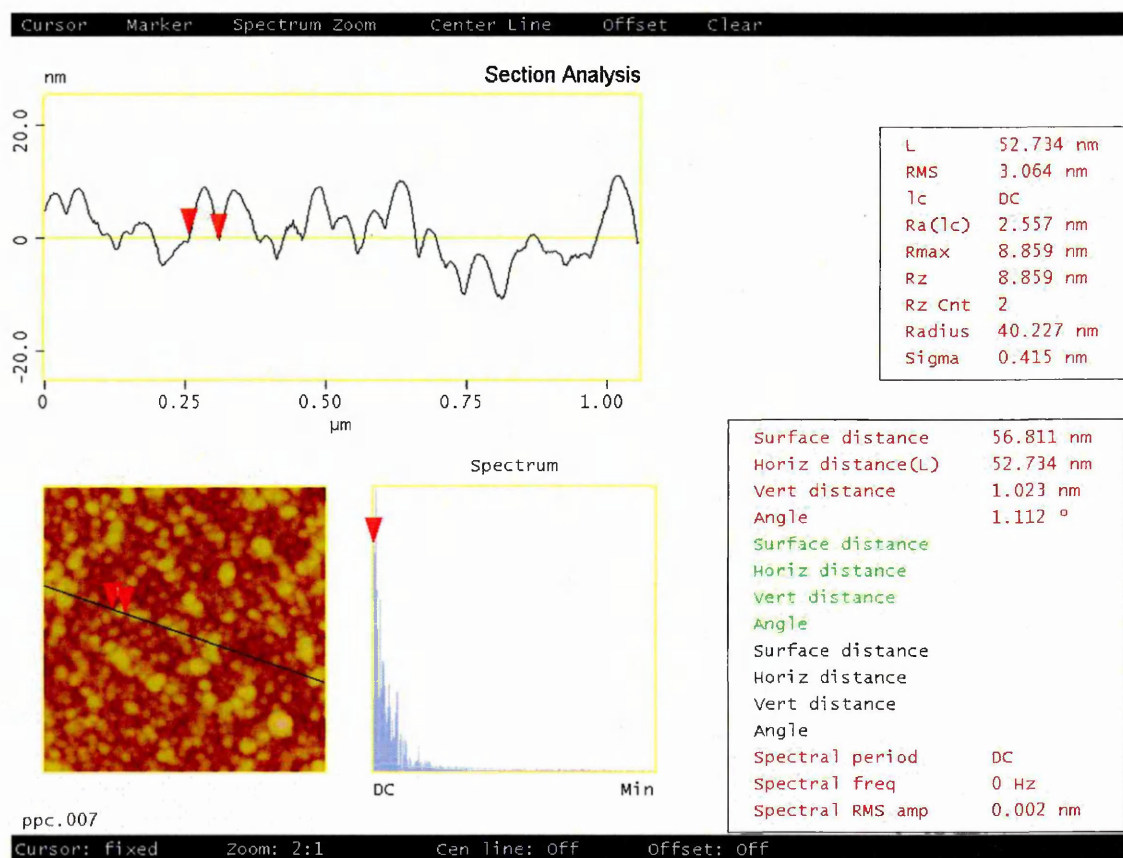


Figure 5.35. Section analysis of tapping mode AFM images (1 μm in size) of the first CdS NH₂⁺ layer.

The particles analysis of the AFM image of the first CdS- NH₂⁺ layer is shown in Figure 5.36. The threshold height of about 5 nm has been chosen on the bases of the particles size obtained. The diameter of around 28 nm was obtained as an average particles size.

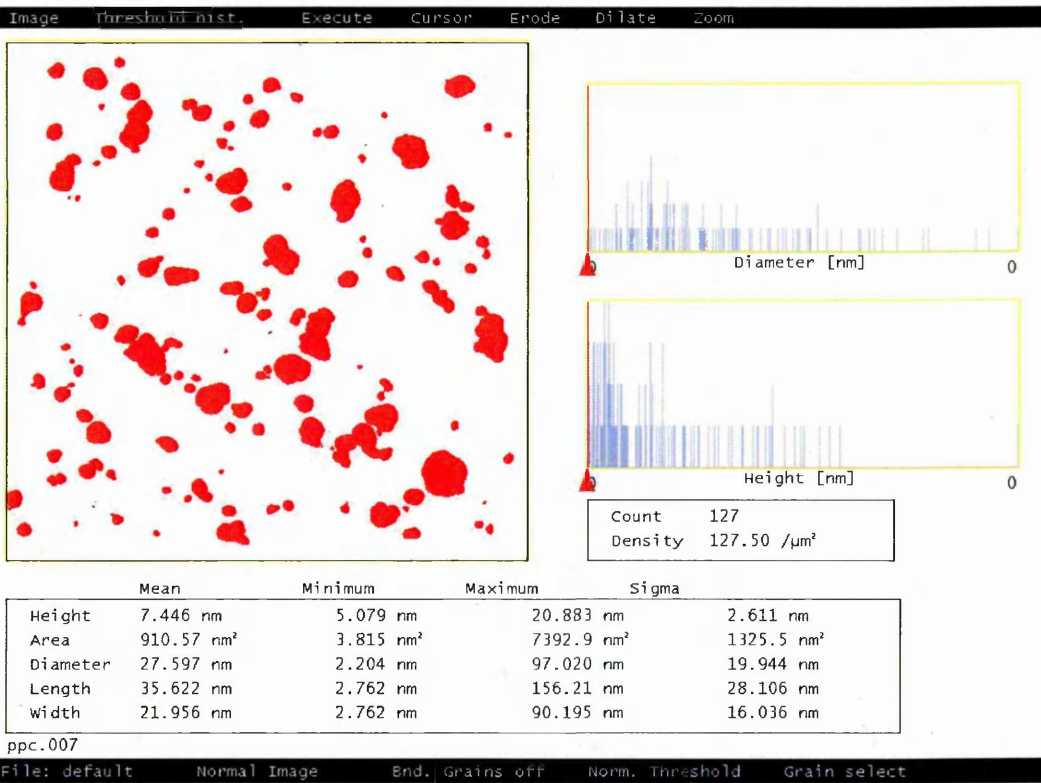
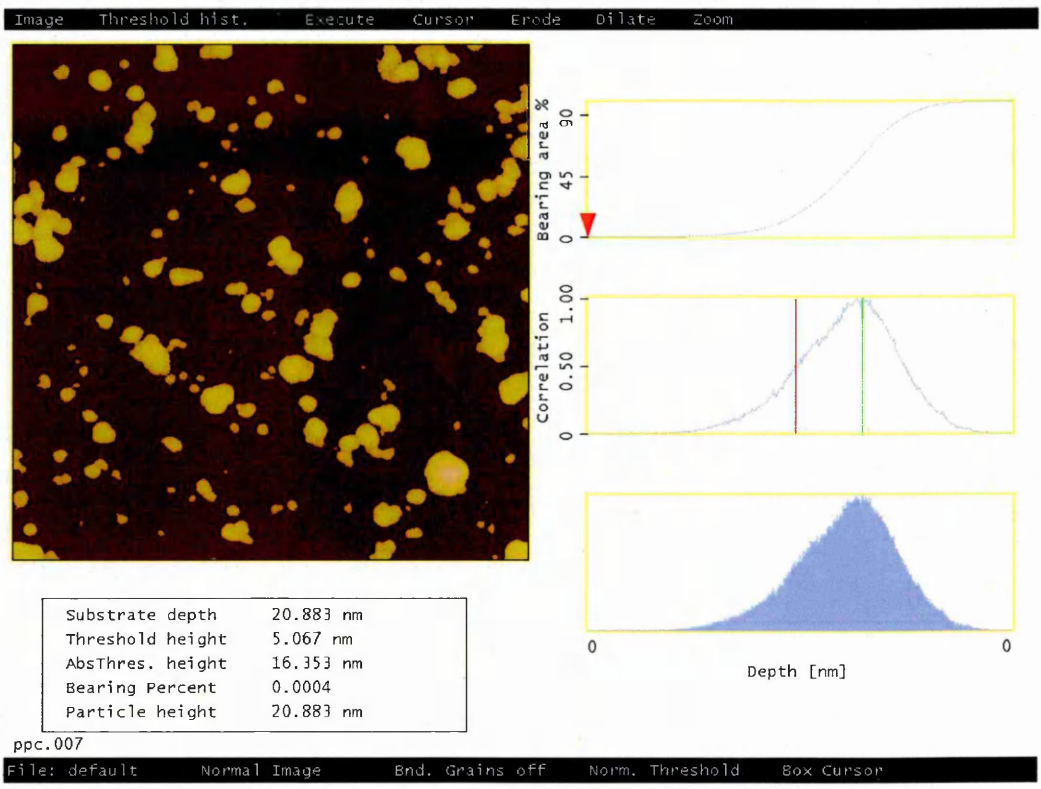


Figure 5.36. Particles analysis of the AFM image of the first CdS-NH₂⁺ layer.

In the case of PAH/ ZnS-SO_3^- films, a similar aggregation is observed (see Figure 5.37). The ZnS-SO_3^- layer which was deposited after PAH shows much better coverage than PAH. The next deposition steps show the formation of bigger aggregates increase corresponding to the number of layers deposited. The size of ZnS-SO_3^- aggregates of about 40-50 nm is obtained.

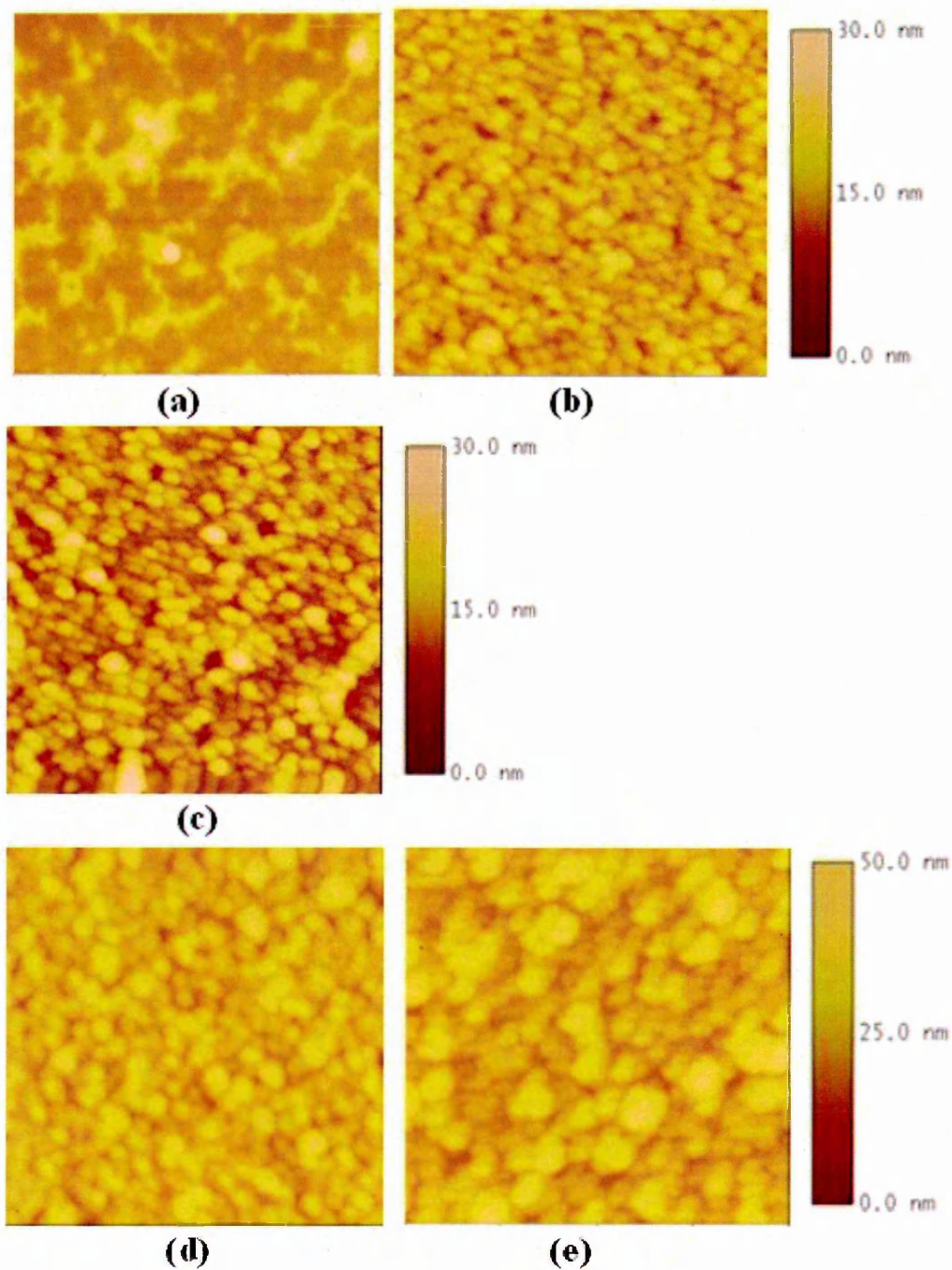


Figure 5.37. Tapping mode AFM images ($1\mu\text{m}$ in size) of consecutively deposited layers of: PAH (a), 1st ZnS-SO_3^- (b), 2nd PAH (c), 2nd ZnS-SO_3^- (d), and 3rd PAH (e).

From roughness analysis of the AFM images, the data is summarized and presented in Table 5.8 and 5.9.

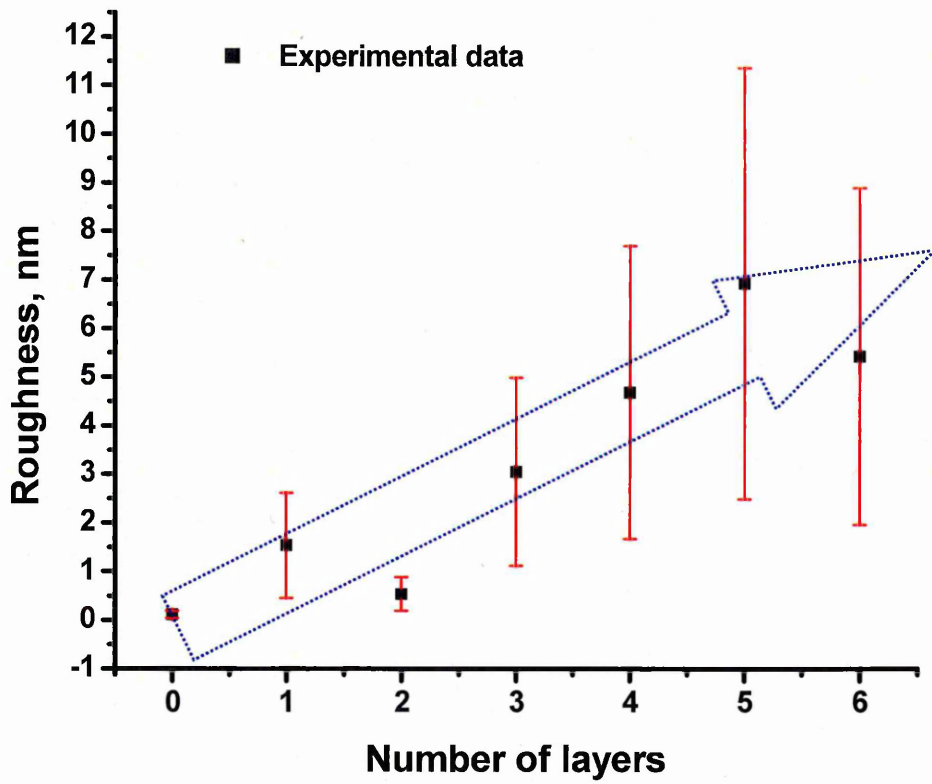
Table 5.8. Summary of roughness parameters of polyelectrolyte/CdS films.

Layer	Z range (nm)	Image RMS (nm)	Image Mean (nm)
Silicon	2.046	0.15	0.112
1 st PAH	30.354	2.155	1.533
1 st PSS	6.921	0.693	0.533
1 st CdS	32.169	3.865	3.047
2 nd PSS	47.685	6.022	4.680
2 nd CdS	61.742	8.873	6.923
3 rd PSS	49.781	6.929	5.424

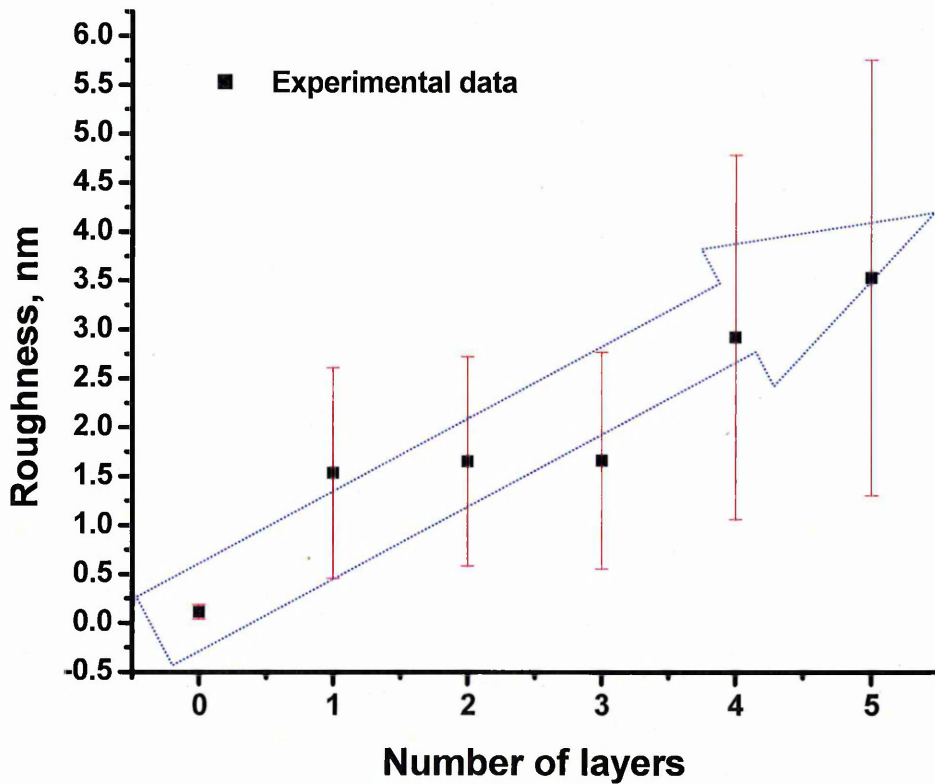
Table 5.9. Summary of roughness parameters of polyelectrolyte/ZnS films.

Layer	Z range (nm)	Image RMS (nm)	Image Mean (nm)
Silicon	2.046	0.15	0.112
1 st PAH	30.354	2.155	1.533
1 st ZnS	19.584	2.141	1.653
2 nd PAH	19.768	2.212	1.661
2 nd ZnS	27.936	3.721	2.924
3 rd PAH	31.852	4.444	3.529

The plot of mean roughness against the number of layers is shown in Figure 5.38. It shows that the film roughness in general is increasing for each layer deposition. Some inconsistencies which are clearly seen are possibly caused by the formation of the aggregation in the films.



(a)



(b)

Figure 5.38. Surface roughness of CdS (a) and ZnS (b) multilayer as a function of number of layer.

It is suggested that the aggregation of either positively or negatively charged semiconductor nanoparticles, could only happen by intercalation of nanoparticles with the layers of polyanions (PSS) or polycations (PAH), respectively, as illustrated schematically in Figure 5.39. This leads to the increase in the effective thickness of nanoparticle layers, often observed for the 2nd and following layers deposited.

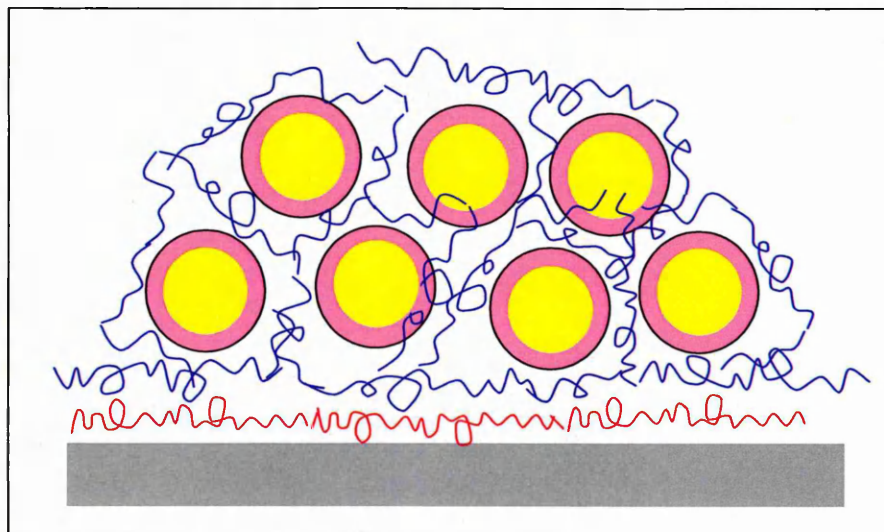
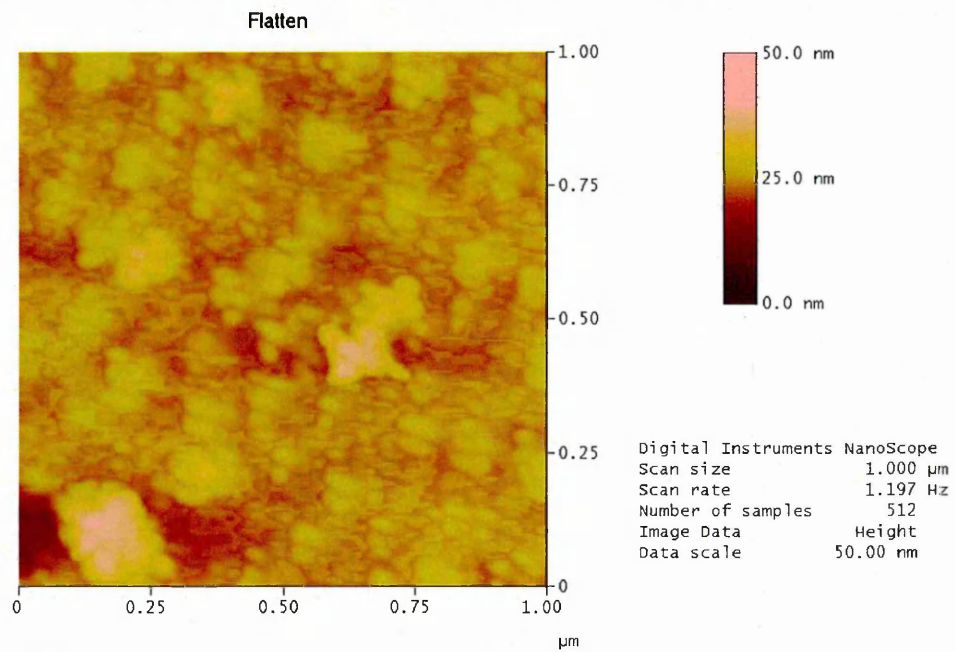


Figure 5.39. The formation of aggregates of electrically charged nanoparticles by intercalation with polyelectrolytes.

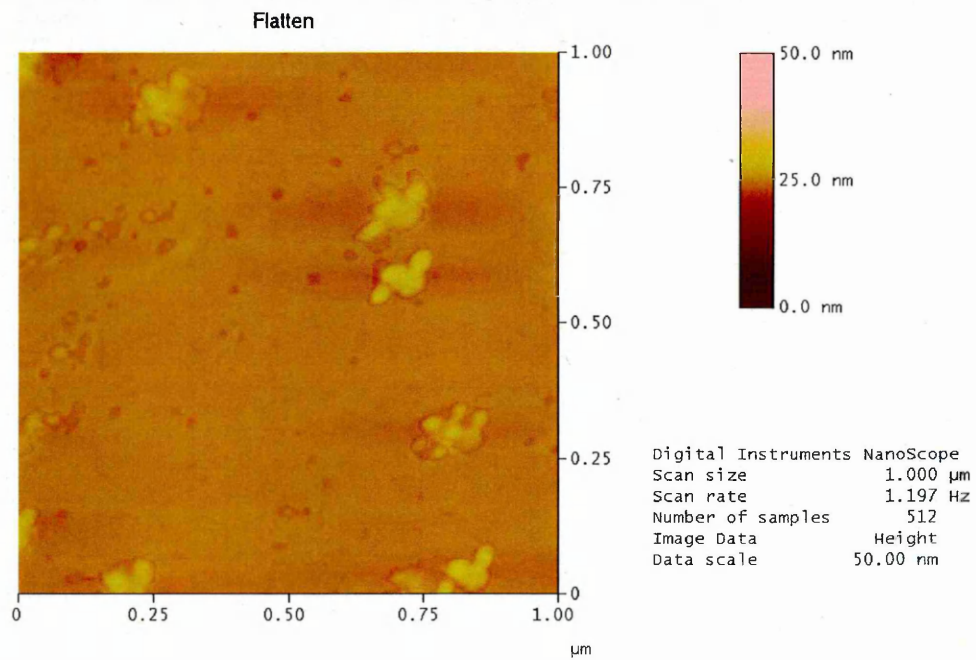
Theoretically, the aggregation of nanoparticles could be reduced by using a very diluted colloid solutions in the deposition process. Therefore monolayer of nanoparticle films were deposited from 100 and 500 times diluted colloid solutions. The results were presented in Figure 5.40. (a) and (b). Smaller size and separate groups of nanoparticle aggregates are clearly visible in both figures.

In the case of 500 times diluted colloid solution, roughness and particle analysis were performed. The roughness analysis presented in Figure 5.41. shows the value of about 10.698 nm obtained for the maximum height of the film. The chosen area at the lowest height shows RMS roughness of the same value as silicon RMS roughness. It confirmed the deposition of nanoparticles monolayer on the substrate.



cds-nh3.012

(a)



cds-nh3.010

(b)

Figure 5.40. Tapping mode AFM images (1 μm in size) of CdS-NH₃⁺ layer deposited from diluted colloid solutions: 100 times (a), 500 times (b).

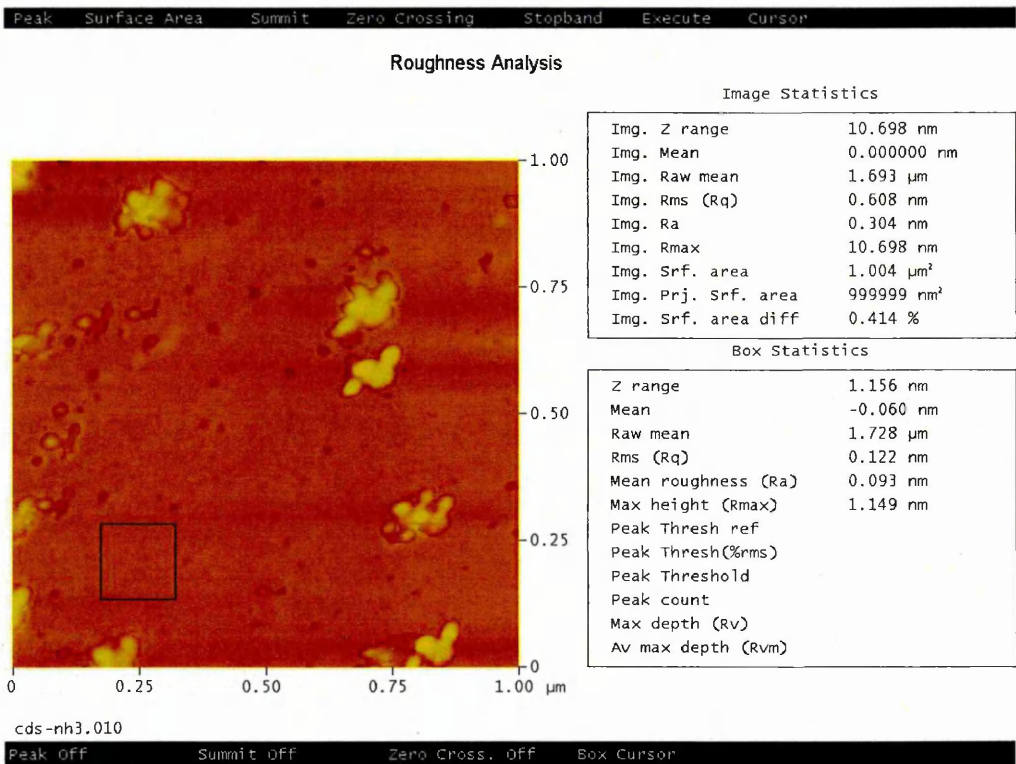


Figure 5.41. Roughness analysis of tapping mode AFM image (1μm in size) of 500 times diluted CdS-NH₃⁺ colloid solution monolayer film.

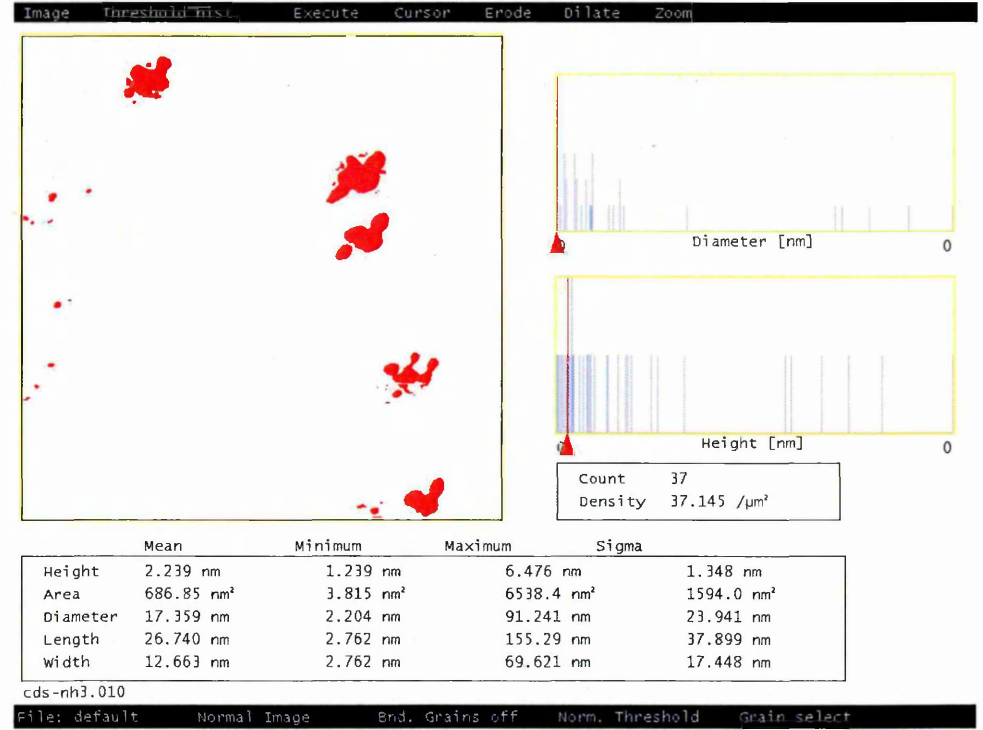


Figure 5.42. Particle analysis of tapping mode AFM image (1μm in size) of 500 times diluted CdS-NH₃⁺ colloid solution monolayer film.

A particle analysis of the image illustrated in Figure 5.40 (b) reveals the average size of the aggregates of about 18 nm (see Figure 5.42). This size corresponds well to a single particle considering the finite radius of the AFM tip (see the scheme in Figure 5.43). If, for example, a single particle with the radius a , is scanned using AFM which typically has tip radius R , the AFM tip moves from left to right. Thus the first contact with the particle will occur on the edge of the tip which is advanced by the value of R as compared to the actual tip position (recorded by the software). The same happened on the other side of the particle. As a result, the AFM features will be larger than the actual particles' size by a factor of $2R$. The maximal effective enlargement could be estimated as:

$$a' = a + 2R \quad (5.4)$$

where a' is the effective particle size, a is the particle radius, and R is the AFM tip radius.

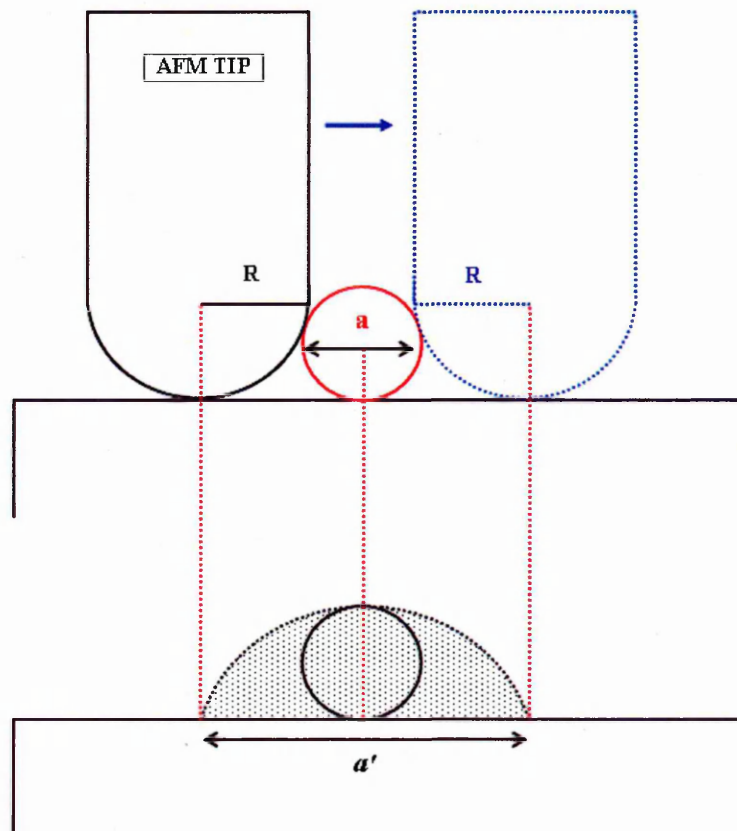


Figure 5.43. The effect of finite radius of the tip on the observed AFM features.

5.4. ELECTRICAL STUDY OF CDS AND ZNS NANOPARTICLES

5.4.1. I-V characteristic of polyelectrolyte films

Typical results of DC I-V characteristics of the first layer of PAH films, deposited onto ITO glass, are shown in Figure 5.44. Voltage sweep in the range from -0.5 to 0.5 volt gave symmetrical I-V curves. The PAH was well adsorbed to the substrate, in this case ITO, which reflects by the difference in the measured current as compared to the data on the blank ITO (blue straight line). The measured current was much lower than the one measured on blank ITO. The measurements at different spots on the sample gave a slightly different values, which is believed to be caused by inhomogeneous coating of PAH film.

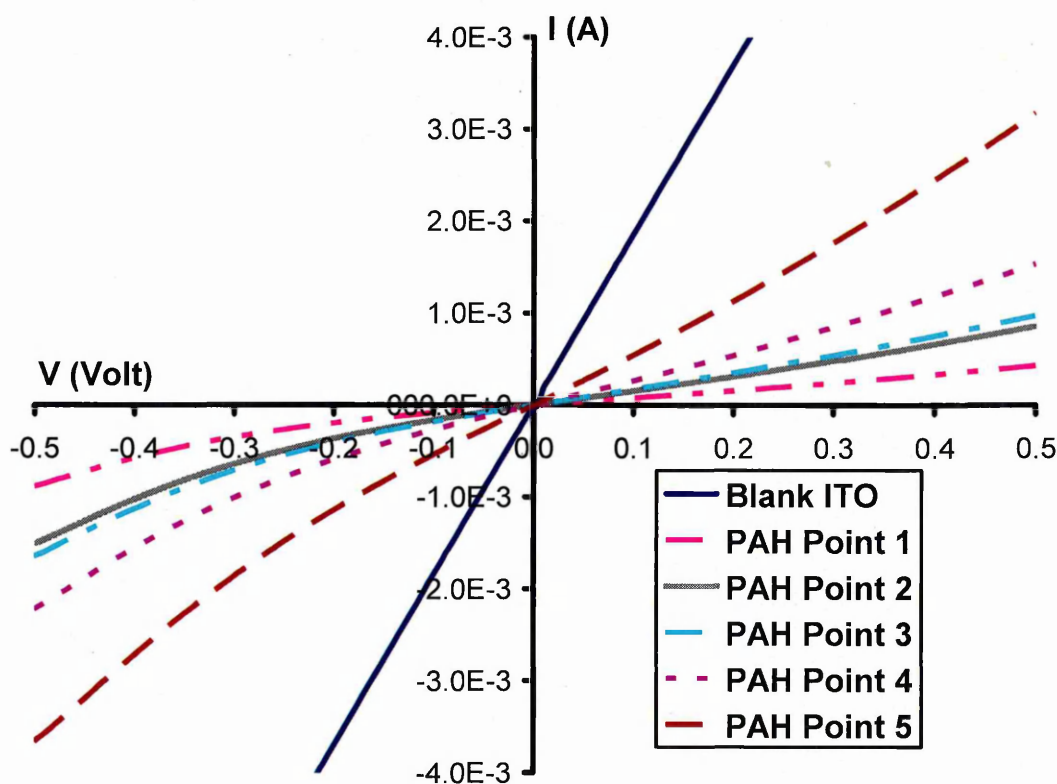


Figure 5.44. Typical DC I-V characteristics of ITO/(PAH/PSS)_N/Hg structure.

For the multilayers of (PAH/PSS)_N deposited onto ITO glass, the I-V characteristic shows the decrease of current corresponding to the increase in the number of the deposited layers (see Figure 5.45 (a)). Since multilayered electrostatically self-

assembled films usually perfectly cover the surface (without pinholes) the mechanism of electron tunnelling through the insulating PAH/PSS films could be suggested.

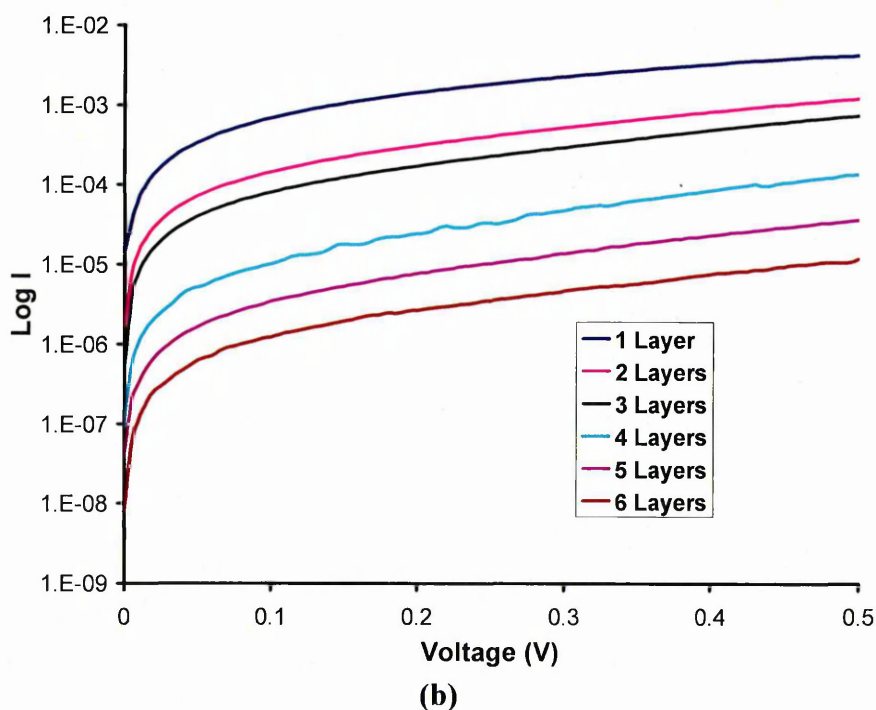
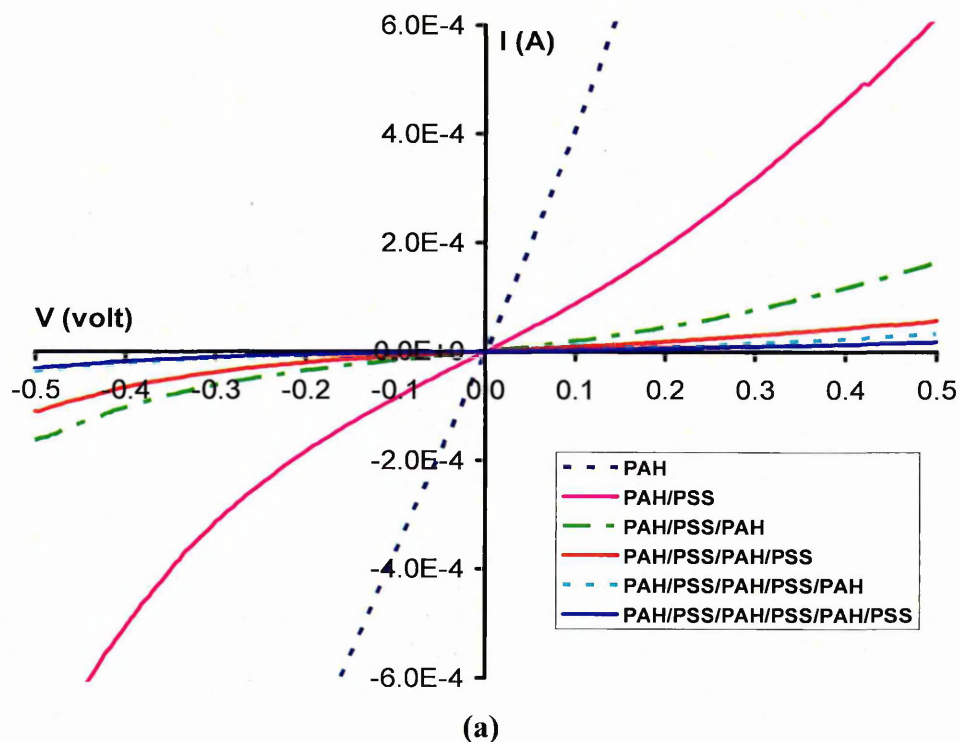


Figure 5.45. Typical DC I-V characteristics of ITO/(PAH/PSS)_N/Hg structure (a) and the same graph in semi-logarithmic scale (b).

It has become clearer when I-V curves were replotted in Figure 5.45 (a) in a semi-logarithmic scale, the value of current at saturation falls exponentially with the increase in the number of layers.

In order to investigate the electron tunnelling phenomenon in the multilayered films, the thickness of (PAH/PSS)_N films deposited on ITO glass was measured with ellipsometry, and the values of thickness obtained by fitting are summarized in Table 5.10, along with the values of current at 0.5 V.

Table 5.10. Thickness and current values of Polyelectrolyte layers (PAH/PSS)

Number of layer	Thickness (nm)	Current at V=0.5 V (A)
1 (PAH)	3.31 ± 0.02	(2.5 ± 1.2) 10 ⁻³
2 (PSS)	4.22 ± 0.04	(1.1 ± 0.4) 10 ⁻³
3 (PAH)	5.49 ± 0.05	(3.9 ± 2.4) 10 ⁻⁴
4 (PSS)	6.23 ± 0.03	(7.5 ± 1.2) 10 ⁻⁵
5 (PAH)	7.14 ± 0.03	(2.4 ± 0.9) 10 ⁻⁵
6 (PSS)	8.54 ± 0.02	(1.3. ± 0.4) 10 ⁻⁵

The dependence of the current at 0.5 V on the PAH/PSS films thickness in Figure 5.46 (a) fits well with the exponential law, which is a clear indication of the tunnelling mechanism of conductivity.

To interpret the above experimental results, the model of electron tunnelling through the trapezoidal barrier was used (revert to Chapter 2, Equation 2.77) [7]. The dependence of the current on the film thickness can be described by the tunnelling law

$$I = I_0 \exp(-\alpha W) \quad (5.5)$$

where α is the tunnelling coefficient and W is the film thickness.

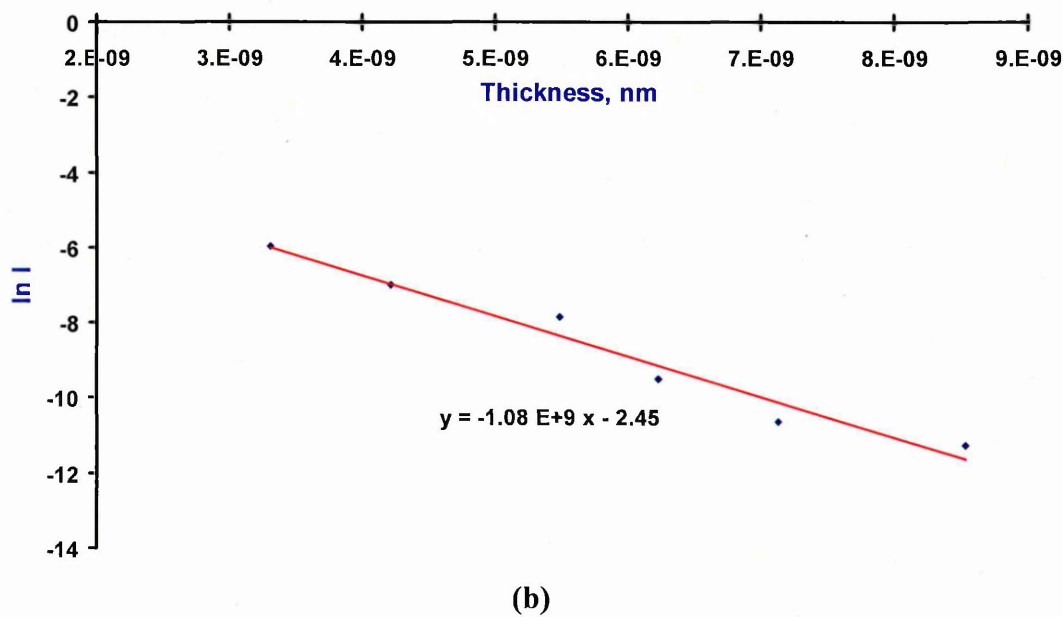
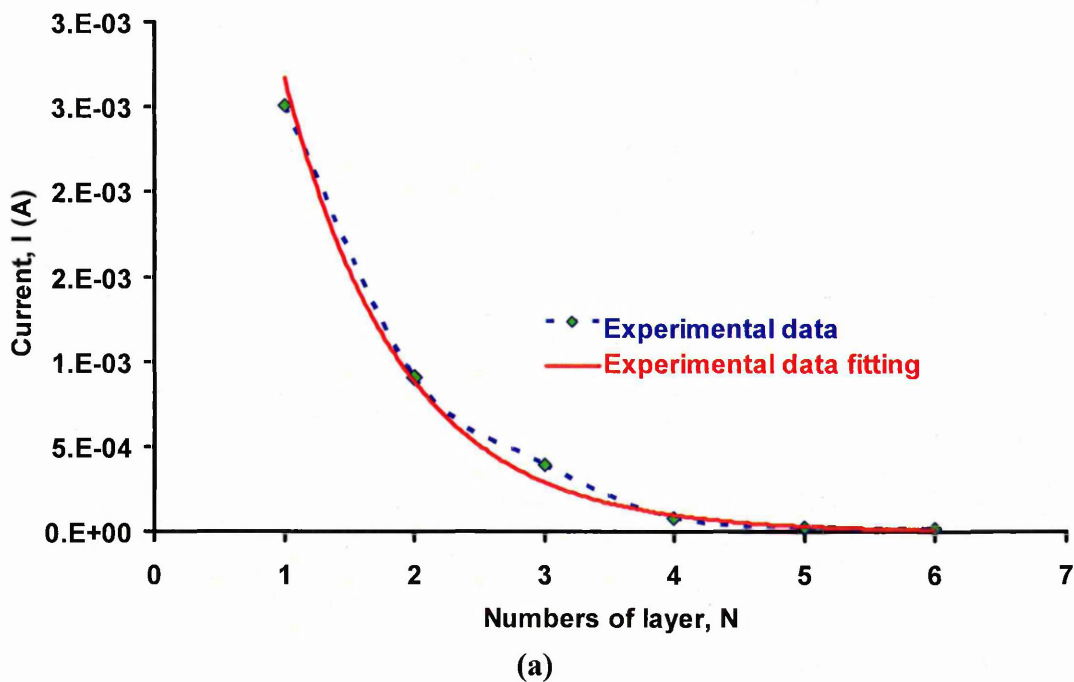


Figure 5.46. The dependence of the current at 0.5 V on the number of polyelectrolyte layers in the ITO/(PAH/PSS)_N/Hg structure (a) and $\ln I$ vs thickness (W) (b).

In order to calculate the tunnelling coefficient the graph was replotted in $\ln I$ as a function of thickness, as shown in Figure 5.46 (b). The fitting equation of the graph yields the value of $\alpha = 1.08 \times 10^9 \text{ m}^{-1}$.

5.4.2. I-V characteristic of films containing CdS (or ZnS) nanoparticles

The presence of CdS or ZnS nanoparticles in the films causes the decrease in current as shown in Figure 5.47 which is believed to be caused by an overall increase in the film thickness due to the aggregation of nanoparticles and intercalation with the polyelectrolyte.

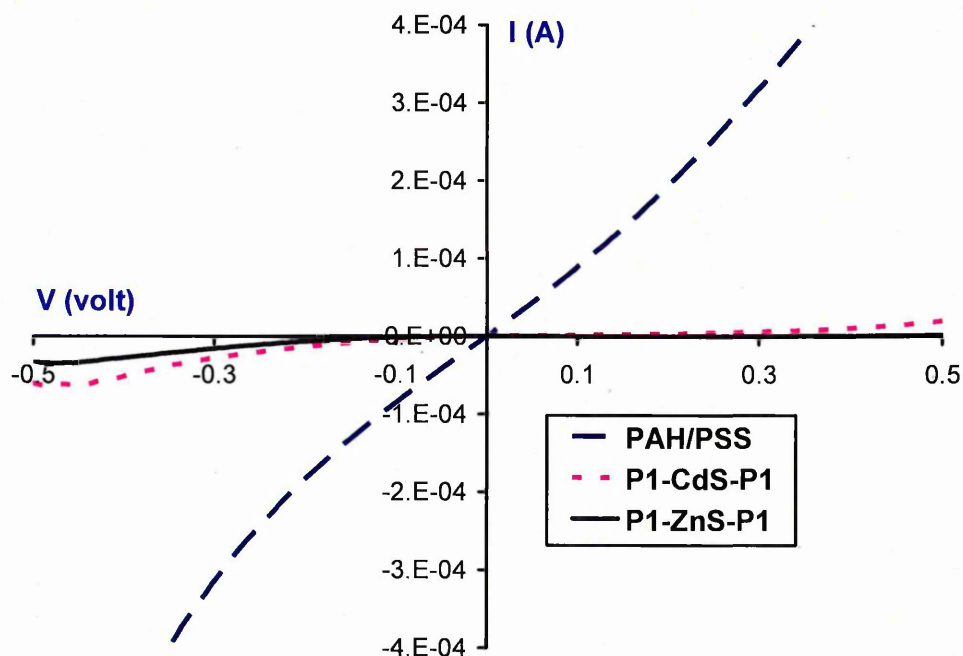
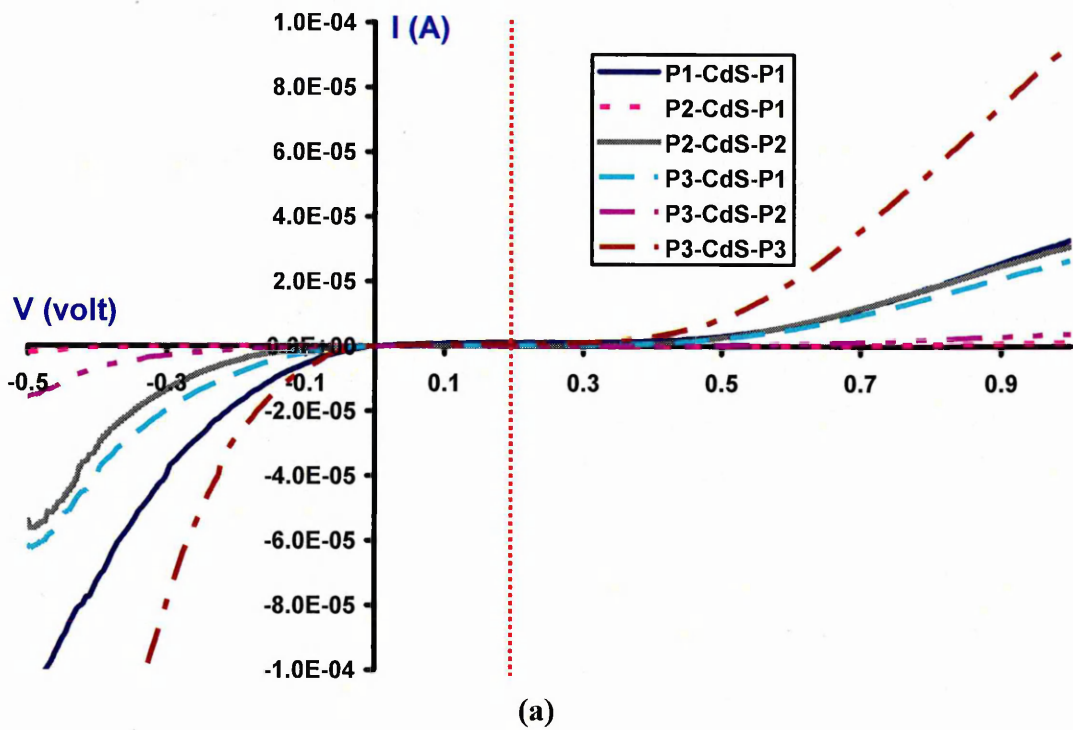
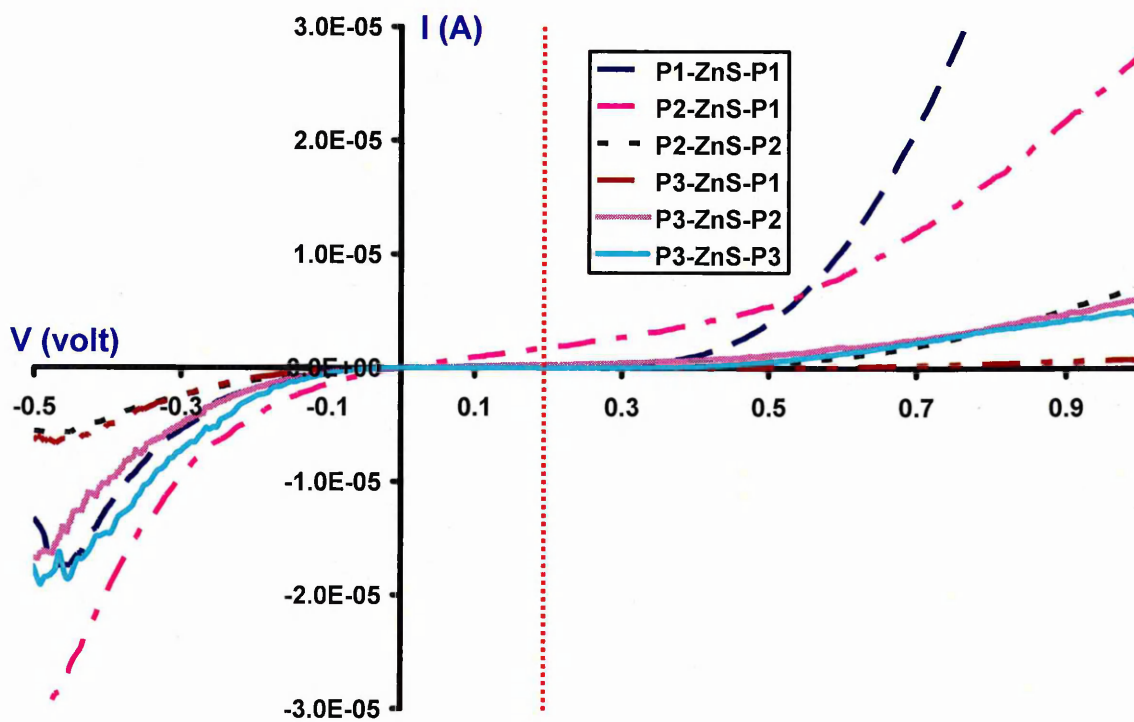


Figure 5.47. Typical DC I-V characteristics (the voltage sweep range: - 0.5 to 1 V, step size: 5 mV) of PAH film compared to the films containing CdS (or ZnS) nanoparticles.

Typical DC I-V characteristics (the voltage sweep range: - 0.5 to 1 V, step size: 5 mV) of the films: polyelectrolyte/CdS/polyelectrolyte and polyelectrolyte/ZnS/polyelectrolyte are shown in Figure 5.48 (a) and (b). It is clearly seen that the I-V curves for both CdS and ZnS are not symmetrical but shifted to the right of about 0.2 V. It is believed that the shift is caused by the work function difference between ITO and Hg electrodes. Indeed, from ref. 8 and 9, the values of ITO and Hg work functions are 4.7 and 4.5 eV, respectively, giving the difference of 0.2 V.



(a)



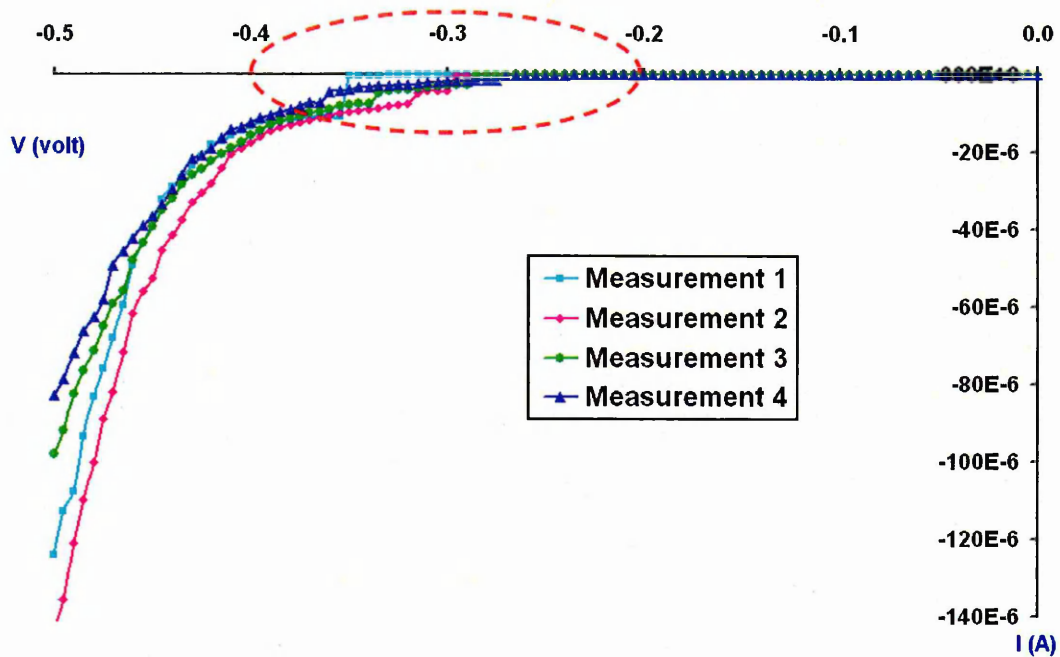
(b)

Figure 5.48. Typical DC I-V characteristics (the voltage sweep range: - 0.5 to 1 V, step size: 5 mV) of the films: polyelectrolyte/CdS/polyelectrolyte (a), and polyelectrolyte/ZnS/polyelectrolyte (b).

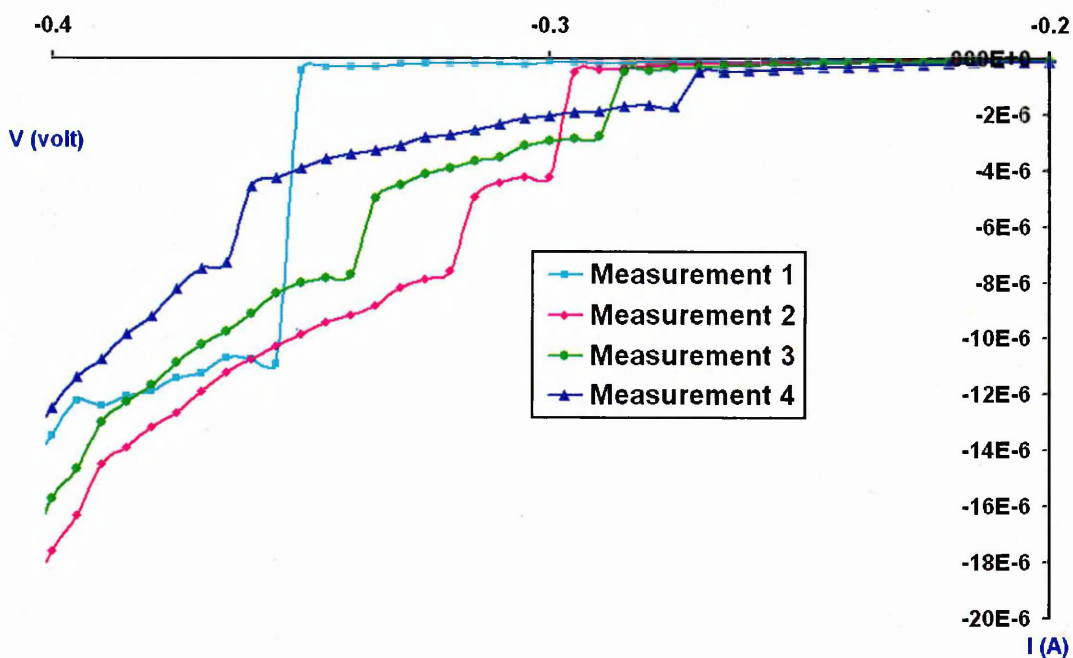
No consistency in the current values was found in Figure 5.48, although each film has different polyelectrolyte composition. This is possibly due to the aggregation of nanoparticles and intercalation of polyelectrolyte which caused uncertainty in the particles-electrode distance. For example, if the electrode is close enough to the collection of nanoparticles, the current will easily pass through the films. As a result, the current will be much larger than in the other cases as illustrated for (P3-CdS-P3) film in Figure 5.48 (a). The (P3-CdS-P3) film has the largest thickness of polyelectrolyte (insulator) layer as compared to the other films but Figure 5.58 (a) shows that this film has the largest current.

The I-V measurements, performed in the bias range from 0 to -0.5 V, gave a different type of I-V curves for the films containing either CdS or ZnS nanoparticles. Figure 5.49 (a) shows the step rise in current followed by its sharp increase. Zooming the encircled part of I-V curves allows the detailed investigation of the current step (see Figure 5.49 (b)), which appeared on every curve but at different positions.

We can only suggest that such behaviour may be related to the resonance tunneling in the system ITO/insulator/CdS (or ZnS)/insulator/Hg through the energy levels in the semiconductor nanoparticles. The presence of two steps on the I-V curve may correspond to two consecutive energy levels. This effect may be accompanied by the electrical charging of CdS (or ZnS) nanoparticles, which causes the instability in the step position.



(a)



(b)

Figure 5.49. Typical DC I-V characteristics of PAH/PSS/ZnS NH_2^+ /PSS/PAH, voltage sweep from 0 to -0.5 volt, step size 5 mV (a), a section of the graph zoomed in (b). The curves 1, 2, 3 and 4 correspond to consecutive measurements.

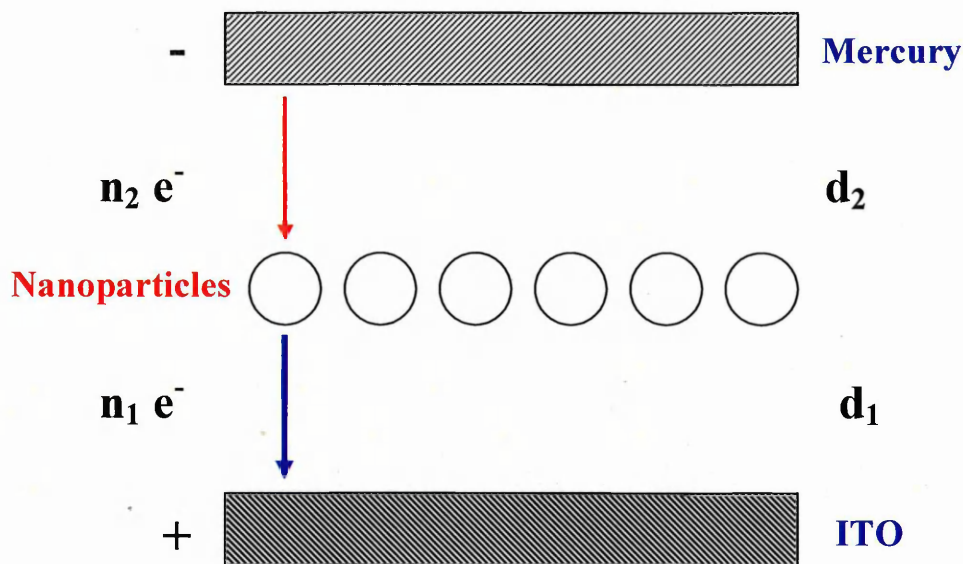


Figure 5.50. Schematic diagram of nanoparticles charging.

The mechanism of nanoparticles charging is schematically explained in Figure 5.50. The tunnelling current, e.g. the number of electrons passing between ITO and nanoparticles (n_1) and between nanoparticles and mercury (n_2) may not be equal, for example, because of different tunnelling distances d_1 and d_2 .

If, for example, $d_1 < d_2$ and thus $n_1 > n_2$, the nanoparticle will be charged positively and may retain this charge for some time. On the next DC voltage sweep, a larger negative potential will be required to overcome the positive charge on the particle. As a result the threshold (step) on I-V curve will shift to the left.

5.4.3. C-V characteristic of films containing CdS (or ZnS) nanoparticles

The AC measurements in sandwich structures as frequency dependencies of the capacitance and their AC conductance as a function of frequency represent a traditional insulating behaviour for all films studied. Figure 5.51 shows typical results of the C-V measurements of sandwich structures (ITO/insulator/CdS /insulator/Hg) as frequency dependencies of the capacitance. As can be seen, the capacitances of the films were not

really correlated to films thicknesses. It might be caused by the random distribution of CdS nanoparticles in the films.

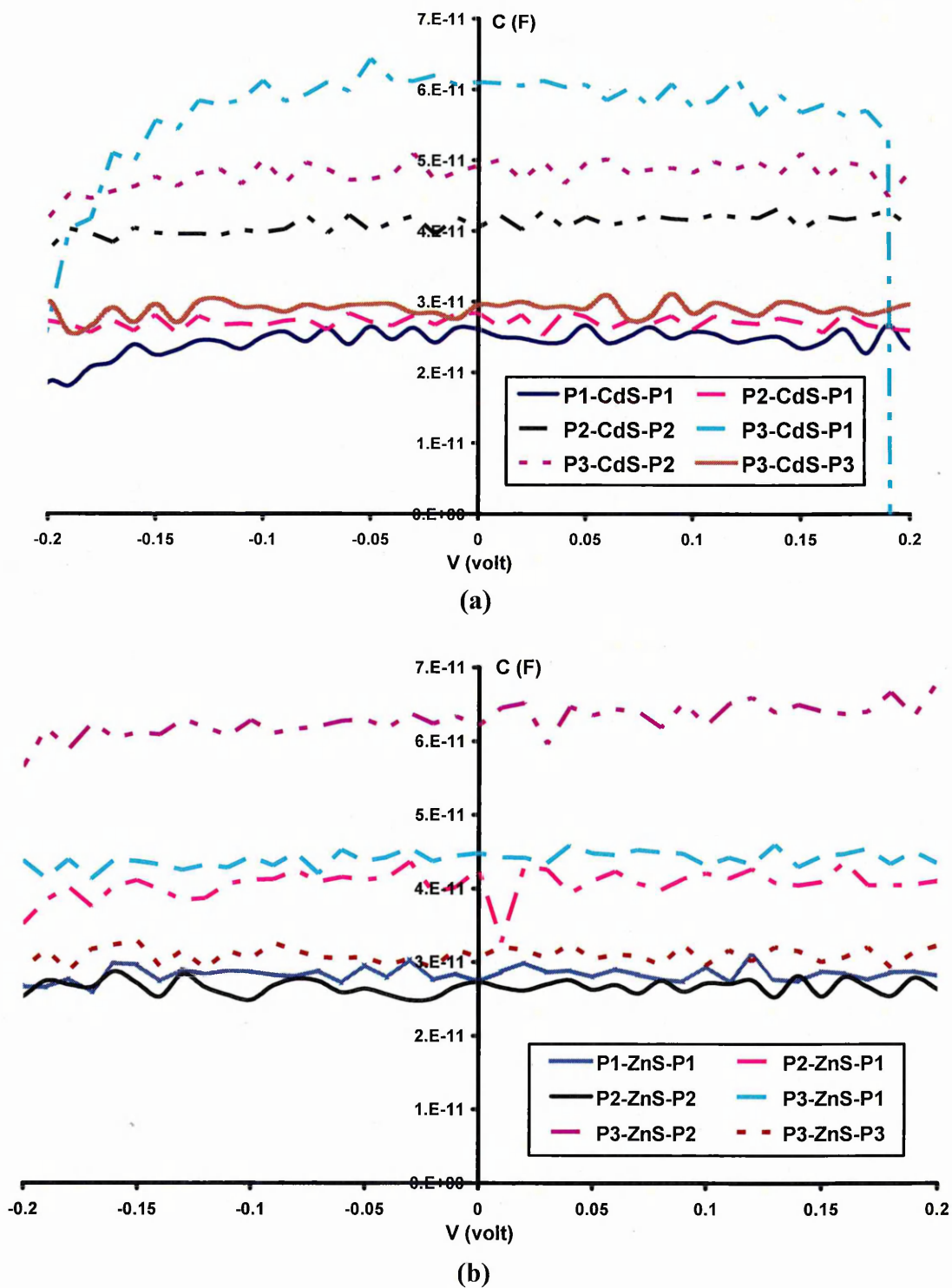


Figure 5.51. C-V characteristic of sandwich structures.

(ITO/insulator/CdS /insulator/Hg) (a) and (ITO/insulator/ZnS /insulator/Hg) (b).

If the system is considered as a plane capacitor, then the capacitance is defined as:

$$C = \frac{\epsilon \epsilon_0 A}{d} \quad (5.6)$$

where A is the cross section area of the capacitor, d is the separate distance, ϵ is the dielectric constant, and ϵ_0 is the electric permittivity in vacuum. Typical diameter of mercury contact was 0.22 ± 0.03 mm giving an active device area of 0.038 ± 0.001 mm². Therefore the calculations of the dielectric constant for the highest capacitance of 0.61 pF from Figure 5.51, with the film thickness of about 5 nm obtained from ellipsometry measurements yield the values of about 0.9 for the films containing CdS nanoparticles and 0.92 for ZnS films. The obtained values of ϵ are less than one, which means that the nanoparticles are conductive so that C-V measurements were affected by the films conductivity only.

This result is supported by the measurements of G-V characteristic, as shown in Figure 5.52. It shows that the conductance was increased at the voltage of 0.2 volt for CdS and at 0.3 volt for ZnS.

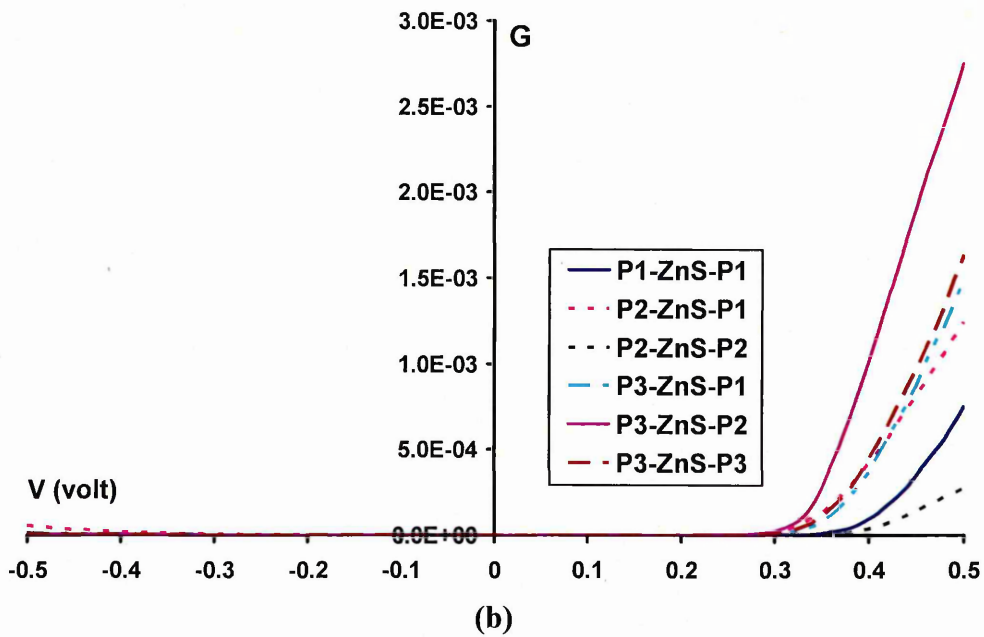
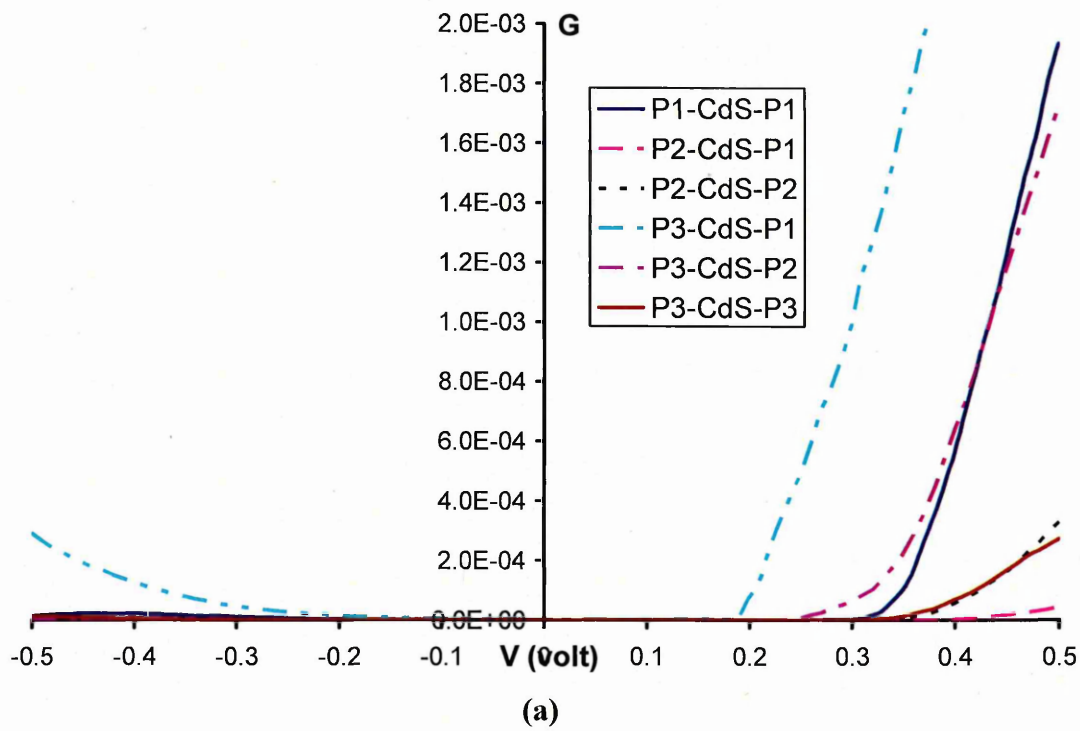
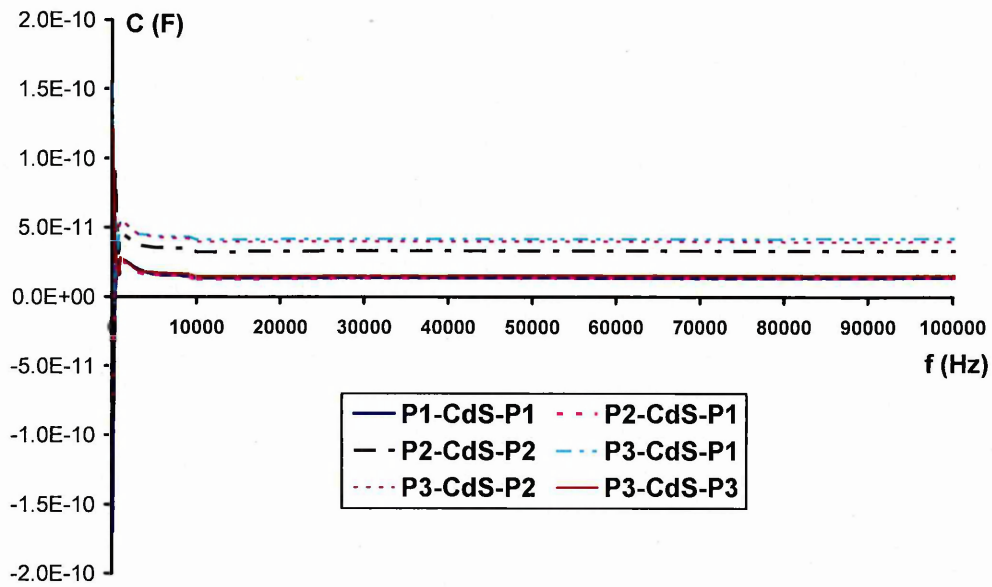
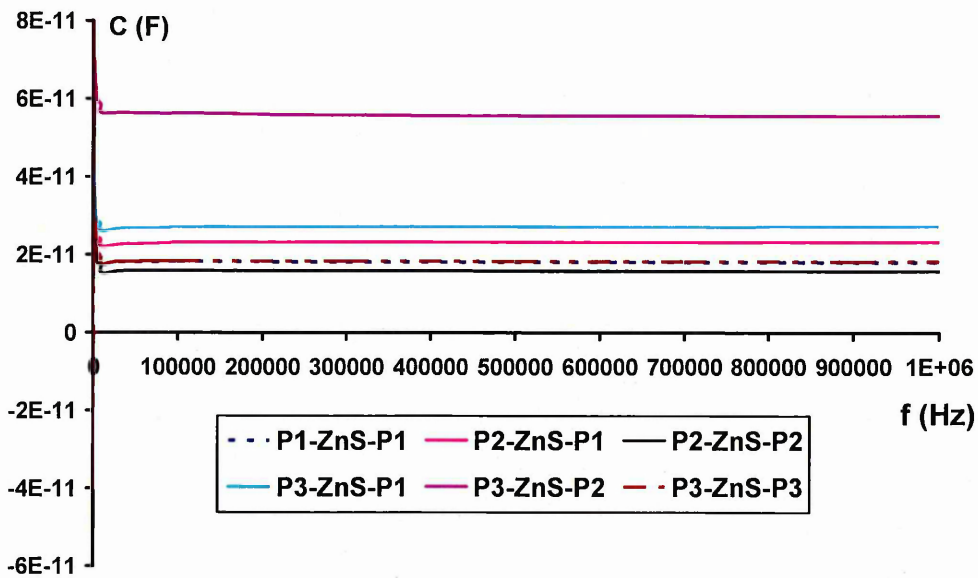


Figure 5.52. G-V characteristic of sandwich structures (ITO/insulator/CdS /insulator/Hg) (a) and (ITO/insulator/ZnS /insulator/Hg) (b).

Figure 5.53 demonstrates the AC conductance as a function of frequency. As can be seen, the capacitance of both CdS and ZnS films is practically independent of frequency over the range of $10^2 - 10^6$ Hz, which could be another proof of the tunnelling behaviour.



(a)



(b)

Figure 5.53. C-f characteristic of sandwich structures (ITO/insulator/CdS /insulator/Hg)

(a) and (ITO/insulator/ZnS /insulator/Hg) (b).

5.5. ELECTROLUMINESCENCE STUDY

Electroluminescence measurements were carried out using a Hamamatsu H7421 photon counter in the spectral range from 380 to 890 nm. The schematic diagram of experiment measurements is shown in Figure 5.54. A transparent electrolyte solution of 1 M NaCl is used in this work.

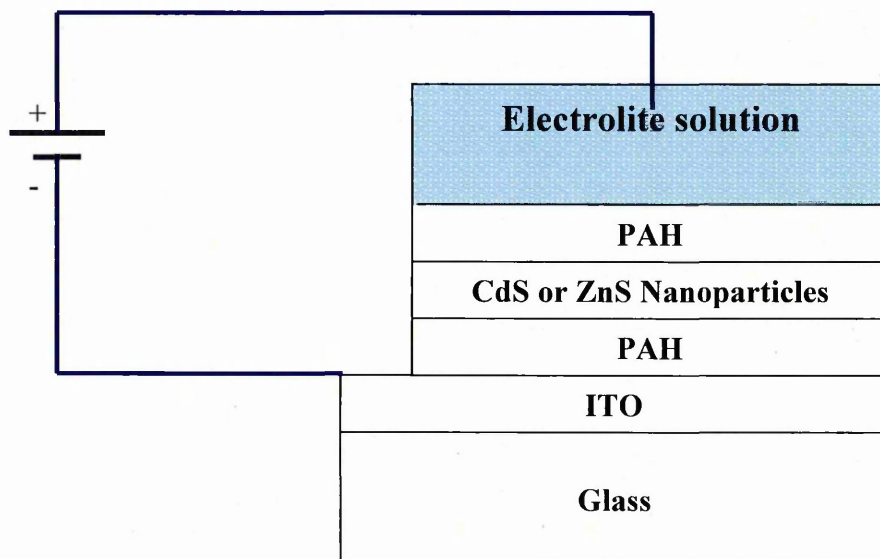


Figure 5.54. Schematic diagram of electroluminescence experiment set-up.

All the prepared samples were listed as follows:

$$P3 = \text{ITO} + \text{PAH}$$

$$P4 = \text{ITO} + \text{PAH} + \text{PSS}$$

$$C1 = \text{ITO} + \text{PAH} + \text{CdS SO}_3^- + \text{PAH}$$

$$C2 = \text{ITO} + \text{PAH} + \text{CdS SO}_3^- + \text{PAH}$$

$$C3 = \text{ITO} + \text{TiO}_2 + \text{PAH} + \text{CdS SO}_3^- + \text{PAH}$$

$$C4 = \text{ITO} + \text{TiO}_2 + \text{PAH} + (\text{CdS SO}_3^- + \text{PAH})_3$$

$$C5 = \text{ITO} + \text{TiO}_2 + \text{PAH} + (\text{CdS SO}_3^- + \text{CdS NH}_2^+)_2 + \text{PSS}$$

$$C6 = \text{ITO} + \text{PAH} + (\text{CdS SO}_3^- + \text{PAH})_3$$

$$C7 = \text{ITO} + \text{PAH} + (\text{CdS SO}_3^- + \text{PAH})_{10}$$

$$C8 = \text{ITO} + \text{PAH} + (\text{CdS SO}_3^- + \text{PAH})_{20}$$

Z1 = ITO + PAH + ZnS SO₃⁻ + PAH

Z2 = ITO + PAH + ZnS SO₃⁻ + PAH

Z3 = ITO + TiO₂ + PAH + ZnS SO₃⁻ + PAH

Z4 = ITO + TiO₂ + PAH + (ZnS SO₃⁻ + PAH)₃

Z5 = ITO + PAH + (ZnS SO₃⁻ + PAH)₃

Firstly, I-V characteristics measurements were performed in order to find the threshold voltage of electroluminescence of the samples. Figure 5.55 shows the forward bias of I-V measurements of all samples. The threshold voltage were found at about 1.5 V for CdS and 0.7 V for ZnS.

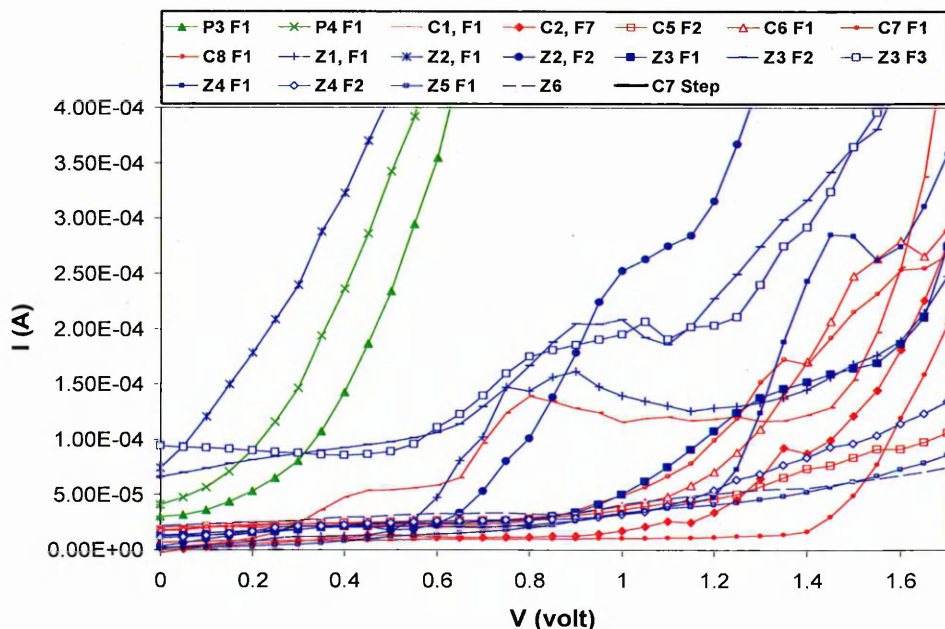


Figure 5.55. I-V measurements of the electroluminescence samples.

Before using the photon counter, the level of the ambient light had to be reduced to the lowest possible level because of a very sensitive photodetector. The instrument's test certificate from Hamamatsu stated that the dark count level of the instrument averaged 22 photons per second (p/s). This could be achieved by turning off the light and covering the detector input window, the results is shown in Figure 5.56.

Photons Per Second 22
Using Black Cover

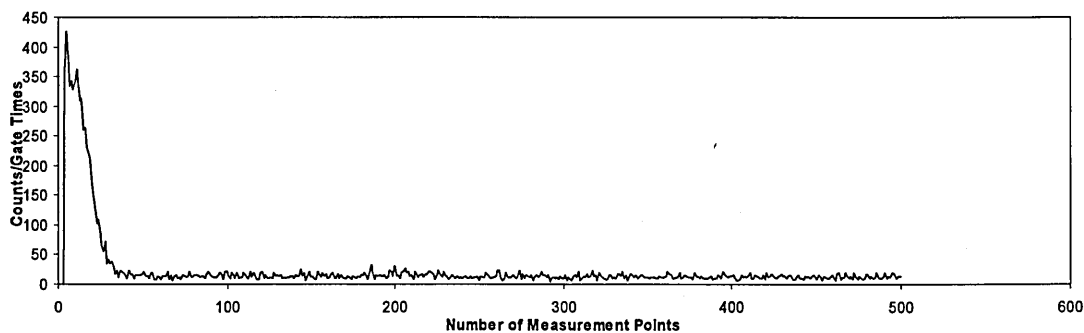


Figure 5.56. The dark count level of the Hamamatsu instrument of averaged 22 photons per second.

The electroluminescence of PAH and PSS films were measured as reference samples and show no luminescence, as the level of photon per second buried in the noise of the instrument. The electroluminescence has been detected on samples of [PAH-(CdS-PAH)₃] structure, deposited on TiO₂ coated ITO, with 2.4 volt of applied voltage. When the voltage was switched on at $t = 8$ s, the number of photons per second increased from the ambient noise to a peak of 15200 photons per second (p/s) in 4 seconds (see Figure 5.57) and then decays exponentially to the value of around 150 p/s, which is higher than the original noise level but small enough to be considered negligible.

C4, 2.4V on at t = 8s

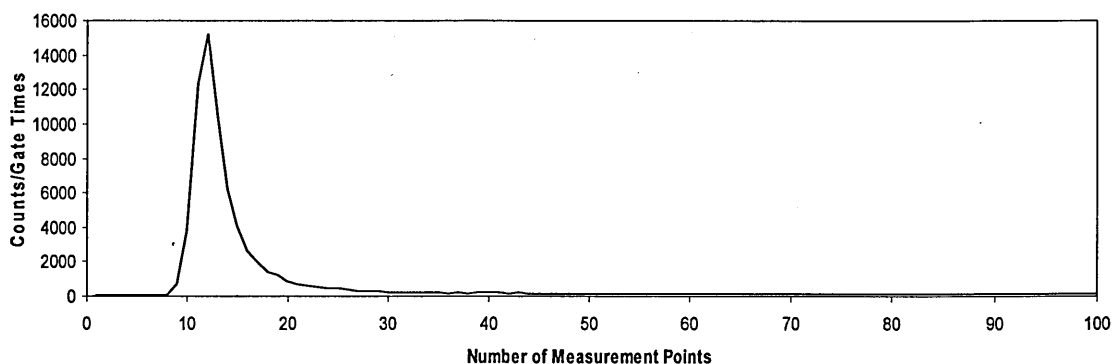


Figure 5.57. The electroluminescence for a sandwich structure of [PAH-(CdS-PAH)₃] on TiO₂.

The effect of the voltage on/off switch on the intensity of electroluminescence was investigated and presented in Figure 5.58. When the voltage was switched off at $t = 53$ s, the intensity was decreased to the dark count level. And then went back to the value at about 150 p/s when the voltage was switched on at $t = 57$ s. It seems that the sample need time to recover before it could be subjected to another test. It must be noted that the intensity in Figure 5.58 is also lower than that in Figure 5.57.

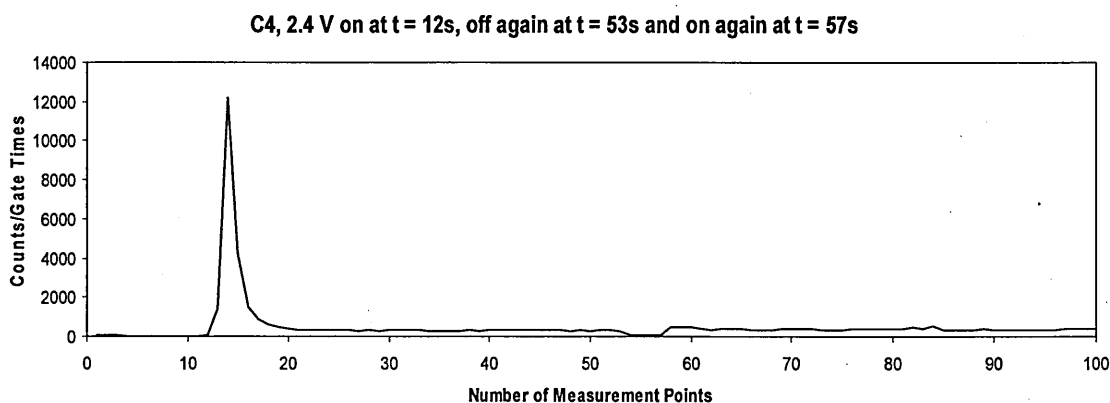


Figure 5.58. The electroluminescence for a sandwich structure of $[\text{PAH}-(\text{CdS}-\text{PAH})_3]$ on TiO_2 with the voltage switch on and off.

The recovery time of the sample was investigated by applying AC voltage with different frequencies. Figure 5.59 shows the responses of polyelectrolyte/nanoparticles films to different frequencies of a 2V RMS signal. From $t = 0$ to $t = 380$ s, the frequency of about 80 mHz was applied and the periodic peaks were clearly seen. Between 380 and 420 s, 800 mHz was applied and no peaks were seen. From 420 to 1000 s, the frequency of 8 mHz gives the periodic peaks with interval of about 125 s. It can be concluded that the best results were achieved at lower frequencies. This could be a result of a limited ion supply in the electrolyte cell, which does not allow the response to switch faster than 100 mHz.

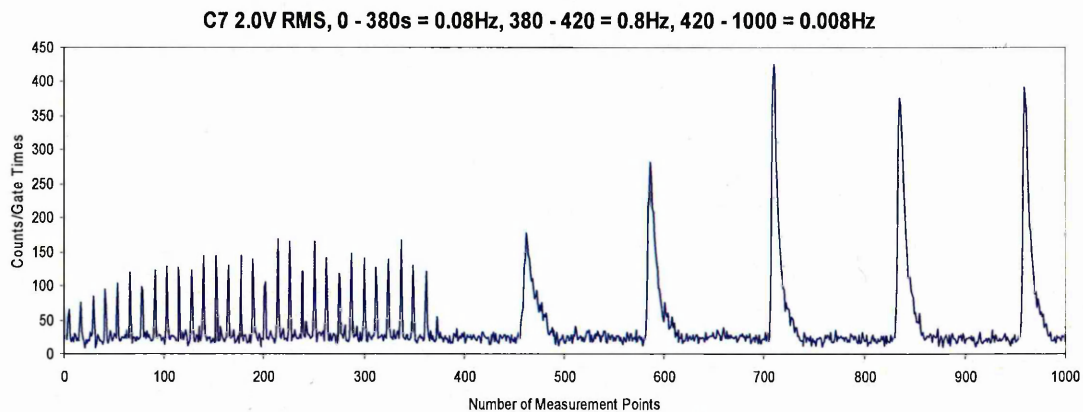


Figure 5.59. The electroluminescence for a sandwich structure of [PAH-(CdS-PAH)₁₀] on ITO with different frequencies signal.

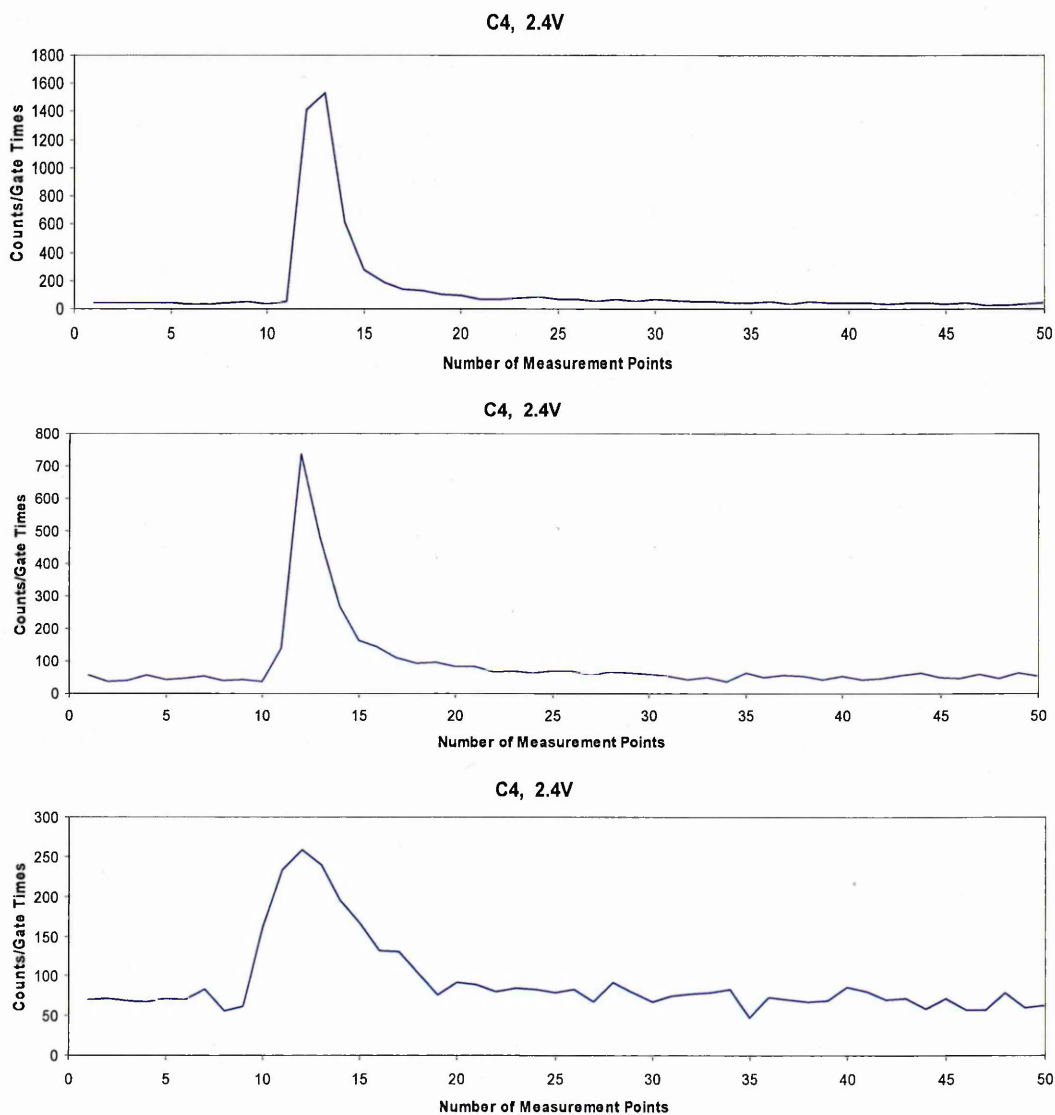


Figure 5.60. Results of several tests of the electroluminescence for a sandwich structure of [PAH-(CdS-PAH)₃] on TiO₂.

As mentioned before, luminescence intensity decrease was observed in a number of test. This phenomenon was verified by measuring the luminescence of the same sample at a certain interval of time (more than 10 s). The results are summarized in Figure 5.60. It shows that the luminescence peak of sample C4 is decreased significantly, from 15200 to 1532 p/s and the latter measurement shows that the intensity decreases further to 258 p/s. Then the sample gives no luminescence anymore which reflects a very short lifetime of the sample.

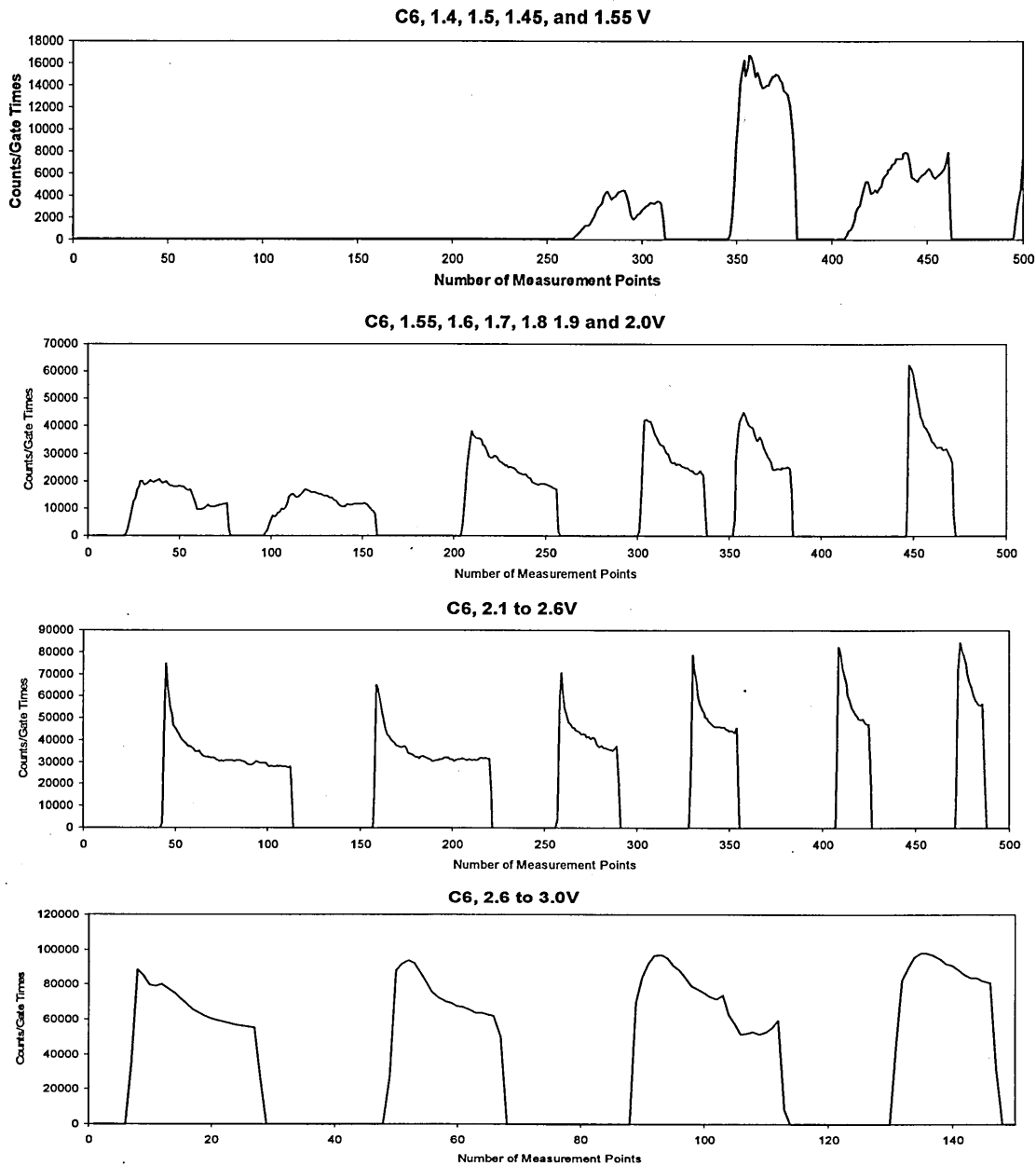


Figure 5.61. The effect of step input voltage to EL intensity.

The effect of the applied voltage increase from 0 to 3 V with a step of 0.1 V on the electroluminescence intensity was investigated, and the results are presented in Figure 5.61. The luminescence started at $V = 1.4$ volt, as predicted from the I-V characteristics (1.5 V for CdS). The results mostly show an irregular increase in the peak intensity as the voltage increases.

The highest points of each peak were taken and plotted as a function of voltage in Figure 5.62. The curve suggests that the behaviour of light emission with the threshold voltage at about 1.4 volt.

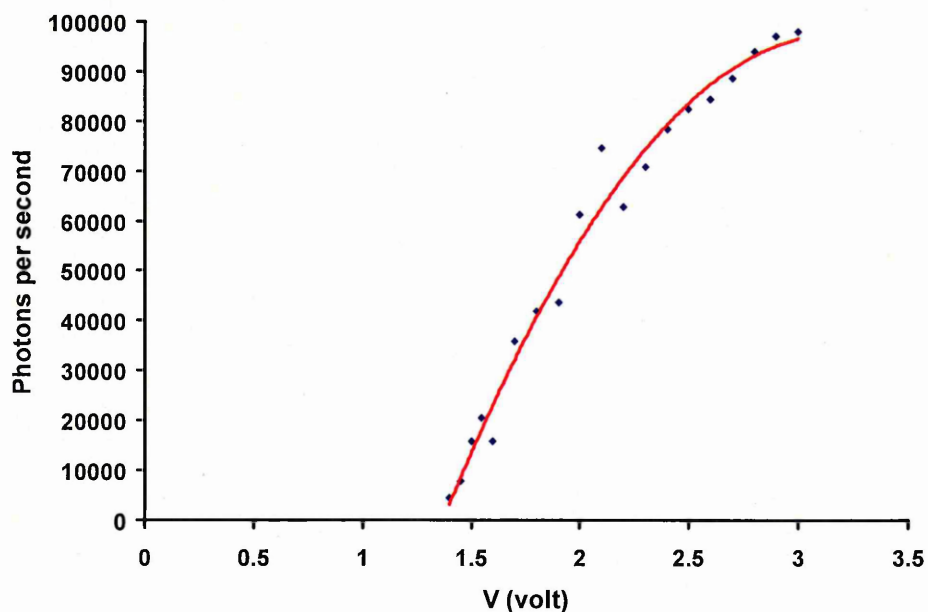


Figure 5.62. The electroluminescence intensity as function of the input voltage.

The luminescence was also detected in sandwich structure of $[\text{PAH}-(\text{CdS}-\text{PAH})_3]$ samples with the peak of about 56201 p/s (see Figure 5.63).

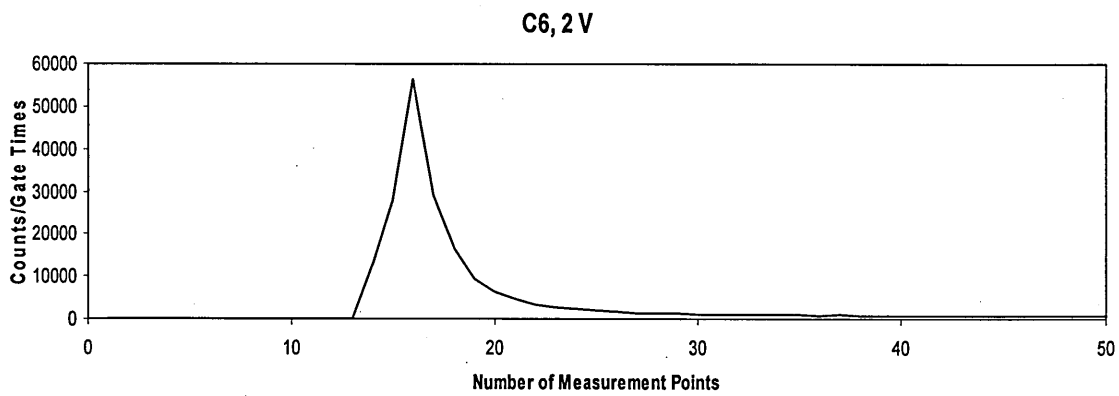


Figure 5.63. The photon count for a sandwich structure of [PAH-(CdS-PAH)₃] on ITO.

Figure 5.64 and 5.65 present the luminescence of 10 and 20 layers of CdS. The highest peaks of 138823 and 266295 p/s were observed, respectively, and then rapidly decayed to a constant level of about 2000 p/s.

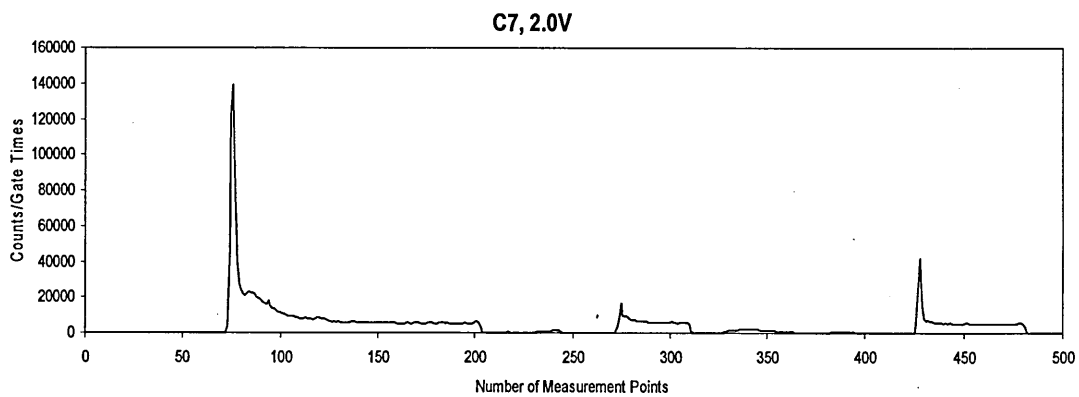


Figure 5.64. The photon count for a sandwich structure of 10 layers of CdS.

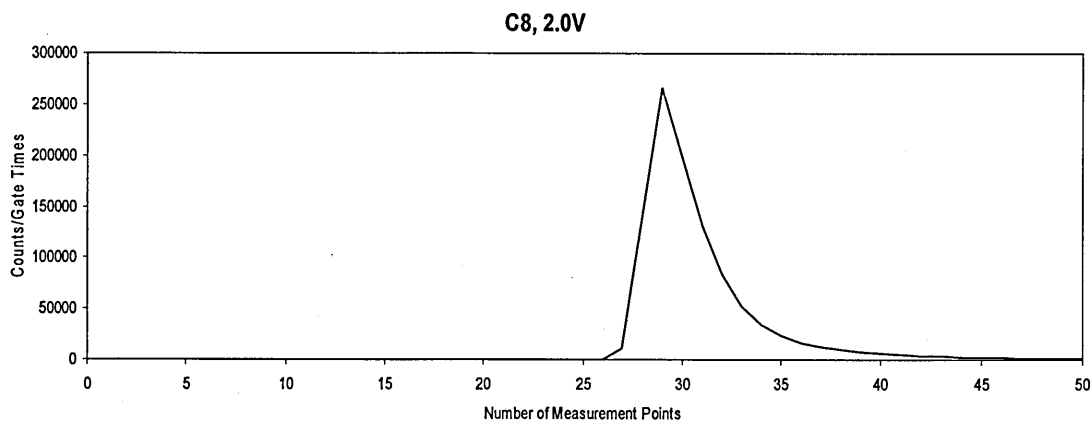


Figure 5.65. The photon count for a sandwich structure of 20 layers of CdS.

From the above results, the increase in the number of CdS layers leads to the increase in the intensity of electroluminescence. By plotting the highest point of the luminescence peaks as a function of the number of layers, the correlation shows a linear dependence in Figure 5.66.

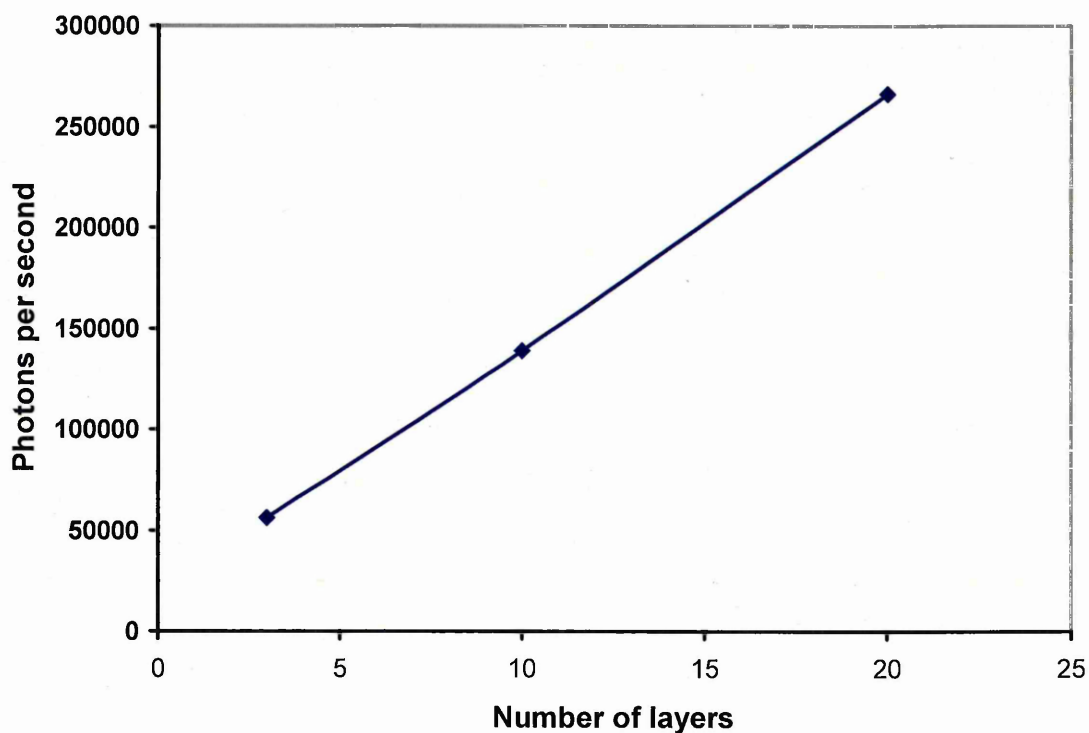


Figure 5.66. The electroluminescence intensity as function of number of layers.

Unfortunately, no trace of luminescence was observed for films containing ZnS nanoparticles. They might emit light in ultra violet region which can not be detected by the particular photon counter detector, as the detector is made from GaAs which can only detect the light in the spectral range of 380 to 850 nm.

REFERENCES

1. Yoffe A. D. "Semiconductor quantum dots and related systems: Electronic, optical, luminescence and related properties of low dimensional systems." *Advances in Physics* 50 (2001): 1-208.
2. Nabok A. V., Richardson T., McCartney C., Cowlam N., Davis F., Stirling C. J. M., Ray A. K., Gacem V., and Gibaud A. "Size-quantization in extremely small CdS clusters formed in calixarene LB films." *Thin Solid Films* 327-329 (1998): 510-514.
3. Nanoparticle Mediated Photodefluorination Monitored by F-19 NMR, 13 August. 2007 <www.chemistry.armstrong.edu/lynch/19FNMR2.pdf>.
4. Lvov Y. M. "Thin film nanofabrication by alternate adsorption of polyions, nanoparticles and proteins." Handbook for Surfaces and Interfaces Vol. 3 Nanostructured Materials. Ed. H Nalwa. New York: Academic, 2001. p. 170-89.
5. Nabok A. V., Richardson T., Davis F., and Stirling C. J. M. "Cadmium sulfide nanoparticles in Langmuir-Blodgett films of calixarenes." *Langmuir* 13 (1997): 3198-3201.
6. *Guide to Using WVASE32*. J. A. Woollam Co., Inc., 2002.
7. Nabok A. V., Massey J., Buttle S., and Ray A. K. "Study of electron tunnelling through thin polymer films using a mercury probe technique." *IEE Proceedings: Circuits, Devices and Systems* 151 (2004): 461-465.
8. Nave, Carl R. "Work Functions for Photoelectric Effect." *Hyperphysics*. 2006. Georgia State University. 13 August. 2007 <<http://hyperphysics.phy-astr.gsu.edu/hbase/tables/photoelec.html>>.
9. Jones R., Krier A., Davidson K., Schmit J.P.N., and Zawadzka J. "Conductivity mechanisms in poly (p-phenylene vinylene) light-emitting diodes at high and low bias." *Thin Solid Films* 340 (1999): 221-229.

CONCLUSIONS AND SUGGESTIONS FOR FUTURE WORK

6.1. CONCLUSIONS

This work demonstrated the feasibility of the electrostatic self-assembly method to fabricate multilayered CdS (or ZnS) nanostructures onto different solid substrates such as silicon, glass, quartz, chromium/gold coated glass, and ITO. Several combinations of CdS (or ZnS) nanostructures assembled from positively and negatively charged CdS (or ZnS) nanoparticles alternated with PAH and PSS binding layers have been prepared. Mixed films containing both CdS and ZnS nanoparticles were also successfully deposited. Optical and electrical properties of the films obtained along with the morphology and electroluminescence were studied using a variety of experimental techniques including UV-visible spectroscopy, spectroscopic ellipsometry, AFM, DC and AC electrical measurements combined with the mercury probe and electroluminescence photon counting.

From UV-Vis spectroscopy measurements, the position of the main absorption band obtained for CdS and ZnS colloid solutions were 410 nm and 295 nm, respectively, while the films containing CdS and ZnS have the values of 405 nm and 290 nm. Both of them show a substantial blue shift with respect to the respective bulk materials (512 nm for CdS, 335 nm for ZnS). The calculations of nanoparticles' radius with Efron model yield the same value of about 1.8-1.9 nm for both CdS and ZnS.

The external reflection spectroscopy ellipsometry measurements of the thin films containing CdS and ZnS, confirmed the deposition of polyelectrolyte and nanoparticles on top of the silicon substrate. The fitting of the ellipsometry data yields the parameters d , n , and k of the films. The thicknesses of nanoparticle layers of around 5 nm were

obtained for both CdS and ZnS. These values correspond well to the size of particles evaluated from UV-vis spectral data if an additional thickness of the organic shell is taken into account. The obtained values of n (of about 2.28) for both CdS and ZnS were slightly smaller than respective values of bulk materials (2.475 for CdS and 2.364 for ZnS), but the value of k (of about 0.76) deviated substantially from the respective values of bulk materials (0.0186 for CdS and 0.0077 for ZnS). This may be attributed to the substantial increase in the oscillator strength in semiconductor nanoparticles.

The $\psi(\lambda)$ and $\Delta(\lambda)$ spectra in total internal reflection ellipsometry (TIRE) measurements clearly show the consecutive deposition of polyelectrolytes and nanoparticles by the shift of $\Delta(\lambda)$ spectra to longer wavelength. The fitting of TIRE spectra using EMA model for mixed polyelectrolyte/nanoparticles films gave the thicknesses of about 7 nm and 12 nm for CdS and ZnS, respectively. This result confirms the formation of three-dimensional aggregates of semiconductor nanoparticles intercalated with the polyelectrolyte.

The dynamic scan of TIRE was used to monitor in-situ the process of alternating deposition of Poly-allylamine Hydrochloride (PAH) and CdS (or ZnS) layers. The results suggested 35 and 28 minutes, respectively for the first PAH and the first nanoparticles layer to saturate. The dynamic scan also shows that the saturation time for the second layer of PAH layer is much faster, of about 24 minutes. The same behaviour was also observed for nanoparticles, the saturation time for the second and the third layer is much faster than that of the first layer.

AFM tapping mode images show the formation of large aggregates of polyelectrolyte and nanoparticles. For the films deposited from undiluted colloid solutions, the aggregates were about 40-50 nm in size, while smaller aggregates, of about 12-20 nm, were obtained if the colloid solutions were diluted.

The DC I-V characteristics of sandwich structures of Hg/polyelectrolyte/ITO show exponential behaviour typical for electron tunneling. The presence of CdS and ZnS nanoparticles in polyelectrolyte films decrease the conductivity value, which is believed to be caused by the increase in the film thickness due to the aggregation of nanoparticles and intercalation with polyelectrolytes. C-V measurements for both CdS and ZnS show very low capacitances which give the value of dielectric constant of $\epsilon < 1$. This indicates that CdS and ZnS nanoparticles are conductive which is also supported by G-V measurements. The measurement of capacitance as a function of frequency of both CdS and ZnS films show that the capacitance is practically independent of frequency over the range of $10^2 - 10^6$ Hz which could be another proof of the tunnelling behaviour.

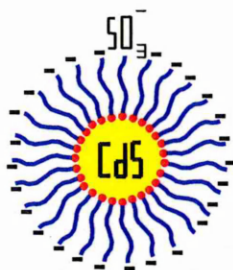
The electroluminescence (EL) from the sandwich structure of (PAH/CdS/PAH)_N was detected using photon counter detector. The luminescence was found to decay rapidly and needs about 10 s before the sample could be subjected to the next measurement. The study shows that the electroluminescence was started at the input voltage of 1.4 V and the intensity was increased by increasing the applied voltage. The intensity of electroluminescence was found to be in linear proportion to the number of nanoparticle layers. In the case of ZnS films, the luminescence can not be found, possibly because the luminescence was out of the range of the photodetector used.

6.2. SUGGESTIONS FOR FUTURE WORK

This section proposes further investigations that will specifically extend the work described in this document.

1. The results of the spectroscopic ellipsometry and AFM show large aggregates of semiconductor nanoparticles intercalated with polyelectrolyte. We suggested that it

was caused by the large number of ions (SO_3^- or NH_2^+) in the organic stabilizing shell.



As a result, the polyelectrolytes are attracted, tangled with polyelectrolyte and formed large aggregates. Using a mixture of charged and neutral capping agents the number of charged ions could be reduced. This idea was attempted but resulted in non-stable colloids. Further alteration in the colloid synthesis is required to produce more regular structures of polyelectrolyte/nanoparticles.

2. This project was mostly focused on the fabrication and characterisation of electrostatically self-assembled films containing CdS (or ZnS) nanoparticles prepared by aqueous-phase method. Although the combination of CdS and ZnS was successfully deposited and the absorption spectra were measured, the films were not fully characterised. It would be very interesting and might be useful, to study in more detail II-VI semiconductor layers containing different nanoparticles.
3. AFM measurements could not image the nanoparticles individually. One of the reasons, is the limited resolution of AFM due to the finite size of the AFM's tip. However, AFM images of films deposited from diluted solutions showed smaller size and separated groups of nanoparticles clusters. Such deposition conditions combined with the use of a very flat substrate such as mica may improve the result. TEM study would be useful to observe individual nanoparticles.
4. Electroluminescence study showed a very short lifetime of luminescence and the samples. More experiments are needed to investigate this matter in more detail and

to improve the lifetime and the intensity of the luminescence. Different structures of nanoparticles doped with other materials could be considered.

5. This work could be expanded towards the use of other metal salts and thus other metal sulphide nanoclusters, such as PbS.